UNIVERSITY OF SOUTHAMPTON

Faculty of Engineering and Physical Sciences

School of Engineering

Electrical-thermal characteristics of HTS winding applications

by

Qingbo Zhang

A thesis submitted for the

degree of Doctor of Philosophy

March 2019

Research Thesis: Declaration of Authorship

Print name: Qingbo Zhang

Title of thesis: Electrical-thermal characteristics of HTS winding applications

I declare that this thesis and the work presented in it are my own and has been generated by me as the result of my own original research.

I confirm that:
This work was done wholly or mainly while in candidature for a research degree at this University;
Where any part of this thesis has previously been submitted for a degree or any other qualification at this University or any other institution, this has been clearly stated;
Where I have consulted the published work of others, this is always clearly attributed;
Where I have quoted from the work of others, the source is always given. With the exception of such quotations, this thesis is entirely my own work;
I have acknowledged all main sources of help;
Where the thesis is based on work done by myself jointly with others, I have made clear exactly what was done by others and what I have contributed myself;
Parts of this work have been published as shown in Appendix II.

Signature: Date:

UNIVERSITY OF SOUTHAMPTON

ABSTRACT

Faculty of Engineering and Physical Sciences

Institute of Cryogenics

Doctor of Philosophy

Electrical-thermal characteristics of HTS winding applications

by Qingbo Zhang

Superconductivity is considered as one of the great scientific discoveries of 20th century. With the advantages of the properties of superconducting materials with zero electrical resistance and perfect diamagnetism. There is a wide range of innovation and developing applications in the field such as large magnets for Nuclear Magnetic Resonance, Magnetic Resonance Imaging, and large scale accelerators for multiphysics. At the end of 1980s, the discovery of High Temperature Superconducting (HTS) materials such as Yttrium Barium Copper Oxide (YBCO) and Bismuth Strontium Calcium Copper Oxide (BSCCO) made it possible to use liquid nitrogen to cool down HTS windings for various electrical power systems, instead of using more expensive liquid helium. Other advantages for using HTS windings instead of copper windings include the ability to manufacture smaller and lighter devices with greater energy saving.

In reference to designing an HTS winding from long lengths of superconducting wire, (which is presently unavoidable without including joints), the electrical contacts themselves must have similar performance. Since the electrical contact resistance of the HTS joint has a significant impact on the thermal stability of the entire system during the operation, a reproducible soldering methodology is required for manufacturing small electrical contacts between current leads and superconductor and or superconductor to superconductor.

A potentially attractive nanobond technique was applied for the first time to HTS tapes at Oxford Instruments for making joints with very low contact resistance, and experimentally characterised at University of Southampton. The nanobond process that used a patented nanofoil offered a possible solution for making reliable and repeatable HTS joints. In parallel, a new methodology was developed for joining 2G-tapes joints in the construction of a long HTS coil. The contact resistance measurements from a series of nano-bonded soldered joints, demonstrated the potential to apply the same technique to make in-situ and reproducible joints of tapes that could be replicated for much longer scale HTS windings.

The 2G YBCO Roebel cable is a promising option for high energy accelerator magnets and Tokamak devices due to its high current carrying capability and compactness. However, its structure and configuration complicate how its current shares, and therefore it is difficult to apply traditional superconductor quench measurement methodologies to characterise Roebel cables in an adiabatic condition. This work reports upon a new methodology developed to study quench of a 2G YBCO Roebel cable pancake coil. The geometrical design was such, that it could be fully immersed in liquid nitrogen (LN2) to perform the experimental

measurements. The initial results from a series of trial quench measurements demonstrated the robustness of the Roebel pancake coil under quench conditions and good agreement between experimental and modelled results to assist in the understanding of current sharing.

The full scope of work presented in this thesis carried out measurements to obtain the thermal, mechanical and electrical properties of nanofoil at cryogenics temperatures. The work progressed to study and developed a new method of formed HTS joints by nanobonds. Finally, the critical current, current injection electrical contacts, and quench characteristics of a Roebel cable were performed and investigated in LN2 at 77 K.

Acknowledgement

I would like to thank my supervisor Professor Yifeng Yang and supervisor Dr. Edward Young for giving me strong supporting and patient instructions during years of my PhD. Without you this work would not have been possible. My thanks to you both, teaching me how to think and tackle problems and training me to become a good researcher.

I am grateful to Dr. Wendell Bailey for his help for teaching me how to work in the laboratory and discussions on experimental design. I would also like thank Professor, Carlo Beduz, Dr. Kevin Goddard for their help at various stages throughout this work.

I would like acknowledge Mr. Mike Webb and Mr. Rob Loades for their help with manufacturing experimental components and setting up equipment, and colleagues at the University of Southampton, Institute of Cryogenics, namely Dr. Iole Falorio, Dr. Jorge Pelegrin-Mosquera, Dr. Jessica Spurrell and Mr. Thom Bostock for their continued help and support. I am very happy to work with my colleagues and friends and thank you for a memorable experience.

Finally, my love to my family and friends for their help and support during my PhD study.

Contents

Research Thesis: Declaration of Authorship I
ABSTRACT III
Acknowledgement V
Contents VII
List of Figure XIII
List of Table XXIII
List of Symbols XXV
List of Abbreviation XXIX
Chapter 1 Introduction 1
1.1 A new nanobond technology in contact joints for HTS applications. 3
1.1.1 Pre-condition for successful joints 4
1.1.2 NiAl films from the reaction of Ni/Al multilayers 5
1.1.3 Physical properties of NiAl 6
1.1.3.1. Electrical resistivity of NiAl 7
1.1.3.2. Thermal conductivity of NiAl 9
1.1.3.3. Heat capacity of NiAl 11
1.1.3.4. Mechanical property of NiAl and its application 12
1.1.4 Background of Aliminum Oxide/Alumina (Al2O3) 14
1.2 Roebel cable from 2G YBCO HTS conductors 15
1.2.1 The design and preparation of Roebel cable 16
1.2.2 The performance of Roebel cable 16
1.2.3 Roebel cable current injection soldering joints 19
1.2.4 Thermal stability of Roebel cable 19
Chapter 2 Background of Superconductivity 21
2.1 Introduction to superconductivity 21
2.2 Introduction to material for HTS winding aplications 23
2.2.1 First generation high temperature superconductors (1G HTS) 23
2.2.2 Second generation high temperature superconductors (2G HTS) 25
2.3 Theory of applied superconductivity 29
2.3.1 Theory of material physical properties 29
2.3.1.1. Theory of electrical resistivity 29
2.3.1.2. Theory of thermal conductivity 29
2.3.1.3. Theory of heat capacity 31

2.3.2 Electrical contact characteristics of HTS joints 31
2.3.2.1. Contact resistance of soldering joints 31
2.3.2.2. Current transfer characteristics in HTS tape joints 32
2.3.2.3. Electrical contact resistance measurements of 2G-tapes soldering joints 34
2.3.2.3.1. 2G tape to 2G tape Soldering joints 34
2.3.2.3.2. 2G-tape to copper soldering joints 35
2.3.3 Critical state of superconductors 35
2.3.4 Non-linear *E-J* characteristics 37
2.3.5 Quench and thermal run away 38
2.3.5.1. Thermal stability 39
2.3.5.2. Minimum Quench Energy (MQE) 40
2.3.5.3. Minimum Propagation Zone (MPZ) 40
2.3.5.4. Current sharing 41
Chapter 3 Nanobond joints in HTS coil application 43
3.1 Introduction 43
3.2 Research aims and objectives 44
3.3 Methods and Experimental Details 44
3.3.1 Nanofoil samples preparation for resistivity, thermal conductivity and heat capacity measurements by PPMS 44
3.3.1.1. TTO samples preparation 45
3.3.1.2. Resistivity option samples preparation 45
3.3.1.3. Heat capacity option samples preparation 46
3.3.2 SEM and XRD samples preparation 47
3.3.3 Electrical contact resistance measurement of HTS nanobond joints 47
3.3.4 Thermal contact resistance measurement of copper/Al2O3 to copper/Al2O3 nanobond joints 48
3.3.5 Lap shear testing of metallic nanobond solder joints 51
3.4 Results and discussion 55
3.4.1 Physical properties measurements results of nanofoil samples by PPMS 55
3.4.1.1. Resistivity of both reacted and unreacted nanofoil 55
3.4.1.2. Thermal conductivity of both reacted and unreacted nanofoil 59
3.4.1.3. Heat capacity of both reacted and unreacted nanofoil 61
3.4.1.4. The cross-section morphology of reacted nanofoil 66
3.4.2 Reacted nanofoil films for SEM with EDX and XRD investigation 66
3.4.2.1. SEM images and EDX analysis of nanofoil films 69
3.4.2.2. XRD patterns of reacted nanofoil films 71

3.4.3 Electrical contact resistance measurement of HTS nanobond joint 74
3.4.4 Thermal resistance of nanobond and Al_2O_3 soldering joints.....79
3.4.5 Lap shear test on nanobond joint samples.....83
3.5 Conclusion 85
Chapter 4 Current transfer characteristics of 2G HTS joints..... 89
4.1 Introduction..... 89
4.2 Research aims and objectives 89
4.3 Methods and Experimental details 90
4.3.1 1D lap joint current transferring Model between two simple conductors.....90
4.3.1.1. Analytical model..... 90
4.3.1.2. Example runs..... 94
4.3.2 Methodology of Nano-heater made 2G-tapes soldering joints 96
4.3.3 Overall electrical contact resistance measurements of on trials of nano-heater made 2G tape joints.....97
4.3.3.1. The electrical contact resistance of two 2G-tape to copper joints..... 97
4.3.3.2. The electrical contact resistance between two 2G-tapes..... 98
4.3.4 A new method for measuring current transfer characteristics and electrical contact resistance 99
4.3.4.1. Sample preparation..... 99
4.3.4.2. Test bed set up 101
4.4 Results and discussion 103
4.4.1 Electrical contact resistance of nano-heater made 2G-tape joints103
4.4.1.1. Electrical contact resistance of 2G-tape to copper joints at different temperatures..... 103
4.4.1.2. Electrical contact resistance of 2G-tape to 2G-tape joint at 77 K ... 104
4.4.1.3. Overall electrical contact resistance comparison of HTS tape joints 105
4.4.2 Results from sliding needle contact resistance measurements 106
4.4.2.1. Measured voltage as a function of the continuous position x..... 106
4.4.2.2. Curve fitting of the measured voltage $V(x)$..... 108
4.4.2.3. 'Shape Prescriptive Modelling' curve fitting 112
4.4.2.4. Current transfer characteristics of HTS joints.....115
4.4.2.5. Overall joint contact resistance comparison among three lap joint samples 117
4.5 Conculsion 120
Chapter 5 Performance and Quench Characteristics of a Pancake Coil Wound with 2G YBCO Roebel Cable 121
5.1 Introduction..... 121

5.2 Research aim and objectives 122
5.3 Methods and Experimental Details 122
5.3.1 Roebel pancake coil 122
5.3.2 Instrumentation 122
5.3.3 Experimental set up 126
5.3.3.1. Current leads injection contact resistance and critical current and measurements 126
5.3.3.2. Quench measurement 128
5.3.4 Data logger and Protection 128
5.4 Results and Discussion 129
5.4.1 Current injection contacts resistance 129
5.4.2 Nonlinearity of the inner contact voltage 131
5.4.3 Current distribution along the outer strand contacts 133
5.4.3.1. Current distribution along the outer contact copper ring at 77 K 133
5.4.3.2. Current distribution along the outer contact copper ring at room temperature 140
5.4.4 'Balanced' inner and outer contact voltages 146
5.4.5 Critical current in the middle of the coil 147
5.4.6 Quench investigation 153
5.4.6.1. Typical recovery and quench event 153
5.4.6.2. Evalution of different pulse power 155
5.4.6.3. Evalution of different transport currents 156
5.4.6.4. The reponse of strand and contact voltages to the heat pulse 157
5.4.6.4.1. 'Unbalanced quench measurement' 157
Quench decription: 157
Recovery decription: 159
5.4.6.4.2. Balanced' quench measurements 161
Quench description: 162
Recover description: 164
5.4.6.5. Dertermination of Minimum Quench Eenergy 165
5.4.6.5.1. MQE versus different heat pulse power 165
5.4.6.5.2. MQE versus different transport currents 167
5.4.6.5.3. The thermal transport effect on MQE estimation 168
5.4.6.5.4. MQE comparison between 'unbalanced' and 'balanced' thermal conditions 170
5.4.6.6. Curent distribution in the Roebel cable during the quench in a 'balanced' condition 171
5.4.6.6.1. Current distribution on strands 171
5.4.6.6.2. Current distribution on current injection contacts 173

5.4.6.6.3. Current distribution on outer contact copper ring 176
5.4.6.7. The new current leads injection design 177
5.5 Conclusion 178
Chapter 6 Conclusion and future works 181
6.1 Nanobond 181
6.2 Nanoheater 183
6.3 Roebel cable 184
Reference 187
Appendix I: MATLAB code 199
Appendix II: Publications 200

List of Figure

Figure 1.1: The cross-section structure of nanofoil. a) Unreacted nanofoil and b) Reacted nanofoil [16]..... 3
Figure 1.2: A schematic structure diagram for standard nanofoil and solder-plated nanofoil [17]..... 4
Figure 1.3: A schematic drawing for the nanobond reaction preparation..... 4
Figure 1.4: Phase diagram of Ni-Al system [25]..... 5
Figure 1.5: Schematic drawing of a Ni/Al multilayer foil structure [19]..... 6
Figure 1.6: A summary of bulk resistivity of NiAl depends on nickel concentration (at. %) at room temperature [19], [34]–[37]..... 7
Figure 1.7: Electrical resistivity of the NiAl in different nickel concentration (at. %) versus the temperature from 4.2 K to 300 K [36]..... 8
Figure 1.8: The plot for a summary of thermal conductivity of NiAl depending on Al concentration (at. %) [45]–[48]..... 10
Figure 1.9: The plot for calculated electron thermal conductivity, phonon thermal conductivity and sum thermal conductivity of NiAl [139] versus the temperature from 100 K to 1000 K compared with experimental results [137]..... 10
Figure 1.10: The plot of specific heat C_p for NiAl with different Ni concentration (at. %) versus the temperature between 1.4 K and 300 K [45], [51]–[55]..... 11
Figure 1.11: The plot of low temperature specific heat C_V in C_V/T for NiAl with different nickel concentration (at. %) versus T^2 compared with the modified specific heat in (C_V-A)/T (that was moved constant A, as described in texts) and the linear curve fitting of each curve profile [52], [53], [56]..... 12
Figure 1.12: The plot of shear strength of stainless joints and Al joints vs. thickness of Ni/Al multilayer foils [59]..... 13
Figure 1.13: The plot of the shear strength for copper to copper nanobond fabricated with different a) thickness of solder at 25 ºC and 100 ºC respectively, b) temperatures under pressure of 0.5 MPa and 2 MPa respectively, c) applied pressure at 25 ºC and 100 ºC respectively [60]. 14
Figure 1.14: a) Schematic drawing of the detailed geometry of two strands for a Roebel cable [77], [78], and b) the picture showing the assembled 15/5.5 (15 strands with 5.5 mm width) Robel cable..... 16
Figure 2.1: Effect of an applied magnetic field on a superconductor. Magnetic field lines are represented as arrows. The Meissner Effect occurs below the lower critical field (H_{c1}) and is the expulsion of an applied magnetic field upon transition from the normal to superconducting state. Between the lower critical field and the upper critical field (H_{c2}) the flux can enter the superconductors as regularly spaced quantized flux vortices..... 21
Figure 2.2: A schematic drawing showing the resistivity of a low temperature superconductor (LTS) and a high temperature superconductor (HTS) and the copper [99]..... 23
Figure 2.3: a) The Schematic drawing of Bi-2223 crystal unit and b) the picture showing the cross-section of a BSCCO HTS tape [102]..... 24
Figure 2.4: Production of Ag/BSCCO tape by OPIT method [105]..... 24
Figure 2.5: Superconducting critical current of BSCCO tape as a function of applied flux density at different temperatures: a) field perpendicular to the tape and b). field parallel to the tape [106]..... 25

Figure 2.6: a) Schematic drawing of YBCO crystal unit, and b) the picture showing the cross-section of a YBCO HTS tape [110]. 26
Figure 2.7: Tape orientation in respect to applied field. 26
Figure 2.8: Production of YBCO tape by MOD/ MOD/RABiTS method [112]. 27
Figure 2.9: Schematic drawing of SuperPower produced 2G HTS conductor architecture [113], [114]. 28
Figure 2.10: The superconducting current capacity for YBCO and BSCCO superconductors as a function of flux density depending on different temperatures: a) field perpendicular to the tape and b) field parallel to the tape [111]. 28
Figure 2.11: The configuration of a lap soldering joint between two 2G HTS tapes. 32
Figure 2.12: The plot of voltage-current (*VI*) characteristics of two 2G-tape soldering joints compared with a single 2G tape at 77 K. 32
Figure 2.13: Schematic drawing of current transfer length measurement configuration for HTS [6], [142], [143]. 33
Figure 2.14: Typical critical surface (J, B and T) for a superconductor [148], [149]. 36
Figure 2.15: The plot for the difference between the upper critical field (B_{c2}) at zero transport current and the critical field B* with a non-zero transport current [148]. 37
Figure 2.16: The plot for *E-J* characteristics of two assumed samples. Sample 1 is a resistive conductor, and sample 2 is a superconductor, which red solid line represents the power law model, and thick black dash line represents the critical state. Thin horizontal dash line represents the electrical criterion of 1 μV/cm [148], [150]. 37
Figure 2.17: Schematic drawing of one dimensional temperature distribution of the normal zone along the superconducting conductor [103], [158]. 40
Figure 3.1: Schematic drawing for the prepration for the reacted nanofoil samples with different cooling conditions. 45
Figure 3.2: a) Photograph showing the reacted samples and the unreacted samples for thermal transport measurements by PPMS, and b) photograph showing a sample mounting in PPMS_TTO sample holder; 4 pre-tinned copper tapes are fixed by clamps. When a constant DC current flows from $I+$ to $I-$, to measure the voltage across $V+$ and $V-$, the resistance R can be evaluated by Ohm's Law. A same measuring method for thermal conductivity, when a constant heat flux flows from $I+$ to $I-$, temperature difference is measured between $V+$and $V-$, the thermal conductivity can be evaluated by Fourier's Law. 46
Figure 3.3: a) Photograph showing both reacted sample and unreacted sample resistivity measurements by PPMS, and b) photograph showing a sample mounting in the PPMS_Resistivity sample holder, and 4 pre-tinned copper wires are fixed by soldering with 4 wires connecting to the module base. When a constant DC current flows from $I+$ to $I-$, to measure the voltage across $V+$ and $V-$, the resistance can be evaulated by Ohm's Law. 46
Figure 3.4: a) The test bed of contact resistance measurement for the nanobond HTS joints, and b) the schematic drawing of the test bed for contact resistance measurement. 48
Figure 3.5: Schematic drawing of the Al_2O_3 to Al_2O_3 nanobond joint sample for thermal resistance measurements. 49
Figure 3.6: Schematic drawing of the Al_2O_3 to copper soldering joint sample and copper to copper nanobond joint sample for thermal resistance measurements. 50
Figure 3.7: OI metallic nanobond joint samples: a) Stainless Steel to Stainless Steel nanobond joint (bonded at 120 ºC), b) Stainless Steel to Stainless Steel nanobond joint (bonded at room temperature), c) Stainless Steel to Stainless Steel nanobond joint (bonded at 120 ºC), d) Stainless Steel to Stainless Steel nanobond joint (bonded at room temperature), e) Stainless Steel to copper nanobond joint (bonded at 120 ºC), f) Stainless Steel to Copper nanobond joint

(bonded at room temperature), g) Stainless Steel to Stainless Steel nanobond joint (bonded at 120 ºC), h) Stainless Steel to Stainless Steel nanobond joint (bonded at room temperature). 52
Figure 3.8: Lap shear test bed set up 53
Figure 3.9: The plot for the resistivity measurements for a) 3 unreacted samples measured by PPMS compared with some nano-scaled nickel and aluminum [126], [127] and b) bulk nickel in purity of 99.99% and bulk aluminum in purity of 99.99% [166] at temperatures from 5 K to 300 K. Unreacted sample 1, 2 were measured with TTO, and unreacted sample 3 has been investigated the magnetoresistance effect via applying a 3 T field with Resistivity option (Un_Naf: unreacted nanofoil sample, BNL:Brookhaven National Laboratory). 56
Figure 3.10: The plot for resistivity for a) 3 reacted nanofoil samples measured by PPMS compared with b) NiAl with different Ni atomic percentage [36] varying with temperature between 5 K and 300 K. Reacted sample 1, 2 and 3 were measured with TTO, and reacted sample 4 and 5 were measured with Resistivity option, and sample 4 was measured with a magnetic field (3 T) and without field (Re_Naf: reacted nanofoil sample). 57
Figure 3.11: The plot for thermal conductivity for the reacted and unreacted nanofoil measured by PPMS_TTO compared with nickel and aluminum in different purities [173] varying with temperature between 5 K and 300 K (Re_Naf: reacted nanofoil sample, Un_Naf: unreacted nanofoil sample, BNL:Brookhaven National Laboratory). 60
Figure 3.12: The plot for Lorenz number varying with temperature for both reacted and unreacted nanofoil samples (Re_Naf: reacted nanofoil sample, Un_Naf: unreacted nanofoil sample). 61
Figure 3.13: The plot for measured heat capacity of unreacted sample 2 and calibrated heat capacity of unreacted sample 2 (minus grease) compared with calculated heat capacity of unreacted nanofoil sample (Ni+Al, 50:50 at. %) [174], [175] and N-type grease (Un_Naf: unreacted sample, BNL:Brookhaven National Laboratory). 62
Figure 3.14: The specific heat capacity in unit of J/(g×K) of reacted nanofoil sample 2 and 3 and unreacted nanofoil sample 2 compared with that of aluminium, nickel and calculated specific heat of unreacted nanofoil (Ni+Al,50:50 at. %) [174], [175] versus the temperature from 1 K to 300 K (Re_Naf: reacted sample, Un_Naf: unreacted sample, BNL:Brookhaven National Laboratory). 63
Figure 3.15: The specific heat capacity in unit of J/(mol×K) of a) unreacted nanofoil sample 2 compared with aluminium, nickel and calculated specific heat of unreacted nanofoil (Ni+Al,50:50 at. %) [174], [175] and b) reacted nanofoil sample 2 and 3 compared with the specific heat of $NiAl_3$ (Ni, 25 at. %) measured by Dunlop et al and reported in [54], NiAl (Ni, 49.3 at. %) measured by Alexander et al [52], NiAl (Ni, 48 or 50 at. %) measured by Seitchikf et al [56], NiAl (Ni, 50 at. %) measured by Sandakova et al reported in [54], NiAl (Ni, 50.5 and 51 at. %) measured by Begot et al [176], Ni_3Al (Ni, 75 at. %) measured by Dood et al [55], $NiAl_3$ (Ni, 25 at. %) measured by Dunlop et al reported in [54] and specific heat of Al_2O_3 and NiO and estimated specific heat of one mole NiAl (80%NiAl +20%(Ni_3Al+$NiAl_3$)) versus the temperature from 1 K to 300 K [177], [178], and dash line shows the molar specific heat constant at room temperature in accordance with the law of Dulong and Petit (Re_Naf: reacted sample, Un_Naf: unreacted sample, BNL:Brookhaven National Laboratory). 64
Figure 3.16: The specific heat capacity divided by temperature (C_V/T) of reacted nanofoil sample 2 and 3 and unreacted nanofoil sample 2 compared with that of aluminium, nickel Ni+Al (50:50, at. %) [174], [175] and heat capacity of NiAl (Ni, 49.3 at. %) measured by Alexander et al [52], NiAl (Ni, 48 or 50 at. %) measured by Seitchikf et al [56], NiAl (Ni, 50.5 and 51 at. %) measured by Begot et al versus the square of the temperature from 1 K to 10 K (Re_Naf: reacted sample, Un_Naf: unreacted sample, BNL: Brookhaven National Laboratory, and dash lines represents the linear part of the curve profiles). 65

Figure 3.17: The picture indicating the cross-section of a piece of reacted nanofoil (Reacted sample 1): a) Rectangulare area: surface indentations, Rounded rectangular area: surface cracks and fragments and b) Oval area: cross-section of indentation; c) Rectangular area: surface void space/indentation, Round area: cross section hole. 66
Figure 3.18: The pictures for reacted nanofoil samples with different cooling conditions: a) air cooling, b) copper cooling, c) rubber cooling, d) A4 paper submerged with water cooling and e) G10 block cooling. 68
Figure 3.19: SEM images of a) cross-sectional and b) surface of unreacted nanofoil. Two square panes (spectrum 1 and spectrum 2) are the EDX scanned area. 69
Figure 3.20: SEM images of the cross-section of a copper cooling reacted nanofoil with a) X850 amplification and b) X5500 amplification, and a rubber cooling reacted nanofoil with c) X850 amplification and d) X5500 amplification, and a G10 cooling reacted nanofoil with e) X850 amplification and f) X5500 amplification. 70
Figure 3.21: SEM image of a copper to copper nanobond joint. 71
Figure 3.22: XRD pattern of an air cooling reacted nanofoil sample versus 2θ from 30° to 100°. 72
Figure 3.23: XRD pattern of a copper cooling reacted nanofoil sample versus 2θ from 30° to 100°. 72
Figure 3.24: XRD patten of an rubber cooling reacted nanofoil sample versus 2θ from 30° to 100°. 73
Figure 3.25: XRD partten of a water submerged towel paper cooling reacted nanofoil sample versus 2θ from 30° to 100°. 73
Figure 3.26: XRD pattern vs. grazing angles between 43° and 46° for reacted nanofoil samples with different cooling conditions. 74
Figure 3.27: Schematic drawing of the cross section (between 2G HTS tape and copper) of Joint (2A-T) contact resistance measurement of sample 2, and arrows represent the direction of the current. 75
Figure 3.28: Schematic drawing of equivalent circuit for contact resistance network. 75
Figure 3.29: The Plot showing current-voltage for parameters measurements of sample 2. 75
Figure 3.30: The plot for a) current-voltage for the joint contact resistance between terminal and 2G-tape for all samples and b) current-voltage for the joint contact resistance between two 2G-tape for all samples. 76
Figure 3.31: The photo showing the cracks at the surface of reacted nanofoil. 78
Figure 3.32: Schematic drawing of simplified equivalent circuit for contact resistance network. 78
Figure 3.33: Thermal resistance of DBC Al2O3 to DBC Al2O3 nanobond joint, DBC Al2O3, copper shim to copper shim nanobond joint from 5 K to 300 K. (S1, S2 and S3: sample 1, sample 2 and sample 3). 80
Figure 3.34: The microscopy image of the cross-section of Sample 1: DBC Al_2O_3 to DBC Al_2O_3 nanobond joint in a) low brightness and b) high brightness. 80
Figure 3.35: The microscopy image of the cross-section of Sample 2: a) Copper shim to copper shim nanobond joint and b) DBC Al_2O_3 to copper shim soldering (240 ºC melting solder) joint. 81
Figure 3.36: Calculated thermal conductivity of DBC Al_2O_3 to DBC Al_2O_3 nanobond joint and copper shim to copper shim nanobond joint compared with the thermal conductivity compared with the thermal conductivity of the reacted nanofoil measured with PPMS, pure tin (extrapolated values between 40 K and 300 K) [183] and Sn60Pb40 (wt. %) [184] from 5 K to 300 K. (S1, S2: sample 1, sample 2). 82

Figure 3.37: Calculated thermal conductivity of DBC Al_2O_3 compared with the thermal conductivity compared with the thermal conductivity of the reacted nanofoil measured with PPMS, and copper (RRR = 10 and RRR = 100) [183] from 5 K to 300 K (S1, S2: sample 1, sample 2). 83
Figure 3.38: The pictures show the fracture surface of a) StSt-StSt hot plated with tin coated, b) StSt-StSt room temperature plated with tin coated, c) StSt-StSt hot plated with gold coated and d) StSt-StSt room temperature plated with gold coated. 84
Figure 3.39: The pictures show the copper yield of a) StSt-Cu hot plated with tin coated, b) StSt-Cu room temperature plated with tin coated, c) StSt-Cu hot plated with gold coated and d) StSt-Cu room temperature plated with gold coated. 85
Figure 3.40: The pictures show the fracture surface of copper to copper nanobond joint with 180 ºC melting solder of a) Sample 9 made at 60 ºC, and b) Sample 10 made at 60 ºC, and c) Sample 11 made at room temperature, and copper to copper nanobond joint with 240 ºC melting solder of d) Sample 12 made at 60 ºC, and e) Sample 13 made at 60 ºC, and f) Sample 14 made at room temperature. 85
Figure 4.1: 1 D model of a lap joint and parameters 90
Figure 4.2: The plot of a) current distribution and b) electrical field distribution within both conductor 1 (I_1 and E_1) and conductor 2 (I_2 and E_2) corresponding to the resistivity variation of two conductors and contact as shown in Table 4.2 95
Figure 4.3: The plot for the resistance ratio (R_J/R_{Jmin}) as versus the length ratio (L/L_{opt}) with different conductor resistance ratio (r_1/r_2). 96
Figure 4.4: The schematic drawing of nano-heater joint manufacturing installment. 97
Figure 4.5: Schematic drawing of the the nano-heater made 2G-tape sample with dimension for contact resistance measurment. Number 1 to 4 show the position of the voltage taps. 98
Figure 4.6: a) The picture of the nano-heater made 2G to 2G joint sample, and b) Schematic drawing of the the nano-heater made 2G to 2G joint sample with dimensions, and number 1 to 7 show the position of the voltage taps. 98
Figure 4.7: Three 2G tape to 2G tape joint nano-heater made samples. 99
Figure 4.8: Schematic drawing (bottom) of the cross section of a 2G-tape to copper joint, and number 1, 2, 3 and 4 show the position of the voltage tap. 100
Figure 4.9: Schematic drawing of the lap joint sample holder, and the number 1, 2, 3 and 4 show the position of the voltage tap 101
Figure 4.10: Sliding need contact test bed for lap joint contact resistance measurement 102
Figure 4.11: Displacement sensor (LVDT) voltage calibration. 103
Figure 4.12: *VI* charactersitics of two 2G-tape to copper joints at a) 77 K, and b) 40 K, and c) 35 K, and d) 25 K and e) 15 K. 104
Figure 4.13: The plots for current-voltage characteristics of the joint contact between 2G-tape to 2G-tape (SuperPower™) joint. 105
Figure 4.14: Left top plot shows a) measured voltage and b) resistance as a function of continuous position on the copper for sample 1, and right top plot shows c) measured voltage and d) resistance as a function of continuous position on the copper for sample 2, and bottom plot shows e) measured voltage and f) resistance as a function of continuous position on the copper for sample 2 with transport current of 30 A, 40 A and 50 A. Three dash lines (black, red and green) as shown in this figure (a, c and e) representing the slope of the voltage as a function of the position of the copper conductor only at 30 A, 40 A and 50 A for each sample. The vertical black dash line in each plot is used for defining the right end of the lap joint for each sample. 107

Figure 4.15: The plot for the measured voltage $V(x)$ for sample 3 compared with the analytical model $V_{Cu\_joint}(x)$ and $V_{Cu}(x)$ versus the continuous position at 40 A with the contact resistance assumed from 960 to 1440 nΩ×cm^2.Vertical dash line represents right end of the joint. 109
Figure 4.16: The plot for the measured voltage $V(x)$ for sample 3 compared with the analytical model $V_{Cu\_joint}(x)$ and $V_{Cu}(x)$ versus the continuous position at 40 A. The superconductor side resistivity (ρ_1) was assumed to be 0, 4.57e-15, 9.14e-15,18.28e-15 and 1.52e-12 Ωm, and the contact resistance was assumed as 960 nΩ×cm^2. 110
Figure 4.17: The plot for the measured voltage $V(x)$ for sample 1 compared with the analytical model $V_{Cu\_joint}(x)$ and $V_{Cu}(x)$ versus the continuous position at 40 A. The superconductor side resistivity (ρ_1) was assumed to be 0, 4.57e-15, 9.14e-15,18.28e-15 and 1.52e-12 Ωm, and the contact resistance was assumed as 1024 nΩ×cm^2. 111
Figure 4.18: The plot for the measured voltage $V(x)$ for sample 2 compared with the analytical model $V_{Cu\_joint}(x)$ and $V_{Cu}(x)$ versus the continuous position at 40 A. The superconductor side resistivity (ρ_1) was assumed to be 0, 4.57e-15, 9.14e-15,18.28e-15 and 1.52e-12 Ωm, and the contact resistance was assumed as 1700 nΩ×cm^2. 111
Figure 4.19: The plot of $V(x)$ for sample 3 as a function of the continuous position along the copper tape at 40 A compared with SLM_$V(x)$ with a) knots = 6, b) knots = 8, c) knots = 9, d) knots = 10, e) knots = 11, f) knots = 12, g) knots =25, and h) knots= 30. 113
Figure 4.20: The plot for first order differential function SLM_$V'(x)$ for sample 3 with a) knots = 6, b) knots = 8, c) knots = 9, d) knots = 10, e) knots = 11, f) knots = 12, g) knots =25, and h) knots= 30. 114
Figure 4.21: The analytical electrical field (SLM_knot_ 12) from the measured $V(x)$_SLM for sample 3 with 12 knots versus the continuous position x compared with the calculated electrical field from the measured $V(x)$ with 20 points of window for averaged smooth at 40 A with the superconductor side resistivity (ρ_1) assumed to be 0, 4.57e-15, 9.14e-15,18.28e-15, 1.52e-12 Ωm and the contact resistance was assumed as 960 nΩ×cm^2. 116
Figure 4.22: The analytical electrical field (SLM_knot_ 10) from the measured $V(x)$_SLM for sample 1 with 10 knots versus the continuous position x compared with the calculated electrical field from the measured $V(x)$ with 20 points of window for averaged smooth at 40 A with the superconductor side resistivity (ρ_1) assumed to be 0, 4.57e-15, 9.14e-15,18.28e-15, 1.52e-12 Ωm and the contact resistance was assumed as 1024 nΩ×cm^2. 116
Figure 4.23: The analytical electrical field (SLM_knot_ 10) from the measured $V(x)$_SLM for sample 2 with 10 knots versus the continuous position x compared with the calculated electrical field from the measured $V(x)$ with 20 points of window for averaged smooth at 40 A with the superconductor side resistivity (ρ_1) assumed to be 0, 4.57e-15, 9.14e-15,18.28e-15, 1.52e-12 Ωm and the contact resistance assumed as 1700 nΩ×cm^2. 117
Figure 5.1: The whole scale view of the Roebel cable instalment. 124
Figure 5.2: Schematic drawing of the a) top view of Roebel pancake coil to show the voltage taps (black points), heaters (red line, heater 1: 33 Ω, heater 2: 18.2 Ω and heater 3: 9.8 Ω) and thermal couple (purple points), and b) the front view of the cross-section of Roebel pancake coil to show the coil lay out and dimensions. 125
Figure 5.3: The picture for the test bed set up. 126
Figure 5.4: The plot of the critical current against temperature for the outer contact, the inner contact and strand 7 in the middle of the coil under different magnetic fields. 127
Figure 5.5: The plot for a) inner (open symbols) and outer (filled symbols) contact voltages (tap on the near end) and b) inner (open symbols) and outer (filled symbols) contact voltages (tap on the far end) of all the strands as a function of transport current at 77 K. 129
Figure 5.6: Apparent inner (solid bars) and outer (open bars) contact resistances according to voltage taps on different strands (outer contact voltage tap is on the near end) at 77 K. 130

Figure 5.7: a) Schematic drawing of the top side of the copper block and b) the assumed copper block model for the inner contact of the pancake coil. 130
Figure 5.8: *VI* characteristics of each strand (end to end) with the current from 0 to 450 A at 77 K..... 131
Figure 5.9: Schematic drawing of the end to end elctrical network of the roebel pancake coil. 131
Figure 5.10: *VI* characteristics (contact resistance subtracted) of each strand inner contact with the current from 0 to 450 A at 77 K, and the blue dash line represents 1 μVcm^{-1} criteria... 132
Figure 5.11: 3D schematic drawing of the outer contact shows the outer contact copper ring with 6 voltage taps layout, and number shows the position of the voltage taps (1: Top far end, 2: Top middle end, 3: Top near end, 4: Bottom near end, 5: Bottom middle end, 6: Bottom far end and 7: Underneath of the copper disk). 133
Figure 5.12: The plot for voltages measured on the outer contact copper ring with a current from 50 A to 450 A at 77 K. 134
Figure 5.13: The plot for the voltage across bottom middle end and copper disk (V57), bottom far end and copper disk (V67) and bottom near end and copper disk (V47) separately with a transport current from 10 A to 50 A at 77 K..... 135
Figure 5.14: Far end, middle end voltage and near end vertical voltages on the copper ring versus the position from far end to near end with different transport currents from 50 to 450 A at 77 K..... 135
Figure 5.15: The geometry plot for the a) Model 1 with current of 300 A that injected at near end and b) Model 2 with current 300 A for block 1-3: 0 A, and block 4-18: 20 A that injected at each block. 138
Figure 5.16: The plot of a) surface electrical potential of model 1 and b) surface electrical potential of model 2 and c) surface arrow of current density for model 1 and d) surface arrow of current density for model 2 and e) line electrical potential of both top and bottom edge of the copper ring with contact resistance from 7.5 to 11.2 $\mu\Omega cm^2$ for model 1 and f) line electrical potential of both top and bottom edge of the copper ring for model 2. The transport current is assumed as 300 A, and the temperature is assumed at 77 K..... 139
Figure 5.17: The plot for voltages measured on outer contact copper ring with a current from 5 A to 40 A at room temperature. 141
Figure 5.18: The plot for *VI* characteristics of each strand within the pancake coil at a transport current from 5 A to 20 A at room temperature. 142
Figure 5.19: The plot for a) both inner and outer contact voltage for each strand at a transport current of 0.5 A and b) inner contact voltage versus the equivalent length between first voltage tap (from inner turn to outer turn) on each strand and the end point of the inner contact, and outer contact voltage versus the equivalent length between last voltage tap (from inner turn to outer turn) on each strand and the start point of the inner contact compared with the voltage across one strand within the pancake coil versus the length, and voltage across voltage tap V7a and Vna (n = 6, 5,…, 1, 15, 14,…, 9, 8) versus the equivalent length between each voltage tap at a transport current of 0.5 A. 143
Figure 5.20: The plot of a) surface electrical potential of model 3 and b) surface electrical potential of model 4 and c) surface arrow of current density for model 3 and d) surface arrow of current density for model 4 and e) line electrical potential of both top and bottom edge of the copper ring for model 3 and f) line electrical potential of both top and bottom edge of the copper ring for model 4 at room temperature. 145
Figure 5.21: The plot for inner (open symbols) and outer (filled symbols) contact voltages of all the strands as a function of current in 'balanced' condition. 146

Figure 5.22: Strand inner contact voltage and outer contact voltage comparison between the 'unbalanced' condition and the 'balanced' condition with transported current at 420 A. ... 147
Figure 5.23: Magnetic field density map of the Roebel pancake coil at 450 A (Left side: inner turns, and right side: outer turns). ... 148
Figure 5.24: Single strand *VI* curve with self field, perpendicular field (0.08T) and parallel field (0.12 T), and blue dash line represents 1 μVcm^{-1} criteria. ... 148
Figure 5.25: Strand voltages as a function of current between 300 A and 470 A in 'unbalanced' condition, and dash line represents 1 μVcm^{-1} criteria. ... 149
Figure 5.26: Voltage across of each strand (1 pitch) across the same current ramping range from 300 A to 470 A (Str_= Strand). ... 149
Figure 5.27: The plot for a) strand voltages in 'unbalanced' condition compared with b) strand voltages in 'balanced' condition as a function of current between 280 A and 460 A, and dash lines represent 1 μVcm^{-1} criteria. ... 150
Figure 5.28: a) The tracing of temperature on strand 7 due to different heater power and b) voltage V7_0 around the hot spot at the corresponding heating power and transport current for the 'unbalanced'thermal condition; c) The tracing of temperature on strand 7 due to different heater power and d) voltage V7_0 around the hot spot at the corresponding heating power and transport current for the 'balanced' thermal condition. Two horizental dash lines in figures represent the standard 1 μVcm^{-1} criteria. ... 151
Figure 5.29: Nominal critical current at different temperature. ... 151
Figure 5.30: Strands voltage and strand 6 and 7 contact voltages at 440 A at 77 K. ... 152
Figure 5.31: a) Strand voltage tracings with a 8.0 V heat pulse on the outer contact joint, and b) Strand inner and outer contact voltage tracings with a 8.0 V heat pulse on the outer contact joint with a transport current of 430 A at 77 K. Strand 6, 7, 9 and 15 are examples of all the strands to show their strand voltages and two contact voltages ... 153
Figure 5.32: The tracing of the response of temperature to a pulse voltage of 4.5 V heat pulse applied Heater 1 with no current in the coil. ... 154
Figure 5.33: The tracing of voltage of each strand, current, temperature and pulse voltage against time with 450 A and different pulse magnitude and length in a 'unbalanced' condition. ... 155
Figure 5.34: The tracing of voltage of each strand, current, temperature and pulse voltage against time with 400 A and different pulse magnitudes at 3.5 V, 4.5 V, 5.5 V and 6.0 V in a 'balanced' condition. ... 156
Figure 5.35: The tracing of voltage of each strand, current, temperature and pulse voltage against time with heat pulse at 6.0V at different transport current (400 A, 410 A, 415 A and 425 A). ... 157
Figure 5.36: The tracing of a) strand voltage, current, temperature and pulse voltage b) strand contact voltage, current and temperature against time for the coil quench case with a transported current at 420 A in 'unbalanced'condition. ... 158
Figure 5.37: The tracing of strand 7 (V7_1 and V7_2), current, temperature and pulse voltage against time for the coil quench case with a transported current at 420 A in 'unbalanced'condition. ... 159
Figure 5.38: The tracing of a) strand voltage, current, temperature and pulse voltage b) strand contact voltage, current and temperature against time for the coil recovery case with a transported current at 420 A in 'unbalanced'condition. ... 160
Figure 5.39: The tracing of strand 7 (V7_1 and V7_2), current, temperature and pulse voltage against time for the coil recovery case with a transported current at 420 A in 'unbalanced'condition. ... 161

Figure 5.40: The tracing of a) strand voltage, current, temperature and pulse voltage b) strand contact voltage, current and temperature against time for the coil quench case with a transported current at 420 A in 'balanced'condition. All the outer contact voltage proflies are below the black dash line. 162
Figure 5.41: The tracing of strand contact out voltage, current and temperature against time for the coil quench case with a transported current at 420 A in 'balanced'condition. 163
Figure 5.42: The tracing of a) strand voltage, current, temperature and pulse voltage b) strand contact voltage, current and temperature against time for the coil recovery case with a transported current at 420 A in 'balanced'condition. 164
Figure 5.43: Experimental MQE and temperature changing (ΔT) between heat pulse triggering on and cutting off, and temperature changing (ΔT) at quench time constant for different transport currents versus different heating power applied on strand 7. 165
Figure 5.44: Quench voltage and steady voltage of strand 7 versus different applied heating power with a transport current at 400 A. 166
Figure 5.45: 'Balanced' experimental MQE of the Roebel cable as a function of scaled current (1-*j*) with different transport current at 77K. Pink round scatter shows the experimental MQE data (corresponding to right y-axis) of a single SuperPower 2G HTS tape with different current at 77 K [103]. 167
Figure 5.46: The self-heating energy at different current compared with the experimental MQE with 6.0 V heat pulse. 169
Figure 5.47: The tracing of voltage of each strand, current, temperature and pulse voltage against time for the coil quench. 170
Figure 5.48: 'Balanced' experimental MQE of the Roebel cable as a function of scaled current (1-*j*) with different transport current at 77K. 171
Figure 5.49: The time for each strand voltage to reach 3 μV, 10 μV, 30 μV and 100 μV at 410 A with a heat pulse at 6.0 V, and the dash line shows the pulse off time. 172
Figure 5.50: The schematic drawing of the Robel cable coil crosssection at the location of Heater 1. 173
Figure 5.51: Strand contact voltage changes for a) inner contact and b) outer contact at different time after the pulse is applied with a transport current around 410 A and a 6.0V heat pulse, the pulse width is 6.17s. 174
Figure 5.52: Strand contact voltage changes for a) inner contact and b) outer contact at different time after the pulse is applied with a transport current around 340 A and a 6.0V heat pulse, the pulse width is 18.44s. 176
Figure 5.53: The tracings of near end voltage, middle end voltage, far end voltage, top near end to top far end voltage, top middle end to top far end voltage, bottom near end to bottom far end voltage and bottom middle end to bottom far end voltage on the copper ring, current, temperatures of Heater 1 and Heater 2 for the quench measurement at around 410 A with a 6.0 V pulse voltage. 177
Figure 5.54: The tracings of near end voltage, middle end voltage, far end voltage, top near end to top far end voltage, top middle end to top far end voltage, bottom near end to bottom far end voltage and bottom middle end to bottom far end voltage on the copper ring, current, temperatures on strand 7 adjacent to Heater 1 and Heater 2 for the quench measurement at around 340 A with a 6.0 V pulse voltage. 177
Figure 5.55: 2D schematic drawing for the current leads with grooves for Roebel cable soldering. 178

List of Table

Table 1.1: A summary of phase fomation of Ni/Al multilayer films and their transformation temperatures [19]. 6
Table 1.2: A summary of physical properties data of NiAl compared with some pure metals [19]. 7
Table 1.3: A summary for the resistivity of the Ni-Al films after 4 hours anneal at 400 °C [19]. 9
Table 1.4: Properties of some Roebel cable samples [9], [76]. 18
Table 2.1: Comparison among the LTS material, 1G HTS material and 2G HTS material [97], [98]. 22
Table 3.1: Dimensions of a list of nanofoil samples applied to TTO measurements. 45
Table 3.2: Dimensions of a list of nanofoil samples applied to resistivity option measurements. 46
Table 3.3: The parameters of three nanofoil samples for heat capacity measurements. 47
Table 3.4: The parameters of each nanobond HTS joint sample. 48
Table 3.5: The estimated thickness of copper for new lap shear tests. 52
Table 3.6: Parameters of OI made metallic nanobond joints for lap shear testing. 54
Table 3.7: Parameters of UoS made copper nanobond joints for lap shear testing. 54
Table 3.8: A list of nanofoil samples applied to physical properties measurements. 55
Table 3.9: Residual resistance ratio (RRR), and resistivity at 4.2 K, 77 K and room temperature of both reacted and unreacted sample compared with the resistivity of bulk nickel and aluminum [166], and nano-scaled nickel [126], [127], and NiAl in stoichiometric ratios [35], [36]. 59
Table 3.10: Calculated α and β from the curve fitting from Figure 3.16 for reacted and unreacted nanofoil samples, aluminium, nickel, Ni+Al (50:50, at. %) [174], [175], NiAl (Ni, 49.3 at. %) measured by Alexander et al [52], NiAl (Ni, 48 or 50 at. %) measured by Seitchikf et al [56], and NiAl (Ni, 50.5 or 51 at. %) measured by Begot et al [176]. 66
Table 3.11: The dimensional parameters and resistivity of each reacted nanofoil samples with different cooling conditions. 68
Table 3.12: Compositional analysis of a) Cross-sectional and b) surface of unreacted nanofoil film by EDX. 69
Table 3.13: Compositional analysis of cross-sectional of a) solder (spectrum 2) and b) reacted nanofoil film (spectrum 3) within a copper to coper nanobond joint by EDX. 71
Table 3.14: Contact resistance of each joint for all the samples. 77
Table 3.15: Parameters of each joint for calculating the area for tin filling into nanofoil cracks. 79
Table 3.16: The shear strength of eight OI metallic nanobond joint samples (StSt: Stainless steel, Cu: copper). 83
Table 3.17: The shear strength of 6 UoS metallic nanobond joint samples (Cu: copper). 85
Table 4.1: Dimensions of the two conductors and the contact. 94
Table 4.2: The resistivity variation of two conductors and the assumed resistivity of the contact. 94
Table 4.3: The dimension parameters of three lap joint samples. 100
Table 4.4: Overall contact resistance of 2G to copper joints at different temperatures. 104

Table 4.5: The overall contact resistance comparison at 77 K among the nanobond, nano-heater and manually soldering HTS-tape joints with different HTS tapes and solders. 106
Table 4.6: The slope for the linear fitting of voltage changes on the copper only verses the distance from the right end of the joint and estimated copper tape resistivity for each sample at 77 K. 108
Table 4.7: The estimated contact resistance, solder resistance, copper resistance and overall contact resistance of three lap joint samples. 119
Table 5.1: *n*-value of each strand in inner turns of the coil. 132
Table 5.2: Vertical current density at near end, middle end and far end positions and estimated transported current at 77 K. 136
Table 5.3: The parameters setting up of two models at 77 K. 137
Table 5.4: The summary of the horizontal voltages along the copper ring in accordance with model 1, model 2 and the experiments results at 77 K (V31: Top near end to top far end, and V32: Top near end to top middle end, V21: Top middle end to top far end, V46: Bottom near end to bottom far end, V45: Bottom near end to bottom middle end and V56: Bottom middle end to bottom far end). The transport current is 300 A. 140
***Table 5.5*:** Vertical current density at near end, middle end and far end positions and estimated transported current at room temperature. 141
Table 5.6: The parameters setting up of two models at room temperature. 144
Table 5.7: The summary of the polarity of horizontal voltages along the copper ring in accordance with model 3, model 4 and the experiments (V31: Top near end to top far end, and V32: Top near end to top middle end, V21: Top middle end to top far end, V46: Bottom near end to bottom far end, V45: Bottom near end to bottom middle end and V56: Bottom middle end to bottom far end). The transport current is 15 A at room temperature. 145
Table 5.8: The comparison of transport current flowing within the coil between 'balanced' and 'unbalanced' condition. 147

List of Symbols

Symbol	Name	Unit
%	Percentage	
ΔI_c	Critical current variation	A
ΔQ_{mqe}	Minimum Quench Energy	J
1-*j*	Scaled current	%
A	Current unit, Ampere	
A	Cross-section area	mm^2
Abbr	Abbreviation	
Ag	Silver	
A_{joint}	Cross-section area of joint	cm^2
Al	Aluminum	
A_{NF}	Cross-section area of nanofoil	cm^2
A_{Sn}	Cross-section area of solder	cm^2
At. %	Atomic percent	
Au	Gold	
B	Magnetic field density	T
$B_{\parallel}$	Parallel field	T
$B_{\perp}$	Perpendicular field	T
Ba	Barium	
Bi	Bismuth	
Ca	Calcium	
$C_{electronic}$	Electronic specific heat	J/(K×mol)
cm	Length unit, Centimeter	
C_p	Specific heat	J/(K×g)
Cu	Copper	
C_V	Specific heat	J/(K×mol)
$C_{vibration}$	vibrational specific heat	J/(K×mol)
D	Distance	mm
E	Electrical field	V/m
E_c	Electrical field criteria	μV/cm
F	Force	N
Fty	Yield point of metal	MPa
G	Giga	
GPa	Pressure unit, Giga-pascal	
H	Magnetic field strength	A/m
h	Thermal transfer coefficient	$W/(K×m^2)$
H_c	Critical magnetic field strength	A/m
Hz	Frequency unit, Hertz	
I	Current	A
I_c	Critical current	A

I_{field}	Field current	A
I_{metal}	Current flowing in the normal metal	A
In	Indium	
I_n	Normnal current	A
I_{outer}	Contact current	A
I_{stator}	Stator current	A
J	Current density	A/m^2
J	Energy unit, Joule	
j	Percentage of the critical current (I/I_c)	%
K	Kelvin	
k	Kilo-	
k_B	Boltzmann's constant	J/K
kW	Power unit, Kilo-Watt	
L	Length	mm
l	Displacement	mm
L	Lorenz number	$W\Omega/K^2$
ℓ	Mean free path	nm
L_d	Sliding path	mm
L_{ISG}	inter-strand gap	mm
L_{joint}	Joint length	mm
l_{MPZ}	Length of minimum propagation zone	mm
L_{nor}	Length of the normal zone	mm
L_T	transposition length	mm
M	Mega-	
m	Length unit, meter	
M5	Screw has a nominal outer diameter of 5 mm	
mA	Mini-amper	
m_e	Mass of the electrons	g/kg/u/MeV
Mg	Magnesium	
min	Time unit, minute	
mm	Millimeter	
MPa	Pressure unit, Mega-pascal	
MVA	Power unit, Mega-volt-ampera	
MW	Power unit, Mega-watt	
n	Nano-	
n	Quality index number	
N_A	Avogadro's number	mol^{-1}
Nb	Niobium	
n_e	Electrons concentration	cm^{-3}
Ni	Nickel	
Nm	Newton metre	
NO.	Number	
N_{Str}	Strand number	

nΩ	Resistance unit, Nano-Ohm	
O	Oxide	
ºC	Degree Celsius	
Pb	Lead	
Q	Thermal energy	J
q	Heat flux	W/m^2
Q_{ini}	Initial thermal energy	J
r	radius	mm
R	Resistance	Ω
R	Gas constant	J/(mol×K)
R_b	Interfacial barrier resistance	nΩ/ nΩ×cm^2
R_{Cu}/R_{Cu}'	Copper conductor/laminate layer resistance	nΩ/ nΩ×cm^2
$R_i/R_{2G\text{-}tape}$	Interfacial resistance	nΩ/ nΩ×cm^2
$R_J/R_{joint}/R_{contact}/R_{con}/R_{out}$	Overall joint contact resistance	nΩ/ nΩ×cm^2
R_{metal}	Metal matric resistance	nΩ/ nΩ×cm^2
R_{NF}	Nanofoil resistance	nΩ/ nΩ×cm^2
R_{solder}/R_{Sn}	Solder resistance	nΩ/ nΩ×cm^2
$R_{solder\text{-}Cu}$	Interfacial resistance between solder and copper	nΩ/ nΩ×cm^2
$R_{thermal}$	Thermal resistance	K/(W×cm^2)
Sn	Tin/Stannum	
Sr	Strontium	
T	Temperature	K, ºC
T	Magnetic field unit, Tesla	
t	Time	s
t/d	Thickness	mm/μm
T_0	Original/operating temperature	K
T_∞	Cryogen temperature	K
T_c	Critical temperature	K
T_D	Debye temperature	K
Ti	Titanium	
t_p	Pulse width	s
t_Q	Quench time constant	s
T_{share}	Current sharing temperature	K
V	Voltage unit, Volt	
V	Voltage	V
V_0	Voltage at the beginning of the contact that current starts to transfer	V
VA	Power unit, Volt-ampera	
$V_{average}$	Average voltage	mV
$V_{con}/V_{contact}/V_{out}$	Overall contact voltage	V
V_{Cu}	Sliding voltage along the copper conductor	V
$V_{Cu\text{-}joint}$	Sliding voltage along the copper overlapped joint	V

V_{field}	Field winding end to end voltage	V
V_{mpz}	Volume of the minimum propagation zone	m^3
V_Q	Quench voltage	mV
V_{source}	DC power source supply voltage	V
W	Tungsten	
w	width	mm
W	Power unit	Watt
w_g	strand-edge clearance	mm
wt. %	Weight percent	
Y	Yttrium	
α	Vibrational specific heat constant	$J/(mol \times K^4)$
β	Electronic specific heat constant	$J/(mol \times K^2)$
ΔT	Temperature difference	K
ΔV	Voltage variation	V
θ	angle	^{o}
κ	Thermal conductivity	W/(K×m)
κ_{el}	Thermal conductivity contributed by electrons	W/(K×m)
κ_{ph}	Thermal conductivity contributed by phonon	W/(K×m)
κ_{sum}	Sum thermal conductivity	W/(K×m)
λ/L_t	Current transfer length	mm
μ	Micro-	
μm	Micrometer	
μV	Voltage unit, Microvolt	
μΩ	Resistance unit, Micro-Ohm	
v_f	Fermi velocity	cm/s
π	Pi/Archimedes' constant	
ρ	Resistivity	Ω×m
ρ_0	Residual resistivity	Ω×m
ρ_c	Resistivity of joint material	nΩ×m
ρ_{copper}	Resistivity of copper	nΩ×m
$\rho_{el\text{-}ph}$	Electron-phono scattering resistivity	Ω×m
ρ_{joint}	Resistivity of joint	nΩ×m
ρ_{NF}	Resistivity of nanofoil	nΩ×m
ρ_{norm}	Resistivity of the conductor at the normal state	Ω×m
ρ_{Sn}	Resistivity of solder	nΩ×m
σ	Electrical conductivity	S/m
τ	150 % of the estimated average shear strength	MPa
τ_{torque}	Torque	N×m
Ω	Resistance unit, Ohm	

List of Abbreviation

1D	One dimensional
1G	First Generation
2G	Second Generation
3D	Three dimensional
ABB	ASEA Brown Boveri
AC	Alternating current
Al_2O_3	Aluminum oxide/Alumina
BCS	Bardeen–Cooper–Schrieffer theory
BNL	Brookhaven National Laboratory
BSCCO/Bi-2212/Bi-2223	Bismuth strontium calcium copper oxide Bi-2212: $Bi_2Sr_2CaCu_2O_{8+x}$ Bi-2223: $Bi_2Sr_2Ca_2Cu_3O_{10+x}$
BZO ($BaZrO_3$)	Barium zirconate
CEC-ICMC	CRYOGENIC Engineering Conference International Cryogenic Materials Conference
CeO_2	Cerium(IV) oxide
CERN	the European Organization for Nuclear Research
DBC	Direct bonded copper
DC	Direct current
DyBCO	Dysprosium barium copper oxide
EDS	Energy dispersive X-ray spectroscopy
EPR	Electron paramagnetic resonance
EURATOM	European Atomic Energy Community
GCS	General Cable Corporation
HTS	High temperature superconductor
IBAD	Ion Beam Assisted Deposition
IRL	Industrial Research Limited
KERI	Korea Electrotechnology Research Institute
KIT	Karlsruhe Institute of Technology
LHe	Liquid helium
LN2	Liquid nitrogen
LTS	Low temperature superconductor
LVDT	Linear variable differential transformer
MBE	Molecular beam epitaxy
MgB_2	Magnesium diboride
MOCVD	Metal-organic-chemical vapor deposition
MOD	Metal Organic Deposition
MQE	Minimum Quench Energy
MRI	Magnetic resonance imaging
NbTi	Niobium-titanium

NI	National Instrument
Ni_xAl_{1-x}	Nickel Aluminide (x is the atomic percent, 0<x<1)
NMR	Nuclear magnetic resonance
OI	Oxford Instrument
OPIT	Oxide Power In Tube
PEEK	Polyether ether ketone
PID	Proportion Integration Differentiation
PPMS	Physical Property Measurement System
PTFE	Polytetrafluoroethylene
RABiTS	Rolling Assisted Bi-axially Textured Substrate
Re_Naf	Reacted nanofoil sample
REBCO	Rare earth barium copper oxide elements
RRR	Residual resistance ratio
SEM	Scanned Electron Microscopy
StSt	Stainless steel
TEM	Transimission electron microscope
TTO	Thermal transport option
Un_Naf	Unreacted nanofoil sample
UoS	University of Southampton
VI	Voltage-current
XRD	X-ray Diffractometer
Y_2O_3	Yttrium (III) oxide
YBCO	Yttrium barium copper oxide
YSZ	Yttria-stabilized-zirconia

Chapter 1
Introduction

HTS REBCO tapes are proving to be a very attractive option for a number of applications [1]–[5]. However, some electrical machines like those that require coils need kilometer-lengths of 2G HTS wires. Consequently, joints need to have the same mechanical and electrical robustness as the non-jointed regions of the wire. Generally, a soldered joint resistance consists of solder resistance, and interfacial stabiliser material resistance such as copper or silver. In an experimental setup, contact resistance can be estimated by the 4-contact method to measure the voltage drop with an applied current across the joint. Voltage-current (*VI*) curves are used for the analysis of the HTS joints contact resistance. There is a linear slope existing in the curve before the HTS layer transfers to the normal state, which refers to the 'contact resistance' in units of nΩ. When the contact area is included in this type of resistive analysis, the contact resistance can be expressed in $n\Omega \times cm^2$. In reference to the HTS-based applications, small contact resistances are expected for the applications. The effect of temperature, time to fabricate the joint, joint material, and the pressure applied to form and hold the joint are important manufacturing parameters and contribute to the joints electrical contact resistance [6]–[8].

Joule heating by the current due to the large contact resistances may cause high thermal energy dissipation into the coil. This thermal energy has a high risk of developing into a quench of the superconducting winding. For instance, superconducting magnet systems are a key part of particle accelerators at CERN-The European Organization for Nuclear Research. The superconducting magnets and bus-bars utilise NbTi as the superconductor and they are cooled at 1.9 K by superfluid helium. The Large Hadron Collider (LHC) particle accelerator was turned on for the first time in September 2008. However, during a power test on 19 September 2008, a major accident was caused by an electrical fault of a soldered joint between two spliced cables of a bus-bar linking two superconducting magnets. As soon as the temperature increased above the critical temperature of the connected superconductors, the connection melted and the current arced to other parts of the machine. The melting issue resulted in punching a hole through the vacuum vessel and the beam pipe, causing six tons of liquid helium to escape through the hole and cause further quenches of the nearby magnets. Finally, this accident resulted in a need for widespread repairs, and 53 magnets had to be replaced. Consequently, the robustness of the contacts has become very important for applied superconducting devices.

The electrical and thermal transport of the HTS joints, electrical resistivity and thermal conductivity of the contact has become an important parameter for the energy dissipaition that relates to the thermal and electrical stability. Besides the thermal and electrical performance, the current leads mounted in high magnetic field environment requires good mechanical strength. A novel nanobond technology was applied for the first time to HTS tapes by Oxford Instruments (OI), and characterised at University of Southampton (UoS). This nanobond technology provides a new in-situ methodology to make reproducible HTS soldered joints. In order to analyse the real soldering contact resistance and estimate current transfer characteristics within a 2G-tape soldering joint, an analytical model was developed to simulate the lap joint between two conductors. The current distribution within two conductors could be verified by a new contact voltage measurement technique. Consequently, a "nano-heater" method was also established and applied to solder the current injection contacts of a 2G tape pancake coil.

With the advantages of high current carrying ability in long lengths, the second generation (2G) tapes show the potential for use in many applications in electrical power system devices, which need higher driven currents to reduce the number of coils for providing field with a smaller inductance. However, most of these devices are operated in an AC current mode, which is an issue for the superconducting applications that require low AC losses [9]. The technologies of low AC losses for high current conventional machine have been investigated for a long time. The first design of an assembled cable with insulated strands was developed by Ludwig Roebel at ASEA Brown Boveri (ABB) Company in Mannheim (Germany), in order to limit AC losses from eddy currents and loops for high current transporting in copper conductors of the large scale of AC devices in 1914 [10]. Roebel bars have since become the standard conductor for stator windings of electrical machines [10], [11].

Referring to the applied superconductivity industry, the first Roebel cable was made from transposed NbTi strands for one unit of superconducting fusion magnet, (EURATOM magnet) [12]. Because of the good ductility of NbTi, the conductors were allowed to bend at quite sharp angles with a short transposition length (280 mm). The Rutherford cable was assembled in a short height and wide board without high stacks of conductors, and applied to dipole magnets fabrication for accelerator at CERN [13]. However, such tight bending in the in-plane direction like those achived by the Rutherford cables are impossible for other HTS conductors assemblies. New solutions were developed for HTS Roebel cables assemblies with the development and the progress of long-scale REBCO coated conductor with homogeneous critical current and robust performance [9]. With the advantages of higher driven current to allow the reduction in the number of coils to provide field with a smaller inductance, Roebel cables were fabricated from meander-shaped 2G-tapes, and this cable optimisted for future high energy accelerators at CERN and Tokamak devices.

However, a complex current sharing and normal zone propagation is expected for Roebel cables due to the non-continuous touch contacts among the assembled strands, which makes it difficult to investigate quench studies on a Roebel cable with long current sharing length like adiabatic short conductors. Consequently, one 2G YBCO Roebel cable was wound into a pancake coil in order to incorporate a cable length to study the full development of current sharing among strands.

The preparation of this pancake coil, localised heater, and instrumentation setup of voltage taps and thermocouples are presented in this work, and the current injection contacts, the critical current and quench characteristics of this pancake coil have been investigated at 77 K in LN2. The performance and quench characteristics of this Roebel pancake coil are more relevant to real applications, and these experimental results can be used to add more details for the developing computer modelling.

1.1 A new nanobond technology in contact joints for HTS applications.

Nanofoil, a nanotechnology reactive multi-layer foil material manufactured by Indium Corporation, can provide repeatable and reliable bonds via the reaction to deliver an instantaneous thermal energy in a controlled and precise manner for soldering components with uniform and significant amount of heat energy across the entire area. In addition, this foil can performs as a heat source [14]. Only local heating of the surface of the substrate can eliminate any heat exposure to the component, with no need for expensive reflow ovens, which are normally used for temperature sensitive components in semiconductor, aerospace, electronics and biomedical applications [15]. Figure 1.1 shows the pictures for the cross-section structure before and after reaction [16]. The reactive multi-layer foil is fabricated by vapor-depositing thousands of alternating nanoscale layers of Aluminum (Al) and Nickel (Ni), and each layer is typically 30-50 nm thick. The outer layer at each side is 1 μm thick alloy of indium, copper and silver [14], [17]. This foil material can be activated by a small pulse of local energy such as electrical, optical or thermal sources, which reacts exothermically to heat up localised temperature to 1500 °C in fractions of a second. After the reaction, there is a nickel aluminide intermetallic with an ordered cubic B2 crystal structure formed [17]. Nanofoil has a standard sheet size of 100 mm × 240 mm, and produced in different thicknesses of 40 μm, 60 μm and 80 μm. The standard nanofoil can be used to join two materials together with solder performing or a solder-coated surface (< 450 ºC), and the thicker nanofoil can be used to join materials in the brazing range of 450 - 700 °C [18]. Nanofoil can be supplied, with an optional 10 μm thick electroplated layer of tin, which is called solder-plated nanofoil as shown in Figure 1.2. [17].

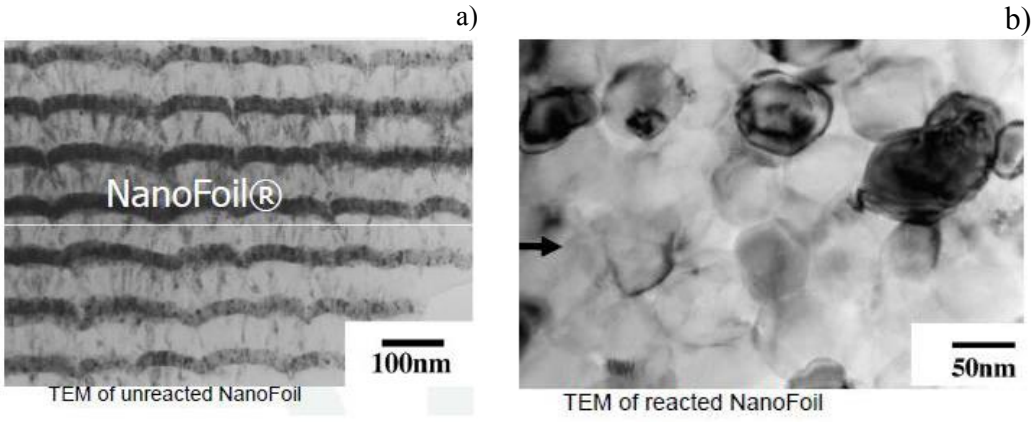

Figure 1.1: The cross-section structure of nanofoil. a) Unreacted nanofoil and b) Reacted nanofoil [16].

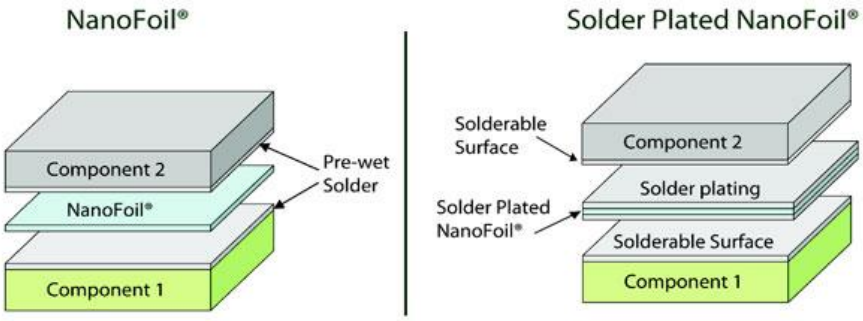

Figure 1.2: A schematic structure diagram for standard nanofoil and solder-plated nanofoil [17].

1.1.1 Pre-condition for successful joints

In order to prepare for successful joining, flat bonding surfaces are required to ensure better contact with the nanofoil and prevent voiding or uneven bonding. OI recommend that to achieve high quality bonds with > 98 % coverage, machined solder layer should be deployed, and a planarity of the surface of around 10 µm/10 mm is suggested [16]. Figure 1.3 shows a schematic drawing for the nanobond reaction preparation. In order to make the sandwich sample surfaces for joining the contact, it is necessary to ensure the pressure to have an alignment with the joint area [16]. A spacer is approached to apply the pressure to the size of parts being joined, and there is a compliant layer such as rubber to spread the load as pressure is applied. Under the compliant layer, a piece of Kapton tape is applied to reduce the heat exchange during the reaction. Furthermore, the constant feedback pressure needs to be maintained during the reaction.

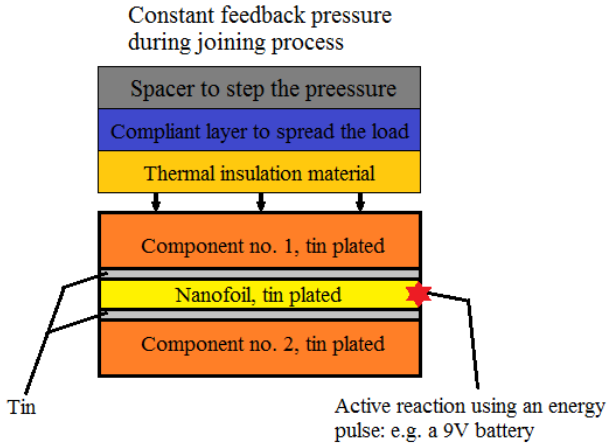

Figure 1.3: A schematic drawing for the nanobond reaction preparation.

The reaction of the nanofoil is initiated at an edge of the foil by using a laser, a heat torch or a 9-volt battery [16], [17]. The principle of the rapid exothermic reaction of the foil is the exothermic reaction produces an intense localised heat that enables adjacent metallic material melting. Then the foil disintegrates into microscopic reaction products and a reaction front propagates through the foil within a few milliseconds. During this process, the two layers of pre-plated solder melt at the surface of foil and fuse with the adjacent material to form a metallic joint.

1.1.2 NiAl films from the reaction of Ni/Al multilayers

A series of studies of the phase-formation of Ni-Al intermetallics from the reaction of Ni/Al multilayers have been published [19]–[23]. According to the phase diagram in Figure 1.4, four intermetallic phases involving $NiAl_3$, Ni_2Al_3, NiAl and Ni_3Al can be formed [19], [20]. The study of early stages of intermetallic formation by Colgan in 1990 shows that $NiAl_3$ was the first phase to form [24]. Howell et al also stated that the film formation starts with the more aluminum rich phases, and the intermetallic formation develops towards more nickel rich phases ($NiAl_3$ → Ni_2Al_3 → NiAl…) during the reaction of Ni/Al multilayers [19]. When the annealing temperature is increasing and the reaction is continuing, the final phase formation depends on the composition on the Ni/Al multilayers [19], [20]. With more investigations into the differences in Ni/Al bi-layer thickness, it is found that $NiAl_3$ is not always the first phase formation from the reaction of Ni/Al multilayers, but the reaction starts to form Al-rich phase first [19].

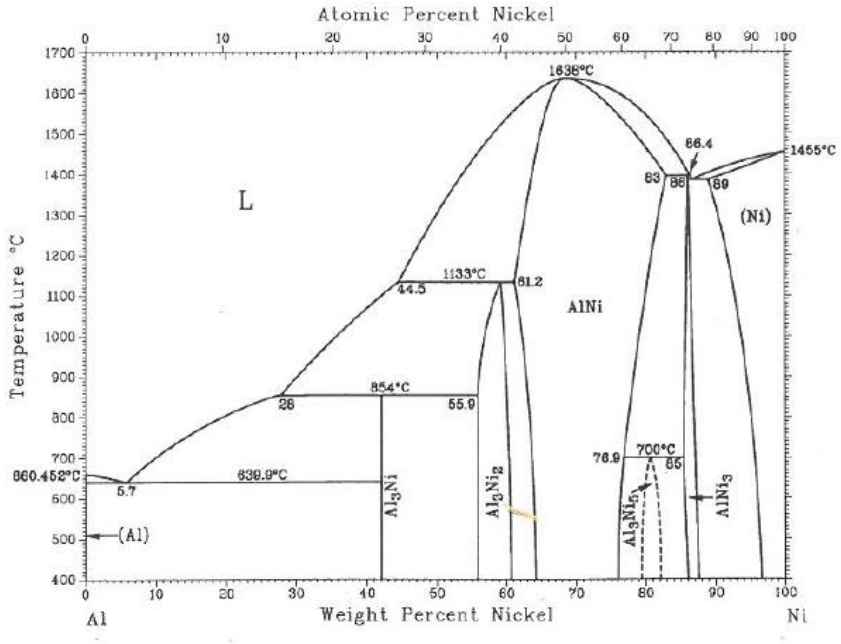

Figure 1.4: Phase diagram of Ni-Al system [25].

Figure 1.5 shows the concept of Ni/Al bi-layer thickness, and a summary of phase formation from the reaction of Ni/Al multilayer is shown in Table 1.1 [19]. When the Ni/Al bi-layer thickness was 10 nm or less, NiAl is the first and only phase to form during the reaction [21]–[23]. When the bi-layer thickness increases to 12.5 nm, $NiAl_3$ became the first phase to form [23], [26], [27]. Ni_2Al_9 was the first intermetallic formation for the bi-layer thickness, ranging between 25 nm and 200 nm [27], [28], and the first to form in the Ni-Al intermetallic when the reaction was rapidly quenched during the melting stage [29]. Furthermore, not only the phase formation depends on the Ni/Al bi-layer thickness, but the transformation temperature also changes when the Ni/Al bi-layer thickness increases [19], [22]. Nanofoil can be ignited by many concentrated energy source, and it is suggested that the ignition is processed under heating up to 200 ºC, at a heating rate of 200 ºC/min, using any heating method, but nanofoil will tend to lose the ablility to self-sustain the reaction, if the nanofoil anneals with a very slow heating rate [17].

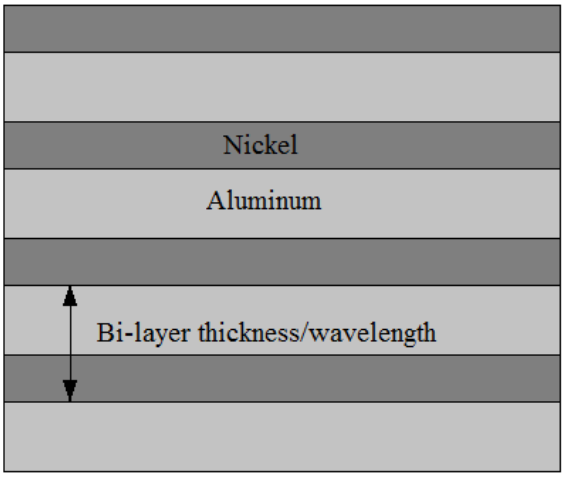

Figure 1.5: Schematic drawing of a Ni/Al multilayer foil structure [19].

Table 1.1: A summary of phase fomation of Ni/Al multilayer films and their transformation temperatures [19].

Wavelength (nm)	First intermetallic formation		NiAl form (°C)	Reaction complete temperature (°C)	Annealing time (min, °C)	Reference
	Temperature (°C)	Formation				
5	150	NiAl	150	275	10 min	[23]
10	175	NiAl			20 °C/min	[22]
10	80-90	63% Al NiAl			40 °C/min	[21]
20	~100	63% Al NiAl	307		40 °C/min	[21]
27.6	230	$NiAl_3$ (Ni_2Al_9)	275-362	362	20 °C/min	[30]
30	125	$NiAl_3$	175	225	10 min	[23]
50.3	160	$NiAl_3$	250	330	45 min	[31]
80	250	Ni_2Al_9	>370		20 °C/min	[22]
140	150	$NiAl_3$	325-425	500	10 min	[23]
500	270	$NiAl_3$	500	600	50 °C/min	[32]

1.1.3 Physical properties of NiAl

It has mentioned that the reacted nanofoil is a nickel aluminide ($Ni_{50}Al_{50}$) intermetallic with an ordered cubic B2 crystal structure formation, from the reaction of a multi-layer foil, fabricated of Al and Ni [14], [16]. According to the phase diagram of Ni-Al system as shown in Figure 1.4 [25], there is a composition range for NiAl, and the stable intermetallic range of NiAl at room temperature is from 41 % to 55 % atmoic Al [33]. The melting temperature of the stoichiometric alloy is 1683 °C, and some physical properties data of NiAl compared with some pure metals is shown in Table 1.2 [19]. For an intermetallic compound of NiAl, a prosmising material with low density, good thermal and electrical conductivity, high melt temperature and a high fracture touughness, and could be applied to electronic metallisation and surface coatings for turbine blades, propulsion systems and aerospace system [19], [33].

Table 1.2: A summary of physical properties data of NiAl compared with some pure metals [19].

Material	Melt temperature (°C)	Resistivity* (μΩ×cm)		Thermal expansion (10^{-6}/ °C)	Fracture toughness (MPa×$m^{1/2}$)	Young's modules (GPa)
		Bulk**	Thin film			
Al	660	2.65	2.9-3.1	23.1		71
Ni	1455	6.84	12.0-19.0	13.4		200
Cu	1080	1.67	2.0	16.5		117
NiAl	1638	10.0-11.0	24.0-60.0	11.9-15.1	6.0-14.0	194-237

*Room temperture
**The material is a single crystal

1.1.3.1. Electrical resistivity of NiAl

The electrical resistivity of bulk NiAl has been measured at room temperature by several groups, and summary of their data is shown in Figure 1.6 [19], [34]–[37]. The stoichiometric bulk NiAl or slight Al-rich (~ 49.6% atomic Ni) compound has a resistivity value range around 8~11 μΩ×cm at room temperature [34]–[40], and around 3 μΩ×cm at 77 K [35], [38], [39], and above 1 μΩ×cm at 4.2 K [35], [36], [38]. The resistivity of NiAl phase in each group of measured data increases when the deviations increases from the stoichiometric composition, and there are obvious differences in the slope of resistivity against composition on each side of minimum resistivity value, except for the data of Butler et al [34].

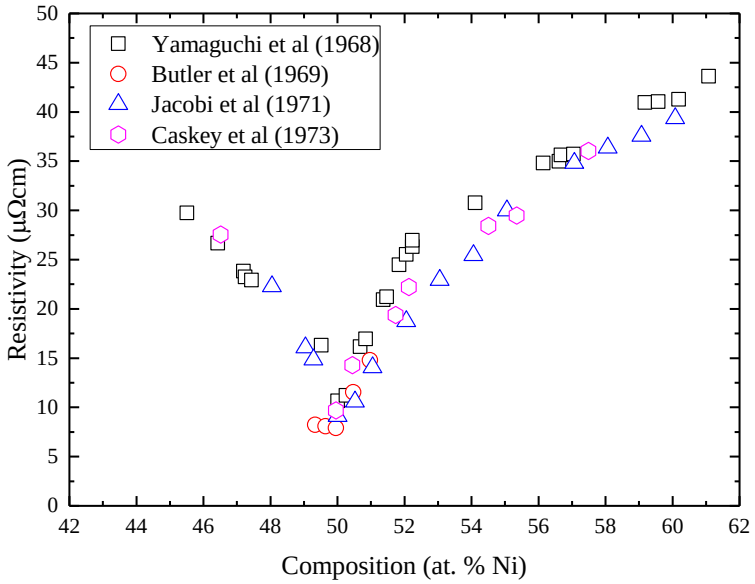

Figure 1.6: A summary of bulk resistivity of NiAl depends on nickel concentration (at. %) at room temperature [19], [34]–[37].

Figure 1.7 shows the resistivity of the bulk NiAl from 4.2 K to 300 K measured by Caskey et al [36], which displays that slightly Al-rich (49.6% atomic Ni) has the lowest resistivity at all temperatures. The temperature dependent part of the resistivity $\rho_{el\text{-}ph}(T)$ of NiAl varies from 13.91 to 16.1 μΩ×cm for the Ni-rich phase between 52.1 and 57.4 at. % Ni, and it varies from 9.1 to 10.1 μΩ×cm for the Al-rich phase between 46.4 and 49.6 at. % Ni [36]. The similar results were observed by Yamaguchi et al, which the results show the resistivity $\rho_{el\text{-}ph}(T)$ has a constant around 14 μΩcm for Ni-rich phase between 52 and 50 at. % Ni and a constant around 11.2 μΩ×cm for

Al-rich phase between 45 and 49 at. % Ni. The resistivity $\rho_{el\text{-}ph}$ (300 K) for NiAl with different nickel percentages, shows a difference in almost 10 μΩ×cm compared with the residual resistivity ρ_0 difference in almost 18 μΩ×cm.

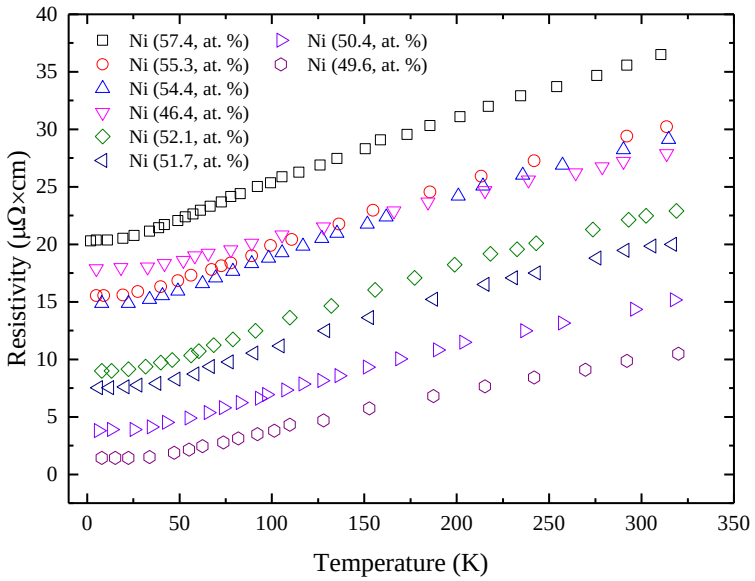

Figure 1.7: Electrical resistivity of the NiAl in different nickel concentration (at. %) versus the temperature from 4.2 K to 300 K [36].

Compared with the measured resistivity of bulk NiAl, the resistivity (24-60 μΩ×cm) of thin film NiAl are larger and more variable, which depends on the order and grain size of crystal structures [19]. Y. P. Lee et al mentioned that NiAl remains ordered up to the melting temperature, and the disordered films could be produced by the deposition onto the substrate with a fast cooling from 507 °C to -123 °C by liquid nitrogen, and the NiAl grain size reduced from 50 nm to 20 nm during the cooling process. Due to the disordered grain growth and reduction of the grain size in the fabrication process, the resistivity of thin film NiAl increased from 31.9 to 53.9 μΩ×cm [19], [41]. Referring to NiAl made by as-deposited sputtering, the products are formed from a compound target onto the substrates at room temperature, which has a resistivity value around 45 μΩ×cm [42]. Referring to NiAl made by co-deposited method, 2-100 nm thick films are formed from an Al effusion cell and Ni electron beam evaporation in a molecular beam epitaxy (MBE) system at 600 °C. For co-deposited method, the resistivity of NiAl film decreased significantly when the thickness of the NiAl films increased, which has a resistivity value around 24 μΩ×cm with a 100 nm thickness [43]. X. Qin et al has investigated the resistivity of nanostructured NiAl (grain size of 5~6 nm) that has a larger variation from ~100 to 50000 μΩ×cm with decreasing of density at room temperature. The reason for this is considered as the defects like porous [44]. Referring to the formation of NiAl from multilayers of Al and Ni, J. Howell investigate the resistivity of sputtered multilayers samples and e-beam multilayers samples with different layer thickness, and a summary of the resistivity for the Ni-Al films after 4 hours anneal at 400 °C and further anneal at higher temperatures in a few minutes is shown in Table 1.3 [19]. It can be seen that resistivity of all the samples decreases when the layer thickness increases. Furthermore, the resistivity of both nickel rich phase and aluminium rich phase of NiAl films are higher than the resistivity of

stoichiometric NiAl film. For instance, the resistivity of Ni_2Al_3 that is around 50.5 μΩ×cm, and it is almost two times larger than that of NiAl with the same thickness [19].

Table 1.3: A summary for the resistivity of the Ni-Al films after 4 hours anneal at 400 °C [19].

Material description	Layer thickness (nm)*	Annealing conditions		Resistivity (μΩcm)	Best annealing conditions		Lowest Resistivity (μΩ×cm) **
		Temperature (ºC)	Time (h)		Temperature (ºC)	Time (min)	
E-beam multilayer	20.0 (21.4)	400 ºC	4		1000	0.5	16.2
	25.0 (24.0)	400 ºC	4	18.3	700	10	13.3
	33.3 (32.6)	400 ºC	4	24.2	1000	0.5	14.2
E-beam multilayer 50.5% Ni	25.0 (24.0)	400 ºC	4	37.6			
E-beam multilayer 50.5% Al	33.3 (32.6)	400 ºC	4	23.5			
E-beam multilayer Ni_2Al_3	25.0 (23.7)	400 ºC	4	50.5			
Sputtered multilayer	15.4 (15.1)	400 ºC	4		1000	1	16.3
	20.0 (19.3)	400 ºC	4		1000	0.5	14.6
	25.0 (24.1)	400 ºC	4		1000	0.5	15.3
	30.0 (29.8)	400 ºC	4	15.5	800	20	11.0
Sputtered multilayer 0.5% Ag	30.0 (28.7)	400 ºC	4	15.7	800	0.5	12.8

*Values are the expected value for a given deposited. Numbers in parentheses are the actual values calculated from the measured thickness and numbers of layers.
**The best annealing conditions for those that results in the lowest resistivity are achieved.

1.1.3.2. Thermal conductivity of NiAl

The thermal conductivity of NiAl depending on Al concentration (at. %) at room temperature has been investigated by several groups [45]–[48], and the results are shown in Figure 1.8. Compared with the resistivity variation of the NiAl phase with Al composition range from 35 to 55 at. %, the thermal conductivity data measured by Terada et al and Zhao et al implies a mirror profile [46], [48]. It can be seen that thermal conductivity of the NiAl phase exhibits a very strong singularity with a sharp maximum at the stoichiometric, which the thermal conductivity of the stoichiometric NiAl measured by Darolia et al and Walston et al was around 75 W/(m×K) [45], [47]. Referring to the rapid reduction of the thermal conductivity for NiAl that the composition deviates from the stoichiometric, is considered a resultant of the large amount point defects existing in the off-stoichiometric NiAl phase, such as the vacancies of the nickel in aluminium rich phase and the occupancies of the nickel in the nickel rich phase [48], [49].

Walston et al has measured the thermal conductivity of well-ordered stoichiometric NiAl at the temperature from 300 K to 1000 K as shown in Figure 1.9 [45], which implies a slow increasing from 74 to 80 W/(m×K) with the temperature rising up. Tong et al has investigated the thermal conductivity by the analytical calculation via considering phonon-phonon and electron-phonon

scattering with a temperature range from 100 to 1000 K [50]. According to the calculated results, the estimated sum thermal conductivity of NiAl has a reduction from 76 to 68.7 W/K×m with the temperature decreasing from 800 K to 100 K. Furthermore, the thermal conductivity calculated by Tong et al has predicted the electron thermal conductivity (κ_e) is the main contribution to the thermal conductivity with the temperature from 100 K to 1000 K, and the phonon thermal conductivity (κ_{ph}) increase to 40% of the total thermal conductivity for NiAl when the temperature decreases to 100 K [50].

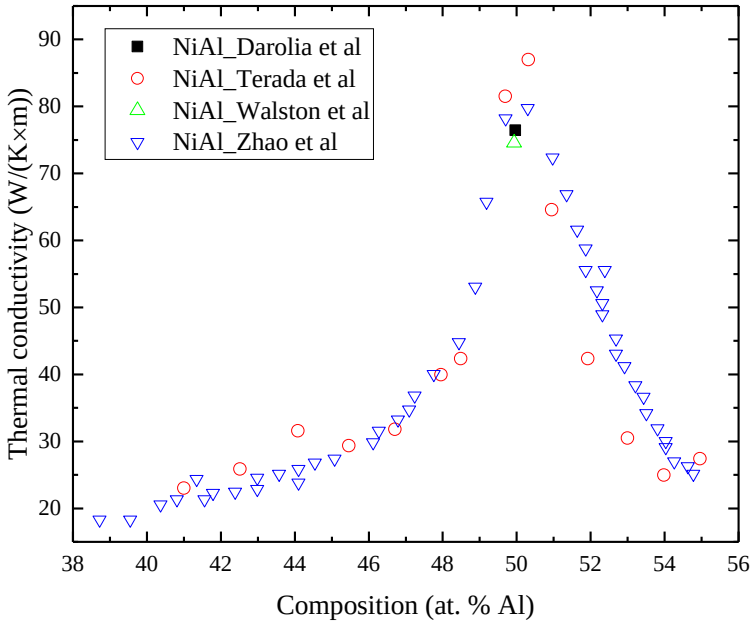

Figure 1.8: The plot for a summary of thermal conductivity of NiAl depending on Al concentration (at. %) [45]–[48].

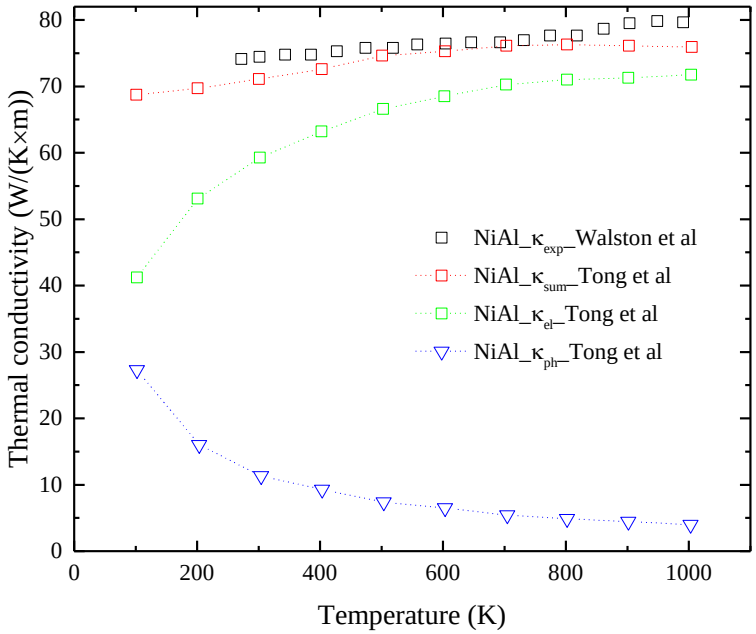

Figure 1.9: The plot for calculated electron thermal conductivity, phonon thermal conductivity and sum thermal conductivity of NiAl [139] versus the temperature from 100 K to 1000 K compared with experimental results [137].

1.1.3.3. Heat capacity of NiAl

Figure 1.10 shows the temperature dependent heat capacity of NiAl from several research groups [45], [51]–[55]. As shown in Figure 1.10, the heat capacity data at room temperature for stoichiometric single crystal NiAl measured by Walston et al [45], alloy powders of NiAl (Ni, 17.4 at. %) measured by Raj et al [51], NiAl film (Ni, 49.3 at. %) measured by Alexander et al [52], and ordered NiAl (Ni, 50.0 at. %) measured by Sandakova et al and reported in [54] are around 58.7 J/(mol×K), 19.6 J/(mol×K), 48.5 J/(mol×K) and 24.0 J/(mol×K) respectively. Sandakova et al has investigated specific heat of ordered NiAl (Ni, 50.0 at. %) at temperature from 60 K to room temperature, which shows a reduction trend of specific heat with the decreasing of the temperature [54]. The specific heat of $NiAl_3$ (Ni, 25.0 at. %), NiAl (Ni, 49.3 at. %) and Ni_3Al (Ni, 75.0 %) have been investigated at low temperatures (< 20 K) by Dunlop et al and reported in [54], Alexander et al [52] and Dood et al [55] respectively, which the results are shown in the same figure.

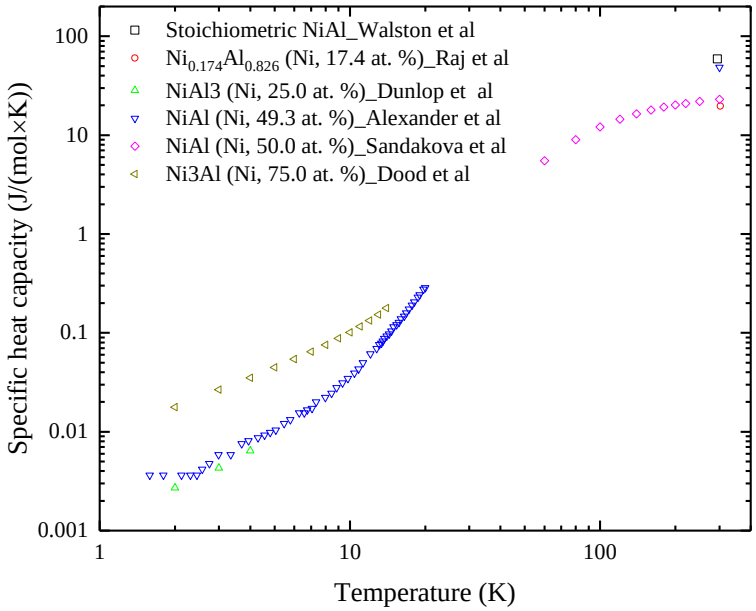

Figure 1.10: The plot of specific heat C_p for NiAl with different Ni concentration (at. %) versus the temperature between 1.4 K and 300 K [45], [51]–[55].

Figure 1.11 shows the plots in a conventional C_V/T versus T^2 at temperatures between 1 K and 10 K from several research groups [52], [53], [56], where C_V is the heat capacity in unit of J/(mol×K) and T is the temperature. Referring to many metals at low temperatures, a plot is a linear function as shown in Equation 1.1. β and α are electronic heat capacity coefficient and lattice heat capacity coefficient respectively, and these two values reflect their contribution on the total heat capacity. But for heat capacity measurements of NiAl as shown in Figure 1.11, Ho et al (black squares) [53] and Alexander et al (green circles) [52] found significant nonlinearity in the plot blow 4 K, however, the results could be fitted by adding a constant term A as shown below:

$$C_V = A + \beta T + \alpha T^2 \qquad 1.1$$

A plot of $(C_V - A)/T$ versus T^2 is also given in Figure 1.11, where the modified plot implies the new linear fitting curve for the data measured by Alexander et al (blue cicles) [52]. Then

electronic heat capacity coefficient β and lattice heat capacity coefficient α are 1.406e-3 J/(mol×K^2) and 2.056e-5 J/(mol×K^4) for NiAl (Ni, 49.3 at. %) from the data measured by Alexander et al [52] respectively. The data measured by Alexander et al implies the value of β_{NiAl} is close to that of aluminium, β_{Al} = 1.35e-3 J/(mol×K^2); The heat capacity for NiAl (Ni, 48 or 50 at. %) measured by Seitchik et al [56] does not exhibit an upturn at low temperatures, and a very low electronic heat capacity coefficient is obtained: β_{NiAl} = 1.26e-3 J/(mol×K^2), which is almost 87% of the pure aluminium. The electronic heat capacity coefficient for NiAl (Ni, 50.5 at. %) measured by Begot et al is 2.64e-3 J/(mol×K^2) [57], which is slightly higher than previous measured results. Ho et al didn't provide the data of the electronic heat capacity coefficient for their results, but it is estimated as a higher value (black squares) in accordance with the plot of C_V/T as shown in Figure 1.11 even the composition of their sample was in Al rich phase.

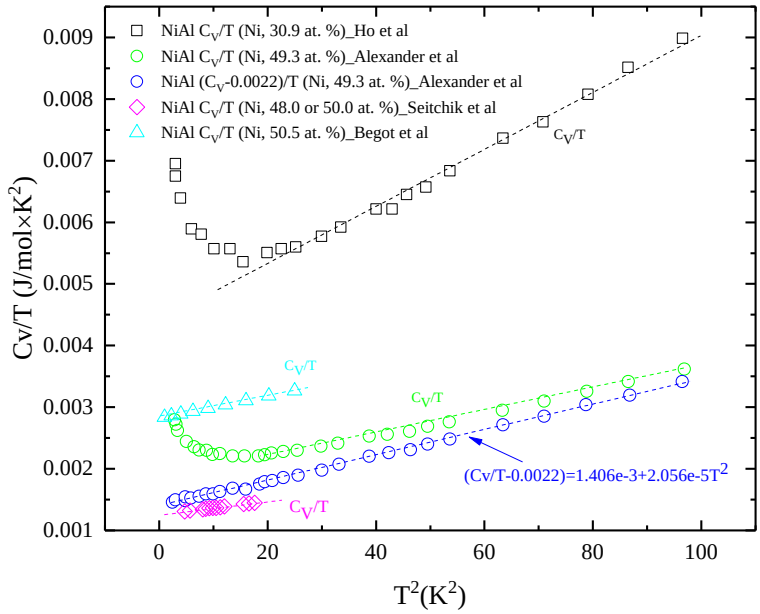

Figure 1.11: The plot of low temperature specific heat C_V in C_V/T for NiAl with different nickel concentration (at. %) versus T^2 compared with the modified specific heat in (C_V-A)/T (that was moved constant A, as described in texts) and the linear curve fitting of each curve profile [52], [53], [56].

1.1.3.4. Mechanical property of NiAl and its application

Two research groups have reviewed and demonstrated the effect of solder thickness, applied pressure and ambient temperatures during manufacture of reliable and strong nanobond joints [58]–[60].

Wang et al has investigated the mechanic characterisations of stainless steel-stainless steel (StSt-StSt) nanobond joints and Aluminum-Aluminum (Al-Al) nanobond joints. The thickness of AuSn solder applied to StSt-StSt joints and Al-Al joints is around 25 µm thick, and the thickness of the applied Ni/Al foils varies from 23 µm to 260 µm [58], [59]. Figure 1.12 shows a summary of shear strengths of the nanobond StSt-StSt joints and Al-Al joints as a function of the increasing Ni/Al foil thickness. The results show that the shear strengths of the StSt-StSt joints and Al-Al joints increase with the increasing of the foil thickness until the foil thickness to reach a constant [59]. Referring to the critical value of the foil thickness for the StSt-StSt joints is around 40 µm,

and average values of shear strength for the higher thickness foil joints is 48 ±3 MPa; referring to the critical value of the foil thickness for the Al-Al joints is around 80 µm, and shear strength of Al-Al joints with the applied Ni/Al foil above this thickness (80 µm) is around 32 ±5 MPa [59]. Furthermore, J. Wang mentioned that the increasing thickness of reactive foils make the AuSn solder melt for longer durations, so that there is more solder wetting of the surfaces. Furthermore, when the thickness of Ni/Al foils increases to above 40 µm, Au and Sn were found to be the dominating elements on the stainless steel fracture surface; for Au coated Al-Al joints, when the thickness of Ni/Al foils increases to 120 µm, the fracture surface shows the good wetting between Al and solder [58], [59].

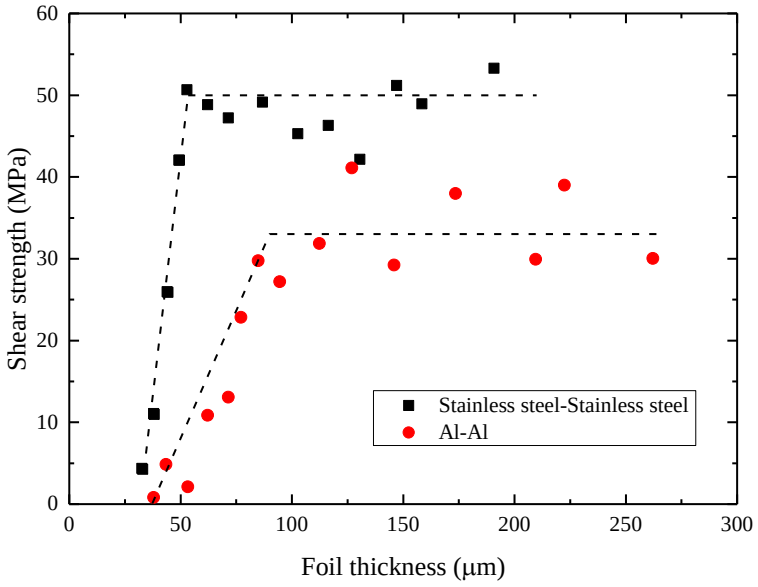

Figure 1.12: The plot of shear strength of stainless joints and Al joints vs. thickness of Ni/Al multilayer foils [59].

Zhu et al has investigated the effect of the solder thickness, ambient temperature and applied loading pressure on the shear strength of the copper to copper nanobond joints, which the results are shown Figure 1.13 [60]. Figure 1.13a shows a parabolic relationship between the shear strength and thickness of the solder layer, the increasing of the shear strength is due to the amount of liquid solder that could fill in the defects and gaps in the solder layer and nanofoil between two bonding components [60]. The following drop of shear strength with the continuous increasing of solder layer thickness above 30 µm exhibits the heat sink due to the reduction of the temperature and duration of the solder melting phase. Figure 1.13b shows that nanobond sample has a higher shear strength with higher ambient temperatures. Furthermore, Figure 1.13c displays a better mechanical performance with higher applied pressure [60]. For instance, the shear strength of sample that was made at room temperature with low loading pressures was less than 10 MPa, but for a sample was made at 100 ºC with a 2 MPa pressure, a strong interconnected nanobond sample can attain around 37 MPa shear strength [60]. Consequently, the shear strength of metallic nanobond joint measurements by Zhu et al and Wang et al show that higher ambient temperature, heavier pressure, and carefully selected solder layer with Ni/Al foil thickness can provide sufficient melting and wetting of the solder for fabricating a nanobond joint with shear strengths above 35 MPa [58]–[60].

The National Institute of Standards and Technology (NIST) solder database published the shear

strengths of Sn-37Pb (wt. %) and Sn-3.8Ag-0.7Cu (wt. %) are 45.5 MPa and 63.8 MPa respectively [61], Pan et al reported that the shear strength of Sn-37Pb solder joints and Sn-3.0Ag-0.5Cu (wt. %) are 69 MPa and 59 MPa [62]. This shows that the conventional soldering method will normally achieve stronger joint compared with nanobond joints. However, the traditional soldering method needs expensive reflow processes, and high operating temperature in the reflow process can damage the components with sensitive temperature limits. For nanobond process, rapid flux free soldering at room temperature with instantaneous reaction can provide a simple and economical way to bond components with no need for reflow equipment. This demonstration shows that it is possible to eliminate any heat exposure to the component being joined with the only local heating on the surface of the substrate [15], and this is very important for 2G-tape soldered joints.

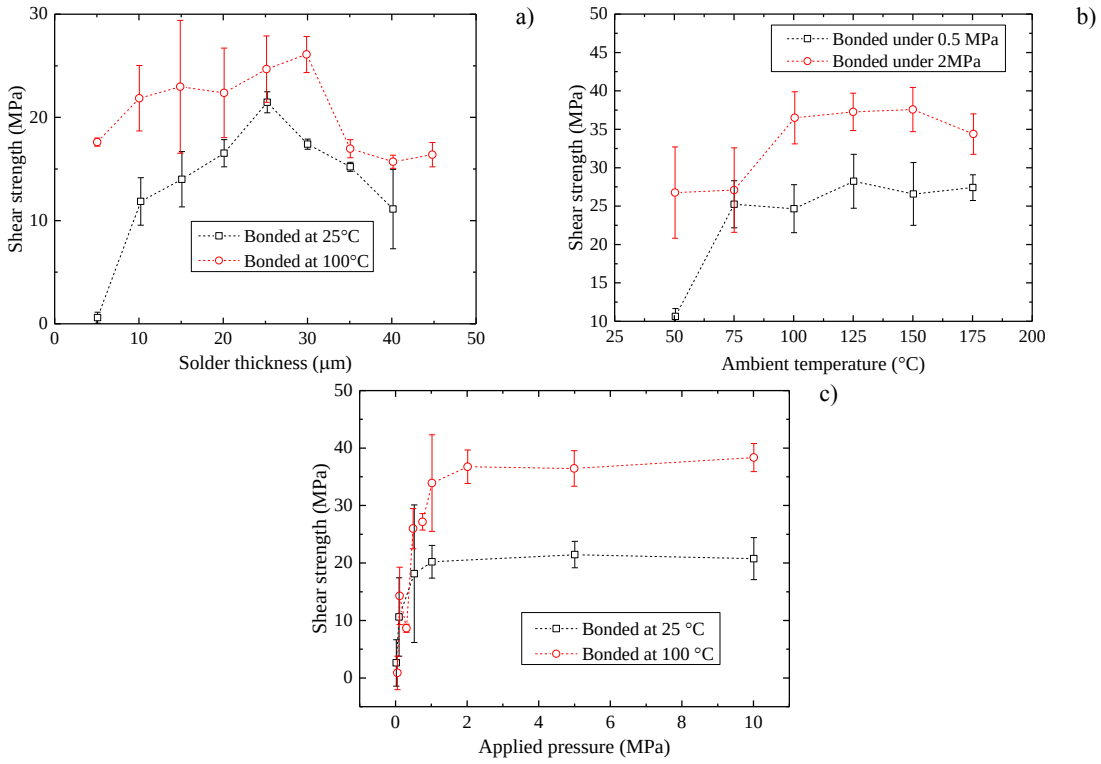

Figure 1.13: The plot of the shear strength for copper to copper nanobond fabricated with different a) thickness of solder at 25 ºC and 100 ºC respectively, b) temperatures under pressure of 0.5 MPa and 2 MPa respectively, c) applied pressure at 25 ºC and 100 ºC respectively [60].

1.1.4 Background of Aliminum Oxide/Alumina (Al2O3)

Alumina is a widely used material in engineering ceramics with a combination of excellent properties such as [63]–[65]:

- Good thermal conductivity (20 to 30 W/(m×K)).
- Excellent dielectric properties (1×10^{14} to 1×10^{15} Ω×cm) from DC to AC (GHz frequencies).
- High hardness (15 to 19 GPa), and very high compressive strength (2000 to 4000 MPa).
- High corrosion for both strong acid and alkali, wear resistance with good gliding properties.

- Low density (3.75 to 3.95 g/cm^3), excellent size and shape capability.
- Available in purity range from 94% (for metallic composition) to 99.8% (for applications at high temperatures operating.

As the excellent physical and chemical properties mentioned above, alumina plays an important role in the application of the power electronic substrates. These electronics substrates can provide a good electrical and thermal interconnection pathway for electric or semiconductor components mounting upon them, which the alumina layer also can provide the electrical insulation according to the requirement within the power module system [64], [66].

Strong bonding of metals to ceramics generally does exist in the application unless an intermediary is presented or formed from the reaction or diffusion, but it needs to be noted that an intermediary layer is not desirable for many applications, since it reduces the thermal conductivity or electrical conductivity performance, or higher resistive bonding than with metal and less corrosion resistant of this layer could cause a premature failure [67]. Solder bonding is not a good option for metal and ceramic bonding, since the large interfacial energy between the lead tin solder and ceramic, the liquid solder would not wet the surface of the ceramic for the bonding formation [68]. Researchers found that the interfacial energy between the molten copper and ceramic decrease dramatically with a small amount of oxygen, and this mechanism for the energy reduction is the formation of the bonding between the ceramic and the Cu_2O [68], [69]. Later the direct bonded copper substrate (DBC) was first developed by Y. S. Sun et al and J. F. Burgess et al [67], [68]. The basic principle of the DBC is to form a liquid metal oxidation skin around the copper interface to the ceramic at high temperatures, where the temperature and pressure require careful control of the melting point of the liquid layer close to the melting point of the copper, so that the soft copper can be shaped easily following the surface of the ceramic [66]–[68]. At this temperature, a copper to oxygen eutectic layer is formed to bond the copper and the ceramic. In the meantime, this layer can maintain the electrical and thermal conductivity compared with the copper, and a thinner thickness of the liquid layer is suggested so that the integral structure of the copper can be maintained [66]–[68]. DBC Al_2O_3 is developing in cryogenics applications such as electrical insulation for current leads in this project.

1.2 Roebel cable from 2G YBCO HTS conductors

Siemens Corporate Technology group designed the first HTS Roebel cables that using BSCCO (Bi-2223) tapes as strands [70]. This cable consisted of 13 strands, with a long transposition length over 2 m due to the limitation of in-plane bending ability of the material. This Roebel cable exhibited a transport current around 400 A at 77 K and demonstrated the ability to reduce AC losses for the motivation of this cable that was for the application in a HTS transformer [71]. The idea of using REBCO tape for Roebel cable structure was developed by Martin Wilson in 1997 at CEC-ICMC conference, but a way to bend the strand, shape of the strand and assemble them was still unknown [9], [72]. A solution was found by Wilfried Goldacker, and he presented a meander-like geometry of the conductor achieved by a precision punching technique that was developed at Karlsruhe Institute of Technology (KIT), which the first cable was fabricated from

16 punched strands from DyBCO (THEVA GmbH) tapes and presented in 2006 [73]. The first Roebel cable could carry around self-field current of 500 A at 77 K, but this cable had no copper stabilising layer and was burned due to not having any quench protection [73]. Later the second Roebel cable was fabricated from 16 punched strands of SuperPower 12 mm wide with copper stabilised tape, and the current carrying ability of this cable achieved 1020 A at 77 K in self-field [74]. Another group at Industrial Research Limited (IRL) have started to investigated the design of long length scale Roebel cable with an automated manufacturing process for industry applications in the meantime [75].

1.2.1 The design and preparation of Roebel cable

For meander-shaped 2G-tape for the Roebel cable fabrication, there are fundamental geometrical parameters were introduced by IRL [9], [76], which the parameters were shown in the schematic drawing of Figure 1.14a. The geometrical parameters w_1 is the strand width, and w_2 is the cross-over width, and w_3 is the original tape width, and w_g is the strand-edge clearance in the middle of the cable, and L_T is the transposition length (one pitch of the meander), and L_{ISG} is the inter-strand gap, and θ is the cross-over angle, and r is the cut-out fillet radius that is not shown in Figure 1.14a, and transposition and straight sections of the strands are highlighted in the same figure. Figure 1.14b is the picture showing the section of a 2 m Roebel cable applied to this project, which was fabricated with 15 strands of 2G YBCO tapes (Bruker GmbH). The strand width and cross-over width is $w_1 = w_2 = 5.5$ mm, and the transposition length is $L_T = 226$ mm, and the cross-over angle $\theta = 30^o$. The performance and quench characteristics of this Roebel cable will be discussed in Chapter 5.

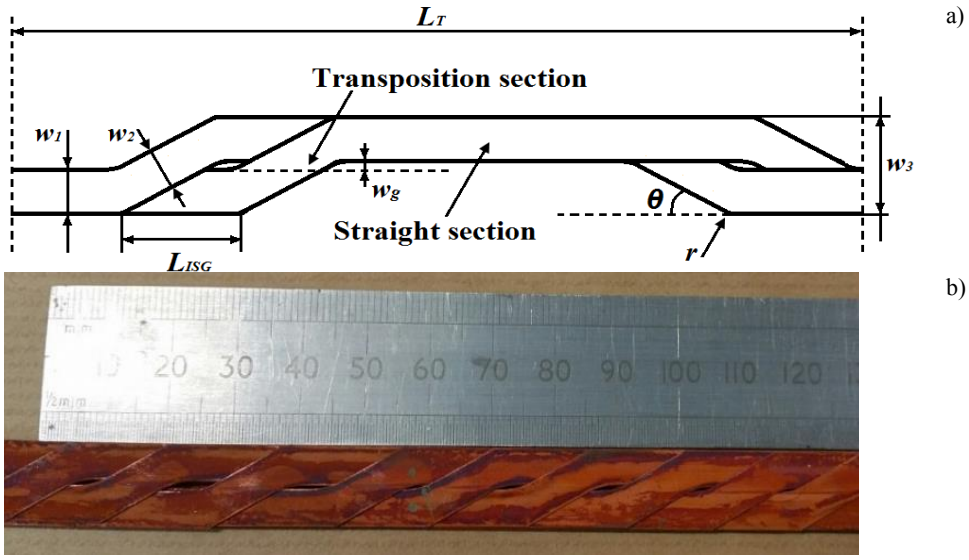

Figure 1.14: a) Schematic drawing of the detailed geometry of two strands for a Roebel cable [77], [78], and b) the picture showing the assembled 15/5.5 (15 strands with 5.5 mm width) Robel cable.

1.2.2 The performance of Roebel cable

Goldacker et al has compared some properties and performance of several Roebel cables manufactured by KIT and General Cable Corporation (GCS) compared with Siemens Bi-2223,

and the data is shown in Table 1.4 [9], [76]. All the Roebel cable samples have been measured with transport currents in LN2 in a self-field, and some of them have been compared the critical current with the original tape and single isolated strand by applying 1 μV/cm criterion [9], [76]. Referring to THEVA tapes without no copper stabilised layer beside the silver cap layer, an external copper foil as a shunt was applied to the critical current measurements. Since the advantage of observing the bypass current in the shunt is helpful for the correction of critical current in the measurement [76].

According to in Table 1.4, except Roebel cable of KIT-3 and GCS-3, other samples' original tapes have exhibited a good current homogeneity with critical current deviation within 10 A. Some cables imply the significant progress with high-reached critical current of KIT-5 (2628 A) and GCS-2 (1420 A), and long length of KIT-6 (5 m) and GCS-3 (21 m), and narrow width (~ 2mm) strands of KIT-4 and GCS-1. It needs to be noted that the decrease of the measured transport current of all the Roebel cable samples reached ~30%, compared with the designed critical current from the sum of the critical current of all the individual strands. For KIT-5 Roebel cable with three-fold together with 15 strands of each, the highest transport current measured among these samples is around 2600 A, but the reduction of the designed critical current was even beyond 60 %. This is considered as the strong effect of the self-field by the transport current.

Table 1.4: Properties of some Roebel cable samples [9], [76].

Cables		**BSSCO**	**KIT-1**	**KIT-2**	**KIT-3**	**KIT-4**	**KIT-5**	**KIT-6**	**GCS-1**	**GCS-2**	**GCS-3**
Strand data	*Tape company*	Siemens	THEVA	Superpower	THEVA	Superpower	Superpower				Superpower
	Type of strand/tape	Bi-2223	DyBCO	YBCO	DyBCO	REBCO	YBCO	REBCO	YBCO	YBCO	YBCO
	Substrate	Ag/AgMg	Hastelloy	Hastelloy	Hastelloy	Hastelloy	Hastelloy	Hastelloy	Hastelloy	Hastelloy	Hastelloy
	Stabilisation	Ag sheath		Cu (20 μm)		Cu (40 μm)	Cu (20 μm)	Cu	Cu	Cu	Cu
	Strand width	4	3.8	5	3.8	1.78-1.82	5	5.4-5.6	2	5	5
	Original I_c (A) @77K		232	189	315	156	188	348			
	Strand I_c (A) @77K	135 A	63±7.56	91.7±1.47	91.5±19.86	62.7±8.4	149.5**	140**		123±1	105.5,125,180.4
Cable data	*Cable length (m)*		0.36	0.36	0.36	1	1.1	5	0.54	5	21
	Cable cross-section (mm^2)	22.5	10	9	6.2	2	27.6	6	2.5	9.6	9.6
	Transposition length (mm)	2457	180	190	123	115.7	188	90	90	300	300
	Number of strands	13	16	16	11	10	3×15*	10	9	15	15
	Calculated I_c, N_{str}× I_c (strand) (A) @77K	1750	1008	1467	1006	640	6727	1400	427	1950	2093.5
	Measured I_c (A) @77K	1180	500	1020		447	2628	936	309	1100	1420
	I_c reduction from self-field (%)	33%	50%	30%		30%	61%	33%	28%	44%	32%
	Engineering current density (A mm^{-2})	5244	5000	11300		223.5	95.2	156	123.6	114.6	147.9
Reference		[70], [71]	[73]	[74]	[76]	[79]	[80]	[81]	[82]	[82]	[83]

*15 stacks of three folds each.
**Estimated value.

Besides the performance of the Roebel cables samples, the methodology of punching process and laser cutting for manufacturing the meander-like tape has been compared in [76], which the punching process was preferred for several advantages. For instance, a good punching can provide sharp cutting at the edge of the tapes to minimize the damage of the coated layer, but laser cutting may cause a rough edge and melting zone at the edge of the superconducting layer. Furthermore, the researchers start to focus on the Roebel cable structure design and modifying to increase the current carrying ability, thermal and mechanical stability. For instance, the multi-stacking with three to five-fold of Roebel cable stacking is applied to achieve higher current carrying ability; and applying higher pressure during the Roebel cable fabrication or including a soldering shunt layer of copper between strands to reduce inter-strand resistance can improve the ability of current sharing among the strands [84].

1.2.3 Roebel cable current injection soldering joints

Goldacker et al has investigated the contact resistance of two current injection joint for KIT-5 Roebel cable, two cable ends were tinned with low temperature solder (Sn50In50, wt. %) and soldered into copper pieces, with a groove matching to cable cross-sectional dimensions, and the resistance measured at 2500 A for selected strand were 0.2 and 0.12 μΩ respectively [80]. However, some research groups reported that an unusual *VI* characteristics were observed among the strands to exhibit some degree of current percolation, which the *VI* profiles of some strands are different from each other [76], [80]. This was considered as the inhomogeneous current injection among the strands of the Roebel cable with the short length (about half of the transposition length) that was overlapped the contact [76], [80]. Consequently, Goldacker et al suggested that the soldering contact length over one transposition of the strand could avoid problems of inhomogeneous current distribution among different strands, and *VI* characteristics looks very similar to each other [9]. Furthermore, the optimum low contact resistance feed-in path is suggested with a section of direct soldering contact between the top superconducting side and current lead [9], and this is a good guideline for our Roebel cable sample current injection contact manufacturing.

1.2.4 Thermal stability of Roebel cable

The current sharing of a Roebel cable during the quench process would become more complex compared with single 2G-tape [9], [85]. Besides current sharing with metal matrix, there would be current redistribution among different strands. The local disturbance of one strand causes the temperature increase of this hot spot by joule heating, and current sharing will occur in this strand. When the temperature of the hot spot is higher than the current sharing temperature ($T > T_{share}$), the current of this strand starts to decrease and redistributes towards the neighboring strands, which the Joule heat propagates towards the further strands in the meantime. Consequently, Goldacker et al suggests that all the strands could be measured in parallel for voltage-current (*VI*) characteristics, which gives more information about the scattering of the properties of the strands in the quench investigation experiments.

Chapter 2
Background of Superconductivity

2.1 Introduction to superconductivity

Generally, the ideal state of superconducting materials has the property of zero resistance for the electric current flow at low temperatures closed to absolute zero [1]. A superconducting material is both a perfect conductor and a perfect diamagnet. The superconductivity was discovered by Heike Kamerlingh Onnes on 8th April [86]. Superconductivity depends upon the temperature, applied magnetic field and current, which these variables are interdependent factors to limit on the superconducting state of the material [86]. Perfect electrical conductivity is considered as a current flowing without resistance under direct current conditions. However, superconductors have small, non-negligible, resistive losses because of the flux vortices, hysteresis and eddy currents under alternating current conditions [87]. Then Meissner and Ochsenfeld discovered that a superconductor can expel applied magnetic fields form its interior side in 1933 [86], which is an important step that finds out how and why superconductivity works. Figure 2.1 shows the Meissner effect in a superconductor below the lower critical field, as well as the applied field is between the lower critical field and the upper critical field, and above the upper critical current [86].

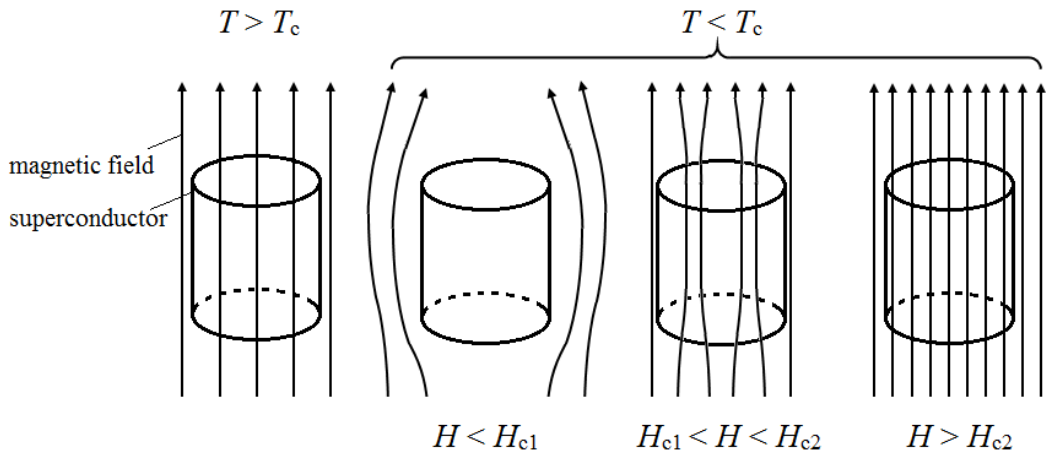

Figure 2.1: Effect of an applied magnetic field on a superconductor. Magnetic field lines are represented as arrows. The Meissner Effect occurs below the lower critical field (H_{c1}) and is the expulsion of an applied magnetic field upon transition from the normal to superconducting state. Between the lower critical field and the upper critical field (H_{c2}) the flux can enter the superconductors as regularly spaced quantized flux vortices.

Bardeen-Cooper-Schrieffer (BCS) theory was formulated in 1957, and this microscopic theory firstly explain the origin of superconductivity phenomenon [88]. For a material in the superconducting state, there are a lot of pairs of electrons with same velocity but which move in opposite spin. These pairs form a very strong and highly collective condensate. The energy required to break any single pair is related to the energy to break all of the pair. Consequently these entire pairs of electrons flow through the material as a whole without experiencing resistance [88]. However, the BCS theory still cannot fully explain the phenomenon and effects of high temperature superconductivity [89].

It is known that the cooling of the superconductor is needed to be below its transition temperature. However, such rigorous low temperature environment has limited the large scales and wide range of applications of the superconductors into the industry for a long time. In 1986, Bednorz and Müller discovered superconductivity in ceramic material at 35 K [90]. Later, the critical temperature for superconductivity increased nearly 100 K from 1986 to 1987, especially the discovery of yttrium barium copper oxide (YBCO) by Dr. Paul Chu in 1987 that made the superconducting material working at high temperature become possible [91]. This progress can make use of liquid nitrogen (LN2) as a refrigerant to replace liquid helium. This led to a fast development of superconductors and its application with large current carrying ability at higher critical temperatures. Due to the perfect conductivity and diamagnetism performance, superconductors have been a various applications in power transmission cables, magnets, medical imaging devices, generators and levitating trains [92]–[95].

Superconductors come in two types in accordance with temperature, low-temperature superconductors (LTS) and high-temperature superconductors (HTS), which depends on the transition temperature that defines the level of the conductors materials need to be cooled to achieve superconducting state [96]. Table 2.1 shows a comparison among the LTS material, 1G HTS material and MetOx 2G HTS material [97], [98]. Figure 2.2 shows the schematic drawing showing the resistivity of a low temperature superconductor (LTS) and a high temperature superconductor (HTS) and the copper [99].

Table 2.1: Comparison among the LTS material, 1G HTS material and 2G HTS material [97], [98].

Feature	LTS	1G HTS	MetOx 2G HTS
Operating Temperature	4 K	77 K	77 K
Performance	300 kA/cm^2	30000 kA/cm^2	2000 kA/cm^2
Coolant	Liquid Helium	Liquid Nitrogen	Liquid Nitrogen
Carrier/Substrate	Copper matrix	Silver matrix	Alloy
Active Layer	NbTi	BSCCO	YBCO
Own operate cost	Extremely High	Moderate	Approach the copper

Superconductors are called low temperature superconductors (LTS) with such low critical temperature, which these materials are usually operated in liquid helium at 4.2 K [87]. The metal alloy LTS such as Niobium-titanium (critical temperature: 10 K) currently being used in magnetic resonance imaging (MRI) magnets, which was the first major commercial application of LTS material and remains as the major market today [96].

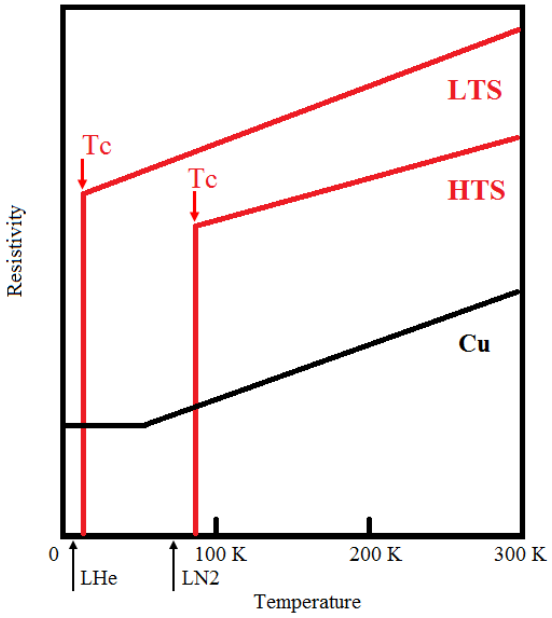

Figure 2.2: A schematic drawing showing the resistivity of a low temperature superconductor (LTS) and a high temperature superconductor (HTS) and the copper [99].

Superconductors are called high temperature superconductors (HTS) when they have the ability to achieve the superconducting state using inexpensive cryogen liquid nitrogen at a temperature of 77 K [96]. The higher operating temperature allows cryogenic savings for the cooling system and the reduced cooling needs of HTS applications can provide better performance advantages for electric power devices like HTS motors and transformers compared with those built with LTS [96].

2.2 Introduction to material for HTS winding aplications

2.2.1 First generation high temperature superconductors (1G HTS)

The first generation of HTS material was based on bismuth strontium calcium copper oxide or BSCCO [96], [97]. There are two common types of BSCCO tapes, Bi-2212 with critical temperature at 85 K and Bi-2223 with critical temperature at 110 K [100]. Bi-2223 has good performance in HTS applications especially in electric power devices. Bi-2212 can be operated below 20 K and performs much better than Bi-2223. Bi-2212 can also tolerate higher external fields therefore outweighing the performance of Nb_3Sn that is used in most LTS applications [101]. Figure 2.3 shows the schematic drawing of Bi-2223 and a picture of the cross-section of a BSSCO HTS tape [102].

As shown in Figure 2.3a, the main characteristics of the Bi-2223 unit cell are the presence of CuO_2 layers that are separated by a Ca layer without oxygen, and the group of CuO_2 are bonded by the layers of BiO and SrO [103]. The distance between the adjacent CuO_2 layers is referred to the critical temperature, observed in bismuth compounds [103]. Moreover, the distance between adjacent copper-oxygen planes has an impact on the way that flux vortices pinned into these compound [104].

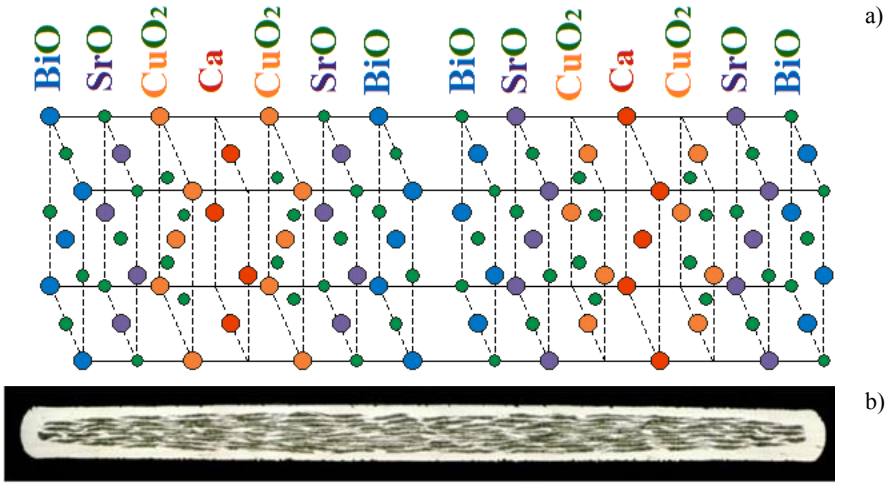

Figure 2.3: a) The Schematic drawing of Bi-2223 crystal unit and b) the picture showing the cross-section of a BSCCO HTS tape [102].

1G superconducting material has a relatively high price and low efficiency that the manufacturing method relies on a power tube utilising an expensive silver matrix. Figure 2.4 shows a schematic drawing for the BSCCO material manufacturing process called Oxide Power In Tube (OPIT) [105]. Ceramic BSCCO powders were filled into silver tubes and compressed into bars isostatically [105]. Later these BSCCO bars were placed into new tubes again and drawn into a mono-filament wire that can be rolled into a final form of tape, and the tapes are heated-treated at temperatures of around 830 °C [105]. Silver has been chosen to apply to manufacturing process due to its high chemical stability and because it has no reaction with superconducting material during the heating treatment and the good oxygen diffusion properties [101].

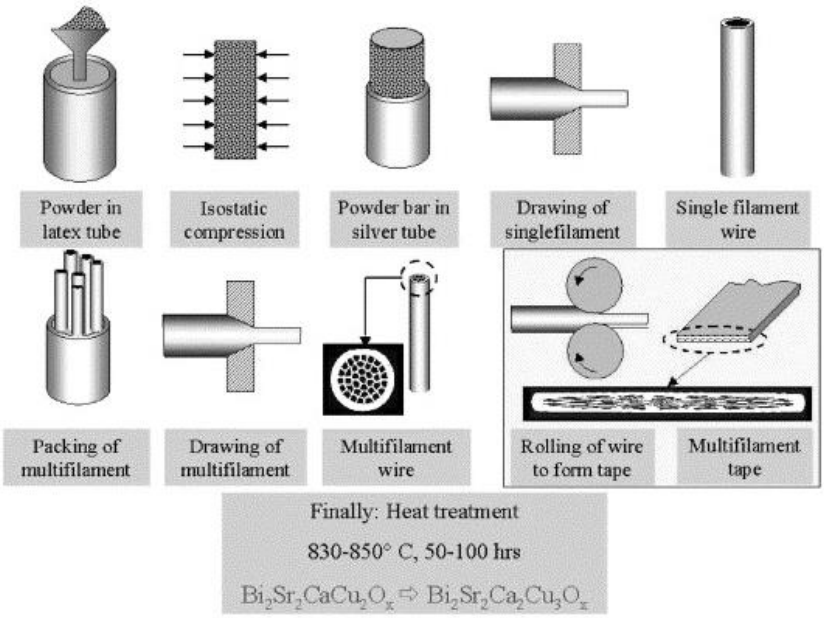

Figure 2.4: Production of Ag/BSCCO tape by OPIT method [105].

A new design superconducting tape with critical current values around 200 A was produced by Sumitomo Electric. An innovative process called “Controlled Over Pressure (CT-OP)” was applied to produce high quality of Bi-based HTS tapes [96], [106]. Figure 2.5 shows the

superconducting critical current as a function of flux density depending on different temperatures for one type of Bi-2223 tape produced by Sumitomo Electric [106], which this type has been chosen to apply to the HTS motor project at University of Southampton [107]–[109].

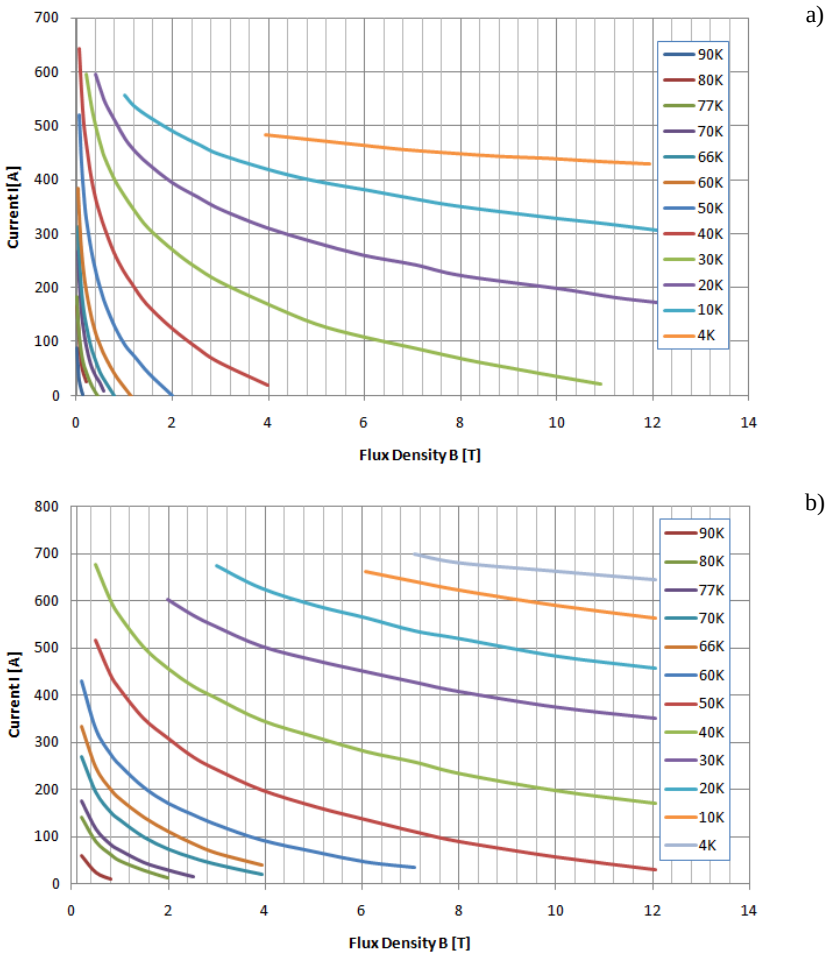

Figure 2.5: Superconducting critical current of BSCCO tape as a function of applied flux density at different temperatures: a) field perpendicular to the tape and b) field parallel to the tape [106].

However, due to high production costs of manufacturing techniques based on the complex stranded architecture and high silver content, there is still no widespread commercial application for BSCCO tapes. But there have been many HTS power device demonstrations, such as transmission cable, transformers, faults current controller and generators.

2.2.2 Second generation high temperature superconductors (2G HTS)

The second generation of HTS material is considerably more effective to carry higher current per unit volume, and 2G HTS conductors retain the performance both operating currents at high temperature and background magnetic field. Figure 2.6 shows the crystal structure of YBCO unit cell and cross-section of one 2G HTS conductor [110]. Moreover, the 2G HTS materials have the potential to reduce the manufacturing complexity with the lower cost. Rare earth elements based HTS materials such as Yttrium, Samarium and Gadolinium have been developed to produce 2G HTS materials [96].

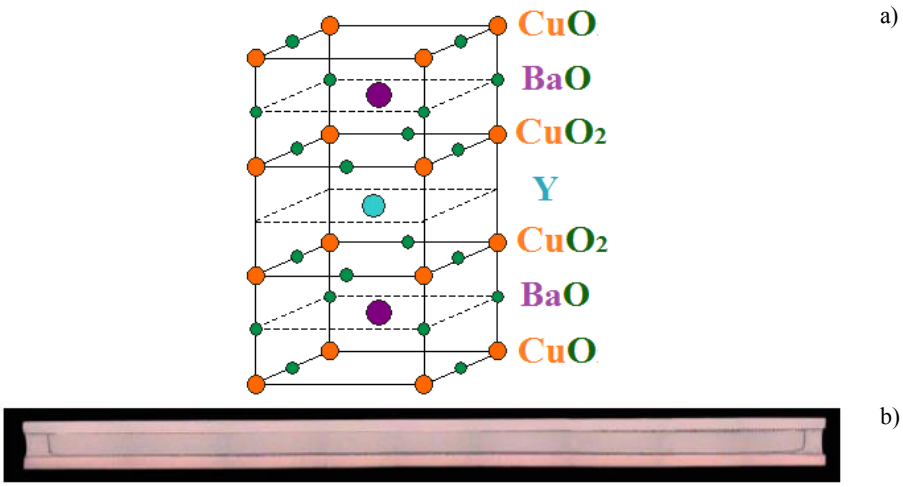

Figure 2.6: a) Schematic drawing of YBCO crystal unit, and b) the picture showing the cross-section of a YBCO HTS tape [110].

For the YBCO crystal unit cell as shown in Figure 2.6a, oxygen and copper are bound in layers containing chains and planes. Yittrium acts as a spacer between two CuO_2 planes Yittrium can be replaced by some other lanthanide series of rare-earth element in ReBCO that keeps superconducting properties without changes [103]. Both at the top and bottom of the crystal unit there is some oxygen missing in copper oxide chains. The oxygen vacancies have an effect on the critical temperature of the superconductors for ReBCO. Similar to BSCCO, CuO_2 are know as the current conduction layer for YBCO superconductors [104]. There is a preferred current flow along CuO_2 planes within YBCO material because of the structure of superconducting crystal, which the CuO_2 planes are called the ab-plane. The axis orthogonal to the ab-plane is called c-axis. It has mentioned that magnetic field has an effect on the current carrying capacity of one superconducting tape. In order to analyse the limiting directions of field in respect to the tape orientation, and Figure 2.7 shows that the field parallel to ab-planes is called parallel field ($B_{\parallel}$), and the field perpendicular to ab-planes is called perpendicular field ($B_{\perp}$) [111]. Hence, in order to achieve higher current carrying capacities, the rolling step in the production process of the HTS layer needs to be aligned in the ab-planes [105]. However, during the coil winding process, the coil will endure the tensile and bending stresses, which may cause the degradation of the superconductors.

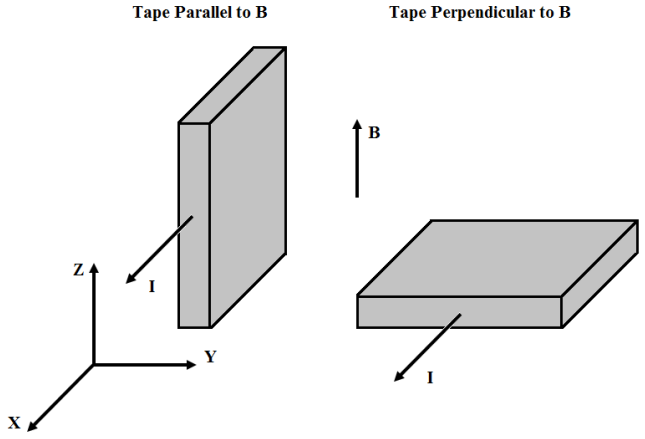

Figure 2.7: Tape orientation in respect to applied field.

2G HTS coated conductors is basing on REBCO such as YBCO with varying thickness of layers with silver and copper oxide elements plus optional insulation [96]. This 2G HTS fabrication process is automated and continues, which utilises the thin film deposition techniques that using in the semiconductor industry to apply the superconducting material on buffered metal substrate [96]. A manufacturing process applied to produce the 2G HTS conductors is called MOD/RABiTS (Metal Organic Deposition/Rolling Assisted Bi-axially Textured Substrate) [112]. Figure 2.8 shows the production of YBCO wire using MOD/RABiTS method that utilises reel-to-reel process from the metal (Ni5 at. %W) alloy through the Ag layer deposition [112]. Epitaxial buffer layers with a stack of Y_2O_3/YSZ/CeO_2 (Yttrium (III) oxide/ Yttria-stabilized-zirconia/ Cerium(IV) oxide) were also deposited in a reel-to-reel continuous process system that is compatible with wire length [112]. During the MOD process, the YBCO forms itself from solution-based precursor present in the buffered substrate [112]. Furthermore, there are several other techniques for approaching appropriate texture for substrate layers besides MOD/RABiTS process. For instance, Ion Beam Assisted Deposition (IBAD) can provide good quality of buffer layers that acts as a template layer to introduce the biaxial texture for the superconducting material [113]. Similar to MOD, Metal-organic-chemical vapor deposition (MOCVD) is an effective and cheap way for metal-organic deposition that can provide good base for YBCO. IBAD and MOCVD are applied to the 2G HTS wires produced by SuperPower [113].

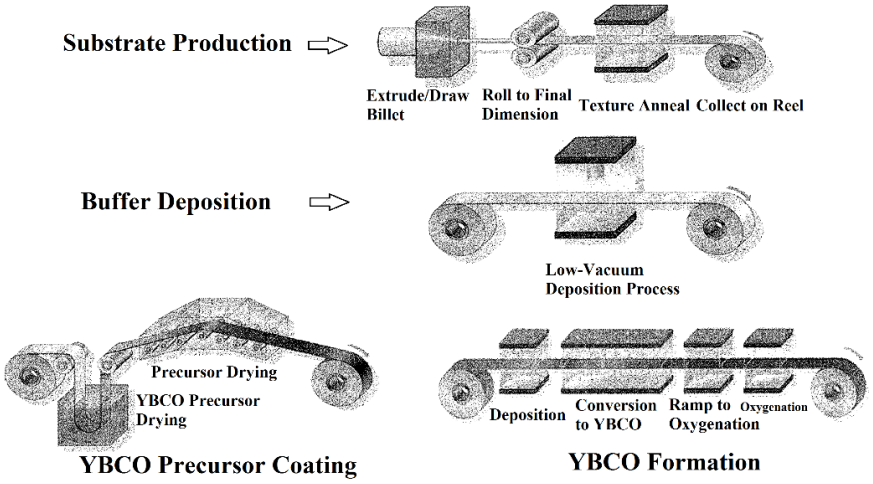

Figure 2.8: Production of YBCO tape by MOD/ MOD/RABiTS method [112].

Figure 2.9 shows the configuration of one 2G HTS tape produced by SuperPower [113], [114]. It can be seen that this 2G HTS conductor is surrounded with copper stabiliser so the conductor can be applied to high voltage applications, and the conductor terminal can be easily soldered for joints [113]. Due to the properties of non-magnetic and highly resistive, the Hastelloy substrate can make the conductor with lower AC losses, lower ferromagnetic losses and less eddy current loss [113]. Moreover, the high strength of Hastelloy substrate provides the conductor better mechanical properties such as the ability to be cut into narrow widths with small twist pitches. Buffer layer with MgO (Magnesium oxide) provide a diffusion barrier between YBCO and metal substrate. The excellent in-field performance at the intermediate temperature (540 A/cm at 40 K under 3 T $B_{\perp}$) and low temperature (480 A/cm at 4.2 K under 10 T $B_{\perp}$) is due to BZO (Barium zirconate) nanorods providing flux pinning sites [113], [115]–[117]. Figure 2.10 shows the

superconducting current capacity for YBCO and BSCCO superconductors as a function of flux density depending on different temperatures [111]. Due to higher energy efficient with loss-free electrical transmission process and the ability to produce stronger magnetic field, 2G HTS wire has a large potential for the application in high energy physics (accelerators and colliders), condensed matter physics (high-resolution NMR & EPR spectroscopy), biology and chemistry research, material sciences [115], [118].

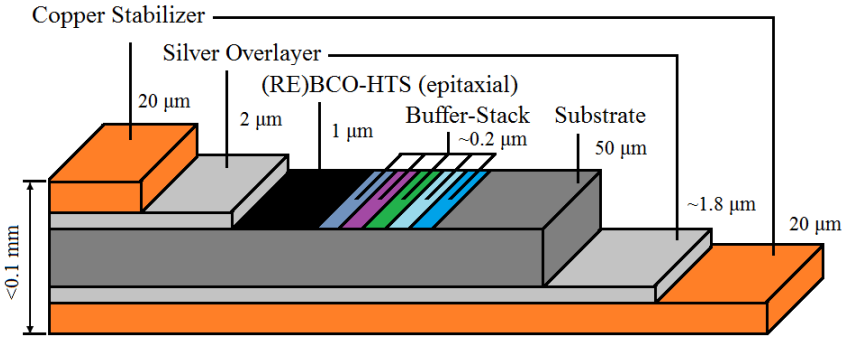

Figure 2.9: Schematic drawing of SuperPower produced 2G HTS conductor architecture [113], [114].

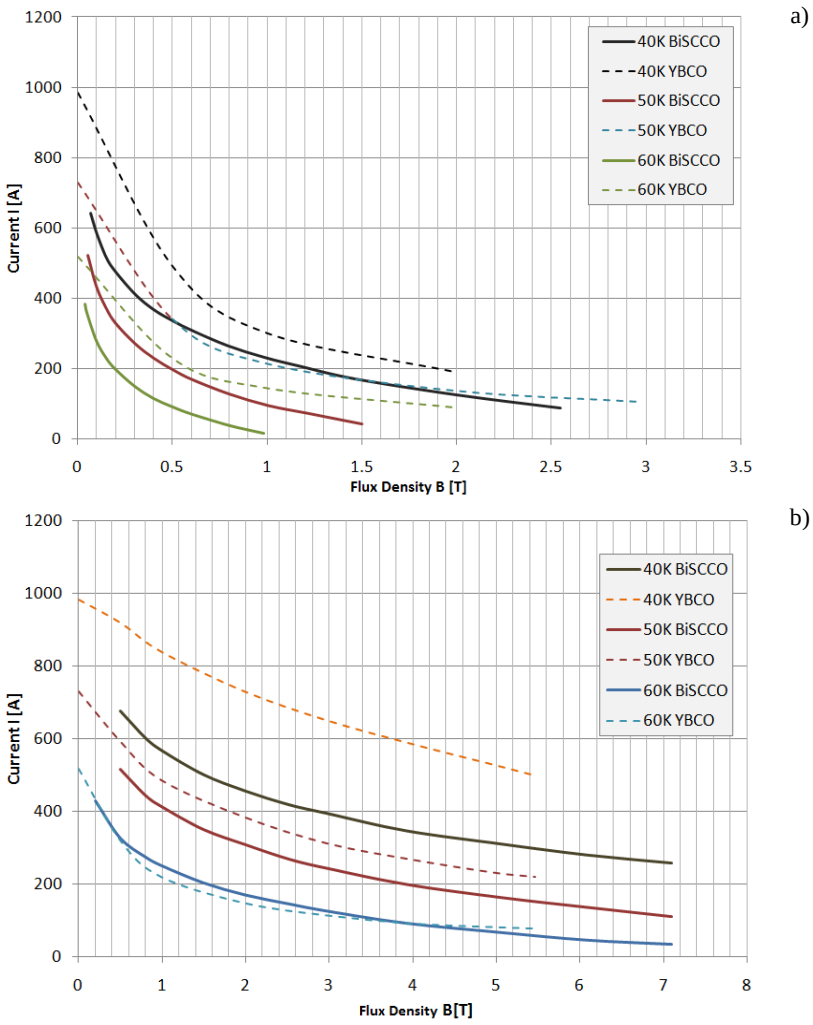

Figure 2.10: The superconducting current capacity for YBCO and BSCCO superconductors as a function of flux density depending on different temperatures: a) field perpendicular to the tape and b) field parallel to the tape [111].

2.3 Theory of applied superconductivity

2.3.1 Theory of material physical properties

2.3.1.1. Theory of electrical resistivity

Electrical resistivity is constant that represents in electrical resistance by Ohm's law for a certain dimension to evaluate electrical transport performance of the electrical conductors such as metals and alloys. According to Matthiessen's rule, the total electrical resistivity can be written as:

$$\rho(T) = \rho_0 + \rho_{el-ph}(T) \quad 2.1$$

Where ρ_0 and $\rho_{el\text{-}ph}(T)$ are residual resistivity and temperature dependent resistivity respectively. The residual resistivity ρ_0 is the resistivity that temperature approaches to zero, and the increasing of ρ_0 is contributed by impurity and lattice defects. The temperature dependent resistivity $\rho_{el\text{-}ph}(T)$, called lattice resistivity, is related to the electron-phonon scattering, which the temperature-dependent part of the resistivity is proportional to the rate at which an electron collides with the thermal phonons and thermal electrons [119], and it is not dependent significant upon small composition changes for a given metal and alloy [120]. Furthermore, the residual resistance ratio (RRR) variation of a material especially for metals can demonstrate clearly amount of the purity and crystal defects [121], which is expressed as:

$$RRR = \frac{\rho_{300K}}{\rho_0} \quad 2.2$$

Where ρ_{300K} and ρ_{0K} are resistivity at 300 K and 0 K respectively.

The electrical resistivity of nanoscale metal increases with their thickness reduces, and this size effect is due to the electron scattering at external surface and grain boundaries [122]–[127] when the grain size is smaller than the mean free path length ℓ of free electrons [127]. The relevant expression is shown below:

$$\ell = \frac{m_e v_f}{n_e e^2 \rho} \quad 2.3$$

Where m_e is the mass of the electrons, and v_f is the Fermi velocity, and n_e is the electrons concentration, and e is the elementary charge, and ρ is the material resistivity. It is expected that the free mean length of the metal would increase with the reduction of the resistivity at lower temperatures [119].

2.3.1.2. Theory of thermal conductivity

Thermal conductivity is a constant in accordance with Fourier's law to measure the heat flux transport of a conductor with certain dimensions as a function of temperature gradient. Referring to good thermal conducting materials such as metals, both electrons and phonons contribute to the thermal transfer within the material, which the sum conductivity κ_{sum} is expressed as [119], [128]:

$$\kappa_{sum} = \kappa_{el} + \kappa_{ph} \quad 2.4$$

Where κ_{el} is the conductivity contributed by electrons, and κ_{ph} is the conductivity contributed by phonons. In pure metals, the thermal conductivity is dominant by electrons at all temperatures. According to the kinetic theory of gases the expression for the thermal conductivity κ is given by:

$$\kappa = \frac{1}{3} C_v v_f \ell \qquad 2.5$$

Where C_V is the specific heat per volume, and v_f is the electron fermi velocity, and ℓ is the mean free path. For the impure metals or in disordered alloys, the electron mean free path is reduced by electron-scattering because of the collision with impurities, and the phonon contribution starts to be comparable with electron contribution. But for the case of insulations, the thermal transmission entirely depends on the phonon contribution. Phonons scattering is dominated in collision at high temperatures [119], [122]. The mean free length is a temperature dependent parameter, which is strongly related to the thermal conductivity temperature dependence. The mean free path is inversely proportional to the temperature, hence the conductivity is inversely proportional to temperature, too. When the temperature becomes lower, the mean free path becomes comparable with the width of the test specimens, and it starts to be limited by the grain size of the material [119], [129]. Consequently, the thermal conductivity becomes a function of the dimensions the specimen, which the size effect becomes dominate like some metals resistivity discussed in [122]–[124], [130]. The only temperature-dependent term is C_V, the specific heat per volume, which is proportional to T^3 at low temperature [119], thus it is expected that thermal conductivity varies with T^3 at low temperatures.

Lorenz number of the Wiedemann-Franz law is a ratio constant of thermal conductivity (κ) and electrical conductivity ($\sigma=1/\rho$) at a certain temperature (T), which the expression is shown in Equation 2.6. The Lorenz number (L) is a temperature dependent term for bulk metals at intermediate temperatures, which Lorenz number is decreasing with the reduction of the temperature, and this is due to the electrical conductivity increasing that is faster than the thermal conductivity with the decreasing of the temperature [120]. The value of Lorenz number is called Sommerfeld constant (2.44×10^{-8}) $W\times\Omega/K^2$ for bulk metals, at both high temperatures (~ 300 K) and low temperatures (a few Kelvins) [131]–[133].

$$L = \frac{\kappa}{\sigma T} = \frac{\kappa\rho}{T} \qquad 2.6$$

Because of the size effect of the measured specimen on thermal conductivity and resistivity, the Lorenz number of nano-crystalline metallic films are larger than the common value of 2.44×10^{-8} $W\times\Omega/K^2$ at room temperature [125], [134], [135]. This is considered size effect that the grain size of the specimen is smaller than the mean free path, which results in the grain boundary-electron and surface-electron scattering becoming more intensive [125], [130]. Consequently, the energy of scattered electrons can be partly transferred across the grain boundary by electron-phonon scattering, because phonons occupy the main contribution to transport energy through the grain boundary at room temperature [50], [125]. This results in the reduced electrical conductivity and less reduced thermal conductivity to cause a larger Lorenz number.

A higher experimental Lorenz number inhibits for alloys compared with their pure metal counterparts [120], [136]. A similar trend for Lorenz number versus temperature curve tends to a

constant at both high temperatures (~ 300 K) and low temperatures (a few Kelvins), and Lorenz number implies slightly below Sommerfeld number for dilute alloys and several times larger than Sommerfield number for some highly alloyed structural materials at intermediate temperatures. The reason for these alloys with large values of Lorenz number is due to the significant presence of lattice conductivity at both room and lower temperatures [120].

2.3.1.3. Theory of heat capacity

The similarity of the molar specific heats referring to some solid elements especially for metals is subject to the Law of Dulong and Petit at room temperature, and the specific heat at constant volume (C_V) is change rate of energy with temperature as shown in below [137]:

$$C_V = \frac{\partial(3k_B T N_A)}{\partial T} = \frac{3k_B N_A}{mole} = 24.94\, J/(mol \times K) \quad 2.7$$

Where k_B is the Boltzmann's constant, and T is the temperature in Kelvins, and N_A is the Avogadro's number, and specific heat C_V in unit of J/(mol×K) can be calculated by Equation 2.8:

$$C_V = C_P \times M \quad 2.8$$

Where C_P is the specific heat in unit of J/(g×K), and M is the mole mass. Referring to the low temperature, the Einstein-Debye phonon model is applied to analysis the heat capacity of metals, which is considered that this model has a good agreement with the temperature cubic dependence of the specific heat. This model combines the lattice vibrational and electron contributions to the specific heat, which the expression is shown below [138]:

$$C_{metal} = C_{electronic} + C_{vibration} = \frac{\pi^2 N_A k^2}{2E_f} T + \frac{12\pi^4 N_A k}{5T_D^3} T^3 \quad 2.9$$

Where electronic specific heat ($C_{electronic}$) is proportional to the temperature T, and vibrational specific heat ($C_{vibration}$) is proportional to the cubic of temperature T^3, and N_A is the Avogadro's number and k is the Boltzmann's constant, and E_f is Fermi energy, and T_D is Debye temperature, and Equation 2.9 has been divided by temperature T as shown in Equation 2.10:

$$\frac{C_V}{T} = \frac{\pi^2 N_A k^2}{2E_f} + \frac{12\pi^4 N_A k}{5T_D^3} T^2 = \beta + \alpha T^2 \quad 2.10$$

Where C_V is the specific heat in unit of J/mol×K, and β is the electronic specific heat constant, and α is vibrational specific heat constant.

2.3.2 Electrical contact characteristics of HTS joints

2.3.2.1. Contact resistance of soldering joints

Schematic drawing of a lap soldering joint between two 2G HTS tapes is shown in Figure 2.11. Generally, the overall soldering joint contact resistance (R_J) consists of solder resistance (R_{solder}), and interfacial stabilizer material resistance (R_i) between copper or silver and the REBCO layer [7]. For the contact resistance, it is given by:

$$R_J = R_{solder} + R_i \quad 2.11$$

In the experiments, contact resistance can be estimated by 4-contact method to measure the voltage drop and applied current across the joint. Voltage-Current (*VI*) curves are applied to the analysis of the HTS joints contact resistance as shown in Figure 2.12 [7]. There is always a linear slope existing in the curve before the HTS layer transitions to normal state, which the slope is called 'contact resistance' in units of nΩ over the joints to perform the contact joints. The contact resistance of two samples were 240 and 280 nΩ as shown in Figure 2.12. When the contact area was involving in the specific resistance analysis, the contact resistance can be express in $n\Omega \times cm^2$. Referring to the HTS-based applications, small contact resistance are expected for the applications. The effect of compressive pressure temperature, joint fabricated time and joint material are important manufacturing parameters on the contribution of the joint electrical contact resistance [139], [140]. Joule heating from the current due to the large contact resistance may cause high thermal energy dissipation into the coil, which has a high risk to lead to the quench of the HTS winding.

Figure 2.11: The configuration of a lap soldering joint between two 2G HTS tapes.

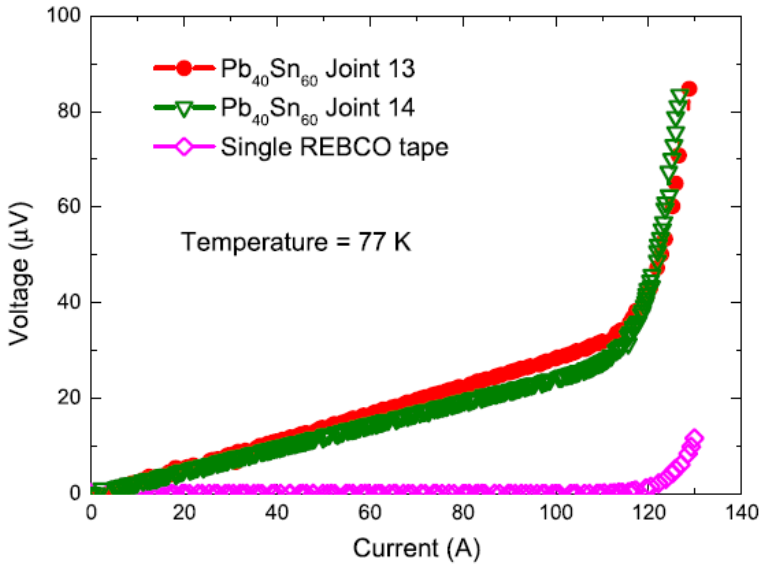

Figure 2.12: The plot of voltage-current (*VI*) characteristics of two 2G-tape soldering joints compared with a single 2G tape at 77 K.

2.3.2.2. Current transfer characteristics in HTS tape joints

The HTS joints contact resistance consists of metal matrix, solder resistance, and interfacial resistance (interfacial resistance between metal laminating layers and HTS layer, interfacial resistance between solder and copper, interfacial resistance between laminating layers) [6]. The metal resistance and solder resistance could be evaluated in accordance with the joint configuration, but the interfacial resistance become the challenges for the contact resistance

estimation. The well-known method to evaluate the interfacial resistance between HTS layer and surrounding metal laminating layer was developed by Polak et al [141], [142]. As shown in Figure 2.13, a schematic drawing of current transfer length measurement configuration is presented [6], [142], [143]. A constant current I_0 was applied to the HTS tape, and voltage tape V_n (n = 0, 1, 2,.., n) were attached to the metal layer to measure the voltage distribution from the contact starting position where the current started to transfer from the HTS tape to the position along the x axis. The voltage tap V_{ref} was placed at a further position from the beginning of the contact. The spacing between each voltage tap should be as small as possible, thus the exponentially voltage changes versus the distance for current transfer into the upper metallic layer can be evaluated. Then the current transfer length (CLT) λ, a characteristics parameter for the current flowing in the metal layer (normal Ag) is describe in Equation 2.12 [141], [144].

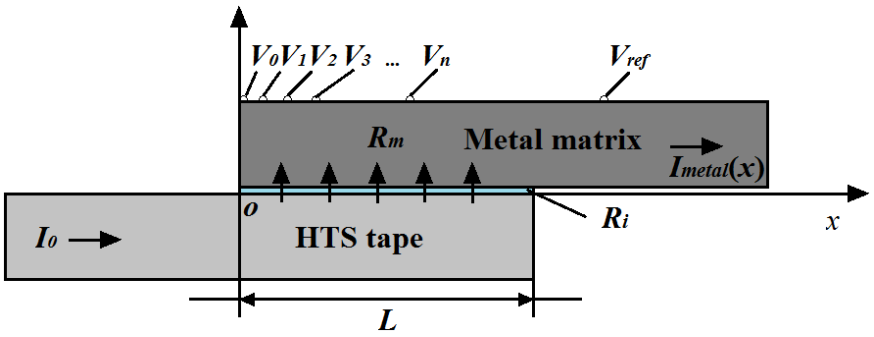

Figure 2.13: Schematic drawing of current transfer length measurement configuration for HTS [6], [142], [143].

$$I_{metal}(x) = I_0 \exp(\frac{-x}{\lambda}) \quad 2.12$$

Where $I_{metal}(x)$ is the current flowing in the normal metal at the distance x from the contact starting point, and voltage as a function of x is shown below [141], [144]:

$$V(x) = V_0 \exp(\frac{-x}{\lambda}) \quad 2.13$$

Where $V(x)$ is the voltage measured at distance x, and V_0 is the voltage measured on the first voltage tap at the beginning of the contact. Then the current transfer length λ can be expressed as [141], [144]:

$$\lambda = x/\ln(V(x)/V_0) \quad 2.14$$

And interfacial resistance R_i can be calculated by [141], [144]:

$$R_i = \lambda^2 \times R_{metal} \times A_1 \quad 2.15$$

Where R_i is the interface resistance, and R_{metal} is the resistance of the metal matrix overlapped the sample per unit length, and A_1 is the area of contact boundary per unit sample length. Polak et al based on Equation 2.14 and 2.15 with experimental voltages to obtain the interfacial resistance and current transfer length between YBCO layer and Ag layer [141], [142], and Bagrets et al applied a same method to investigate the interfacial resistance between ReBCO layer and copper laminate layer, and interfacial resistance between soldered 2G-tape and 2G-tape/copper joints for different commercial HTS tapes [6], [145].

Bagrets et al applied 40 μm wide contact to bond their voltage tap with 80-100 μm distance between each in their measurements, which the distance error was estimated to be 10 μm [6]. The manual voltage tap soldering method become impossible for such small distance, and voltage taps have to be limited in the micrometer scale. Consequently, a continuous sliding attaching voltage tap was considered and developed in our contact resistance measurements. Kursumovic et al [143] and Stenvall et al [146] take geometry into consideration and built an analytical model for the current transfer between superconducting layer and metal matrix based on Ohm's law; They provided the formula to analyse the current distribution along both superconducting layer and metal matrix layer, to compute the current transfer length in accordance with the electrical field criteria. More details referring to current transfer characteristics model and HTS joints contact resistance measurements will be discussed in Chapter 4.

2.3.2.3. Electrical contact resistance measurements of 2G-tapes soldering joints

2.3.2.3.1. 2G tape to 2G tape Soldering joints

The lap joint contact resistance between superconducting 2G-tapes from different commercial HTS tapes and different solders were investigated experimentally in [7], [8], [142]–[145], [147].

Referring to the contact resistance of soldering joints between two 2G-tapes, Dreuth et al found that the electrical resistance between metal and YBCO could varied from 1 to 10^4 nΩ×cm^2 [147], and Polak et al have investigated YBCO/Ag interfacial resistance that was varied from 20 to 370 nΩ×cm^2 [142]. Later Tsui et al and Bagrets et al have investigated the overall resistance of solder joints between two 2G-tapes with more details [7], [144], and they considered that contribution from copper and silver of 2G-tape could be negligible. Because the limitation of thin layer of silver (~1-2 μm) and copper (25-50 μm) at 77 K, the contribution of resistance (< 1 nΩ×cm^2) from Cu/Ag laminating layers is very small compared with YBCO/Ag interfacial resistance [7], [144]. Consequently, the interfacial resistance between superconducting layer and the metal laminating layer would dominate the main resistance in R_i and has a main contribution on the overall contact resistance R_J.

Tsui et al have investigated overall resistance R_J of five In52Sn48 (wt. %) joints, R_J = ~47-59 nΩ×cm^2, and six Pb38Sn62 (wt. %) joints, R_J = 34-66 nΩ×cm^2, between two SuperPower 2G-tapes at 77 K [7]. For In52Sn48 (wt. %) joints, the average solder thickness of these joints were 22 ± 2 μm and the joint area varied from 10.8 to 16 mm^2 [7]. The temperature independent terms considered as the interfacial stabiliser material resistance were measured around 20-27 nΩ×cm^2 [7]; For Pb38Sn62 (wt. %) joints, a larger variation of results were exhibited compared with the In52Sn48 results. When the solder thickness was varied from 23 to 25 μm and contact area varied from 14.4 to 15.2 mm^2, the interfacial stabiliser material (resistance R_i) were measured between 24 and 26 nΩ×cm^2 [7]. But the results became no reproducible and non-physical, when the solder layer thickness varied from 35-90 μm and contact area varied between 13.2 and 15.6 mm^2 [7]. For another two Pb40Sn60 (wt. %) joints between two 2G-tapes with solder layer thickness (~25 μm) and area (26.4 and 32.4 mm^2), the overall contact resistances were 73.92 and 77.76 nΩ×cm^2 at 77 K respectively [7].

Bagrets et al have measured overall resistance R_J of serval Sn63Pb37 (wt. %) joints between two 2G-tapes from Superpower and SuNAM with different loading pressure (0-25 MPa). The effective overlap area of these joints were ~2.4 cm^2 [144]. The average overall contact resistance of SuperPower 2G-tape joints and SuNAM 2G-tape joints were 41 $n\Omega \times cm^2$ and 280 $n\Omega \times cm^2$ respectively. Referring to interfacial stabiliser material resistance R_i for SuperPower 2G-tapes and SuNAM 2G-tape were 20.5 and 140 $n\Omega \times cm^2$ respectively [144]. The interfacial resistance of SuperPower 2G-tapes measured by Bagrets et al were consistent with the results measured by Tsui et al. In order to find the reason for such difference of interfacial stabiliser material resistance between SuperPower tapes and SuNAM tapes, Bagrets et al has investigated the copper morphology of both SuperPower tapes and SuNAM tapes by the Scanning Electron Microscope (SEM) [144]. Barget et al found that the copper layer of SuperPower was rougher with larger grains compared with flat surface and fine grains of SuNAM tapes. Consequently, the copper layer of SuperPower tapes would have larger contact area with silver and better solder wettability to exhibit better interfacial contact performance.

2.3.2.3.2. 2G-tape to copper soldering joints

Compared with the overall contact resistance between two 2G-tapes, there were more resistive elements between solder and copper conductor ($R_{solder\text{-}Cu}$), copper conductor resistance (R_{Cu}) besides the interfacial stabilizer material resistance (R_i) taking into account for the overall contact R_J of a 2G-tape to copper joint, which the expression is shown below:

$$R_J = R_{solder} + R_i + R_{solder-Cu} + R_{Cu} \qquad 2.16$$

Bagrets et al also have investigated overall resistance R_J of serval Sn63Pb37 (wt. %) joints between 2G-tape (Superpower tapes and SuNAM tapes) and copper tape with a same effective overlap area (0.6 cm^2) but different loading pressure (2.5-3.0 MPa) [144]. The measured average value of overall contact resistance of 2G-tape to copper joints were ~660 $n\Omega \times cm^2$ for SuperPower samples and 695 $n\Omega \times cm^2$ for SuNAM samples respectively [144]. Bagrets et al stated that the copper resistance R_{Cu} is estimated around 190 nΩ with a cross-section of 0.2 cm^2, and the sum of R_{solder}, R_i, and $R_{solder\text{-}Cu}$ was 546 $n\Omega \times cm^2$ for SuperPower samples and 581 $n\Omega \times cm^2$ for SuNAM samples [144]. The resistance R_{solder} and resistance of silver and copper layer within the 2G-tape could be neglected, and R_i has been described in the review of 2G tape to 2G tape joints, which were 20.5 and 140 $n\Omega \times cm^2$ for SuperPower tapes and SuNAM tapes respectively. Thus the mean value of $R_{solder\text{-}Cu}$ were 525.5 $n\Omega \times cm^2$ for SuperPower one and 441 $n\Omega \times cm^2$ for SuNAM one [144]. Furthermore, Bagrets et al found that the main differences in $R_{solder\text{-}Cu}$ were correlated to the copper tape surface roughness, which there was a nearly inversely proportional relationship between the interface resistance and roughness [144].

2.3.3 Critical state of superconductors

Figure 2.14 shows the *J*, *B* and *T* surface that displays the boundary of the superconducting state [148]. Superconducting state was defined below this surface, and the above is the normal state in the practical purpose. Referring to the boundary of this surface, the critical temperature T_c is a material property and is one of the three defining characteristics of a superconductor, the others

being critical magnetic field, B_c, and critical current, I_c. Critical current density J_c can be used instead of I_c, where $J_c = I_c/A$, and A is the cross-section of the conductor. Then in other words, if a temperature is provided below T_c, and the transport current is provided without exceeding J_c and magnetic field is below the critical value, the material will be superconducting; otherwise it will be resistive. The transition between the superconducting and normal states depending on the changes in temperature above or below T_c is direct. However, the nature of the transition because of a change in magnetic field is more complicated.

It has discussed that the upper critical field (B_{c2}) is applied to distinguish it from the lower critical field (B_{c1}) that the magnetic flux starts to penetrate as discussed in Figure 2.1 for Meissner effect. Consequently, the lower critical field shows whether the material transition from the pure diamagnetic state of Type I to the mixed state of Type II superconductor, which the mixed state is the region between B_{c1} and B_{c2}. Due to low current carrying ability, Type I superconductors are not further interested in practical applications. *J*, *B* and *T*, three critical properties, become a surface that is associated to the condition for defining the superconducting state of a material, which T_c and B_{c2} are intrinsic parameters of any superconductor, and J_c is an extrinsic parameter that can be affected by many factors, such as processing route for the superconductor manufacturing [148].

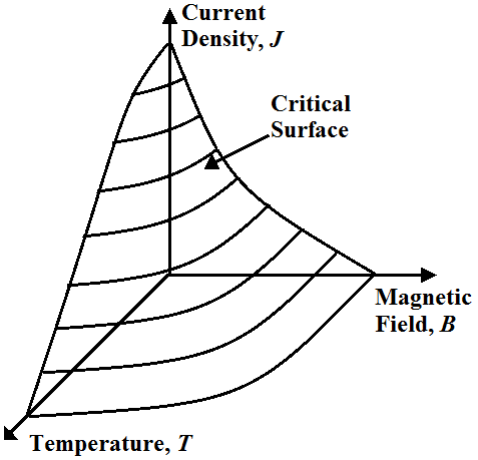

Figure 2.14: Typical critical surface (*J*, *B* and *T*) for a superconductor [148], [149].

Figure 2.15 shows the upper magnetic field (B_{c2}) varying with temperatures (T) in the absence of transport current, which $B_{c2}(T)$ as a function of temperature normally can be written as [148]:

$$B_{c2}(T) = B_{c2}(0)(1 - (T/T_c)^2) \qquad 2.17$$

Where $B_{c2}(0)$ is the upper magnetic field at absolute zero temperature, and T_c is the critical temperature. But for the critical field at a given temperature to define the critical current, the variation of $B^*(T)$ as a function of temperature become true as shown in Figure 2.15 [148]. For LTS materials, the difference between B^* and B_{c2} is very small. However, there is a large difference between B^* and B_{c2} for HTS material, which B^* profile was named as irreversibility line or flux lattice melting line. When the applied field, involving self-field and external field, is below the B^* at each temperature, the HTS can carry the useful current density. However, it is unlikely for HTS material to carry higher current densities in such high field at higher temperatures [148].

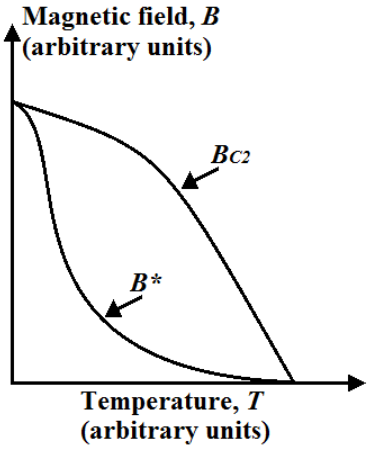

Figure 2.15: The plot for the difference between the upper critical field (B_{c2}) at zero transport current and the critical field B* with a non-zero transport current [148].

Referring to the criteria for critical current, there are two criteria used to define the critical current, which are electrical field and resistivity respectively. For electrical field, critical current is defined when the current that give rise to a voltage that reaches a determined electrical field (E) along the superconductor in voltage-current (VI) characteristics plot, which the most common values used for criteria of E are 10 and 100 μV/m [148]. For resistivity, the critical current is defined when the current give rise to an effective level for the resistivity values from 10^{-14} to 10^{-12} Ω×m [148].

2.3.4 Non-linear *E-J* characteristics

The transport critical current I_c is not a quantity that can be determined directly through measurements. The previous section has stated that a critical current value can be obtained by applying electrical field or resistivity criteria from the measured VI characteristic plot of the applied samples. For instance, Figure 2.16 shows the plot for two assumed samples, which sample 1 is a completely resistive sample, and sample 2 is a superconductor [148], [150]. 1 μV/cm criteria (thin horizontal dash line) was applied to define the critical current. Sample 1 shows the ideal linear voltage-current relationship in accordance with Ohm's law. Attention should be paid on sample 2.

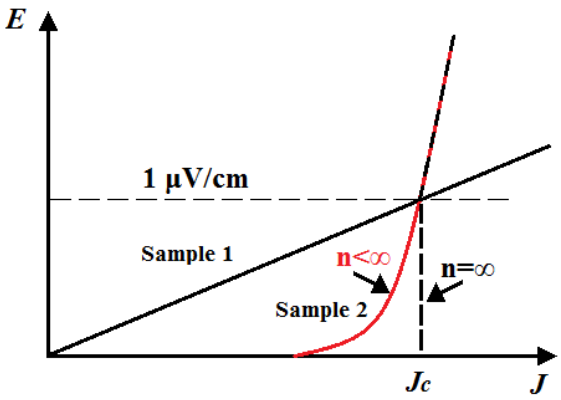

Figure 2.16: The plot for *E-J* characteristics of two assumed samples. Sample 1 is a resistive conductor, and sample 2 is a superconductor, which red solid line represents the power law model, and thick black dash line represents the critical state. Thin horizontal dash line represents the electrical criterion of 1 μV/cm [148], [150].

The power law was applied to analyse the non-linear *E-J* characteristic:

$$E = E_0 \times (\frac{J}{J_c})^n \qquad 2.18$$

Where E_0 and J_c are electrical field criterion and critical current density respectively, and the index number *n* is a parameter to exhibit the strength of the non-linearity of the *E-J* characteristics. For an ideal homogeneous superconductor condition, as current is increased, the sample reaches the critical state, where the thick dash line represents a sudden transition for sample 2 from superconducting state to reach the critical state, and the index *n* is expected to be infinite. For the real case, a non-linear *E-J* characteristic was observed for the transition with the appearance of finite voltage below J_c, whilst the practical superconductors are characterised by $n < \infty$. There are different reasons for the observed non-linearity of the transition characteristics, both microscopic effect, such as flux creep and non-linear flux motion [148], and macroscopic effects, such as the spatial non-uniform critical current [103]. Hence, the index number *n* is used for the criteria to show the homogeneity of the sample with good critical current distribution, which the higher value of *n* shows the better performance of the applied superconductor.

Flux pining is the mechanism for the dissipative movement of the flux under the Lorentz force that is prevented by flux pining that may be caused by some defects such as the dislocations, precipitates and grain boundaries [148]. The sustained superconducting transport current within the material needs good flux pinning. For LTS materials, defects in the microstructure act as flux-pinning sites. The critical current would become low at temperatures closing to T_c for superconductor under magnetic fields. But for LTS materials, very low operating temperature caused the thermal effects that were negligible in terms of the *E-J* characteristic plot from the 4-pin technique. Consequently, the distribution of pinning strengths can contribute to non-linear portion of the *E-J* curve for LTS sample. For HTS material, Because of the effect thermal fluctuations, when the HTS materials was operated at high temperatures, the non-linearity is due to different reasons, such as flux creep, nonlinearity of flux motion by thermal effects, and non-uniformity of critical current of the superconductor [103], [148].

2.3.5 Quench and thermal run away

Quench occurs locally in the superconducting coil and can propagate to the whole winding like a superconducting magnet. When a quench is induced by a disturbance, the transport current in the superconductor transfers into the stabilisation matrix, resulting in the local temperature increasing. In order to limit the increasing temperature, the transport current in the superconducting magnet should decay, and energy stored in the magnet needs to be absorbed by the magnet itself or transferred into the protection system. Disturbance would disappear when the temperature of the hot spot in the magnet starts to decrease. Studies of the quench on the superconducting magnet includes the quench process and related variation of the physical parameters and hazard assessment, meanwhile, the detection and protection methods have been developed and investigated to prevent the damaging the superconducting magnet after the quench.

Basically, the numerical equation for heat diffusion is given by:

$$\frac{d}{dx}\left((\kappa(T_1))\frac{dT}{dx}\right) + Q_{ini}(T_1) = C_p(T_1)\frac{dT}{dt} \qquad 2.19$$

But for a case of a pancake coil would with 2G YBCO Roebel cable with epoxy impreganted that was performed in LN2 at 77 K. The heat diffusion would evolve in all three directions; i.e. the longtitude direction along the strand, the radially direction among the different strands stack, and the heat leak from the interface between the LN2 and the thermal insulated layer at the top of the coil. All the strands were assumed as a lump conductor and neglected the heat diffusion in radial direction, then Equation 2.19 can be rewritten basing on heat diffusion equation by Wilson et al [151]:

$$\frac{d}{dx}\left((\kappa(T_1))\frac{dT}{dx}\right) + J \times E(T_1, J) + Q_{ini}(T_1) - h(T_\infty)(T_\infty - T_2) = C_p(T_1)\frac{dT}{dt} \qquad 2.20$$

Where κ_1 is the thermal conductivity of the superconductor, and T_1 is the temperature changing along the longtitude direction along the coil, and Q_{ini} is the initial energy applied from the heat pulse, and h is the heat transfer coefficient of the LN2, and A_2 is the top area of the thermal epoxy bathing with the LN2, and T_∞ is the temperature of the LN2, and T_2 is the temperature at the top surface, the current density $J = I/A$ and A is the total cross section of the tape, and E is the electrical field along the strand, and the overall thermal-electrical properties such as thermal conductivity (κ) and heat capacity (c_p) and resistivity (ρ_T) of the superconductor need to be defined.

2.3.5.1. Thermal stability

The thermal stability analysis is significant important for the superconducting magnets design and quench protection, which the analysis is based on the normal zone determination and its propagation, which is strongly related to the minimum propagation zone (MPZ) and the minimum local energy (MQE) release required for a quench occurring [152]. Starting from Equation 2.20, it is to evalute the ability of intial disturbance (Q_{ini}) to cause a thermal run away, and the quench and recover process depends on heat generation ($J \times E$) and heat transfer power ($\kappa \times dT/dx$). If energy of the superconducting magnet is absorbed by external protection shunt resistance. Some magnets are heavy and have a large heat capacity so they can absorb the stored energy themselves, which can maintain the temperature below the designed safety temperature margin. However, heat and electromagnetic disturbances with high intensity, usually lead to an uncontrollable propagation of the normal zone on the magnet, which make it impossible for magnet to recover, and this may damage the superconducting magnet, if there were no quench protection and or appropriate current decay.

Compared with LTS conductors, the thermal stability of HTS tape is more complex. There are several reasons for this, such as the extended current sharing with stabiliser, the non-linear heat generation, and the temperature dependence terms of resistivity. Specific heat and thermal conductivity at related to the higher temperature range [103]. There are several quench studies implying the HTS conductors have higher tolerance from the larger disturbance to induce quench, due to the higher heat capacity at their working temperatures [153]–[157]. For Roebel cable with 15 strands with larger current carrying ability and complex current sharing and bigger mass, it is expected to have a higher tolerance of disturbance to induce quench compared with a single HTS

wire. But the problem is how to build up an adiabatic system to keep thermal stability for such a long cable like 1D quench of adiabatic conductors. For instance, the first Roebel cable (KIT-1) made of DyBCO tape without copper stabiliser layer was burned without quench protection during the critical measurements at 77K [9]. Consequently, the geometry design and quench protection become important to investigate the thermal stability of the Roebel cable.

2.3.5.2. Minimum Quench Energy (MQE)

The enegy to induce a quench for a minimum propagation zone setting up is called Minimum Quench Energy (MQE), ΔQ_{mqe}, which can be calculated by [103], [152]:

$$\Delta Q_{mqe} = V_{mpz} \int_{T_0}^{T_c} C_p\,(T) dT \qquad 2.21$$

Where V_{mpz} is the volume of the minimum propagation zone, and T_c and T_0 are the operating temperature and the temperature of the normal zone respectively. In our case, experimental MQE can be estimated from the intial energy Q_{ini} of the heat pulse. Normally the MQE is evaluated with different fractions of the critical current in the experiments, and MQE is defined by taking the mean value between two pulses, which approaches an irreversible quench and is just able to recover.

2.3.5.3. Minimum Propagation Zone (MPZ)

As the previous discussion, the local disturbances could occurs at a spot in the HTS conductor and subsequently increases the spot temperature, causing current sharing between the superconductor and metal matrix. Once the temperature of this "hot spot" is above the critical temperature (T_c), a normal zone was formed as shown in Figure 2.17 [103], and L_{norm} is the length of the normal zone. The minimum section of the normal zone to induce the quench is called minimum propagation zone (MPZ), and the length of this section is called the length of MPZ (l_{MPZ}).

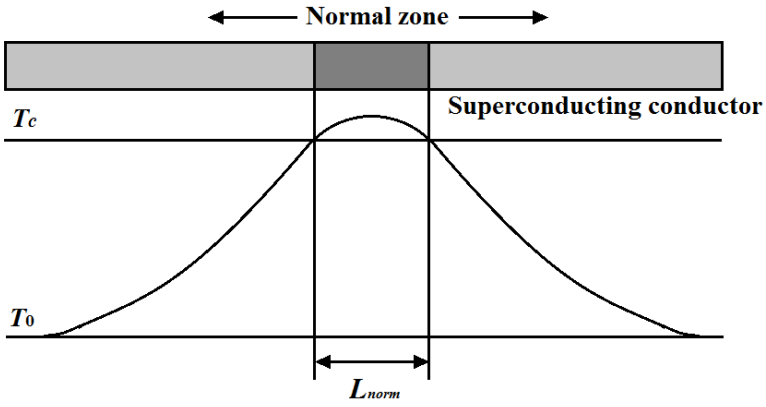

Figure 2.17: Schematic drawing of one dimensional temperature distribution of the normal zone along the superconducting conductor [103], [158].

For a single HTS wire, the l_{MPZ} estimation can be computed in 1D model. The temperature of the normal zone with length L_{norm} is assumed as T_c, and the boundary temperature of the

superconductor is assumed as T_0. The simplified temperature gradient across the normal zone is assumed as $2(T_c\text{-}T_0)/L_{norm}$. Then the expression of l_{MPZ} estimation is shown below:

$$\kappa \frac{2(T_c - T_0)}{l_{MPZ}} = J^2 \rho_{norm} l_{MPZ} \quad 2.22$$

And Equation 2.22 can be transferred to:

$$l_{MPZ} = \sqrt{\frac{2\kappa(T_c - T_0)}{J^2 \rho_{norm}}} \quad 2.23$$

Where κ is the thermal conductivity, and J is the operating current density,and ρ_{norm} is the resistivity of the conductor at the normal state.

2.3.5.4. Current sharing

Compared with LTS, current sharing in HTS cannot be considered to jump from the fully superconducting state to the fully normal conductor state [159], because transport current is shared by the stabiliser of a HTS superconductor to a varying extent depending on temperature. [160], which is mainly due to the temperature dependent Power-Law of superconductor as discussed in non-linear *E-J* characteristic:

$$\frac{E}{E_0} = (\frac{J}{J_c})^{n(T)} \quad 2.24$$

Where E_0 and J_c are the electrical field criteria (1 μV/cm) and critical current density of the superconductor, and n is the quality index number. Assuming the superconductors operated with a transport current J_0 at a temperature at T_0 ($T_0 < T_c$) in safe conditions, and current sharing occurs at a temperature at T_{share} ($T_0 < T_{share} < T_c$), which the current is divided into both superconductor and metal matrix, resulting in and dissipation in both superconductor and matrix with less heat generation compared with LTS. This heat generation would strongly affects the thermal behaviour of the quench process [103], [161].

Chapter 3
Nanobond joints in HTS coil application

3.1 Introduction

A simple and reproducible process for fabricating joints is required for future HTS-based applications. Soldering instructions for 2G HTS tapes with copper stabilisers is provided by SuperPower [162]:

- The soldering surface of the 2G wire joint or the area of current lead for 2G tape needs to be cleaned and an appropriate resin flux applied compatible with Pb40Sn60 (wt. %) solder.
- Compression should be gently applied to 2G tapes joint.
- The heating applied to melt the solder needs to be regulated, for example, for the Pb40Sn60 (wt. %) solder, the recommended soldering temperature is around 200 °C, and the time heat it is applied should less than 5 minutes. Higher soldering temperatures and longer application times can cause the degradation in superconducting layer within the 2G tape.

According to statements the SuperPower technical report, the typical joint resistance measured was less than 20 nΩ for a 100 mm overlap joint [163]. Ideal soldering conditions could provide smaller contact resistances, but the manufacturing process requires very clean surfaces and good control of the soldering temperature. This type of work can be performed in the lab on short lengths, but it is difficult to provide reproducible work upon kilometer-length of HTS wires for industrial applications. Any degradation in a single location in the coil developed during the manufacturing process, could be the source for initiating a quench during operation.

The collaborative work between Oxford Instruments (OI) and University of Southampton (UoS) has been ongoing since 2013. One output from the design and measurement of HTS coils as part of the Tokomak Energy program was a requirement for a more detailed study on HTS joints. At the same time, a novel nanobond technology was applied for the first time to HTS tapes at OI, and characterised at UoS. The nanobond process that uses a patented nanofoil, offers a possible solution for reliable and reproducible HTS joints for numerous HTS winding applications.

3.2 Research aims and objectives

The electrical and mechanical properties of nanofoil at room temperature have been reviewed in Chapter 1. In reference to nanobond joints in HTS winding applications operating at cryogenic temperatures, the physical properties of nanofoil operating below 77 K need to be further investigated. For instance, the electrical and thermal transport properties of the HTS joints, e.g. electrical resistivity and thermal conductivity become important parameters to determine their energy dissipation and thermal and electrical stability. In addition to its thermal and electrical performance, mechanical robustness is also required in high magnetic field environments. Consequently, the resistivity, thermal conductivity and mechanical properties of nanofoil at low temperatures and the interaction between these properties have been measured and presented in this work. The outline of this chapter is presented below:

- Measure the resistivity, thermal conductivity and heat capacity of reacted and unreacted nanofoil by Physical Property Measurement System (PPMS).
- Investigate phase formation of reacted nanofoil with different conduction cooling in the reaction process by Scanned Electron Microscopy (SEM) with Energy dispersive X-ray spectroscopy (EDS) and X-ray Diffractometer (XRD).
- Measure the electrical contact characteristics of 2G/copper tape to 2G tape nanobond joints at 77 K.
- Evaluate the thermal contact characteristics of alumina/copper to alumina nanobond joints at low temperature.
- Measure the lap shear strength of metallic nanobond lap joints at room temperature.

3.3 Methods and Experimental Details

3.3.1 Nanofoil samples preparation for resistivity, thermal conductivity and heat capacity measurements by PPMS

All nanofoil samples prepared for measurement inside the PPMS were cut from Indium Corporation (60 μm thick nanofoil sheet). The nanofoil strips were ignited with a 9 V electrical pulse at room temperature and held between different materials such as copper, aluminium, silicone rubber, A4 printing/towel paper soaked with water and G10 blocks as shown in Figure 3.1, and these materials can provide different thermal conductions. The PPMS provides an automated physical properties measurement with variable temperature and magnetic field control. The thermal conductivity, resistivity and specific heat of both reacted and unreacted nanofoil were measured by using the PPMS, with the appropriate thermal transport, resistivity and heat capacity options enabled.

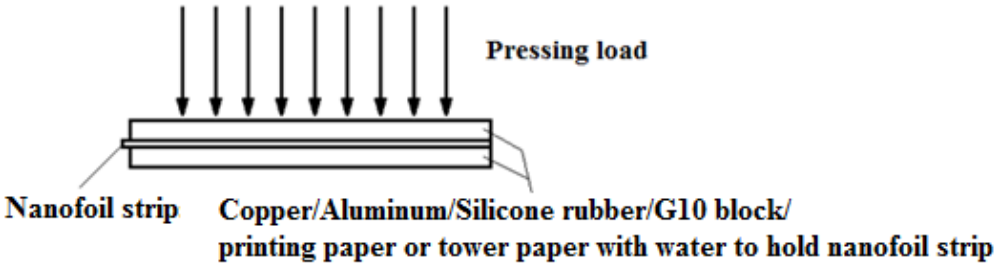

Figure 3.1: Schematic drawing for the prepration for the reacted nanofoil samples with different cooling conditions.

3.3.1.1. TTO samples preparation

The PPMS thermal transport option (TTO) produced the resistivity and thermal conductivity measurements for the applied nanofoil samples using a 4-pin contact method. In total, three rectangle strips of reacted nanofoil and two rectangle strips of unreacted nanofoil were measured, with all the sample dimensions presented in Table 3.1. Figure 3.2a shows two examples for both reacted and unreacted nanofoil samples soldered with 4 voltage taps, and Figure 3.2b shows the sample holder used for the TTO measurements. The two reacted nanofoil samples (reacted sample 1 and 2 respectively) were ignited by a 9 V pulse between a silicone rubber sheet and an aluminum block (Al to Silicone). Reacted sample 3 was ignited between two silicone rubber sheets (Silicone to Silicone). Reacted samples 1 and 2 were bonded with four pre-tinned copper strips by the nanobond reaction and reacted sample 3 bonded with four silver painted copper strips. Unreacted sample 1 was fabricated with an unreacted nanofoil soldered with four pre-tinned copper tapes with 70 °C melting solder (In66.3Bi33.7, wt. %), and unreacted sample 2 was fabricated with four silver painted copper strips. In addition, all pre-tinned copper strips were plated with 180 °C (Sn60Pb40, wt. %) solder. The resistivity and thermal conductivity of these samples were measured between 5 K and 300 K.

Table 3.1: Dimensions of a list of nanofoil samples applied to TTO measurements.

Parameters / Samples	Dimensions	
	Distance between two voltage taps (mm)	**Cross section area (mm^2)**
Unreacted sample 1	8.50	0.240
Unreacted sample 2	1.90	0.114
Reacted sample 1	8.50	0.240
Reacted sample 2	4.62	0.178
Reacted sample 3	6.57	0.216

3.3.1.2. Resistivity option samples preparation

The PPMS resistivity option not only provides the resistivity measurements, but it also enables measurements in a magnetic field to investigate the magnetoresistance of the samples. Resistivity measurements were performed on two strips of reacted nanofoil and one strip unreacted nanofoil samples, and all the sample dimensions are shown in Table 3.2. Figure 3.3a shows examples of both reacted and unreacted nanofoil samples soldered with 4 voltage taps, and Figure 3.3b shows the PPMS sample mounting arrangement. Three reacted samples (samples 4, 5 and 6) were bonded with 4 pre-tinned copper wires between silicone rubber sheet and an aluminum block. A

240 °C solder (Sn99.3Cu0.3, wt. %) was used to solder the unreacted samples with pre-tinned copper wires. All the copper wires were plated with 180 °C melting solder (Sn60Pb40, wt. %). Moreover, a 3 T magnetic field applied to unreacted sample 3 and reacted sample 4 to investigate the magnetoresistance effect.

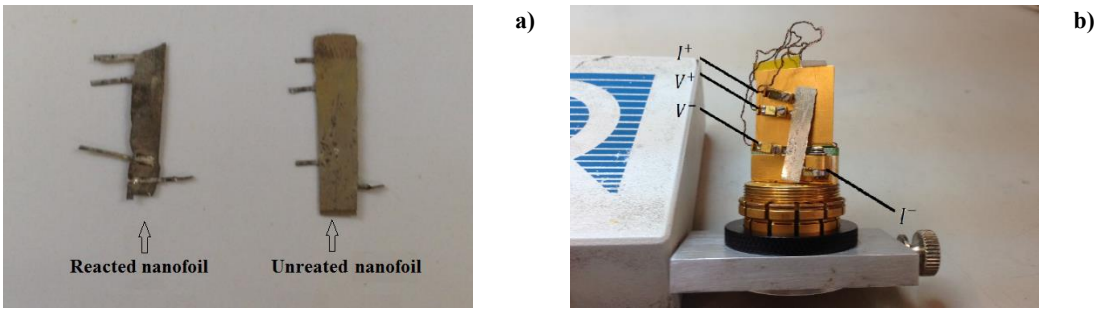

Figure 3.2: a) Photograph showing the reacted samples and the unreacted samples for thermal transport measurements by PPMS, and b) photograph showing a sample mounting in PPMS_TTO sample holder; 4 pre-tinned copper tapes are fixed by clamps. When a constant DC current flows from I^+ to I^-, to measure the voltage across V^+ and V^-, the resistance *R* can be evaluated by Ohm's Law. A same measuring method for thermal conductivity, when a constant heat flux flows from I^+ to I^-, temperature difference is measured between V^+ and V^-, the thermal conductivity can be evaluated by Fourier's Law.

Table 3.2: Dimensions of a list of nanofoil samples applied to resistivity option measurements.

Parameters / Samples	Dimensions	
	Distance between two voltage taps (mm)	**Cross section area (mm^2)**
Unreacted sample 3	4.44	0.151
Reacted sample 4	2.94	0.162
Reacted sample 5	3.48	0.167

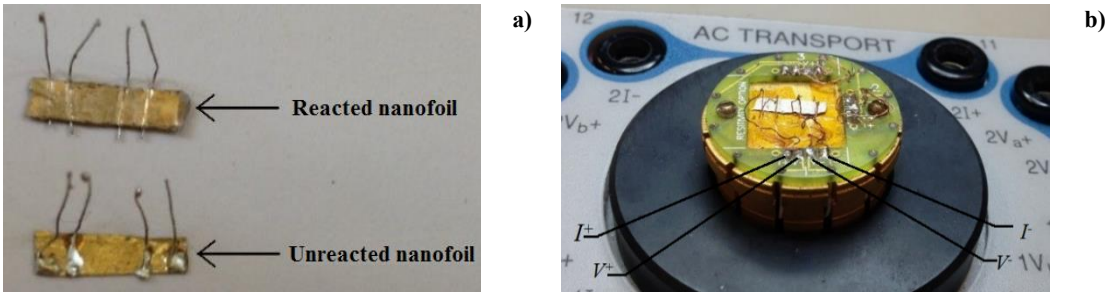

Figure 3.3: a) Photograph showing both reacted sample and unreacted sample resistivity measurements by PPMS, and b) photograph showing a sample mounting in the PPMS_Resistivity sample holder, and 4 pre-tinned copper wires are fixed by soldering with 4 wires connecting to the module base. When a constant DC current flows from I^+ to I^-, to measure the voltage across V^+ and V^-, the resistance can be evaulated by Ohm's Law.

3.3.1.3. Heat capacity option samples preparation

The PPMS heat capacity option provided heat capacity measurements of the solid film. Three small pieces of nanofoil were prepared for measurements, one cut from unreacted nanofoil, and two from reacted nanofoil. The reacted nanofoil were prepared differently, one produced by sandwiching between silicone rubber-aluminium and the other silicone rubber-silicone rubber. The sample dimensions are shown in Table 3.3. Approximately, 0.1 mg of N-grease was applied

Table 3.3: The parameters of three nanofoil samples for heat capacity measurements.

Samples	Mass (mg)	Dimensions (mm)			Applied grease (mg)
		Length	Width	Thickness	
Reacted sample 2	2.4	2.4	1.2	0.060	0.1
Reacted sample 3	1.2	1.2	1.2	0.060	0.1
Unreacted sample 2	1.2	1.2	1.2	0.060	0.1

to improve the thermal contact between the sample holder and the nanofoil. The heat capacity of each sample was measured inside the PPMS from 5 K to 300 K.

3.3.2 SEM and XRD samples preparation

Several nanofoil strips were ignited at the room temperature with different thermal conduction conditions. These samples were soldered with a 100 μm thick pre-tinned copper wires, using 180 °C melting solder (Sn60Pb40, wt. %). The resistivity of the reacted nanofoil strips was measured by the 4-pin contact method at the room temperature. Afterwards, some of these samples were broken into smaller pieces and the fractured cross-sections of these samples investigated by Scanned Electron Microscope (SEM) with energy dispersive X-ray spectroscopy (EDX). Both reacted and unreacted nanofoil strips were scanned with X-ray Diffractometer (XRD) to investigate the composition of the samples. Furthermore, an alumina stripe was measured in a parallel position with these nanofoil samples at a same height for XRD scan, and the XRD pattern results were calibrated in accordance with Al_2O_3 XRD database.

3.3.3 Electrical contact resistance measurement of HTS nanobond joints

A series of nanobond joint contact resistance measurements were performed in LN2 at 77 K. Figure 3.4 shows the picture and schematic drawing of the test bed for electrical contact resistance measurements. As shown in Figure 3.4a, two 2G HTS tapes with 12 mm width crossed at 90° (Joint T-T') were bonded by pre-tinned Nanofoil, and at each terminal of the HTS tape was bonded with a piece of copper sheet with 24 mm width by pre-tinned NanoFoil (Joint A'-T and Joint B'-T'). Figure 3.4b displays the position of the voltage taps and current leads. Table 3.4 shows the parameters of six samples produced for electrical resistance measurements, and also describes the tin plating method for the copper terminals and 2G-tapes and the respective plating thickness, nanofoil tin plating and thicknesses, the cross-section area of each joint, and the loading pressure applied to each nanobond joint. All of the measurements were performed by submerging the test bed inside a bath of LN2 at 77 K. Current was injected in incremental steps until the critical current criteria was observed, with voltage acquired at each step over 100-line cycles using a Keithley 2000 digital voltmeter.

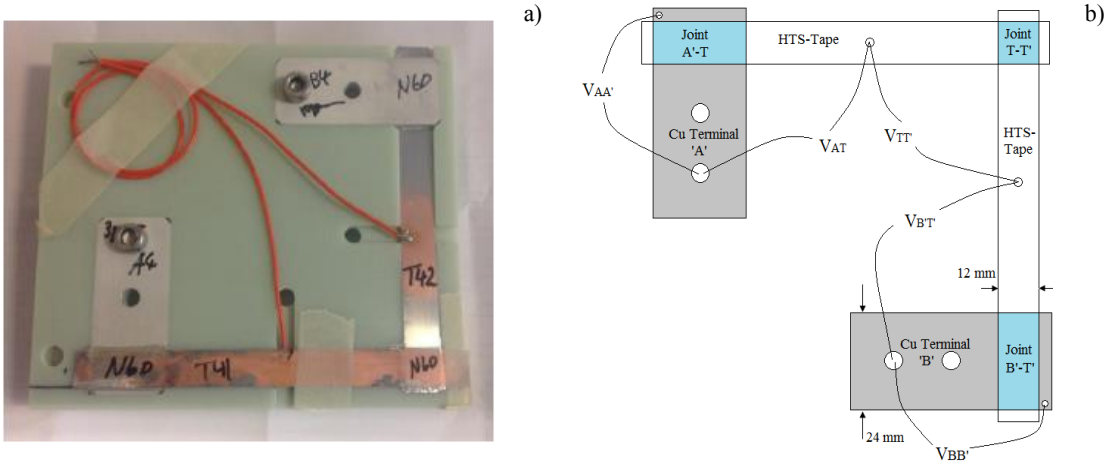

Figure 3.4: a) The test bed of contact resistance measurement for the nanobond HTS joints, and b) the schematic drawing of the test bed for contact resistance measurement.

Table 3.4: The parameters of each nanobond HTS joint sample.

NO.	Terminals		HTS tape	NanoFoil		Joint		Pressure
	electroplated Sn 10µm	electroplated Sn 3µm	Sn - manual application	40µm + 10µm Sn both sides	60µm + 10µm Sn both sides	Joint No.	Joint area [mm^2]	
1	1A-A'		1T	x		1A'-T	12 × 24	5.0 bar
		1B-B'	1T'	x		1B'-T'	12 × 24	5.0 bar
			1T-T'	x		1T-T'	12 × 12	2.5 bar
2	2A-A'		2T	x		2A'-T	12 × 24	5.0 bar
		2B-B'	2T'	x		2B'-T'	12 × 24	5.0 bar
			2T-T'	x		2T-T'	12 × 12	2.5 bar
3	3A-A'		3T		x	3A'-T	12 × 24	5.0 bar
		3B-B'	3T'		x	3B'-T'	12 × 24	5.0 bar
			3T-T'		x	3T-T'	12 × 12	2.5 bar
4	4A-A'		4T		x	4A'-T	12 × 24	5.0 bar
		4B-B'	4T'		x	4B'-T'	12 × 24	5.0 bar
			4T-T'		x	4T-T'	12 × 12	2.5 bar
5	5A-A'		5T		x	5A'-T	12 × 24	10.0 bar
		5B-B'	5T'		x	5B'-T'	12 × 24	10.0 bar
			5T-T'		x	5T-T'	12 × 12	5.0 bar
6	6A-A'		6T		x	6A'-T	12 × 24	5.0 bar
		6B-B'	6T'		x	6B'-T'	12 × 24	5.0 bar
			6T-T'		x	6T-T'	12 × 12	2.5 bar

3.3.4 Thermal contact resistance measurement of copper/Al2O3 to copper/Al2O3 nanobond joints

All the DBC Al_2O_3 samples were provided by Oxford Instruments (OI). The Al_2O_3 (380 µm thick) were double sided, bonded with copper 200 µm thick each) and gold (0.03 µm thick) coating on the surface. Al_2O_3 to Al_2O_3 nanobond joint samples were bonded with a both sides solder-plated (10 µm thick) nanofoil (60 µm thick) between two DBC Al_2O_3 plates with pre-tin (3 to 7 µm

Sn/Ni) electroless plated. Two Al_2O_3 to copper soldering samples were manufactured at University of Southampton (UoS). The thermal contraction between Al_2O_3 and copper with cooling cycles may cause the Al_2O_3 to initiate cracks, as a result of the components of the composite having very different thermal conductivities. Consequently, the thermal contact resistance of Alumina and nanobond joint samples were measured at different temperatures. All of the samples were installed on the second stage of a variable temperature cryostat rig. The base temperature of the sample was varied from 4.2 K to 60 K via a 100 Ω, 100 W heater, which was controlled by a Lakeshore 366 Proportion Integration Differentiation (PID) controller. A constant power was applied to the top of the sample via a 47 Ω, 50 W heater. The temperature difference across the joint was measured and recorded when all the temperatures reached steady state. Later, the dynamic temperature difference across the joint was measured when the rig was warming up from 50 K to 300 K, with a constant power applied to the top of the sample. A National Instrument (NI) SCXI-1000 data logger was applied to record the temperature data. Afterwards, all the samples were epoxy impregnated and polished for optical morphology investigation.

Sample 1 preparation

The schematic drawing of sample 1 for a DBC Al_2O_3 to DBC Al_2O_3 nanobond joint is shown in Figure 3.5. Al_2O_3 to Al_2O_3 nanobond joint sample was bonded via a both sides solder-plated (10 µm thick) nanofoil (60 µm thick) between two electroless plated (3 to 7 µm Sn/Ni) DBC Al_2O_3 plates (38 mm × 42 mm × 0.78 mm each), and the surface area of the bonding joint was 100 mm^2. The ignition of the nanofoil to bond the sample was a 9 V voltage pulse with a 5 bar loading pressure on the joint sample. Heater 1 (47 Ω, 50 W), soldering at the top of the top Al_2O_3 sample with 180 ºC melting solder, was applied to provide a constant power to pass through the joint. Two copper blocks, the cernox anchors, were bolted at the bottom of the top DBC Al_2O_3 and the top of the bottom DBC Al_2O_3 respectively. The copper plate was the sample base, and the top surface of the copper plate was cleaned with Acetone and coated with flux, and it was soldered with the DBC Al_2O_3 to DBC Al_2O_3 nanobond joint sample via 146 ºC melting solder (In97Ag3, wt.%) on a hot plate at temperature of 160 ºC. Then this palte was bolted at the second stage of a varable temperature cryostat rig.

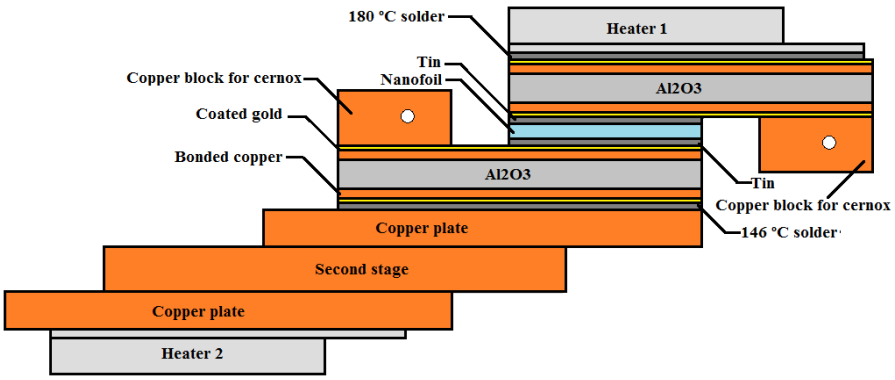

Figure 3.5: Schematic drawing of the Al_2O_3 to Al_2O_3 nanobond joint sample for thermal resistance measurements.

Sample 2 preparation

A schematic drawing of sample 2, a DBC Al_2O_3 to copper shim (200 µm thick) soldered joint and a copper shim to copper shim nanobond joint, is shown in Figure 3.6. All of the compontent

surfaces (10 mm × 14 mm) were cleaned for soldering with Acetone and then coated with soldering flux. Firstly, the bottom surface of the copper spacer and top surface of the copper plate were pre-tinned with 240 °C (Sn99.3Cu0.7, wt.%) solder on a hot plate at 250 °C, and the excess flux and solder were wiped away by tissue paper. Afterwards, the joint between the copper spacer and the plated copper was soldered on a hot plate at 250 °C, followed by the DBC Al_2O_3 to copper shim joint using the same method. The top surface of the copper shim (200 μm thick) was soldered with Heater 1 by using 180 °C (Sn60Pb40, wt.%) solder. The preperation of the copper shim to copper shim nanobond joint sample was as follows; the surfaces of the two copper shims were pre-tinned with 180 °C solder, and excess flux and solder were removed by wiping the surface. Two additional pieces of rolled 180 °C solder strips (~ 35 μm thick) were cut to the same size of the bonding area and cleaned with Acetone. The arrangement of the stack of nanobond sample materials from the bottom to the top was as follows; pre-tinned copper shim, 180 °C rolled solder strip, nanofoil (60 μm thick), 180 °C rolled solder strip and pre-tinned copper shim. Finally, all the components, involving DBC Al_2O_3 sample, nanobond sample and copper spacer, were arranged as shown in Figure 3.6, and they were soldered via 146 °C (In97Ag3, wt.%) solder on a hot plate at 160 °C. The nanofoil was ignited with a 9 V electric pulse under 5 bar of compressive loading pressure.

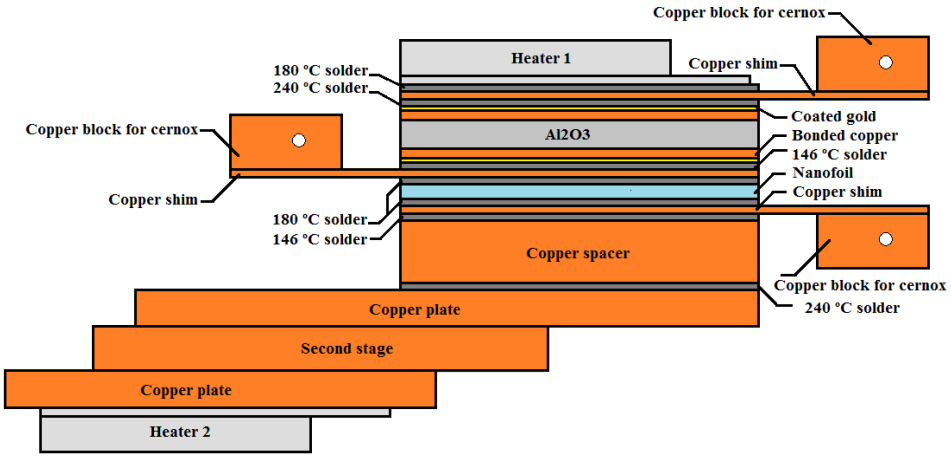

Figure 3.6: Schematic drawing of the Al_2O_3 to copper soldering joint sample and copper to copper nanobond joint sample for thermal resistance measurements.

Heater 2 was mounted underneath the second stage to control the base temperature, and its power output was controlled by a Lakeshore PID controller. The Cernox thermometer was used to measure the temperature of the nanobond jointed sample. Heater 1 was used to provide constant power to the joint at specific test temperatures. Once at a test temperature and equilibrium achieved, the temperature differences across the joint was recorded and the thermal resistance calculated using Equation 3.1 in accordance with Fourier's law:

$$R_{thermal} = \frac{\Delta T}{PA} = \frac{\Delta x}{\kappa A} \qquad 3.1$$

Where ΔT is the temperature difference between two ends for thermal conduction, and P is the applied heat power on Heater 1, and A is the area of each sample joint, and Δx is the distance between two ends for thermal conduction, and κ and $R_{thermal}$ are the thermal conductivity and thermal resistance of the applied sample respectively.

3.3.5 Lap shear testing of metallic nanobond solder joints

A series of mechanical lap shear tests of the metallic nanobond joints were performed upon an Instron 3369 universal test machine. A total of four stainless steel to stainless steel (StSt-StSt) nanobond jointed samples and four stainless steel to copper (StSt-Cu) nanobond jointed samples were supplied by OI for testing and are as shown in Figure 3.7. A list of key properties for the eight metallic nanobond joints are presented in Table 3.6. All of the metallic strips used in forming the samples in this batch of test specimens were tin/gold-plated, and included 60 μm thick nanofoil with 10 μm thick solder placed either side of the foil during fabrication of the joint. After completing the fabrication of the nanobond sample sheets, a set of dog-bone shape specimens were water jet cut prepare for mechanical testing. The gauge length, specimen widths and lapped area and thickness were measured as shown in Table 3.6.

The copper sheets of all the StSt-Cu nanobond jointed samples would yield without failing/fracturing. Consequently, another six copper to copper (Cu-Cu) nanobond joint specimens were fabricated at the UoS, with the thickness of the copper strips increased. The design and final geometry of the specimens was based on Equation 3.2 to produce specimens with lengths and thicknesses to induce failure within the bonded region [164]:

$$L=Fty\times t/\tau \qquad 3.2$$

Where L is the length of the overlap; t is the thickness of the metal, Fty is the yield point of the bonding material; τ is 150 percent of the average shear strength. Fty of copper is around 70 MPa [165], and τ is assumed as 16 × 150 % MPa according to the results from the previous StSt-StSt lap shear strength tests. The length (L) was assumed as 10 mm, 15 mm, 20 mm and 25 mm respectively and the corresponding thicknesses of the copper was calculated and presented in Table 3.5. In the final design of the Cu-Cu copper nanobond specimens for the lap shear tests, copper strips (60×10×6 mm) were chosen to prepare samples for the mechanical tests with a lapped area of 10×10 mm^2.

For the nanobond joints, three copper strips (6 mm thick) were initially pre-tinned with 180 °C (Sn60Pb40, wt.%) solder. To form the nanobond joint, a piece of nanofoil was sandwiched between two rolled strips of 35 μm thick 180 °C solder and this sandwich stacked between two pre-tinned copper strips. A 9 V voltage pulse was applied to ignite the nanofoil with 5 bars of compressive load applied to the lapped region to form the nanobond joint. Two nanonond joint samples were formed on a hot plate at 60 °C, and one sample was formed at room temperature. In fact, many of the initial mechanical specimens produced were formed at room temperature, but they were found to have relatively weak bonds. For these specimens, the thicker copper strips behaved like a large heat sink for the local energy to dissipate during the nanofoil reaction. This was caused by a large thermal resistance between the solder and copper, so the solder was not able to wet the copper surface very well. Consequently, the hot plate was applied to increase the specimen's ambient temperature during the joint fabrication, and this improved the solder wetting on the copper surface during the nanobond reaction. Hence, the nanobond jointed specimens were reproducible when the sample ambient temperature was increased up to 60°C. After the lap shear tests of the nanobond joints made with 180 °C solder, the surface of all the copper strips were

polished and cleaned. Another three Cu-Cu nanobond jointed specimens were fabricated with 240 °C (Sn99.3Cu0.7, wt. %) solder in the same method. All the metallic nanobond joint specimens prepared for the lap shear tests were clamped into the Instron test machine as shown in Figure 3.8, and the speed of the machine crosshead set at 1.3mm/min.

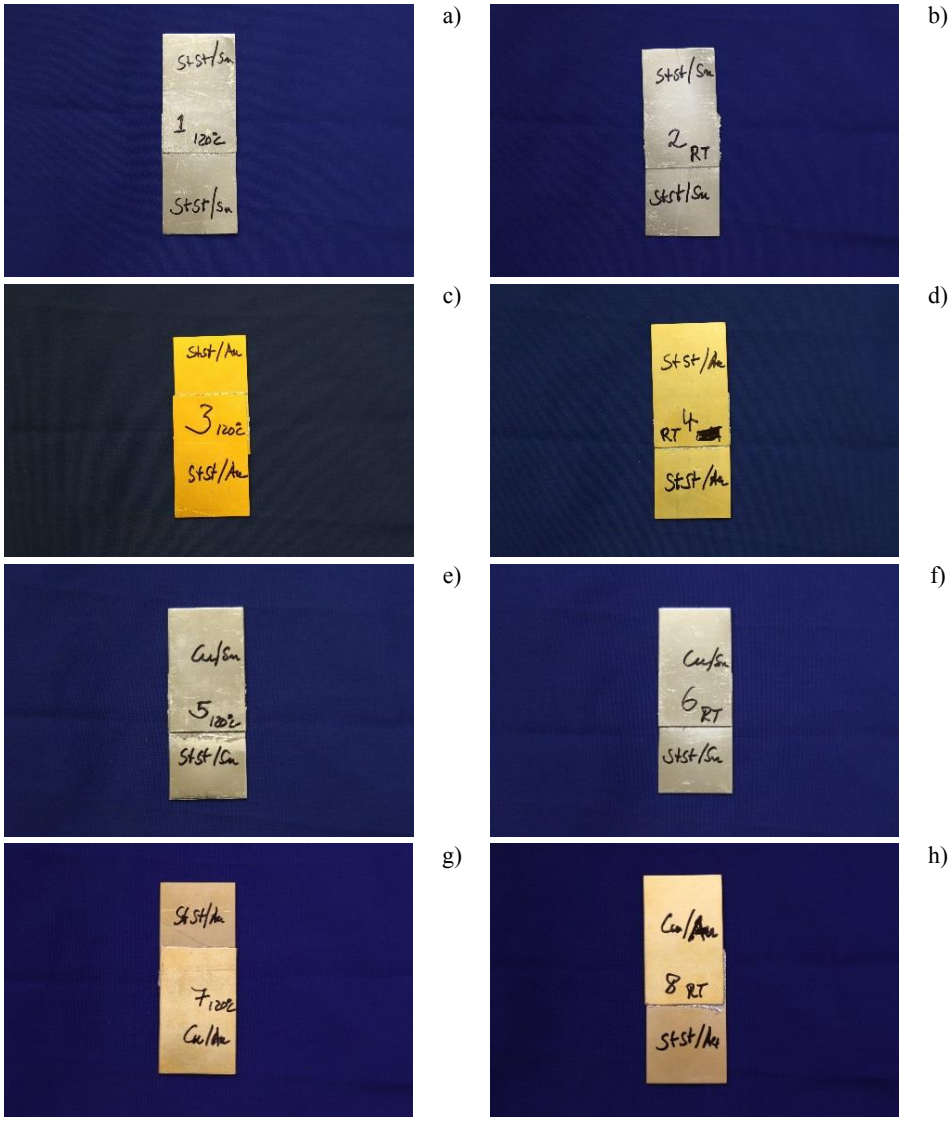

Figure 3.7: OI metallic nanobond joint samples: a) Stainless Steel to Stainless Steel nanobond joint (bonded at 120 ºC), b) Stainless Steel to Stainless Steel nanobond joint (bonded at room temperature), c) Stainless Steel to Stainless Steel nanobond joint (bonded at 120 ºC), d) Stainless Steel to Stainless Steel nanobond joint (bonded at room temperature), e) Stainless Steel to copper nanobond joint (bonded at 120 ºC), f) Stainless Steel to Copper nanobond joint (bonded at room temperature), g) Stainless Steel to Stainless Steel nanobond joint (bonded at 120 ºC), h) Stainless Steel to Stainless Steel nanobond joint (bonded at room temperature).

Table 3.5: The estimated thickness of copper for new lap shear tests.

L (mm)	Fty (MPa)	τ (MPa)	t (mm)
10	70	16×150%	3.43
15	70	16×150%	5.14
20	70	16×150%	6.86
25	70	16×150%	8.57

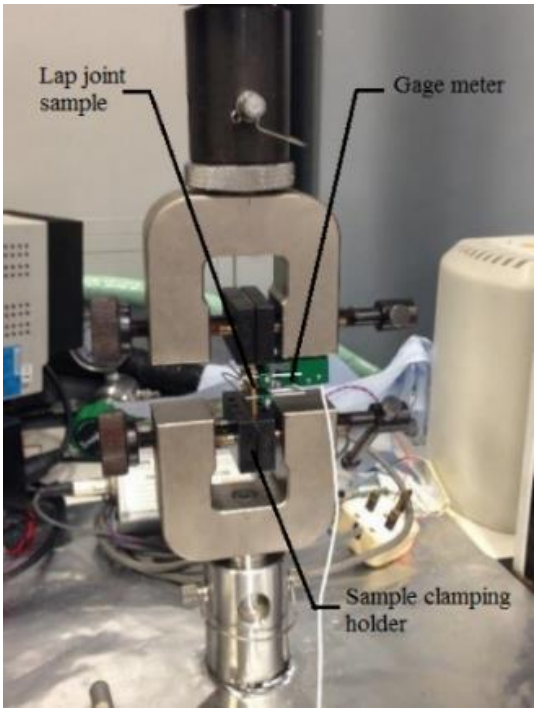

Figure 3.8: Lap shear test bed set up.

Table 3.6: Parameters of OI made metallic nanobond joints for lap shear testing.

NO.	Sample Material				Hot plate temperature before the bonding (°C)	Nanofoil 60µm + 10µm Sn both sides	Pressure (Bar)	Dog bone joint dimensions			
	Top		Bottom								
	Base[#]	Coating*	Base	Coating				Length (mm)	Width (mm)	Thickness (mm)	Joint area (mm^2)
1	Stainless Steel	Sn	Stainless Steel	Sn	120 °C	x	5	20.44	6.00	0.03	122.64
2	Stainless Steel	Sn	Stainless Steel	Sn	Room Temperature	x	5	26.50	6.00	0.04	159.00
3	Stainless Steel	Au	Stainless Steel	Au	120 °C	x	5	30.44	6.00	0.08	182.64
4	Stainless Steel	Au	Stainless Steel	Au	Room Temperature	x	5	26.00	6.00	0.07	156.00
5	Copper	Sn	Stainless Steel	Sn	120 °C	x	5	28.50	6.00	0.06	171.00
6	Copper	Sn	Stainless Steel	Sn	Room Temperature	x	5	27.50	6.00	0.06	165.00
7	Copper	Au	Stainless Steel	Au	120 °C	x	5	28.50	6.00	0.08	171.00
8	Copper	Au	Stainless Steel	Au	Room Temperature	x	5	24.00	6.00	0.07	144.00

[#]Stainless Steel sheet base: 35 × 60 × 1mm; copper sheet base: 35 × 60 × 0.9mm.
*Electroless Ni-Sn: 3-7µm Ni (>11.2% + 1%P) + 10-15µm tin; electroless Ni-Au: 3-7µm Ni (>11.2% + 1%P) + 0.05-0.1µm gold.

Table 3.7: Parameters of UoS made copper nanobond joints for lap shear testing.

NO.	Sample Material				Plate temperature before the bonding (°C)	Nanofoil 60µm +	35-40 µm solder film both sides	Pressure (Bar)	Joint dimensions			
	Top		Bottom									
	Base[##]	Pre-tin plated[**]	Base	Pre-tin plated					Length (mm)	Width (mm)	Thickness (mm)	Joint area (mm^2)
9	Copper	Sn60Pb40	Copper	Sn60Pb40	60 °C	x	Sn60Pb40	5	10.00	10.00	0.109	100.00
10	Copper	Sn60Pb40	Copper	Sn60Pb40	60 °C	x	Sn60Pb40	5	10.00	10.00	0.097	100.00
11	Copper	Sn60Pb40	Copper	Sn60Pb40	Room Temperature	x	Sn60Pb40	5	10.00	10.00	0.079	100.00
12	Copper	Sn99.3Cu0.7	Copper	Sn99.3Cu0.7	60 °C	x	Sn99.3Cu0.7	5	10.00	10.00	0.098	100.00
13	Copper	Sn99.3Cu0.7	Copper	Sn99.3Cu0.7	60 °C	x	Sn99.3Cu0.7	5	10.00	10.00	0.082	100.00
14	Copper	Sn99.3Cu0.7	Copper	Sn99.3Cu0.7	Room Temperature	x	Sn99.3Cu0.7	5	10.00	10.00	0.072	100.00

[##]Copper bar base: 60 ×10 × 6 mm.
[**]Manually pre-tin (180 °C melting solder) plated: 3-5 µm Sn60Pb40; manually pre-tin (240 °C melting solder) plated: 3-5 µm Sn99.3Cu0.7.

54

3.4 Results and discussion

3.4.1 Physical properties measurements results of nanofoil samples by PPMS

The PPMS options and the type of the base holding material used to produce each sample are presented in Table 3.8. The following sections discuss more details of resistivity, thermal conductivity and heat capacity of the nanofoil measurements performed at low temperatures.

Table 3.8: A list of nanofoil samples applied to physical properties measurements.

Sample	Abbr.	TTO	Resistivity	Heat capacity	Cooling condition
Reacted sample 1	Re_Naf_1	x			Al to silicone
Reacted sample 2	Re_Naf_2	x		x	Al to silicone
Reacted sample 3	Re_Naf_3	x		x	Silicone to silicone
Reacted sample 4	Re_Naf_4		x		Al to silicone
Reacted sample 5	Re_Naf_5		x		Al to silicone
Unreacted sample 1	Un_Naf_1	x			N/A
Unreacted sample 2	Un_Naf_2	x		x	N/A
Unreacted sample 3	Un_Naf_3		x		N/A

3.4.1.1. Resistivity of both reacted and unreacted nanofoil

Figure 3.9 shows the plot of the resistivity measurements for 3 unreacted samples measured by PPMS compared with nano-scaled thick nickel and aluminum [126], [127] and the resistivity of bulk nickel and aluminum [166] at temperatures from 5 K to 300 K. Unreacted sample 3 was used to investigate the magnetoresistance effect by applying a 3 T field. It was apparent that the residual resistivity of all the unreacted samples were more than 10 times larger than that of the bulk metals. The resistivity of unreacted sample 2 almost coincides with that of unreacted sample 1 at all temperatures, which these two samples have a similar scale of resistivity at each temperature compared with 30 nm scaled nickel nano-wire. The resistivity of unreacted sample 2 has a similar reducing trend compared with the other two unreacted samples, but it is around 22 % to 35 % higher than that of other two unreacted samples at temperatures from 5 K to 300 K. There was no magnetoresistance effect observed on the unreacted sample 3, since the resistivity measurements with and without magnetic field coincide.

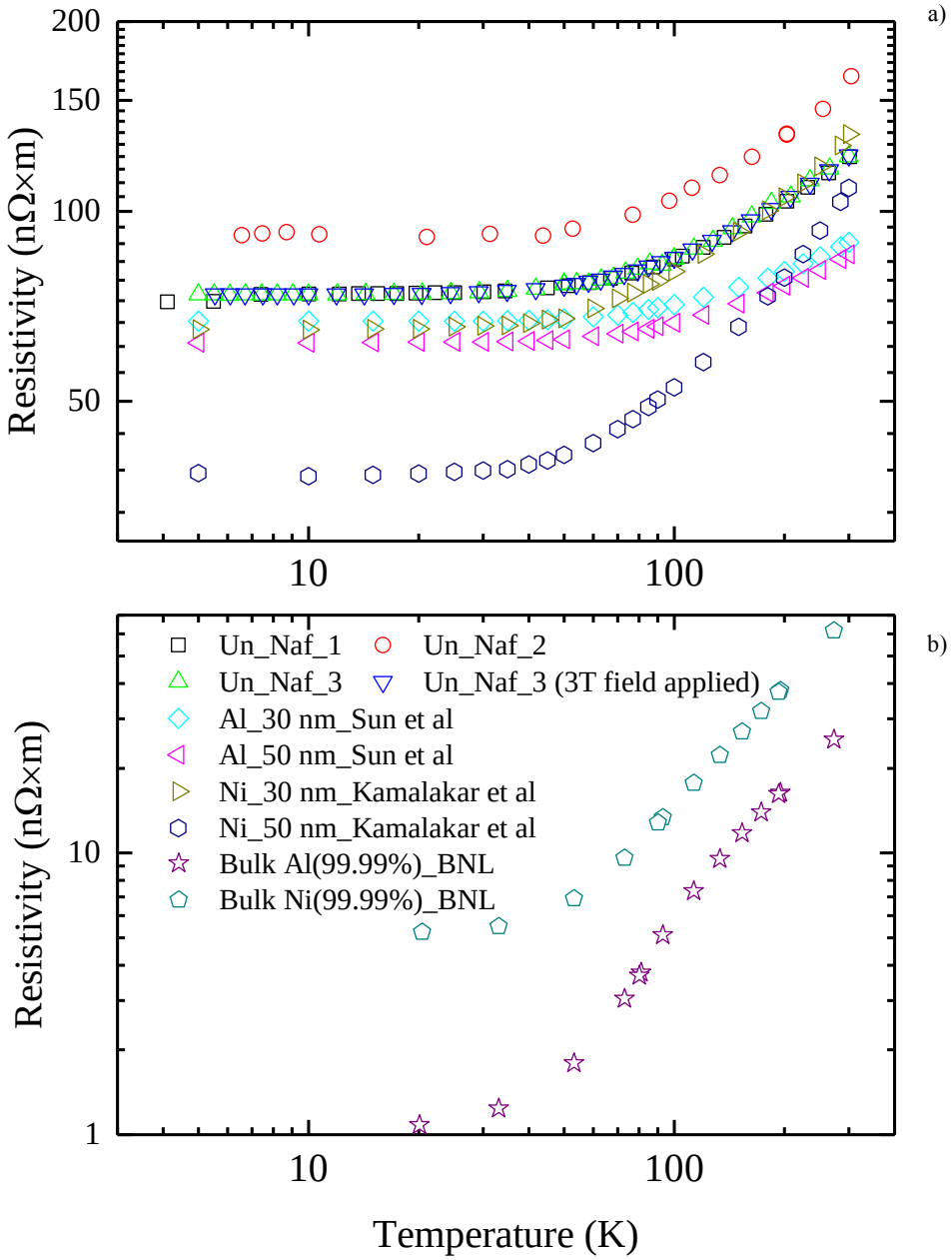

Figure 3.9: The plot for the resistivity measurements for a) 3 unreacted samples measured by PPMS compared with some nano-scaled nickel and aluminum [126], [127] and b) bulk nickel in purity of 99.99% and bulk aluminum in purity of 99.99% [166] at temperatures from 5 K to 300 K. Unreacted sample 1, 2 were measured with TTO, and unreacted sample 3 has been investigated the magnetoresistance effect via applying a 3 T field with Resistivity option (Un_Naf: unreacted nanofoil sample, BNL:Brookhaven National Laboratory).

Figure 3.10 shows the plot of the resistivity measurements for five reacted samples compared with the results of NiAl films [36] in different Ni atomic percentage at a temperature from 5 K to 300 K. Reacted sample 4 was used to investigate the magnetoresistance effect by applying a 3 T field. It was found that the resistivity of the reacted samples were much larger than the unreacted samples over the entire temperature range, which implies a difference in the resistivity between the intermetallic NiAl and the foil consisting of the two metals (aluminum and nickel). The resistivity of the reacted nanofoil at room temperature varies from 390 to 520 nΩ×m, which is almost around four times of the value (~100 nΩ×m) produced by the Indium Corporation [14].

The temperature dependence of resistivity among the reacted nanofoil samples are not consistent, despite some of them being ignited in the same way. For instance, the resistivity of reacted sample 4 (390 nΩ×m) at room temperature is smaller than the residual resistivity of reacted sample 3 (408 nΩ×m); reacted samples (1, 2 and 5) were ignited with same cooling condition (Al to silicone), and resistivity of reacted sample 5 (472 nΩ×m) was smaller than that reacted sample 1 (503 nΩ×m) and 2 (498 nΩ×m) at room temperature, but resistivity of reacted sample 5 (376 nΩ×m) is larger than that of reacted sample 1 (364 nΩ×m) and 2 (330 nΩ×m) at 10 K. There is almost no resistivity difference observed on reacted sample 4 with and without a magnetic field applied, which implies a minimum magnetoresistance effect on the resistivity of reacted nanofoil.

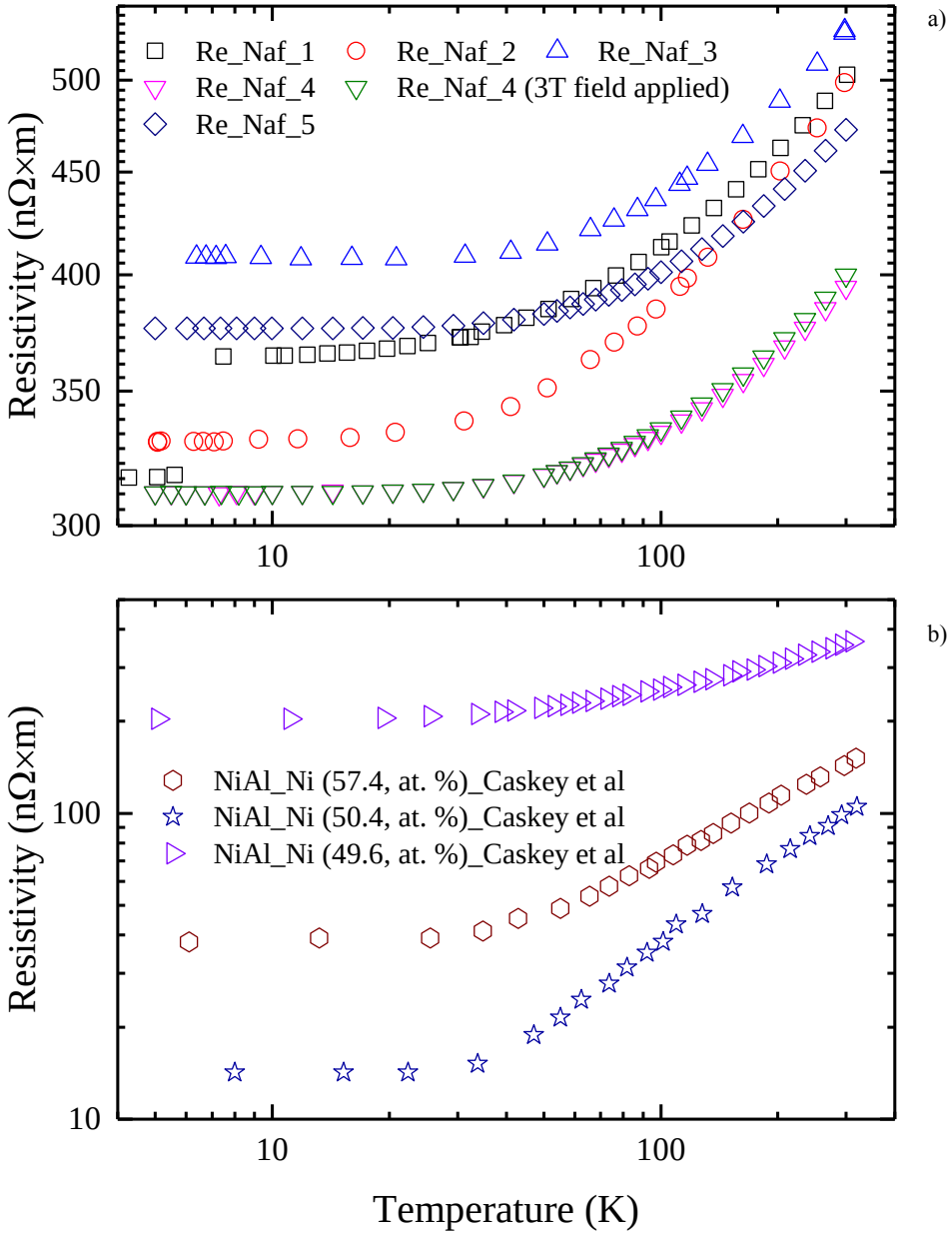

Figure 3.10: The plot for resistivity for a) 3 reacted nanofoil samples measured by PPMS compared with b) NiAl with different Ni atomic percentage [36] varying with temperature between 5 K and 300 K. Reacted sample 1, 2 and 3 were measured with TTO, and reacted sample 4 and 5 were measured with Resistivity option, and sample 4 was measured with a magnetic field (3 T) and without field (Re_Naf: reacted nanofoil sample).

Both reacted sample 1 and unreacted sample 1 have a sharp transition between 5 K and 7.5 K. The component of nanofoil, Aluminium/Al, critical temperature is 1.2 K; and components of 180°C melting solder, lead/Pb and tin/Sn, critical temperature are 7.193 K and 3.722 K respectively, and components of 70 °C solder, bismuth/Bi and indium/In, critical temperature are 0.53 mK [167] and 3.408 K [168] respectively. Consequently, the "lead" can be the reason to cause this transition occurring. It was considered that the solder from the pre-tinned voltage tap melted and diffused onto the sample surface when the nanofoil was ignited and the reaction temperature increased up to more than 1500 °C. Later silver painting was applied to the voltage taps for the preparation of the other samples, and there was no transition observed.

Table 3.9 shows the residual resistivity (ρ_{5K}), and temperature dependent resistivity $\rho_{el\text{-}ph}$ (300 K) and the residual resistance ratio (RRR= ρ_{300K}/ρ_{5K}) compared with the resistivity of nickel in purity of 99.99% and aluminum in purity of 99.99% [166], and some nano-scaled nickel and aluminum [126], [127], and bulk NiAl [35], [36]. Compared with nickel and aluminum, the low RRR and higher residual resistivity of unreacted nanofoil samples imply the contribution of the structural defects on the residual resistivity at low temperature, this may be due to poor grain growth in the sputtering fabrication process of the unreacted nanofoil. Referring to the temperature dependent resistivity $\rho_{el\text{-}ph}$(300 K), the phonon-electron scattering dominated the bulk material resistivity at room temperature [124], [169], and the free mean length of electrons is inversely proportional to the phonon-electron scattering at high temperature [122], where the free mean length for bulk nickel and aluminum at room temperature is 5.87 nm and 18.9 nm at room temperature [122]. Consequently, the thickness (30-50 nm) of altered layer of aluminum and nickel would not impose a limitation on free mean length if aluminum and nickel of the unreacted nanofoil have the same grain size of the bulk materials. Furthermore, average $\rho_{el\text{-}ph}$(300 K) of unreacted nanofoil (~55 nΩ×m) is almost the same as that of bulk nickel (~56 nΩ×m), which implies the effect of phonon-electron scattering is not main reason for unreacted nanofoil has a higher resistivity at room temperature.

Referring to the reacted samples, all of them have much higher resistivity at each temperature and smaller RRR compared with NiAl in two different stoichiometric ratios as shown in Table 3.9. Reacted sample 1 and reacted sample 2 have a similar resistivity (500 nΩ×m) at room temperature, and RRR of reacted sample 2 is slightly higher, but this cannot confirm reacted sample 2 has a higher purity because of nanofoil itself is the intermetallic of aluminum and nickel unless there is other nickel aluminide phase formation. Other reacted samples (3-5) have a very similar RRR (1.25 to 1.29) so that there was minimum possibility for more defects to cause 31%-35% resistivity gap among these samples at all temperatures. The resistivity of NiAl has the lowest value when the stoichiometric ratio between Ni and Al is getting close to 50:50 (at. %), and it increase in both nickel rich phase and aluminum rich phase. For instance, the formation of Ni_2Al_3 (at. %), one intermediate product in the reaction of nanofoil, has a resistivity around 500 nΩ×m that is more than 30 % higher than $Ni_{0.5}Al_{0.5}$ (at. %) at room temperature. Furthermore, it needs to be noted that the cooling condition of reacted sample 3 is different from other reacted samples, and it seems that a slow cooling rate that results in a higher resistivity of the reacted nanofoil, and cooling rate relates to the alloy grain size during the solidification process [170]–[172]. Consequently, the dependence of phase formation or grain size is assumed to explain the

resistivity difference among the reacted samples, but this assumption needs more evidences to be investigated via SEM with EDX and XRD.

Table 3.9: Residual resistance ratio (RRR), and resistivity at 4.2 K, 77 K and room temperature of both reacted and unreacted sample compared with the resistivity of bulk nickel and aluminum [166], and nano-scaled nickel [126], [127], and NiAl in stoichiometric ratios [35], [36].

Sample	Residual Resistivity ρ_0 (nΩ×m)	Temperature dependent resistivity $\rho_{el\text{-}ph}$ at 300 K (nΩ×m)	RRR	Free Mean Length (nm)
Re_Naf_1	364	139	1.38	N/A
Re_Naf_2	330	168	1.51	N/A
Re_Naf_3	408	120	1.29	N/A
Re_Naf_4	311	79	1.25	N/A
Re_Naf_5	376	96	1.25	N/A
Un_Naf_1	74	47	1.63	N/A
Un_Naf_2	92	70	1.77	N/A
Un_Naf_3	74	49	1.66	N/A
Bulk Al	~1.1	24.2	~23.00	18.9
Bulk Ni	~5.2	56.4	~11.85	5.87
30 nm Ni	65.0	67	2.03	N/A
NiAl (50.4%Ni, at. %)	38.6	106.4	3.76	N/A
NiAl (49.6%Ni, at. %)	13.5	86.5	7.41	N/A

3.4.1.2. Thermal conductivity of both reacted and unreacted nanofoil

Figure 3.11 shows the plot of thermal conductivity for both unreacted samples (1 and 2) and reacted samples (1, 2 and 3), nickel (99.99% and 99%) and aluminum (99.996% and 99%) at 5 K to 300 K. The thermal conductivity values of both unreacted samples and reacted samples have a reducing trend, and thermal conductivity of the unreacted samples is larger than reacted samples over the temperature range.

The temperature dependence of thermal conductivity for unreacted nanofoil is very different from pure metals even though the unreacted nanofoil is fabricated with many thousands of layers of aluminum and nickel. The purity of the metals has a significant influence on their thermal conductivity as shown in Figure 3.11, but this cannot explain the reason why unreacted nanofoil has a thermal conductivity of ~79 W/(K×m) at room temperature. For the reacted samples, the temperature dependent thermal conductivity variation among the different reacted nanofoil samples is rather consistent compared with the resistivity. The thermal conductivity of the reacted nanofoil is ~34 W/K×m at room temperature, and is slightly higher than the data (25-30 W/(K×m)) provided by Indium Corporation [14], but lower than the stoichiometric NiAl (~75 W/(K×m)) measured by Darolia et al and Walston et al [45], [47].

The Lorenz number of both reacted and unreacted nanofoil at all temperatures was calculated by Wiedemann-Franz law. The Lorenz number of all reacted samples varies between 5.1×10^{-8} $W\Omega/K^2$ and 6.5×10^{-8} $W\Omega/K^2$ at room temperature, which are larger than the Sommerfeld constant 2.44×10^{-8} $W\Omega/K^2$. The Lorenz number of the reacted samples implies a similar temperature-dependent variation with the reduction of the temperature. When the temperature decreases below

160 K, the value drops to below 5.0×10^{-8} WΩ/K^2. Thereafter, these values start to increase with decreasing temperature, and reaches a peak value (above 6.9×10^{-8} WΩ/K^2) at ~23 K. Finally, the curves decrease in the range between 5.5×10^{-8} WΩ/K^2 and 6.3×10^{-8} WΩ/K^2 at 5 K and are in a similar range at room temperature. The reason for larger Lorenz number is the significance of lattice conductivity in alloys at intermediate temperatures [120].

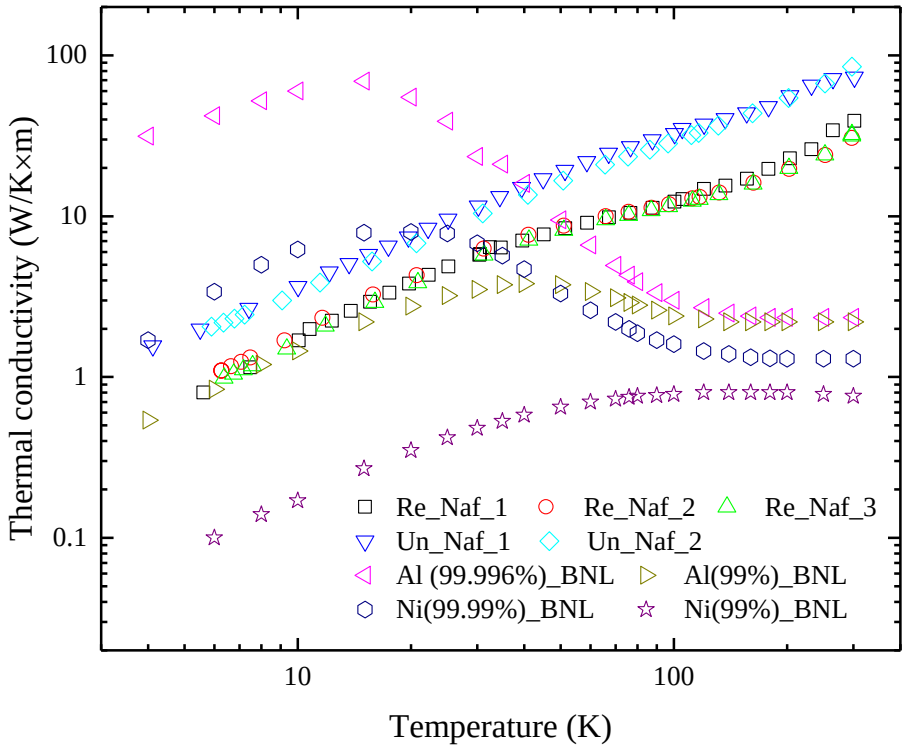

Figure 3.11: The plot for thermal conductivity for the reacted and unreacted nanofoil measured by PPMS_TTO compared with nickel and aluminum in different purities [173] varying with temperature between 5 K and 300 K (Re_Naf: reacted nanofoil sample, Un_Naf: unreacted nanofoil sample, BNL:Brookhaven National Laboratory).

For the unreacted samples, the Lorenz number of unreacted sample 1 is 2.99×10^{-8} WΩ/K^2 at room temperature, which is close to the Sommerfeld constant. This is dictated by the electron's contribution on the conductivity for pure metals. The Lorenz number of unreacted sample 2 has a temperature dependence when temperature is above 100 K. The reason for this may be due to a short distance (1.4 mm) between two thermocouples compared with other unreacted samples (> 4 mm). Therefore, the thermal diffusion, small temperature gradient and a higher resistivity measured all contribute to increasing the error in the Lorenz number. Compared with metals, there was no temperature dependence measured for unreacted samples at intermediate temperatures, which are almost constant at 2.99×10^{-8} WΩ/K^2 between 10 K and 100 K. This may be due to the unreacted nanofoil that causes a reduction trend of thermal conductivity with the decreasing of temperature instead of the increasing trend normally observed in high purity metals.

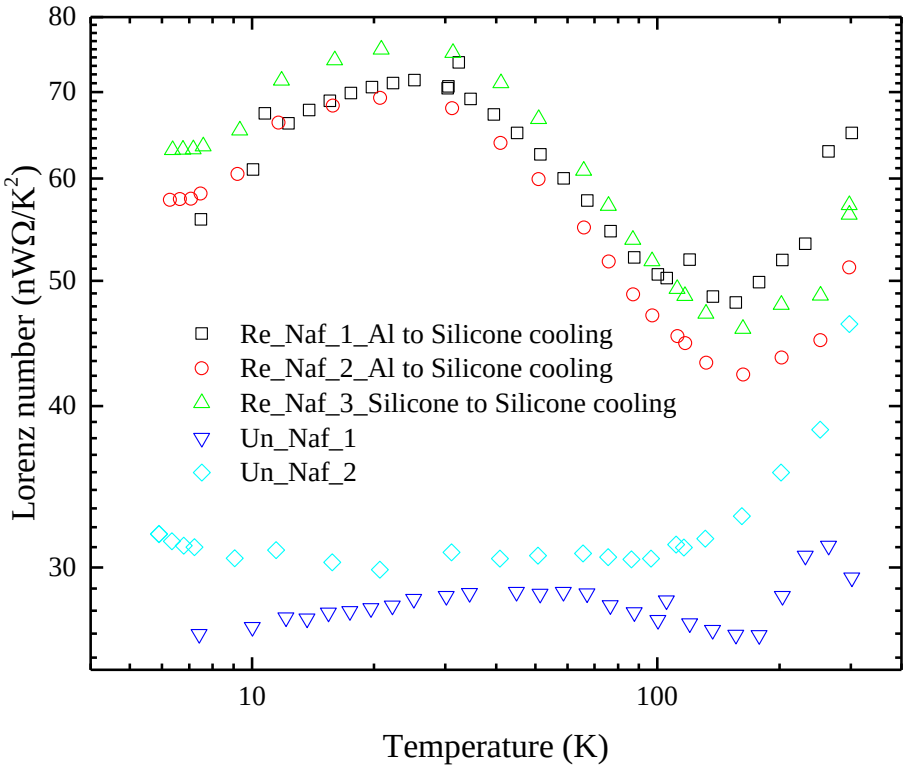

Figure 3.12: The plot for Lorenz number varying with temperature for both reacted and unreacted nanofoil samples (Re_Naf: reacted nanofoil sample, Un_Naf: unreacted nanofoil sample).

3.4.1.3. Heat capacity of both reacted and unreacted nanofoil

In the heat capacity measurements performed in this work, the heat capacity measurements for both reacted and unreacted nanofoil included the heat capacity of grease which had to be subtracted from the measured results. Taking unreacted sample 2 (Un_Naf_2) as an example, Figure 3.13 shows the measured heat capacity of unreacted sample 2 and calibrated heat capacity of unreacted sample 2 (minus grease) compared with the calculated heat capacity of unreacted nanofoil sample (Ni+Al, 50:50 at. %) [174], [175] and N-type grease. The heat capacity of grease is achieved determined by: C_p (grease) × m (0.1 mg), and the calibrated result was obtained via subtracting the grease contribution from the measured result. The calibrated results with error bars are shown in Figure 3.13 that take the mass of grease into consideration. Furthermore, the calculated heat capacity of unreacted nanofoil sample (Ni+Al, 50:50 at. %) is calculated in accordance with the heat capacity of nickel and aluminium evaluated by:

$$C_p(\mathrm{Ni+Al, 50{:}50\ at.\%}) = C_p(\mathrm{Ni})\frac{M(\mathrm{Ni})}{M(\mathrm{Sum})} + C_p(\mathrm{Al})\frac{M(\mathrm{Al})}{M(\mathrm{Sum})} \qquad 3.3$$

Where C_p is the specific heat in unit of J/(g×K), and M is the molar mass. The trend of calibrated heat capacity results (red circles) follows that of the calculated nickel-aluminium nanofoil (Ni+Al, 50:50 at. %, green solid line), and has a good fitting at high temperatures, but the measured values are slightly higher at lower temperatures. Note, all of the measured specific heat capacities presented in Figure 3.13 for both reacted and unreacted samples have been calibrated in a same method.

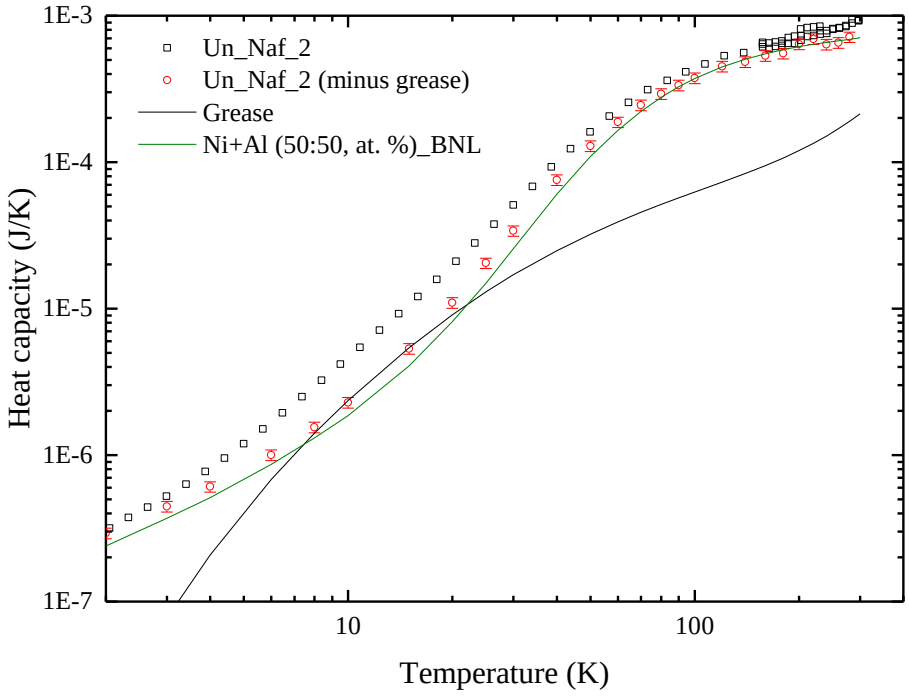

Figure 3.13: The plot for measured heat capacity of unreacted sample 2 and calibrated heat capacity of unreacted sample 2 (minus grease) compared with calculated heat capacity of unreacted nanofoil sample (Ni+Al, 50:50 at. %) [174], [175] and N-type grease (Un_Naf: unreacted sample, BNL:Brookhaven National Laboratory).

Figure 3.14 shows the measured specific heat capacity (J/(g×K)) of three reacted samples (2 and 3) and unreacted sample 2 compared with aluminium, nickel and calculated specific heat of unreacted nanofoil (Ni+Al, 50:50 at. %) at the temperature from 1 K to 300 K. The specific heat capacity of these three samples has an increasing trend with the temperature rising up from 1 K to 300 K. The specific heat capacity of the reacted nanofoil produced with silicone rubber placed in contact with an aluminium block for cooling, and reacted nanofoil produced with silicone rubber placed in contact with silicone rubber for cooling at 300 K are around 0.55 J/(g×K) and 0.51 J/(g×K) respectively, which are smaller than results for the reacted nanofoil that has a specific heat capacity of 0.64 J/(g×K), which is data provided by Indium Corporation [14].

In order to compare the molar heat capacity constant (C_V = 24.94 J/(mol×K)) in accordance with the Law of Dulong and Petit at room temperature, the specific heat (C_V) in units of J/(mol×K) of unreacted samples 2 and 3 and unreacted sample 3 plotted against the cube of temperature T^3 (1 K < T < 300 K) as shown in Figure 3.15. This graph therefore compares the specific heat capacity of aluminium, nickel, the calculated specific heat capacity of unreacted nanofoil (Ni+Al, 50:50 at. %), and specific heat capacity of NiAl (Ni, 49.3 at. %) measured by Alexander et al [52], NiAl (Ni, 48 or 50 at. %) measured by Seitchikf et al [56], NiAl (Ni, 50.5 and 51 at. %) measured by Begot et al [176], and specific heat capacity of Al_2O_3 and NiO [177], [178] is very close to the molar heat capacity constant at the room temperature, and is compared with aluminium, C_V = 24.33 J/(mol×K), and nickel, C_V = 26.12 J/(mol×K), and calculated specific heat of unreacted nanofoil (Ni+Al, 50:50 at. %), C_V = 25.22 J/(mol×K).

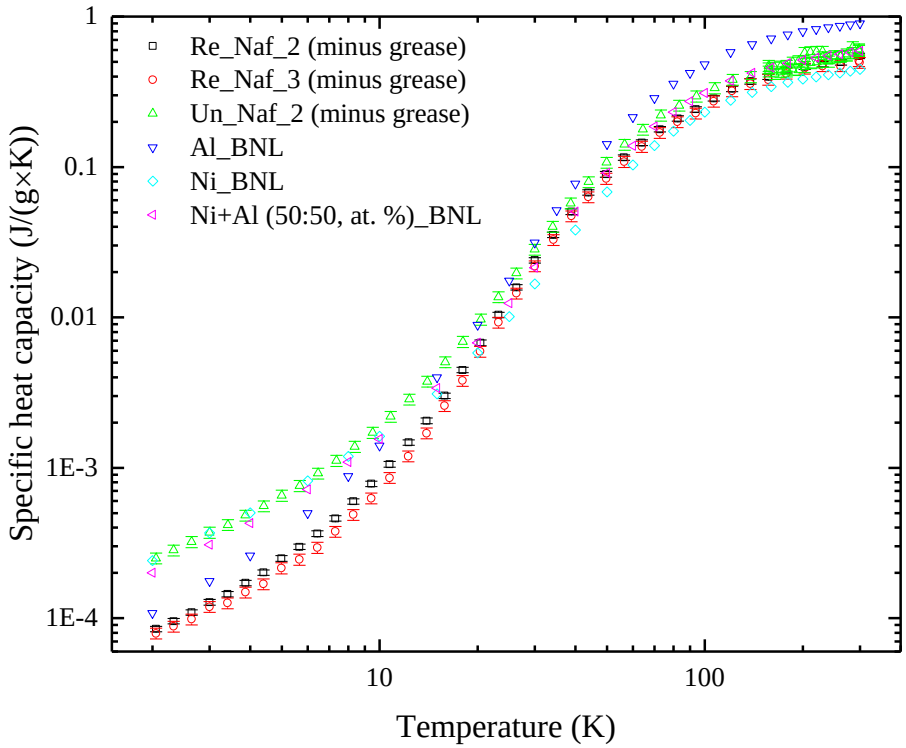

Figure 3.14: The specific heat capacity in unit of J/(g×K) of reacted nanofoil sample 2 and 3 and unreacted nanofoil sample 2 compared with that of aluminium, nickel and calculated specific heat of unreacted nanofoil (Ni+Al,50:50 at. %) [174], [175] versus the temperature from 1 K to 300 K (Re_Naf: reacted sample, Un_Naf: unreacted sample, BNL:Brookhaven National Laboratory).

The experimental results of C_V for all the reacted samples at room temperature are 46.86 J/(mol×K) and 43.51 (J/mol×K) for reacted sample 2 and 3 respectively and these values are very similar to the specific heat capacities of NiAl (Ni, 49.3 at. %), C_V = 48.5 J/(mol×K) measured by Alexander et al [52], but larger than the molar heat capacity constant of metals and NiAl (Ni, 50 at. %), C_V = 23.01 J/(mol×K)) measured by Sandakova et al [54]. At lower temperatures (< 20 K), the experimental C_V of the two reacted samples are higher than the heat capacities of NiAl measured by other groups. The first possibility to account for such difference may be associated to nickel and aluminium having a reaction with oxygen gas during processing. The specific heat capacity of Al_2O_3 and NiO are plotted in the same figure to provide a comparison and shows the C_V of Al_2O_3 is higher than the measured results and NiO is similar to the measured results. However, the very low C_V of Al_2O_3 and NiO below 20 K cannot be explained by the higher measured results of reacted nanofoil over the same temperature range. The second possibility considers different compositions, where nickel rich phase nickel aluminide exists within the reacted nanofoils. For instance, the specific heat capacity of Ni_3Al at lower temperature (< 20 K) were higher than our measured results. An assumption of one mole of reacted nanofoil that consists of a% ($0 < a < 100$) mole of NiAl and (100% - a%) mole of Ni_3Al and $NiAl_3$ was applied to the estimated specific heat capacity in conjunction, with the specific heat capacity of NiAl (Ni, 49.3 at. %) measured by Alexander et al [52], specific heat of Ni_3Al (Ni, 75 at. %) measured by Dood et al [55] and specific heat capacity of $NiAl_3$ (Ni, 25 at. %) measured by Dunlop et al [54]. The estimated specific heat with 80% NiAl and 20% of Ni_3Al and $NiAl_3$ in one mole of reacted nanofoil has a good fitting with experimental values. However, there are no references that mention Ni_3Al as an intermediate

product in the reaction of nanofoil. This existence of this product needs to be verified by SEM with EDX and XRD as part of further work.

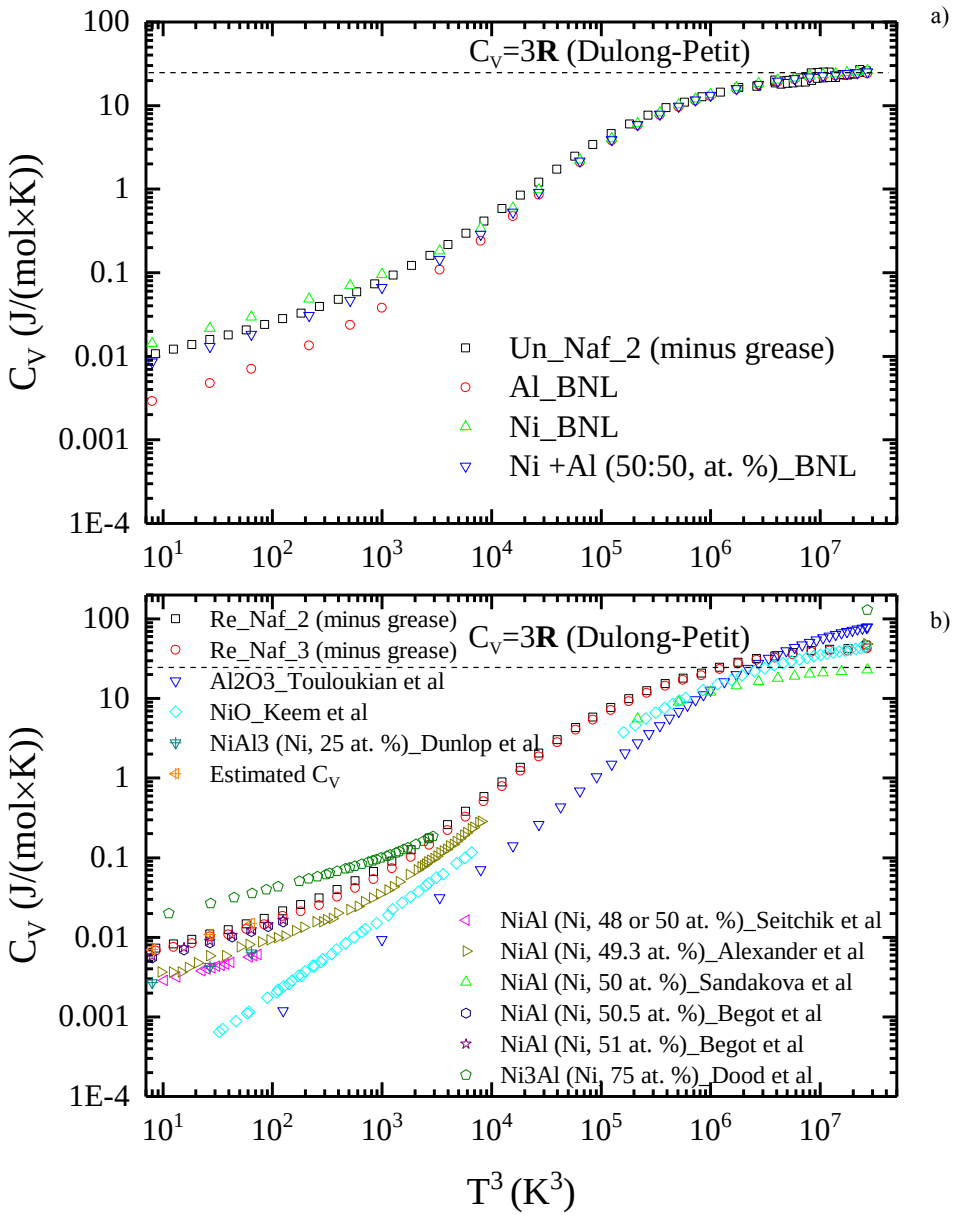

Figure 3.15: The specific heat capacity in unit of J/(mol×K) of a) unreacted nanofoil sample 2 compared with aluminium, nickel and calculated specific heat of unreacted nanofoil (Ni+Al,50:50 at. %) [174], [175] and b) reacted nanofoil sample 2 and 3 compared with the specific heat of $NiAl_3$ (Ni, 25 at. %) measured by Dunlop et al and reported in [54], NiAl (Ni, 49.3 at. %) measured by Alexander et al [52], NiAl (Ni, 48 or 50 at. %) measured by Seitchikf et al [56], NiAl (Ni, 50 at. %) measured by Sandakova et al reported in [54], NiAl (Ni, 50.5 and 51 at. %) measured by Begot et al [176], Ni_3Al (Ni, 75 at. %) measured by Dood et al [55], $NiAl_3$ (Ni, 25 at. %) measured by Dunlop et al reported in [54] and specific heat of Al_2O_3 and NiO and estimated specific heat of one mole NiAl (80%NiAl +20%(Ni_3Al+$NiAl_3$)) versus the temperature from 1 K to 300 K [177], [178], and dash line shows the molar specific heat constant at room temperature in accordance with the law of Dulong and Petit (Re_Naf: reacted sample, Un_Naf: unreacted sample, BNL:Brookhaven National Laboratory).

Figure 3.16 presents curves of C_V/T versus T^2 for samples 2 and 3 and unreacted nanofoil sample 2 compared with curves for aluminium, nickel and for the calculated specific heat capacities of unreacted nanofoil (Ni+Al, 50:50 at. %) [174], [175], NiAl (Ni, 49.3 at. %) measured by

Alexander et al, NiAl (Ni, 48 or 50 at. %) measured by Seitchikf et al [56], NiAl (Ni, 50.5 and 51 at. %) measured by Begot et al [176] over the temperature range of (1 K < T < 10 K). The low temperature heat capacity of metals can be expressed as: $C_V/T = \beta+\alpha T^2$ in accordance with the Einstein-Debye phonon model and shows a good linear fitting between C_V/T and T^2, where β is the electronic specific heat constant, and α is vibrational specific heat constant. The values of α and β for both reacted and unreacted nanofoil samples are shown in Table 3.10. Several articles seem to imply there is nonlinearity in the heat capacity for NiAl with respects to C_V/T, and highlighted in the curve shown as a sudden rise when the temperature is below 4 K [52], [53]. The same result was also fitted by adding a constant A: $C_V = A+\beta T+\alpha T^2$. The adjusted heat capacity of NiAl (measured by Alexander et al) plotted with respects to C_V/T and $(C_V - A)/T$ is shown in Figure 3.16, and where the calculation of α and β is taken from $(C_V - A)/T$. However, there is no change in slope observed in our measurement upon reacted samples.

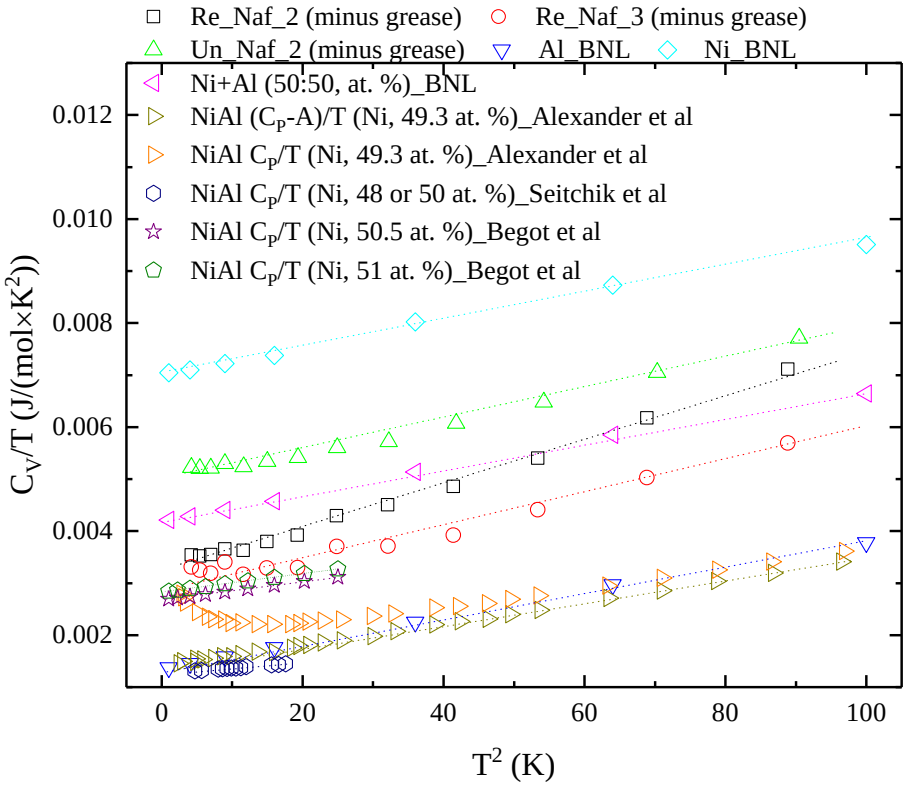

Figure 3.16: The specific heat capacity divided by temperature (C_V/T) of reacted nanofoil sample 2 and 3 and unreacted nanofoil sample 2 compared with that of aluminium, nickel Ni+Al (50:50, at. %) [174], [175] and heat capacity of NiAl (Ni, 49.3 at. %) measured by Alexander et al [52], NiAl (Ni, 48 or 50 at. %) measured by Seitchikf et al [56], NiAl (Ni, 50.5 and 51 at. %) measured by Begot et al versus the square of the temperature from 1 K to 10 K (Re_Naf: reacted sample, Un_Naf: unreacted sample, BNL: Brookhaven National Laboratory, and dash lines represents the linear part of the curve profiles).

In Table 3.10, the, α and β values for reacted sample 2 are 4.094e-5 J/(mol×K^4) and 0.00324 J/(mol×K^2) receptively. For reacted sample 3, α = 2.650e-5 J/(mol×K^4) and β = 0.00299 J/(mol×K^2), and both values are slightly smaller compared to those previously calculated. The value of β_{NiAl} for both reacted samples are smaller than β_{Ni} = 0.00702 J/(mol×K^2) (for nickel), but larger than β_{Al} = 0.00135 J/(mol×K^2) (for aluminium). When comparing these values against α =

2.056e-4 J/(mol×K^4) and β = 0.00141 J/(mol×K^2) obtained from the heat capacity of NiAl (Ni, 49.3 at. %) [52], both of the reacted samples 2 and 3 produced larger values of β.

Table 3.10: Calculated α and β from the curve fitting from Figure 3.16 for reacted and unreacted nanofoil samples, aluminium, nickel, Ni+Al (50:50, at. %) [174], [175], NiAl (Ni, 49.3 at. %) measured by Alexander et al [52], NiAl (Ni, 48 or 50 at. %) measured by Seitchikf et al [56], and NiAl (Ni, 50.5 or 51 at. %) measured by Begot et al [176].

Sample	α (J/(mol×K^4))	β (J/(mol×K^2))	C_V at room temperature (J/(mol×K))
Re_Naf_2	4.094E-5	0.00324	46.86
Re_Naf_3	2.650E-5	0.00299	43.51
Un_Naf_2	3.067E-5	0.00484	25.08
Al	2.400E-5	0.00137	24.33
Ni	2.559E-5	0.00702	26.12
Ni+Al (50:50, at. %)	2.499E-5	0.00419	25.22
NiAl (Ni, 49.3 at. %)	2.056E-5	0.00141	48.53
NiAl (Ni, 48 or 50 at. %)	1.070E-5	0.00126	N/A
NiAl (Ni, 50.5 at. %)	1.780E-5	0.00267	N/A
NiAl (Ni, 51 at. %)	1.790E-5	0.00282	N/A

3.4.1.4. The cross-section morphology of reacted nanofoil

In order to investigate the effects of microcracks upon the resistivity and thermal conductivity of reacted nanofoils, reacted sample 1 was potted with and epoxy resin and polished to produce a cross-sectioned specimen that could be viewed under microscope. Three images of the cross-section are shown in Figure 3.17. No obvious cracks were observed, but some holes and indents of variable size were found, and void spaces located near the edge of the potted specimen. These indentations and void space that appear within the nanofoil could prevent effective current and thermal transfer through the nanobond joints. However, the solder would tend to fill the cracks and void spaces during the formation of the joint and improve the thermal conduction and reduce the joints electrical resistance.

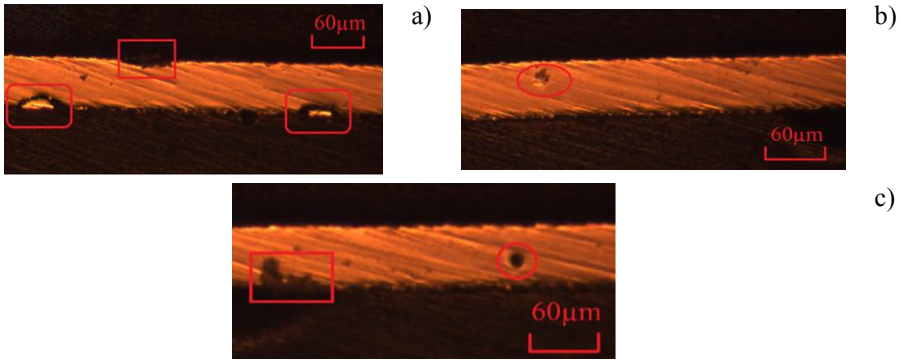

Figure 3.17: The picture indicating the cross-section of a piece of reacted nanofoil (Reacted sample 1): a) Rectangulare area: surface indentations, Rounded rectangular area: surface cracks and fragments and b) Oval area: cross-section of indentation; c) Rectangular area: surface void space/indentation, Round area: cross section hole.

3.4.2 Reacted nanofoil films for SEM with EDX and XRD investigation

The resistivity of several reacted nanofoil samples at temperatures from 5 K to 300 K have been measured by using the PPMS. Differences in the phase formation and grain size in the reacted

nanofoil could be influenced by the type and the rate of reaction cooling. This assumption was assumed as a possible reason for the variations in resistivity observed among different samples. Consequently, additional reacted nanofoil samples were fabricated by applying different cooling conditions and using a range of different sample holding materials.

Table 3.11 lists the cooling conditions, dimensions and resistivity of each sample at room temperatures. Figure 3.18 show five images of reacted nanofoil samples produced under different cooling conditions. The surface of reacted nanofoil cooled with air is dark grey, and the nanofoil sample appeared became darker after the reaction. The resistivity was estimated around 50 μΩ×cm. In comparison, the reacted nanofoil produced by copper cooling remained unoxidised with a shiny silver surface (Figure 3.18b). The reacted nanofoil produced with aluminium cooling also had an unoxidised and clean surface. Eight reacted samples were fabricated using the copper cooling block, and a further two were fabricated upon a hot plate at 100 ºC. The resistivity of the reacted nanofoil produced with copper cooling varied from 47 to 73 μΩ×cm. The resistivity of the nanofoils produced on the hot plate were > 70 μΩ×cm, however, the two samples were found to be very brittle and easy to fracture. A further set of four additional reacted samples were produced by igniting the joint placed between two silicone rubber sheets and a single sample was produced by igniting the joint placed between two sheets of wet printing paper. The colour of the surfaces after ignition was generally grey and intermixed with smaller areas of light purple as shown in Figure 3.18 (c and d). The resistivity of the sample prepared between silicone rubber sheets varied from 43 to 49 μΩ×cm, and between wet paper was 56 μΩ×cm. The appearance of samples prepared using G10 blocks as the cooling interface, were covered with non-homogeneous regions of dark purple, and the resistivity of these samples varied from 51 to 65 μΩ×cm. Furthermore, the G10 blocks left surface indentations on the reacted nanofoil samples, which is further evidence that the nanofoil material did indeed melt during the reaction process. Having reviewed the resistivities measured from all the samples prepared for this particular investigation upon cooling conditions and cooling rates; the original assumption that suggests that slower cooling rate will tend to produce nanofoil specimens with higher resistivities does not hold, given the scatter in the results generated during this investigation.

However, most of the measured resistivity values are within a reasonable range (24 μΩcm-60 μΩcm) and comparable to other published results upon NiAl films [19], [41]–[44], [179], but they are much higher than bulk ordered NiAl (~10 μΩcm) [36]–[38], [40]. Furthermore, the variation in the measured resistivity reported in this work, is likely influenced by the thermal contact with the substrate materials rather than by the cooling conditions. For instance, the silicone rubber material is soft and compliant compared with other materials, and therefore the overall average of the measured resistivity value of reacted nanofoil samples is possibly more consistent compared with other samples prepared between harder materials such as copper and G10 blocks.

Table 3.11: The dimensional parameters and resistivity of each reacted nanofoil samples with different cooling conditions.

Cooling condition	Length (cm)	Width (cm)	Thickness (µm)	Cross section (cm)	Resistance (Ω)	Resistivity (µΩ×cm)	Mean value (µΩ×cm)
Copper	0.914	0.477	63	0.003	1.648E-02	53.40±4.17	57.28±19.72
	0.809	0.415	62	0.003	1.488E-02	47.32±1.62	
	0.793	0.362	62	0.002	2.585E-02	73.16±4.73*	
	0.704	0.459	62	0.003	1.789E-02	71.81±6.14*	
	0.545	0.530	62	0.003	8.457E-03	50.99±1.87	
	0.562	0.545	62	0.003	1.019E-02	56.21±2.38	
	1.109	0.608	62	0.004	1.410E-02	47.22±3.19	
	0.763	0.637	62	0.004	9.914E-03	51.32±0.85	
	0.366	0.496	62	0.003	6.608E-03	55.52±2.62	
	0.570	0.544	62	0.003	1.105E-02	65.36±3.68	
Silicone Rubber	0.899	0.603	64	0.004	1.021E-02	43.81±3.40	46.61±4.30
	0.926	0.609	64	0.004	1.104E-02	46.45±3.90	
	1.076	0.666	64	0.004	1.182E-02	46.80±4.11	
	0.923	0.384	62	0.002	1.914E-02	49.38±1.57	
Printing paper with water	0.976	0.473	63	0.003	1.837E-02	56.07±5.20	56.07±5.20
G10	1.121	0.616	63	0.004	1.488E-02	51.50±3.61	58.40±11.70
	1.005	0.658	63	0.004	1.577E-02	65.06±5.12	
	0.723	0.657	62	0.004	1.040E-02	58.42±1.05	
	0.363	0.438	63	0.003	7.708E-03	58.59±1.31	

*Copper was heating up to 100 °C on a hot plate.

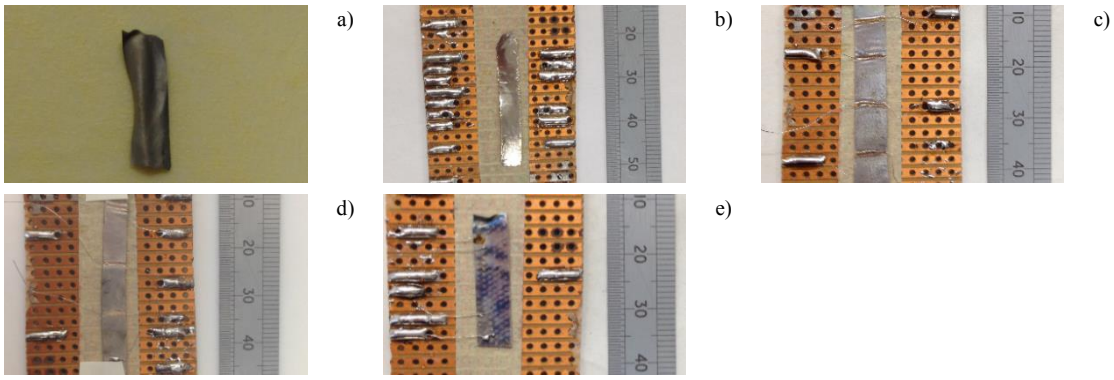

Figure 3.18: The pictures for reacted nanofoil samples with different cooling conditions: a) air cooling, b) copper cooling, c) rubber cooling, d) A4 paper submerged with water cooling and e) G10 block cooling.

Several literatures exhibit that annealing process of the reacted Ni/Al multilayer samples is helpful to reduce the resistivity of NiAl by increasing the crystal grain size [19]. However, the differences observed in surface colour of the reacted nanofoil samples, are not related to any differences identified in the crystal grain size or microstructure. In fact, when the surface of the silicone was sprayed with water during preparation of the nanofoil, the grey colour changed only slightly with less visibility of purple. Furthermore, it needs to be noted that the melting point of copper is 1085 ºC. Silicone rubber and G10 start to degrade at 300 ºC and 117 ºC respectively, and they were all

below the reaction temperature (1400 ºC to 1800 ºC) of nanofoil. Consequently, the SEM with EDX compositional analysis and XRD compositional analysis were introduced to investigate and changes in grain size and microstructure of these reacted nanofoil samples in more detail. The studies upon the microstructures were applied to those specimens in each batch with the lowest resistivity.

3.4.2.1. SEM images and EDX analysis of nanofoil films

Figure 3.19 shows the fractual cross-section and the surface images of a unreacted nanofoil film, and the corresponding selected area compositional analysis by EDX is shown in Table 3.12. The fold zone as shown in Figure 3.19a consists of thousands of alterred layers of nickel or aluminum. There is an outer layer at the edge of the foil, which is 1 μm thick copper/silver/indium layer. It is difficult to say if the stack lines are perpendicular to the alternating outer layer of Al and Ni (30~50 nm) as shown in Figure 3.19a. It needs to be noted that the TEM image of the cross-section of the nanofoil show the outer alloy layer is parallel to the Al/Ni multilayers [180]. Table 3.12a shows the EDX compositional analysis that gives the atomic quantities of Ni (51.31%, %. at) and Al (49.69%, %. at) of the scanned area shown in Figure 3.19a, The atomic quanities measured in samples prepared in this work, match the stoichiometric ratio 50:50 between Ni and Al as stated in [14]. Figure 3.19b shows the surface of the unreacted nanofoil. The image on the left shows the stacked layers at the fractual edge. Table 3.12b shows the EDX compositional anlysis results of the scanned area highlighted in Figure 3.19b. The results confirm the presence of two elements, (copper and silver), that form the outer coating in the unreacted nanofoils [14].

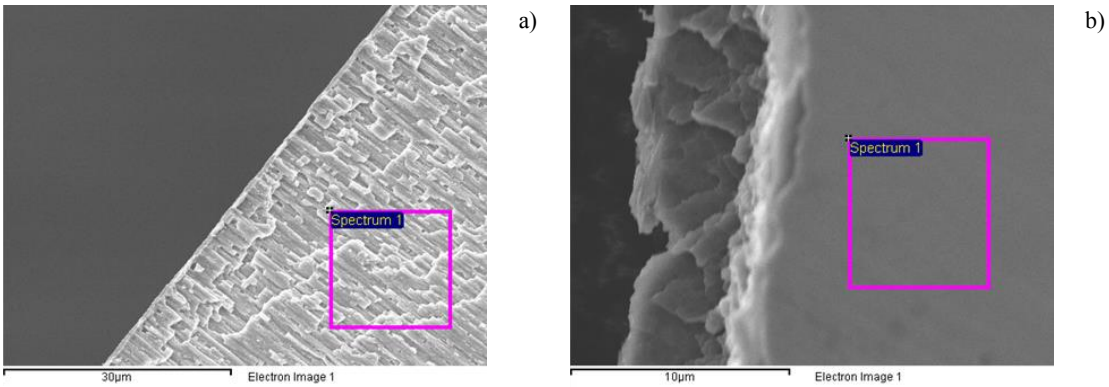

Figure 3.19: SEM images of a) cross-sectional and b) surface of unreacted nanofoil. Two square panes (spectrum 1 and spectrum 2) are the EDX scanned area.

Table 3.12: Compositional analysis of a) Cross-sectional and b) surface of unreacted nanofoil film by EDX.

a)

Element	Weight %	Atomic %
Ni	67.38	51.31
Al	32.62	48.69

b)

Element	Weight %	Atomic %
Cu	18.69	28.07
Ag	81.31	71.93

The fracture cross-sectional SEM images of the reacted nanofoil with copper cooling, rubber cooling and G10 cooling with a zoom of X850 and a zoom of X5500 are shown in Figure 3.20, which these images give detailed microstructure morphology of the fracture surface of these reacted nanofoil samples. Figure 3.20a shows there are some intermediate grain growth (3-5 μm) paralled to the outer edge of the copper cooling sample, then the grain tends to be larger and

become vertical towards the bottom side of the foil; Figure 3.20c shows that there are a few more larger grain growth (5-10 μm) in the middle of the cross-section of the rubber cooling sample; Figure 3.20e shows more even and smaller grain growth (2-3 μm) of the G10 cooling sample compared with previous two samples. Larger zoom of X5500 images as shown in Figure 3.20 (b, d, f) display the irregular fold, and the similar grain size and morpgology of each sample. But the finer grain size of G10 cooling sample can explain a higher resistivity value of ~51 μΩ×cm compare with rubber cooling sample (~43 μΩ×cm) and copper cooling sample (~42 μΩ×cm).

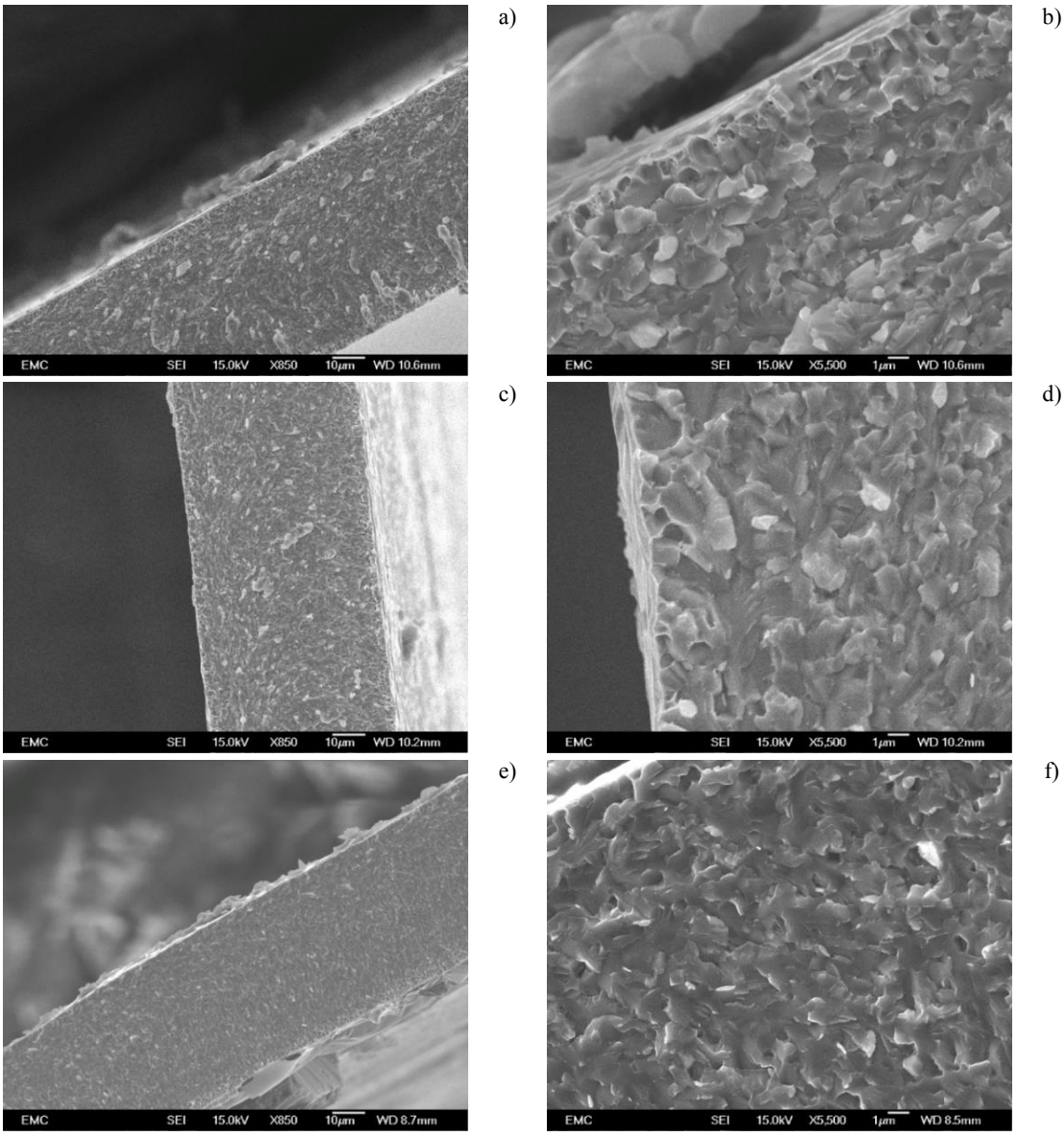

Figure 3.20: SEM images of the cross-section of a copper cooling reacted nanofoil with a) X850 amplification and b) X5500 amplification, and a rubber cooling reacted nanofoil with c) X850 amplification and d) X5500 amplification, and a G10 cooling reacted nanofoil with e) X850 amplification and f) X5500 amplification.

Figure 3.21 shows a copper to copper nanobond joint specimen with 240 °C solder (Sn99.3Cu0.7, wt. %). Cracking (red circle) of the reacted foil was observed in this joint, and it's clear that the solder was filling into the cracking space. The existing of the crack within nanobond joint is due to the thermal contraction between the foil densification and surrounding material during the

cooling process from the high temperature reaction [58]. Table 3.13 shows the composition quantities of the two scanned spots in the joint by EDX, which Table 3.13a reaffirms the solder components, and Table 3.13b shows a slight Al-rich compostions (55.34% atomic Al) phase at this scanned spot.

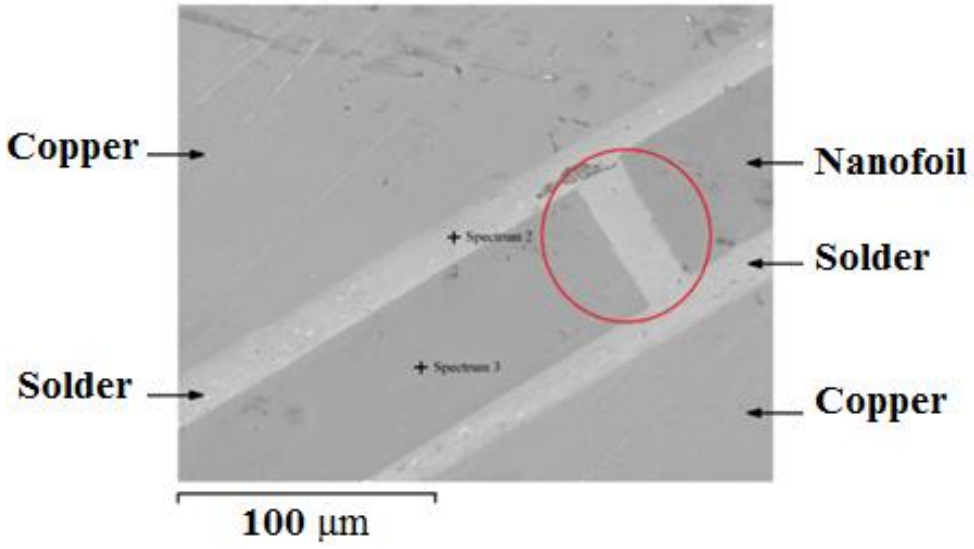

Figure 3.21: SEM image of a copper to copper nanobond joint.

Table 3.13: Compositional analysis of cross-sectional of a) solder (spectrum 2) and b) reacted nanofoil film (spectrum 3) within a copper to coper nanobond joint by EDX.

Element	Weight %	Atomic %
Sn	100	100

a)

Element	Weight %	Atomic %
Ni	72.94	55.34
Al	27.06	44.66

b)

3.4.2.2. XRD patterns of reacted nanofoil films

Four reacted nanofoil samples with air cooling, copper cooling, silicone rubber cooling and towel paper submerged with water cooling and an Al_2O_3 strip were applied to XRD compositional analysis. Figure 3.22-3.25 show the XRD pattern of each sample versus the grazing angles (2θ) from 30° to 100° compared with XRD database of Ni-Al intermetallic phases [24] and Al_2O_3 [25].

Seven NiAl peaks and most Al_2O_3 peaks can be found in all the XRD patterns with highlights in accordance with the database, which implies the main production phase of the reacted nanofoil is NiAl. The attention should be paid on the XRD patterns differences and the uncertain peaks among four samples. The first uncertain peak appears at 2θ around 40.50° as shown in arrow 1 in Figure 3.22, arrow 4 in Figure 3.23, arrow 7 in Figure 3.24 and arrow 10 in Figure 3.25, which $NiAl_3$ has the peaks at 39.86° and 41.38° that 2θ is close to around 40.50°. The second one appears at 2θ around 42.55° as shown in arrow 5 in Figure 3.23, arrow 8 in Figure 3.24 and arrow 11 in Figure 3.25, which Ni_5Al_3 has a peak at 43.45°, and Ni_3Al has a peak at 43.69°, and $NiAl_3$ has a peak at 41.67°, and Al_2O_3 has a peak at 41.67° and 43.36°. The third peak appears at 2θ around 95.6° in arrow 3 in Figure 3.22, arrow 6 in Figure 3.23, arrow 9 in Figure 3.24 and arrow 12 in Figure 3.25, which Ni_5Al_3 has the peak at 95.96°, Ni_3Al has the peak at 95.58°, and $NiAl_3$ has a peak at 94.96°, and Al_2O_3 has the peak at 95.25°.

It's possible that the appearance of Al-rich phase that composition of $NiAl_3$ and Ni_2Al_3 are the intermediate products of Ni/Al multilayers reaction. It needs to be noted that there is no reference to mention the Ni-rich phase of Ni_5Al_3 and Ni_3Al are the intermediate products in the nanofoil reaction, and Ni was the component that has to continue to react with $NiAl_3$ and Ni_2Al_3 to form NiAl during the reaction. Furthermore, the presence of these peaks are independent with very small peaks, the related Al-rich phase products would be the minimum amount in the reacted nanofoil.

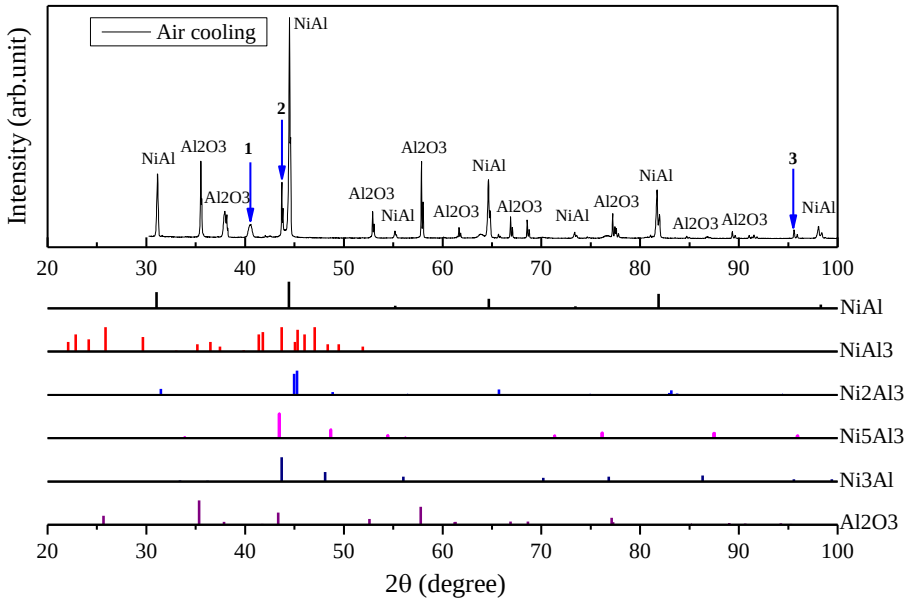

Figure 3.22: XRD pattern of an air cooling reacted nanofoil sample versus 2θ from 30° to 100°.

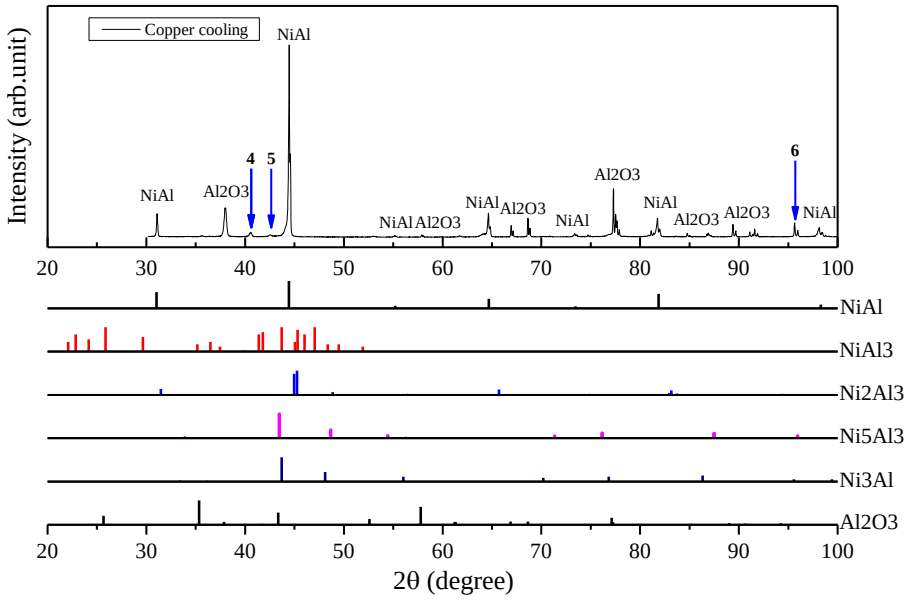

Figure 3.23: XRD pattern of a copper cooling reacted nanofoil sample versus 2θ from 30° to 100°.

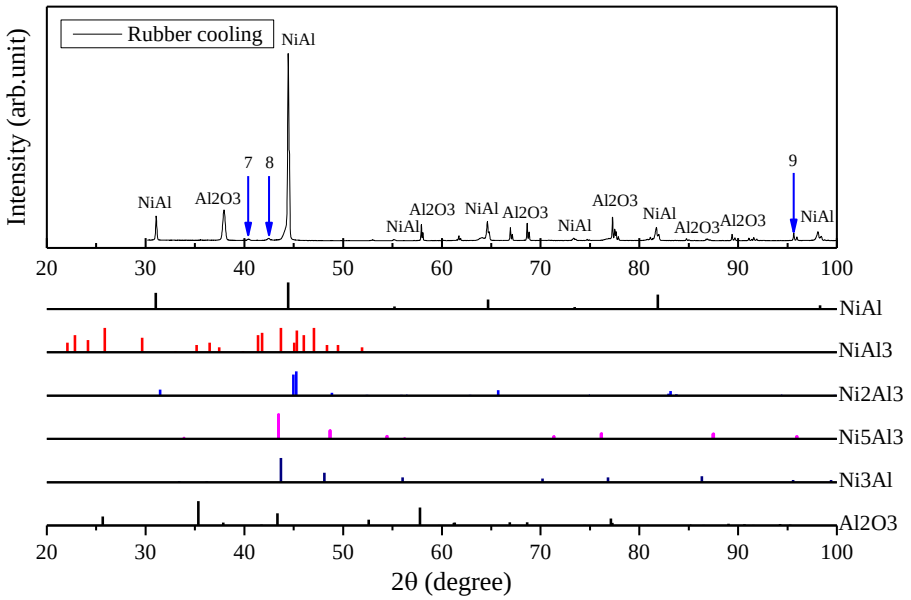

Figure 3.24: XRD patten of an rubber cooling reacted nanofoil sample versus 2θ from 30° to 100°.

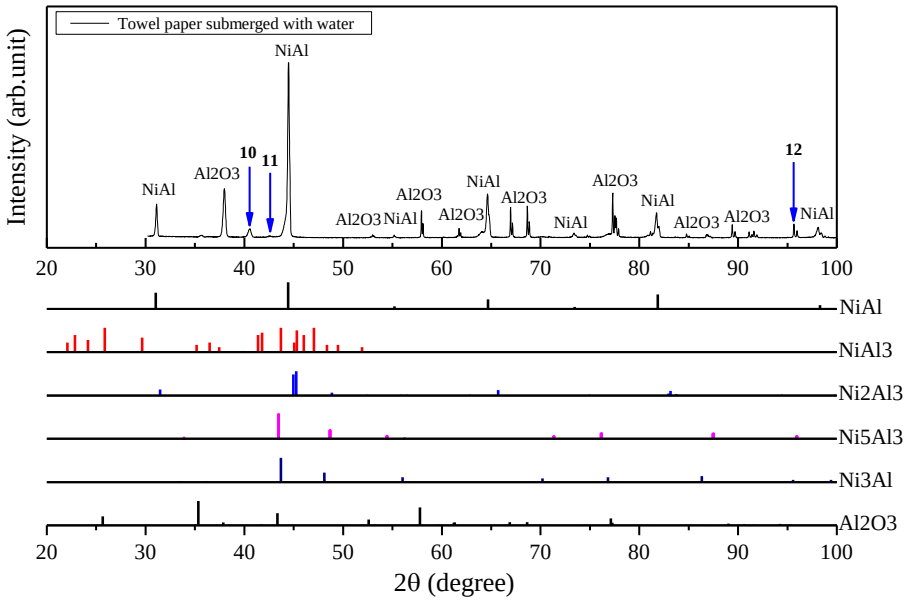

Figure 3.25: XRD partten of a water submerged towel paper cooling reacted nanofoil sample versus 2θ from 30° to 100°.

Figure 3.26 shows the XRD pattern versus the grazing angles between 43° and 46° for reacted nanofoil samples with different cooling conditions, which shows the highest peak of the XRD pattern for each sample at this 2θ range. This peak is consistent with the database of NiAl has the highest intensity at 2θ of 44.45°. All the peaks have a shoulder at the right side, and copper cooling sample even has a multi-peak, which implies the possibility of the multi-phase formation existing. The Ni_2Al_3 (2θ = 44.97°) is the phase that the position is close to NiAl at 2θ of 44.45°, and resistivity of Ni_2Al_3 is higher than that of NiAl, which the value shows in Table 1.3 from the literature is 50.5 μΩ×cm, and most measured resistivity as shown in Table 3.11 are around this value. Thus the appearance of Ni_2Al_3 could explain the measured resistivity values of NiAl are in the high values range. For the XRD pattern peak of each sample appears at 2θ of 44.45°, the smooth and the highest intensity of XRD pattern for the rubber cooling sample implies

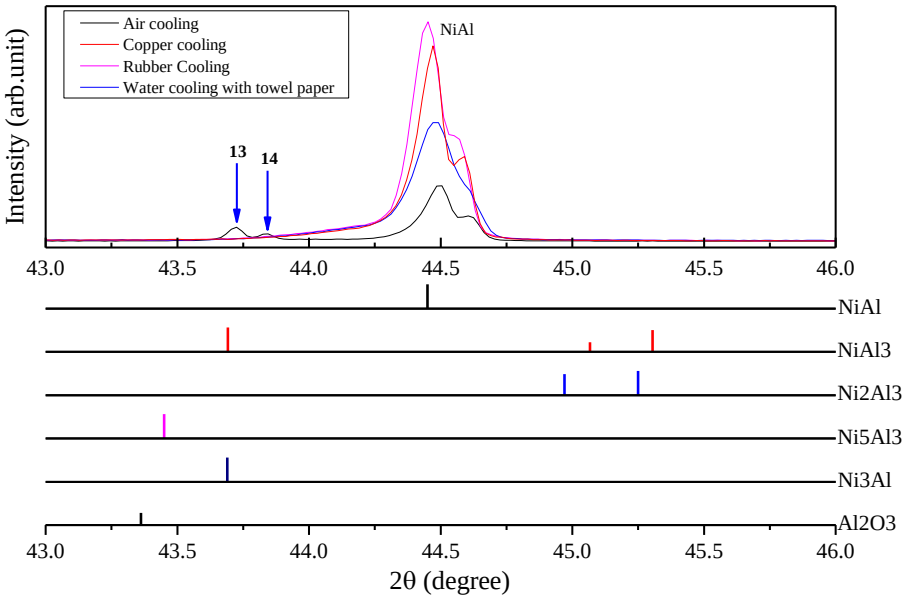

Figure 3.26: XRD pattern vs. grazing angles between 43° and 46° for reacted nanofoil samples with different cooling conditions.

that the high extent of reaction completeness. Consequently, the rubber cooling sample has the lowest resistivity among these samples (43.8 μΩ×cm).

The resistivity of most reacted nanofoil samples varies between 45 and 60 μΩ×cm in a 33% difference at room temperature. SEM investigation shows that there is no obvious difference of the grain growth among the reacted nanofoil with different cooling conditions. The XRD patterns inhibits NiAl is the main reaction products, and there is the possibility for other phase existing with a small amount. The fine/small grain growth and Al-rich phase can be the reason for the higher resistivity of the reacted nanofoil than the ordered bulk NiAl film. It is suggested that annealing process is a good option to reduce the resistivity of the reacted nanofoil. However, this process is difficult to achieve for nanobond soldering joints.

3.4.3 Electrical contact resistance measurement of HTS nanobond joint

This section evaluates the electrical contacts performance of the nanobond application in HTS joints basing on the electrical resistivity of the reacted nanofoil. Figure 3.27 illustrates the schematic drawing of a copper terminal to HTS Joint (2A-T) of sample 2 in the HTS nanobond joints test in LN2 at 77 K. One voltage tap (A) was placed on the current lead, and the second one (A′) was placed on the copper lead nearby the corner of the contact, and the third tap (T) was placed at the top of the 2G tape. The voltage (V_{AT}) across the 2G tape to copper joint including the copper (R_{Cu}), solder (R_{Sn}), nanofoil (R_{NF}), 2G-Tape ($R_{2G\text{-}Tape}$), and copper around the 2G tape (R_{Cu}') were measured. The resistance network measurement and equivalent circuit is shown in Figure 3.28, and Equations 3.4-3.6 for the calculation of the contact resistance of Joint (2A-T) are shown below:

$$R_{Contact} = A_{joint} \times ((V_{A'T} - V_{AA'})/I \qquad 3.4$$

$$R_{Contact} = A_{joint} \times \left(R_{Cu} + R_{Sn} + R_{NF} + R_{2G-Tape} + R_{Cu'} - R_{Cu}\right) \qquad 3.5$$

$$R_{contact} = A_{joint} \times R_{joint} \quad 3.6$$

Where $R_{contact}$ is the area contact resistance, and A_{joint} is the joint area, and I is the injected current, and R_{joint} is the area electrical resistance of Joint (2A-T'). Similarly, Joint (2T-T′) and Joint (2B′-T′) area contact resistances can be obtained in the same way. Figure 3.29 shows the plot of voltage-current (*VI*) characteristics of each measured voltage of sample 2 from 0 to 400 A, and the slope of each profile is the resistance in accordance of Ohm's law.

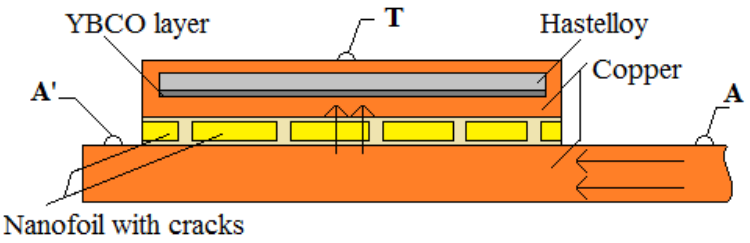

Figure 3.27: Schematic drawing of the cross section (between 2G HTS tape and copper) of Joint (2A-T) contact resistance measurement of sample 2, and arrows represent the direction of the current.

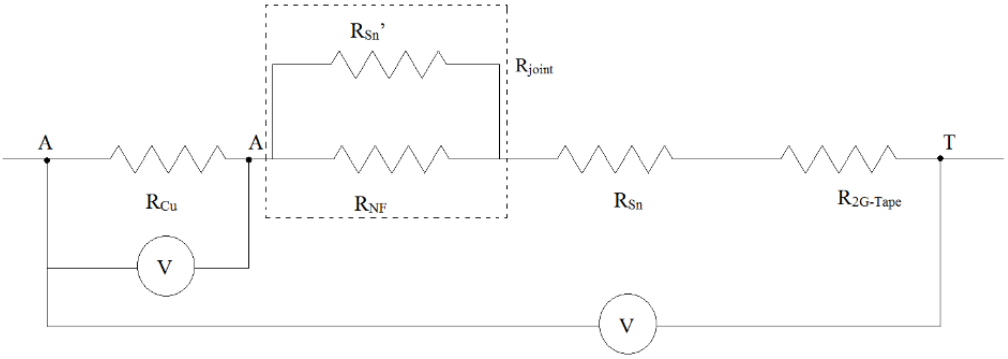

Figure 3.28: Schematic drawing of equivalent circuit for contact resistance network.

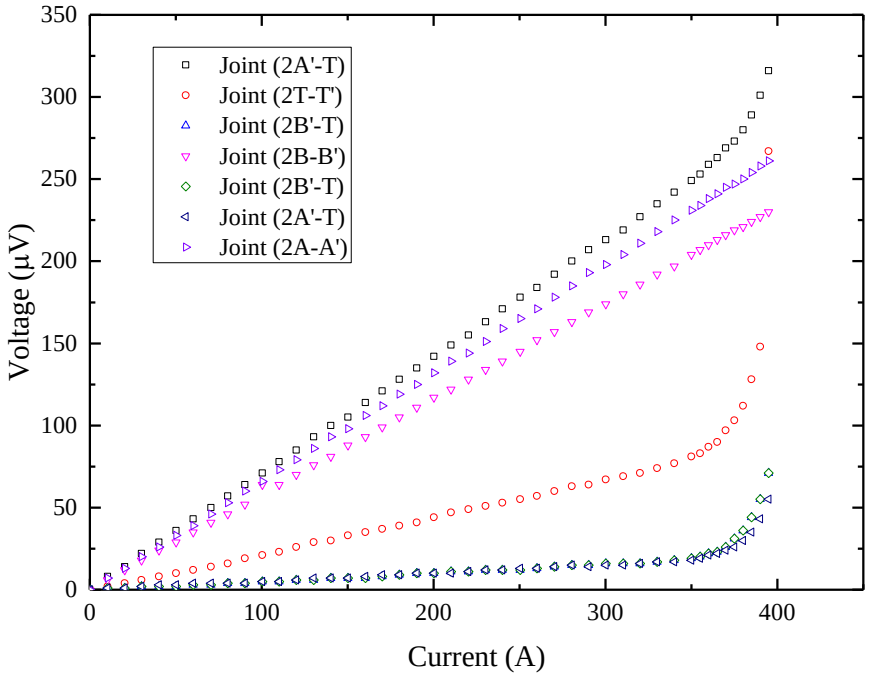

Figure 3.29: The Plot showing current-voltage for parameters measurements of sample 2.

The same resistance network was applied to other samples to produce the *VI* characteristics diagrams of each sample presented in Figure 3.30. Figure 3.30a shows the *VI* plot for the joint contact resistance between the copper terminal and 2G-tape for all of the samples measured at 77 K. Figure 3.30b shows the *VI* plots for the joint contact resistance between two 2G-tapes for all samples measured at 77 K. Joint (5B T-T′) was measured with a magnetic field applied to the top of Joint (5 T-T′). The application of the external field resulted in a reduction in the critical current by almost half compared with other measurements performed without an applied field.

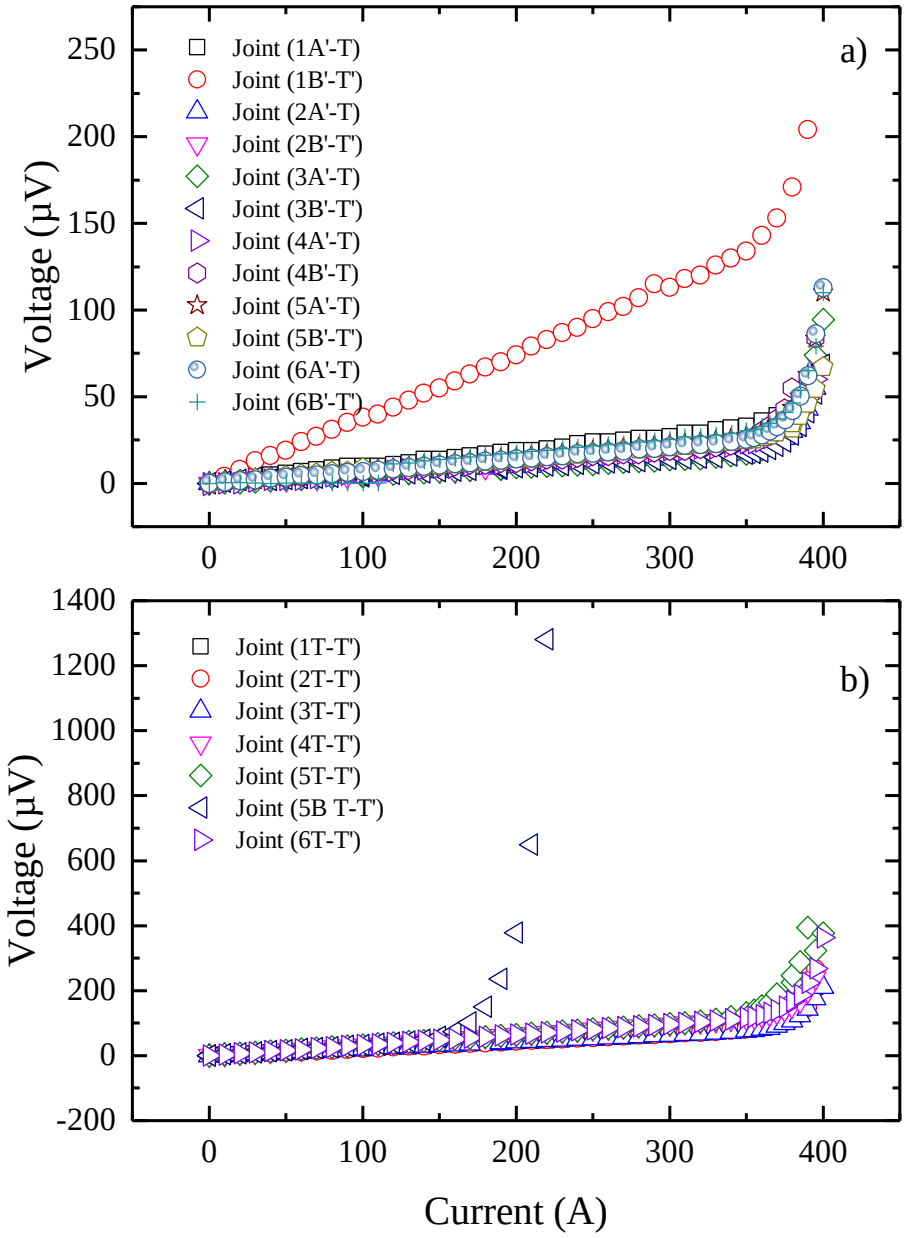

Figure 3.30: The plot for a) current-voltage for the joint contact resistance between terminal and 2G-tape for all samples and b) current-voltage for the joint contact resistance between two 2G-tape for all samples.

Table 3.14 shows the joint contact resistance of all the samples, and shows that the contact resistance of each joint is different from each other, and the resistance of 2G-tape to 2G-tape joints (Joint (T-T′)) for all the samples is found to be larger than that measured in the copper to 2G-tape joints (Joint (A′-T) and Joint (B′-T′)) except one joint in sample 1. All of the contact resistances

have been transferred into resistivity in order to compare with the resistivity of the reacted nanofoil later.

In order to investigate the morphology of the joint and to evaluate the contact soldering condition, a copper to 2G-tape joint of sample 5 was polished and the cross-section is shown in Figure 3.31, where the shiny elements in the images are assumed to be the solder filling in cracks of the reacted nanofoil. This has been confirmed by SEM investigations as shown in Figure 3.21. The model of contact resistance (R_{joint}) discussed previously can be simplified into a parallel network for Joint (2A′-T) between nanofoil resistance R_{NF} and solder resistance R_{Sn}'. In order to verify this assumption, it is necessary to calculate how much area of reacted nanofoil was filled with solder. The resistivity of the nanofoil and solder at 77 K needs to be known for this calculation. The resistivities of the reacted nanofoil measured by the PPMS were applied to this analysis.

Table 3.14: Contact resistance of each joint for all the samples.

Sample	Joint	Contact Resistance ($R_{contact}$/nΩcm²)	Joint resistance (R_{joint} /nΩ)	Joint Resistivity (ρ_{joint}/nΩ×m)
1	1A'-T	273.70	95.04	684.25
	1B'-T'	1082.46	375.85	2706.15
	1T-T'	311.83	216.55	779.57
2	2A'-T	155.46	53.98	388.66
	2B'-T'	146.80	50.97	367.01
	2T-T'	306.77	213.03	766.92
3	3A'-T	122.90	42.67	204.83
	3B'-T'	147.52	51.22	245.87
	3T-T'	300.42	208.63	500.70
4	4A'-T	176.85	61.41	294.75
	4B'-T'	191.62	66.54	319.37
	4T-T'	458.59	318.47	764.32
5	5A'-T	213.50	74.13	355.84
	5B'-T'	209.86	72.87	349.77
	5T-T'	466.46	323.93	777.43
	5B T-T'	470.25	326.56	783.75
6	6A'-T	197.70	68.65	329.50
	6B'-T'	252.95	87.83	421.59
	6T-T'	459.11	318.83	765.18

Because the resistivity (326-427 nΩ×m) of nanofoil is much larger than the sum of the following resistivities, solder (22.5 nΩ), copper (1.8 nΩ×m), and 2G-Tape at 77 K, these three values of R_{Sn}, R_{Cu} and $R_{2G\text{-}tape}$ can be neglected in the resistance network calculation [166]. According to the contact resistance network equivalent circuit (Joint 2A-T) from Figure 3.32 and using Equations 3.7-3.10; the derivation of the calculation for the area of the solder filling into the cracks of the nanofoil is as follows:

$$R_{joint} = \left(\frac{1}{R_{NF}} + \frac{1}{R_{Sn}'}\right)^{-1} \qquad 3.7$$

$$R_{Sn}{}' = \frac{1}{R_{joint}} + \frac{1}{R_{NF}} \quad 3.8$$

$$\rho_{Sn} \times L_{joint}/A_{Sn} = (1/(\rho_{NF} \times \frac{L_{joint}}{A_{joint}}) - 1/(\rho_{NF} \times \frac{L_{joint}}{A_{NF}}))^{-1} \quad 3.9$$

$$A_{Sn} = (1/(\rho_{joint} \times \frac{L_{joint}}{A_{joint}}) - 1/(\rho_{NF} \times \frac{L_{joint}}{A_{NF}})) \times \rho_{Sn} \times L_{joint} \quad 3.10$$

Where A_{Sn} is the area of the solder filling into the cracks of nanofoil, A_{joint} is the total area of the joint, A_{NF} is the area of nanofoil accounting for the joint, ρ_{Sn} is the resistivity of solder at 77 K, ρ_{joint} is the resistivity of the joint at 77 K, ρ_{NF} is the resistivity of nanofoil at 77 K, and L_{joint} is the thickness of the joint (almost 60μm). A_{NF} can be replaced by Equation 3.11:

$$A_{NF} = A_{joint} - A_{Sn} \quad 3.11$$

Then A_{Sn} can be achieved by Equation 3.12:

$$A_{Sn} = A_{joint} \times \frac{\frac{\rho_{Sn}}{\rho_{joint}} - \frac{\rho_{Sn}}{\rho_{NF}}}{1 - \frac{\rho_{Sn}}{\rho_{NF}}} \quad 3.12$$

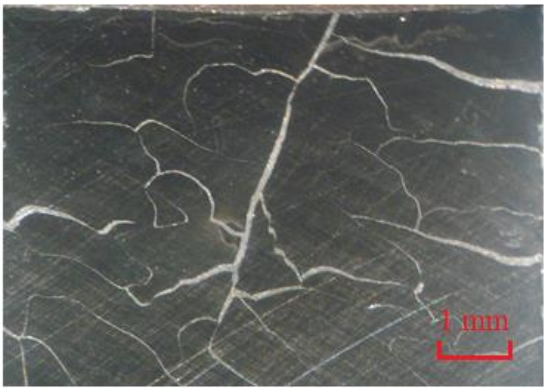

Figure 3.31: The photo showing the cracks at the surface of reacted nanofoil.

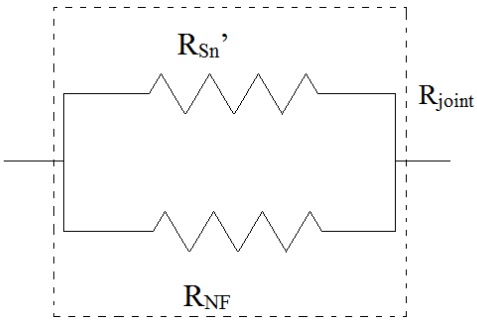

Figure 3.32: Schematic drawing of simplified equivalent circuit for contact resistance network.

Table 3.15 shows the parameters of each joint for the calculation of A_{Sn} based on the resistivity of 327 nΩ×m for the reacted nanofoil. Substituting these values into Equation 3.12, the area of solder filling in the nanofoil was calculated corresponding to the different reacted nanofoil resistivity values. In Table 3.15, only 4 of 12 copper to 2G-Tape joints confirmed the assumption; referring to a higher resistivity ρ_{NF}= 399 nΩ×m, 9 of 12 copper to 2G-Tape joints confirmed the assumption;

for the highest resistivity ρ_{NF} = 427 nΩ×m and 10 of 12 copper terminals to 2G-Tape joints confirmed the same assumption. No assumption was made for the joints between two 2G-tapes compared with copper to 2G-Tape joints. The resistance of all the joints between two 2G-Tapes were more than one third higher than that of the nanofoil. The resistance of the reacted nanofoil contributed to the main part the electrical contact resistance among these HTS nanobond joints.

Table 3.15: Parameters of each joint for calculating the area for tin filling into nanofoil cracks.

Sample	Joint	A_{joint} (cm^2)	ρ_{Sn} (nΩ×m)	ρ_{joint} (nΩ×m)	ρ_{NF} (nΩ×m)	Area of tin filling in the nanofoil (cm^2)
1	1A'-T	2.88	22.5	684.25	327	N/A
	1B'-T'	2.88	22.5	2706.15	327	N/A
	1T-T'	1.44	22.5	779.57	327	N/A
2	2A'-T	2.88	22.5	388.66	327	N/A
	2B'-T'	2.88	22.5	367.01	327	N/A
	2T-T'	1.44	22.5	766.92	327	N/A
3	3A'-T	2.88	22.5	204.83	327	0.127
	3B'-T'	2.88	22.5	245.87	327	0.070
	3T-T'	1.44	22.5	500.70	327	N/A
4	4A'-T	2.88	22.5	294.75	327	0.023
	4B'-T'	2.88	22.5	319.37	327	0.005
	4T-T'	1.44	22.5	764.32	327	N/A
5	5A'-T	2.88	22.5	355.84	327	N/A
	5B'-T'	2.88	22.5	349.77	327	N/A
	5T-T'	1.44	22.5	777.43	327	N/A
	5B T-T'	1.44	22.5	783.75	327	N/A
6	6A'-T	2.88	22.5	329.50	327	N/A
	6B'-T'	2.88	22.5	421.59	327	N/A
	6T-T'	1.44	22.5	765.18	327	N/A

3.4.4 Thermal resistance of nanobond and Al_2O_3 soldering joints

This section evaluates the thermal contact performance of the nanobond soldered joints between metallic and alumina components. Figure 3.33 shows the thermal resistance of a DBC Al_2O_3 to DBC Al_2O_3 nanobond joint, DBC Al_2O_3, copper shim to copper shim nanobond joint measured from 5 K to 300 K. All the samples show a drop in thermal resistance at a certain temperature. Two of the nanobond joint samples show a reduction in thermal resistance with increasing temperature when the base temperature is below 30 K. When the temperature is below 30 K, the thermal resistance of the copper shim to copper shim nanobond joint varies between 0.3 K/(W×cm^2) and 3 K/(W×cm^2), and the DBC Al_2O_3 to DBC Al_2O_3 nanobond joint varies between 0.5 K/(W×cm^2) and 1.4 K/(W×cm^2). The thermal resistance of the two nanobond joint samples crossover at 20 K, and the DBC Al_2O_3 to DBC Al_2O_3 nanobond joint starts to exhibit a higher value and increases faster between 30 K and 300 K. The thermal resistance of the DBC Al_2O_3 exhibits a decreasing trend until the temperature increases to 80 K, where the contact resistance varies from 0.13 K/(W×cm^2) to 16.2 K/(W×cm^2) between 5 K and 80 K. Thereafter, the thermal resistance of the DBC Al_2O_3 sample continues to increase to around 0.4 K/(W×cm^2), between 80 K and 300 K.

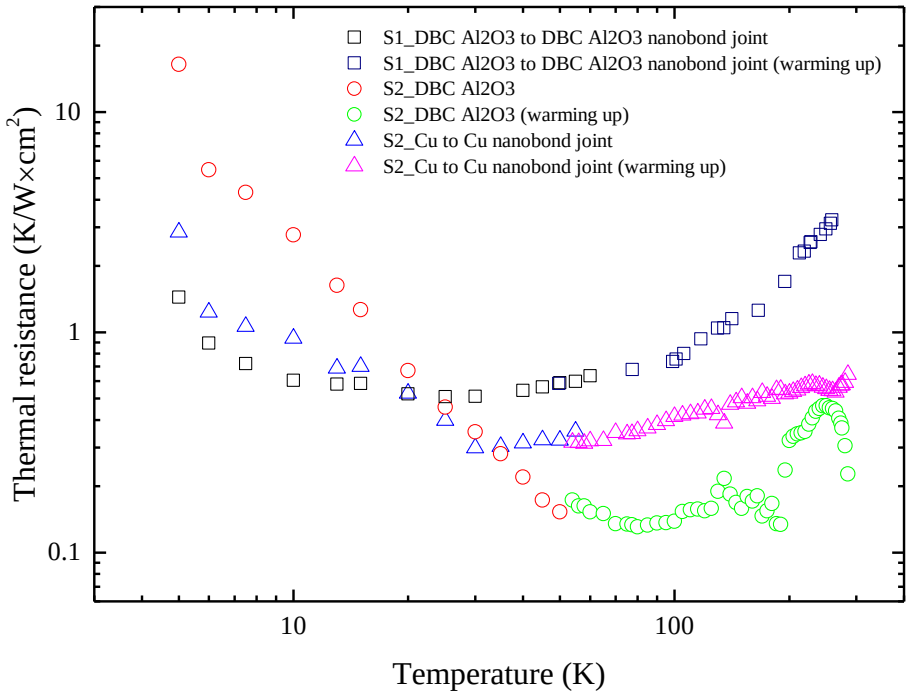

Figure 3.33: Thermal resistance of DBC Al2O3 to DBC Al2O3 nanobond joint, DBC Al2O3, copper shim to copper shim nanobond joint from 5 K to 300 K. (S1, S2 and S3: sample 1, sample 2 and sample 3).

Optical microscopy investigation was introduced to inspect the morphology of the cross-section of each soldering joint and Al_2O_3 sample. Figure 3.34 shows the image of the cross-section of the DBC Al_2O_3 to DBC Al_2O_3 nanobond joint. Figure 3.34a shows more details of the nanobond joint with the components highlight in a low brightness. The red circles in Figure 3.34a highlight the region where the solder fills the cracks of the reacted nanofoil. The solder film at the top and bottom of the reacted nanofoil is very thin, and there is evidence of a void space between the bottom solder film and bottom copper strip. Consequently, the nanofoil and the void space would contribute increasing the thermal resistance of the nanobond joint. A bright light was applied to show more details of the grain of the Al_2O_3 in Figure 3.34b. Fortunately, no cracks were observed within the Al_2O_3 phase in this nanobond joint sample.

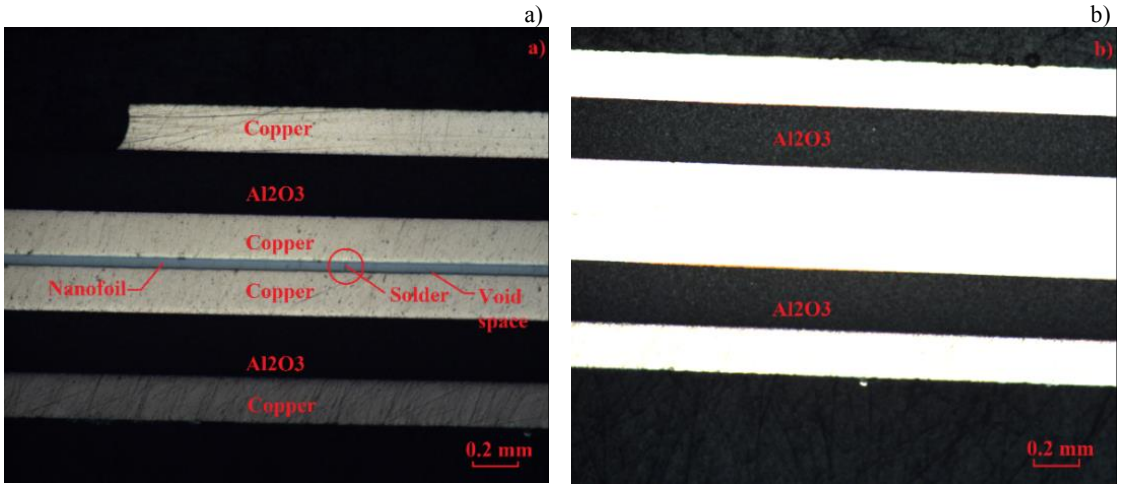

Figure 3.34: The microscopy image of the cross-section of Sample 1: DBC Al_2O_3 to DBC Al_2O_3 nanobond joint in a) low brightness and b) high brightness.

Figure 3.35 shows microscopy images of the cross-section of Sample 2. Figure 3.35a shows the copper shim to copper shim nanobond joint and Figure 3.35b shows the DBC Al_2O_3 to copper shim soldering (240 ºC solder) joint. When comparing the DBC Al_2O_3 to DBC Al_2O_3 nanobond joint, and the copper to nanobond joint samples they both show how the solder was filling into the cracks (shown by the red circles). Similarly, for the DBC Al2O3 to DBC AL2O3 nanobond joint sample, there are still void spaces within the copper to copper nanobond joint. Some solder was found to spill out during the nanobond reaction due to the high energy release, and this would tend to create new void spaces in the joint. The number of void spaces in the DBC Al_2O_3 to copper soldered joint was higher, and only a few points would be soldered together along the length of the two components.

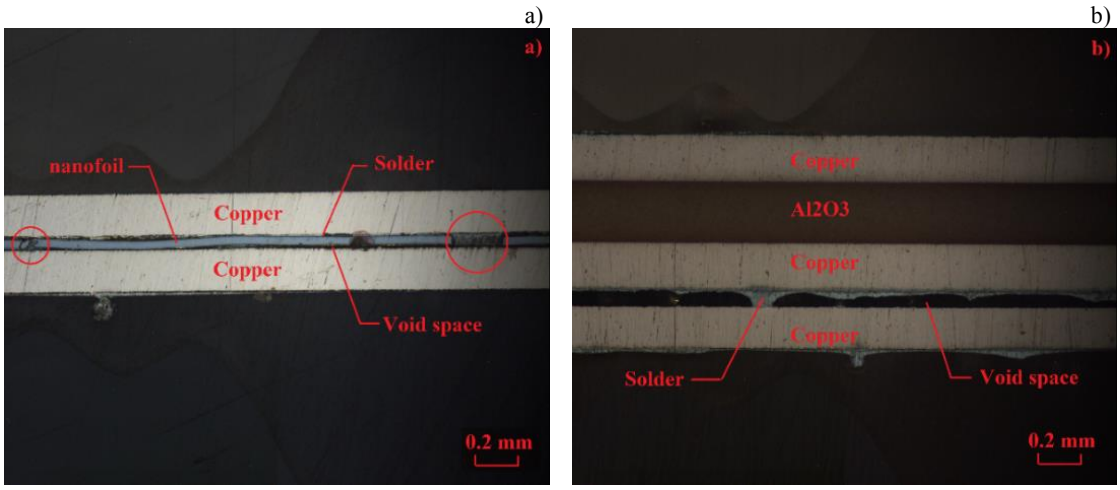

Figure 3.35: The microscopy image of the cross-section of Sample 2: a) Copper shim to copper shim nanobond joint and b) DBC Al_2O_3 to copper shim soldering (240 ºC melting solder) joint.

The optical investigations show how the components interconnect in the bonding region of the joint. In order to verify the effect of these components on the joints, the measured thermal resistance of two nanobond joint samples and DBC Al_2O_3 have been transferred into the thermal conductivity to compare with the reacted nanofoil film and dense Al_2O_3.

Figure 3.36 shows the calculated thermal conductivity of DBC Al_2O_3 to DBC Al_2O_3 nanobond joint and copper shim to copper shim nanobond joint. These are compared with the thermal conductivity of the reacted nanofoil measured in the PPMS, pure tin [183] and solder Sn60Pb40 (wt. %) between temperatures of 5 K to 300 K [184]. The thermal conductivity of all of the materials except for reacted nanofoil show a peak at cryogenics temperatures below 40 K. Tin and Sn60Pb40 (wt. %) peaks in thermal conductivity of tin and Sn60Pb40 (wt. %) are 2500 W/(K×m) at 4 K and 110 W/(K×m) at 12 K respectively. According to optical investigations shown in Figure 3.34a and Figure 3.35a the melting solder was shown to fill in the cracks in the nanofoil during the reaction and this would therefore improve the thermal conductivity of two nanobond joints samples. However, the thermal conductivities calculations established a lower thermal conduction compared with the reacted nanofoil, for the two nanobond joints. There was a larger difference in thermal conductivity evaluated at a higher temperature between two nanobond joints samples and the reacted nanofoil sample. Furthermore, there is no other material showing a similar peak of thermal conductivity at 30 K or variation compared with that of

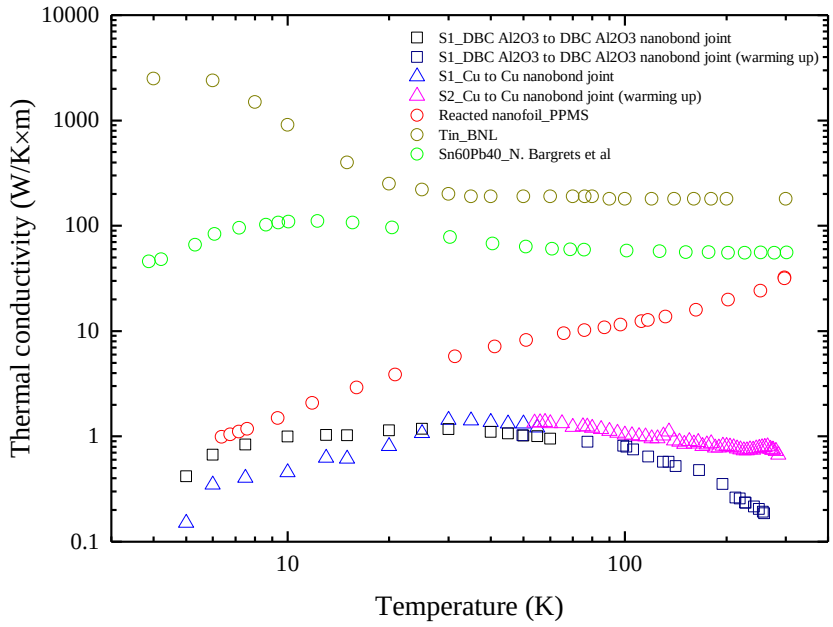

Figure 3.36: Calculated thermal conductivity of DBC Al_2O_3 to DBC Al_2O_3 nanobond joint and copper shim to copper shim nanobond joint compared with the thermal conductivity compared with the thermal conductivity of the reacted nanofoil measured with PPMS, pure tin (extrapolated values between 40 K and 300 K) [183] and Sn60Pb40 (wt. %) [184] from 5 K to 300 K. (S1, S2: sample 1, sample 2).

two nanobond joints in the same figure.

Figure 3.37 shows the calculated thermal conductivity of DBC Al_2O_3 compared with the thermal conductivity of the reacted nanofoil measured by PPMS, and copper (RRR = 10 and RRR = 100) [183] from 5 K to 300 K. All the materials show the peak thermal conductivity at cryogenics temperatures below 100 K, and the peak thermal conductivity of copper (RRR = 10) and dense Al_2O_3 are 635 W/(K×m) at 40 K and 74 W/(K×m) at 88 K respectively. The copper exhibits a better thermal conduction compared with dense Al_2O_3 at each temperature. Consequently, it was thought that the thermal resistance of Al_2O_3 would make the greatest contribution to the DBC Al_2O_3 sample. A similar trend is observed in the calculated thermal conductivity determined for the DBC Al_2O_3 sample, compared with the dense Al_2O_3 shown in Figure 3.37. The calculated thermal conductivity of DBC Al_2O_3 increases from 0.4 W/(K×m) to 18 W/(K×m) between 5 K and 85 K, and begins to decrease steadily from 85 K to 300 K. It needs to be noted that the calculated thermal conductivity of DBC Al_2O_3 only accounts for around 28% to 45% of the thermal conductivity of Al_2O_3 over the same range of temperatures. This is due to a poorly soldered joint formed between DBC Al_2O_3 and copper shim and is confirmed by the microscopic images as shown in Figure 3.35b. A possible reason for the poorly soldered joint could be caused by the gold present, which has a good dissolution in the tin-based alloy that could contribute restrict the wetting of the solder. However, as the nanobond reaction continues, the tin-based alloy may tend to deplete the gold, leaving a bare substrate for soldering. This process can lead to de-wetting and joint fracture of the soldering surface [185], [186]. The gold coating of the DBC Al_2O_3 sample is only 0.03 μm, so it is feasible for the gold coating to be completely dissolved by the 240 ºC solder during the pre-tinning process. Subsequently, this may result in the surfaces of

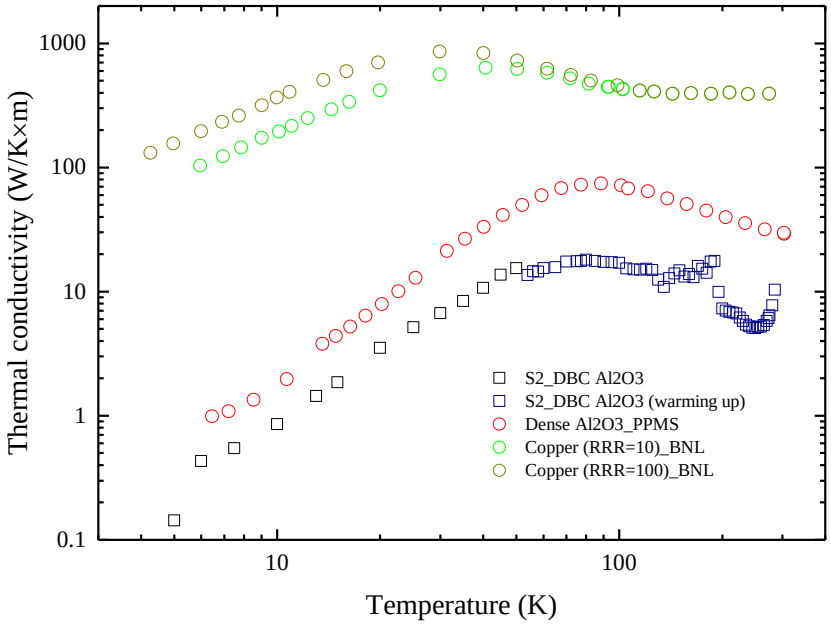

Figure 3.37: Calculated thermal conductivity of DBC Al_2O_3 compared with the thermal conductivity compared with the thermal conductivity of the reacted nanofoil measured with PPMS, and copper (RRR = 10 and RRR = 100) [183] from 5 K to 300 K (S1, S2: sample 1, sample 2).

copper shim becoming difficult to wet with the re-molten solder. Taking this issue into consideration, the soldering joint between the DBC Al_2O_3 and copper should be made in a single step.

3.4.5 Lap shear test on nanobond joint samples

Table 3.16 shows the lap shear strength results of eight OI metallic nanobond jointed samples. The nanobond joints of the stainless steel to stainless steel (stst to stst) samples 1-4 all failed during the measurements, and the shear strength of these samples varies from 11.1 to 16.4 MPa. This results is similar to the lap shear strengths measured by Zhu et al [60] (15 MPa) for copper to copper nanobond joints under same compressive load (5 bar). In comparison, the lap shear strength measured by Wang et al [59] was 40 MPa for stst to stst nanobond joints under 100 bar of compressive load. Unfortunately, these results did not report the effects of the ambient temperature on shear strength of nanobond joints.

Table 3.16: The shear strength of eight OI metallic nanobond joint samples (StSt: Stainless steel, Cu: copper).

Sample No.	**1**	**2**	**3**	**4**	**5**	**6**	**7**	**8**
Base	StSt to StSt	StSt to StSt	StSt to StSt	StSt to StSt	StSt to Cu	StSt to Cu	StSt to Cu	StSt to Cu
Joint failed strength (MPa)	16.44	12.62	11.07	12.46	N/A	N/A	N/A	N/A

Figure 3.38 (a-d) show the fractured surfaces of the samples after testing. The pictures show how the solder remain intact and covers most of the bonded area of each specimen. This demonstrated that each specimen was indeed well adhered and the preparation of the soldered adhesion between the substrates was effective. In comparison, the red circles in Figure 3.38 highlight some bare

regions on the plated stainless-steel specimens. Sample 3 in particular had the lowest coverage and also recorded the lowest shear strength. The stainless steel to copper nanobond joints (sample 5-8), presented in Figure 3.39 (a-d) show how the copper substrates yielded during the measurements. The copper failed in a similar location in each sample at the edge of joint and at the end of stainless steel. The copper (C101) has a yield strength of ~40 MPa [187], and therefore this implies that these samples were well adhered, but the thickness of the copper must be optimised in order to initiate failure of the joint.

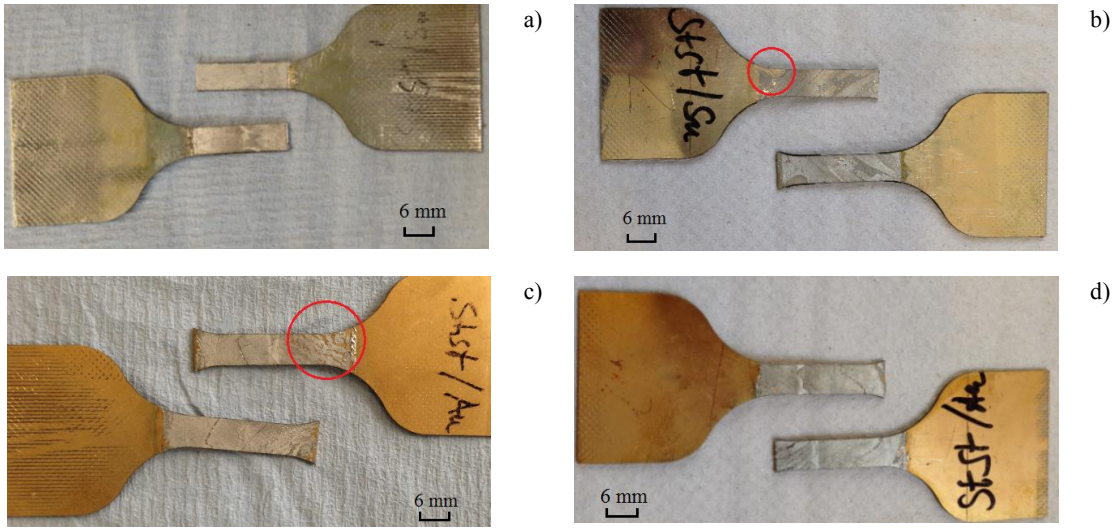

Figure 3.38: The pictures show the fracture surface of a) StSt-StSt hot plated with tin coated, b) StSt-StSt room temperature plated with tin coated, c) StSt-StSt hot plated with gold coated and d) StSt-StSt room temperature plated with gold coated.

Samples 9-11 were made with copper plated with 180 ºC solder (Sn60Pb40, wt. %), and samples 12-14 were made with copper plated with 240 ºC solder (Sn99.3Pb0.7, wt. %). Furthermore, samples 9, 10, 12 and 13 were fabricated at 60 ºC, and samples 11 and 14 were fabricated at room temperature. Table 3.17 shows the shear strength of six copper to copper nanobond joints. Obviously, the joints made at 60 ºC were stronger than those made at room temperature. The shear strength of the samples made at 60 ºC varied between 11.5 MPa and 16.3 MPa, which is similar to OI stainless steel to stainless steel nanobond joints. Furthermore, the shear strength of nanobond joint produced with 180 ºC solder were higher than those produced with 240 ºC solder. This result suggests the 180 ºC solder has better wetting properties than the 240 ºC solder when working with copper.

Figure 3.40 shows the fractured surfaces of the six copper to copper nanobond jointed samples. Figure 3.40 (a-c) shows those made with 180 ºC, and Figure 3.40 (e-f) shows the joints made with 240 ºC solder. Figure 3.40 (a and b, d and e) show examples of good adhesive bonding. In contrast, sample 11 in Figure 3.40c shows how a relatively large proportion (approximately a third) of the fractured surface was removed from the right-hand copper substrate, and remain attached to the left-hand substrate. The bare region implies the solder did not wet very well during the nanofoil reaction. Sample 14 also shows evidence of poor wetting as shown in Figure 3.40f.

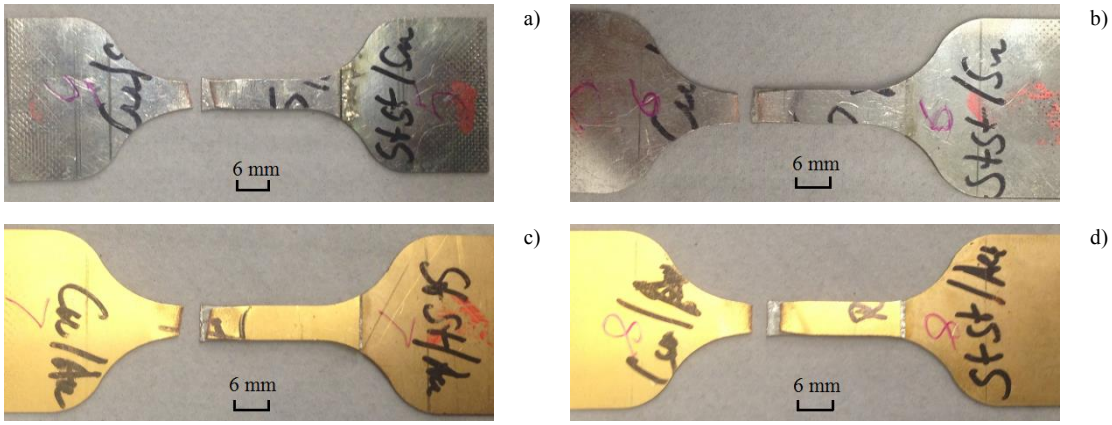

Figure 3.39: The pictures show the copper yield of a) StSt-Cu hot plated with tin coated, b) StSt-Cu room temperature plated with tin coated, c) StSt-Cu hot plated with gold coated and d) StSt-Cu room temperature plated with gold coated.

Table 3.17: The shear strength of 6 UoS metallic nanobond joint samples (Cu: copper).

Sample No.	**9**	**10**	**11**	**12**	**13**	**14**
Base	Cu to Cu	Cu to Cu	Cu to Cu	Cu to Cu	Cu to Cu	Cu to Cu
Joint failed strength (MPa)	16.27	15.20	4.97	12.79	11.48	3.50

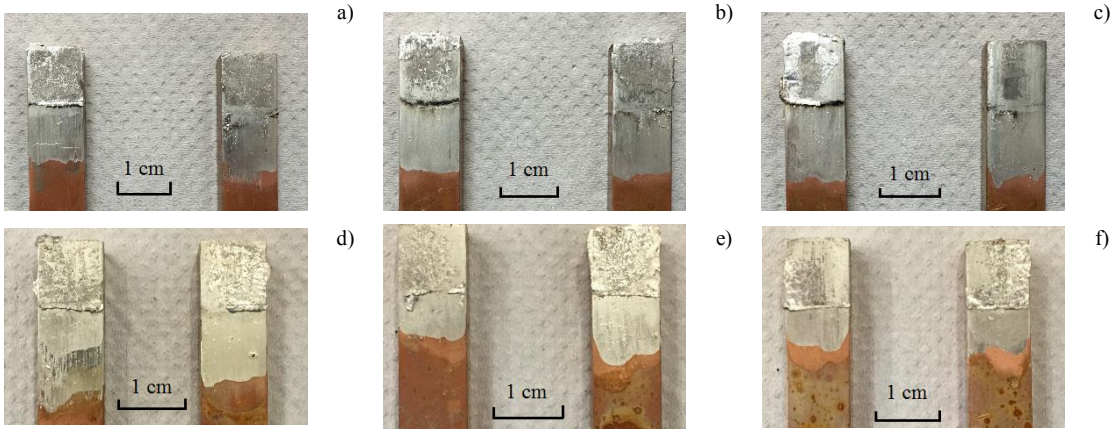

Figure 3.40: The pictures show the fracture surface of copper to copper nanobond joint with 180 ºC melting solder of a) Sample 9 made at 60 ºC, and b) Sample 10 made at 60 ºC, and c) Sample 11 made at room temperature, and copper to copper nanobond joint with 240 ºC melting solder of d) Sample 12 made at 60 ºC, and e) Sample 13 made at 60 ºC, and f) Sample 14 made at room temperature.

3.5 Conclusion

The fabrication of HTS soldering joints requires soldering work of a high standard to produce joints with low electrical contact resistance. However, the manufacturing process must ensure the surfaces remain in a clean condition and the temperature of soldering iron is well controlled. It is very difficult to produce this type of reproducible work over kilometer-lengths of HTS wires for industrial applications. Any degradation in a single spot in an HTS coil may cause further damage of the entire HTS component or system. A novel nanobond technology was applied for the first time to HTS tapes at Oxford Instruments (OI), and this has provided a new option to produce soldered joints between HTS tapes in-situ at room temperatures.

For HTS winding applications, the joint materials require low resistivity and high thermal conductivity. Consequently, physical properties involving resistivity, thermal conductivity and specific heat capacity of both reacted and unreacted nanofoil have been investigated by PPMS measurements. It is known that the main products reacted nanofoil is NiAl, and the related measured physical properties have been analysed and compared with literatures data, which the electrical contact resistance of nanobond made 2G-tape joints at 77 K, and thermal resistance of copper to copper nanobond joint and Al_2O_3 to Al_2O_3 nanobond joint at temperatures from 4 K to 70 K, and lap shear strength of metallic nanobond joints at room temperature have been performed in this work.

The resistivity of reacted nanofoil (NiAl) at room temperature varies from 390 to 730 nΩm in different thermal conduction conditions, which the measured results were four times larger than that of single crystal stoichiometric NiAl. SEM with EDX and XRD were applied to investigate the compositions and grain differences among reacted nanofoil samples. SEM images taken of the same samples showed the minor differences in fractural grain size among different samples. XRD pattern shows that NiAl are the main reaction products of all the samples. The possibility of the Ni_2Al_3 (intermediate reaction products) phase in the reacted nanofoil may contribute higher resistivity in our samples. Furthermore, the crack and void space were found in reacted nanofoil via optical microscopy investigation. The microscopy of a 2G-tape to copper nanobond joint and SEM investigation of the morphology of a copper to copper nanobond joint found that cracks in the reacted nanofoil were filled with sufficient solder, and is good news for thermal and electrical stability of nanobond joints. Consequently, a simple model for parallel electrical network between nanofoil and solder was applied to evaluate the contact resistance of twelve copper to 2G tape joints and six 2G tape to 2G tape joints, and we found that the reacted nanofoil (NiAl) made the main contribution to the overall contact resistance.

The thermal conductivity of reacted nanofoil was 34 W/K×m at room temperature, which the value is slightly higher than the data (25-30 W/K×m) provided by Indium Corporation, but it is smaller than the stoichiometric NiAl (~ 75 W/K×m) measured by Darolia et al and Walston et al. The Lorenz number of all the reacted samples varies between 5.1×10^{-8} WΩ/K^2 and 6.5×10^{-8} WΩ/K^2 at room temperature, which are larger than the constant 2.44×10^{-8} WΩ/K^2. The thermal resistance of one copper to copper nanobond joint and one Al_2O_3 to Al_2O_3 nanobond joint were performed from 4 K to 60 K. Further dynamic thermal resistance of these two samples were measured when the test rig was warming up to room temperature. The thermal resistance of both samples vary from 0.3 to 2 K/(W×cm^2) from 4 K to 30 K, and they increase slightly to above 0.4 K/(W×cm^2) at room temperature, but variation of thermal conductivities for these samples are different from reacted nanofoil samples. The optical morphology investigation shows the inter connection within the joints. The solder was found to fill the crack, which is considered to be helpful to improve the thermal transport. It is suggested that DBC Al2O3 to copper shim joint sample should be made in one attempt, to avoid gold dissolution, the thermal resistance of these new joints at different temperatures will be measured in the future works.

The specific heat capacity of the reacted nanofoil via silicone rubber to aluminium cooling and reacted nanofoil via silicone rubber to silicone rubber cooling at 300 K are 0.55 J/(g×K) and 0.51

J/(g×K) respectively. At low temperatures, the specific heat capacity was dominated by electronic vibration, and the electronic specific heat constant β of two reacted nanofoil is 0.00330 J/(mol×K^2) and 0.00305 J/(mol×K^2) respectively, are smaller than nickel, β_{Ni} = 0.00702 J/(mol×K^2) and bigger than aluminium, β_{Al}=0.00135 J/(mol×K^2), and there is no upturns observed below 4 K which is different from the results measured by Alexander et al [52].

Lap shear tests show the mechanical properties of the nanobond joints. Shear strength of four stainless steel to stainless steel dog bone lap joints were measured and produced an average shear strength of 11-16 MPa. The homogeneous fracture of the soldered surface of both joints, indicate good adhesion within the nanobond joint. However, the copper specimens of all the stainless steel to copper nanobond joints yielded. Six further copper to copper (6 mm thick) nanobond joints were fabricated with 240 ºC solder and 180 ºC solder respectively. For each type of solder, two sample were made at 60 ºC, and one made at room temperature. The shear strength of the four copper to copper nanobond joints made at 60 ºC were between 11 MPa to15 MPa, and all samples made at room temperature exhibited poor shear strength. In order to further prove the application of nanobond joints, these shear strength values must be compared directly to joints made by conventional and manual soldering techniques. A batch of lapped joint samples could be produced with 180 ºC and 240 ºC solders and the same mechanical test repeated. Furthermore, the lap shear strength testing of metallic nanobond joint samples could be performed at cryogenics temperatures to validate the shear performance for HTS applications.

Chapter 4
Current transfer characteristics of 2G HTS joints

4.1 Introduction

The normal 4-contact method for the electrical resistance measurements of a HTS soldering joints is used to measure the overall contact resistance, which involves the solder resistance, the barrier resistance between the superconductor and stabliser and the metal matrix resistance. Some literature shows that the barrier resistance between the superconductor and metal matrix resistance are negligible compared with the interficial contact resistance between the superconductor and stabliser [7]. Larger lengths of the joint may be a solution to reduce the contact resistance by extending contact area. However, longer conductors would also contribute the overall contact resistance and leads to more heat dissipation into the coil through conduction. Consequently, the understanding of current transfer characteristics become important for the lap joint design. A 1D analytical model is constructed to analyse the contact resistance and estimate current distribution of a lap soldering joint between two simple conductors.

The performance of the nanobond 2G-tape joints have been dicussed in the previous chapter, which implies the reacted nanofoil (NiAl) as the main electrical resistance within the contacts. The annealing process is an effective way to reduce the resistivity of NiAl, but this is not suitable for 2G-tape joints with low temperature solder. We are looking for a soldering method that can make use of the advantages of the simple manufacturing and fast energy dissipation of nanobond reaction process. Then a new methodology, nano-heater, was developed for the first time. The overall contact resistance of nano-heater made HTS joint samples was measured in LN2 at 77 K. Later a needle sliding contact method was developed to evaluate the current distribution and contact resistance of several 2G-tape soldered to copper in LN2 at 77 K combined with a 1D lap joint analytical model.

4.2 Research aims and objectives

In order to analyse the real contact resistance and investigate the current transfer characteritics within a 2G-tape soldering joint, an analytical model with a formula for lap joint between two

conductors was developed. Due to the high resistivity of the reacted nanofoil within the nanobond 2G-tape soldering joints, a new method called nano-heater for HTS soldering joint manufacturing will be introduced in this chapter. A Superpower 2G-tape sample was soldered with two copper shims by nano-heater method, and the overall contact resistance of these two joints was measured in a variable temperature rig. Another 2G-tape to 2G-tape (Superpower) soldering joint was made using the same method, and joint electrical contact resistance was measured in LN2 at 77 K. In order to capture the real current distribution within the conductor that was overlapped with the joint, a sliding needle contact method was developed, which can trace the voltage continuously along the conductor overlapped joint. By combining the experimental results with analytical lap joint model, an indication for a Robel cable current injection soldering contact resistance was presented.

- To construct an analytical model to analyse the current transfer characteristics within a soldering contact between two composite conductors and give the analytical formula.
- To conduct the first trials of nano-heater bonding for 2G-tape joints.
- To investigate overall electrical contact resistance of nano-heater made 2G-tape joints.
- To investigate current transfer characteristics of 2G tape to copper lap joints by sliding contact method in LN2 at 77 K compared with the analytical lap joint model.

4.3 Methods and Experimental details

4.3.1 1D lap joint current transferring Model between two simple conductors

4.3.1.1. Analytical model

A One-Dimensional (1D) model of a lap joint between two conductors is developed. The model and parameters are shown in Figure 4.1. The resistivity of two conductors are ρ_1 and ρ_2 with a joint material resistivity ρ_c. The resistivity of the conductors are ρ_1 and ρ_2 with a joint material resistivity ρ_c. The thicknesses of the two conductors and the contact are d_1, d_2 and d_c respectviely with overlap length L and uniform width w. Then the resistance per unit length r_1 and r_2 of conductor 1 and conductor 2 are shown in Equation 4.1 and Equation 4.2, and contact resistance (r_c) is shown in Equation 4.3.

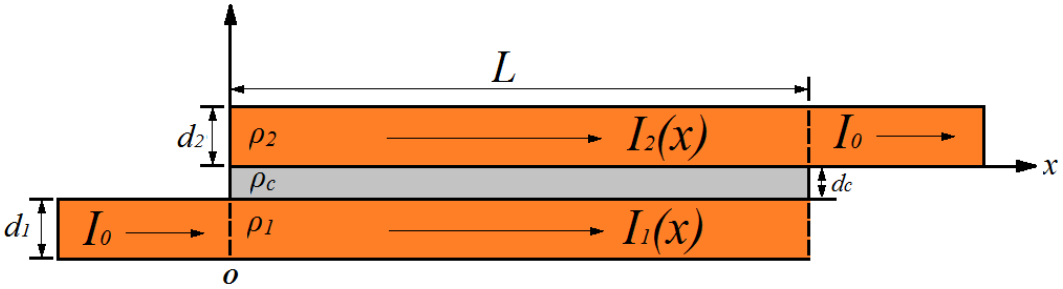

Figure 4.1: 1 D model of a lap joint and parameters.

$$r_1 = \rho_1 (d_1 w)^{-1} \quad 4.1$$

And

$$r_2 = \rho_2 (d_2 w)^{-1} \quad 4.2$$

And

$$r_c = \rho_c (d_c w)^{-1} \quad 4.3$$

In this 1-D model, a constant DC current I_0 is fed into the left end of conductor 1 and left from the right end of conductor 2. $I_1(x)$ and $I_2(x)$ are the currents as the function of contiuous position x along the conductor 1 and conductor 2 within the joint section. The joint (left end) is assumed as 0. According to Ohm's law, we have the two derivative voltage function $V_1(x)$ and $V_2(x)$ as a function of position x for conductor 1 and conductor 2 as shown below:

$$-\frac{dV_1(x)}{dx} = r_1 I_1(x) \quad 4.4$$

And

$$-\frac{dV_2(x)}{dx} = r_2 I_2(x) \quad 4.5$$

Referring to the contact we have:

$$V_1(x) - V_2(x) = -r_c \frac{dI_1(x)}{dx} = r_c \frac{dI_2(x)}{dx} = r_c j_c(x) \quad 4.6$$

Where $j_c(x)$ is the current transfer rate as a function of the position x. The total current I_0 is shown below:

$$I_0 = I_1(x) + I_2(x) \quad 4.7$$

Then we define the transfer length between the contact and the two conductors [188], [189]:

$$L_t = \sqrt{\frac{r_c}{r_1 + r_2}} \quad 4.8$$

To combine Equations 4.4-4.8, we have the differential equation:

$$\frac{d^2 I_1(x)}{dx^2} - \frac{1}{L_t^2} I_1(x) = \frac{I_0 r_2}{L_t^2 (r_1 + r_2)} \quad 4.9$$

Boundary conditions at $x = 0$ and $x = L$ are:

$$I_1(0) = I_2(L) = I_0 \quad 4.10$$

And

$$I_1(L) = I_2(0) = 0 \quad 4.11$$

In a similar 1-D lap joint electrical contact model derived by Stenvall et al, they treat the boundary conditions as the current ratio between the metal matrix and superconductor at an infinite distance as inversely proportional to the resistivities per unit length of the corresponding components [146]. But in our case, the current was transferred from conductor 1 to conductor 2 through a lap joint within a finite length, and all the currents will pass through the contact at the end of the joint, thus the current flowing in conductor 1 was I_0 at $x = 0$ and decrease to 0 at $x = L$. Taking boundary conditions into Equation 4.9, the general solution for $I_1(x)$ for conductor 1 is shown below:

$$I_1(x) = \frac{I_0}{r_1 + r_2} \frac{r_2\left(\sinh\left(\frac{L}{L_t}\right) - \sinh\left(\frac{x}{L_t}\right)\right) + r_1 \sinh(\frac{L-x}{L_t})}{\sinh(\frac{L}{L_t})} \quad 4.12$$

And current versus x in conductor 2 is shown below:

$$I_2(x) = I_0 - \frac{I_0}{r_1 + r_2} \frac{r_2\left(\sinh\left(\frac{L}{L_t}\right) - \sinh\left(\frac{x}{L_t}\right)\right) + r_1 \sinh(\frac{L-x}{L_t})}{\sinh(\frac{L}{L_t})} \quad 4.13$$

Then $j_c(x)$ can be achieved as:

$$j_c(x) = -\frac{dI_1(x)}{dx} = \frac{I_0}{L_t(r_1 + r_2)} \frac{r_2 \cosh\left(\frac{x}{L_t}\right) + r_1 \cosh(\frac{L-x}{L_t})}{\sinh(\frac{L}{L_t})} \quad 4.14$$

And for conductor 1,

$$V_1(0) - V_1(x) = \int_0^x r_1 I_1(x) dx$$
$$= \frac{I_0 r_1}{r_1 + r_2} \frac{x r_2 \sinh\left(\frac{L}{L_t}\right) - r_2 L_t\left(\cosh\left(\frac{x}{L_t}\right) - 1\right) - r_1 L_t(\cosh\left(\frac{L-x}{L_t}\right) - \cosh(\frac{L}{L_t}))}{\sinh(\frac{L}{L_t})} \quad 4.15$$

The overall joint resistance R_J ($x = L$) can be evaluated by:

$$R_J = \frac{V_1(0) - V_2(L)}{I_0} = \frac{V_1(0) - V_1(L) + V_1(L) - V_2(L)}{I_0} = \frac{V_1(0) - V_1(L)}{I_0} + \frac{j_c(L) r_c}{I_0}$$
$$= \frac{r_1}{r_1 + r_2} \frac{L r_2 \sinh\left(\frac{L}{L_t}\right) - (r_2 - r_1) L_t\left(\cosh\left(\frac{L}{L_t}\right) - 1\right)}{\sinh(\frac{L}{L_t})} + \frac{r_c}{L_t(r_1 + r_2)} \frac{r_2 \cosh\left(\frac{x}{L_t}\right) + r_1}{\sinh(\frac{L}{L_t})} \quad 4.16$$

Then Equation 4.16 can be simplified:

$$R_J = \frac{1}{r_1 + r_2}(r_1 r_2 L - \frac{L_t}{\sinh\left(\frac{L}{L_t}\right)}(r_1(r_2 - r_1)\left(\cosh\left(\frac{L}{L_t}\right) - 1\right) - \frac{r_c}{L_t^2}(r_2 \cosh\left(\frac{x}{L_t}\right) + r_1))) \quad 4.17$$

Which has limits of:

$$R_J = \begin{cases} \dfrac{r_c}{L_t \sinh(\frac{L}{L_t})} & L \to 0 \\ \dfrac{r_1 r_2}{r_1 + r_2} L & L \to \infty \end{cases} \quad 4.18$$

The equation above reflects that the overall contact resistance is dominated by the contact resistance of the short joints and the parallel resistance of the conductors for the long joints respectively. It is known that $r_c = L_t^2 (r_1 + r_2)$, then Equation 4.17 can be simplified as:

$$R_J = \frac{r_1 r_2 L}{r_1 + r_2}(1 + \frac{L_t}{L sinh\left(\frac{L}{L_t}\right)}(\frac{r_1^2 + r_2^2}{r_1 r_2} cosh\left(\frac{L}{L_t}\right) + 2)) \quad 4.19$$

The minimum between two extremes can be achieved with $dR_J/dL = 0$.

$$\frac{dR_J}{dL} = \frac{r_1 r_2}{(r_1+r_2)}\left(1 - \frac{2\cosh\left(\frac{L}{L_t}\right) + \frac{r_1^2 + r_2^2}{r_1 r_2}}{sinh^2\left(\frac{L}{L_t}\right)}\right) \quad 4.20$$

The minimum between two extremes can be achieved when:

$$\frac{r_1 r_2}{(r_1+r_2)}\left(1 - \frac{2\cosh\left(\frac{L}{L_t}\right) + \frac{r_1^2 + r_2^2}{r_1 r_2}}{sinh^2\left(\frac{L}{L_t}\right)}\right) = 0 \quad 4.21$$

$$sinh^2\left(\frac{L}{L_t}\right) = 2\cosh\left(\frac{L}{L_t}\right) + \frac{r_1^2 + r_2^2}{r_1 r_2} = cosh^2\left(\frac{L}{L_t}\right) - 1 \quad 4.22$$

$$\left(\cosh\left(\frac{L}{L_t}\right) - 1\right)^2 = 2 + \frac{r_1^2 + r_2^2}{r_1 r_2} = \frac{(r_1+r_2)^2}{r_1 r_2} \quad 4.23$$

$$\cosh\left(\frac{L}{L_t}\right) = 1 + \frac{r_1+r_2}{\sqrt{r_1 r_2}} \quad 4.24$$

Here $1 + (r_1 + r_2)/\sqrt{r_1 r_2} > 1$, then according to the inverse hyperbolic function, Equation 4.24 can be rewritten as:

$$L_{opt} = L_t \ln\left(1 + \frac{r_1+r_2}{\sqrt{r_1 r_2}} + \sqrt{\left(1 + \frac{r_1+r_2}{\sqrt{r_1 r_2}}\right)^2 - 1}\right) \quad 4.25$$

Where L_{opt} is the optimized length of the joint. Then the minimum joint resistance $R_{J,min}$ is:

$$R_{J,min} = \frac{r_1 r_2 L_t}{(r_1+r_2)}\left(\ln\left(1 + \frac{r_1+r_2}{\sqrt{r_1 r_2}} + \sqrt{\left(1 + \frac{r_1+r_2}{\sqrt{r_1 r_2}}\right)^2 - 1}\right) + \frac{1}{\sqrt{\left(1 + \frac{r_1+r_2}{\sqrt{r_1 r_2}}\right)^2 - 1}}\left(\frac{r_1^2 + r_2^2}{r_1 r_2}\left(1 + \frac{r_1+r_2}{\sqrt{r_1 r_2}}\right) + 2\right)\right) \quad 4.26$$

Assuming:

$$z = \frac{r_1+r_2}{\sqrt{r_1 r_2}} = \frac{1}{\sqrt{r}} + \sqrt{r} \geq 2 \quad 4.27$$

Where r is r_1/r_2, and $L_t = \sqrt{r_c/(r_1 + r_2)}$, then $R_{J,min}$ can be rewritten as:

$$R_{J,min} = \sqrt{\frac{r_c\sqrt{r_1 r_2}}{z^3}}\left(ln\left(1 + z + \sqrt{(1+z)^2 - 1}\right) + (z-1)\sqrt{z(z+2)}\right) \quad 4.28$$

And L_{opt} can be rewritten as:

$$L_{opt} = L_t\left(1 + z + \sqrt{(1+z)^2 - 1}\right) \quad 4.29$$

Here assuming $r_1 = r_2$, we have the minimum joint resistance $R_{J,min} = \sqrt{r_1 r_c}\left(\ln\left(3 + 2\sqrt{2}\right) + 2\sqrt{2}\right)/2\sqrt{2}$, around $1.623\sqrt{r_1 r_c}$, and optimized joint length $L_{opt} = L_t \ln\left(3 + 2\sqrt{2}\right)$, around $1.763L_t$.

4.3.1.2. Example runs

In order to evaluate the effect of r_1, r_2 and r_c on the current distribution within two conductors, a 10 mm long lap joint was investigated by the analytical model with assumed conductor resistance, contact resistance, joint dimensions and other parameters as shown in Table 4.1 and Table 4.2. In all computations, a transport current of 40 A was assumed to pass through this lap joint from conductor 1 to conductor 2.

Table 4.1: Dimensions of the two conductors and the contact.

Tape width, w	5 mm
Tape thickness, d_1=d_2	100 μm
Solder thickness, d_c	30 μm
Contact length, L	10 mm

Table 4.2: The resistivity variation of two conductors and the assumed resistivity of the contact.

No.	ρ_1 (Ωm)	r_1 (Ω/m)	ρ_2 (Ωm)	r_2 (Ωm)	ρ_c (Ωm)	r_c (μΩcm)
Case 1	1.8e-9	0.0036	0	0	25e-8	0.15
Case 2	1.8e-9	0.0036	1.8e-9	0.0036	25e-8	0.15
Case 3	0	0	1.8e-9	0.0036	25e-8	0.15
Case 4	1.8e-9	0.0036	1.8e-9	0.0036	50e-8	0.3
Case 5	1.8e-9	0.0036	1.8e-9	0.0036	100e-8	0.6
Case 6	0.4e-9	0.0008	1.8e-9	0.0036	100e-8	0.6
Case 7	0.9e-9	0.0018	1.8e-9	0.0036	100e-8	0.6

Figure 4.2 shows the current profiles and electrical field of conductor 1 (I_1 and E_1) and conductor 2 (I_2 and E_2) for different cases. According to Equation 4.4 and 4.5, the electrical field E ($dV(x)/dx$) along the joint is proportional to the local current density at each position of the joint, thus the trend variation of both electrical field E and local current I for two conductors are the same in each case.

For case 1, conductor 1 was assumed as copper (ρ_1 = 1.8e-9 Ω m) and conductor 2 was assumed as a superconductor (ρ_2 = 0), with a current profile that exhibits that all the current has been transferred from conductor 1 to conductor 2 within the left half joint. The material of the two conductors in case 3 has been revised from case 1, where the current profile implies a mirror-image relationship with case 1.

For case 2, 4 and 5, two conductors have been assumed as the same material (copper) with different resistivities (25e-8 Ωm, 50e-8 Ω m and 100e-8 Ωm) for the contact. The current starts to reduce by half within the first half length of conductor 1, and on the other half continuously to reduces to zero until the right end of the joint, and the amount of current increasing in conductor 2 is same to the amount that reduces in conductor 1 at each position of the joint. Furthermore, a higher contact resistance was taken into account, and this joint exhibits a slower current transferring rate with a longer current transfer length. The trend variation of the electrical field at each position of the joint for each conductor is proportional to the changes of the local current, and the electrical field peak of each conductor is only related to the resistivity of the conductor.

For case 5, 6 and 7, the material of conductor 2 was assumed as copper, and the resistivity of conductor 1 was assumed as 1.8e-9 Ωm, 0.4e-9 Ωm and 0.9e-9 Ωm respectively, and the contact resistance was assumed as the same for these three cases. For conductor 1, with a lower resistivity among the three cases, the current reduces more slowly in the left half path within this conductor, and the rest of the current reduces faster in the right half of this conductor. This implies that current prefers to flow within the conductor with the lower resistivity before the end of the joint when the contact resistance of these joints are the same.

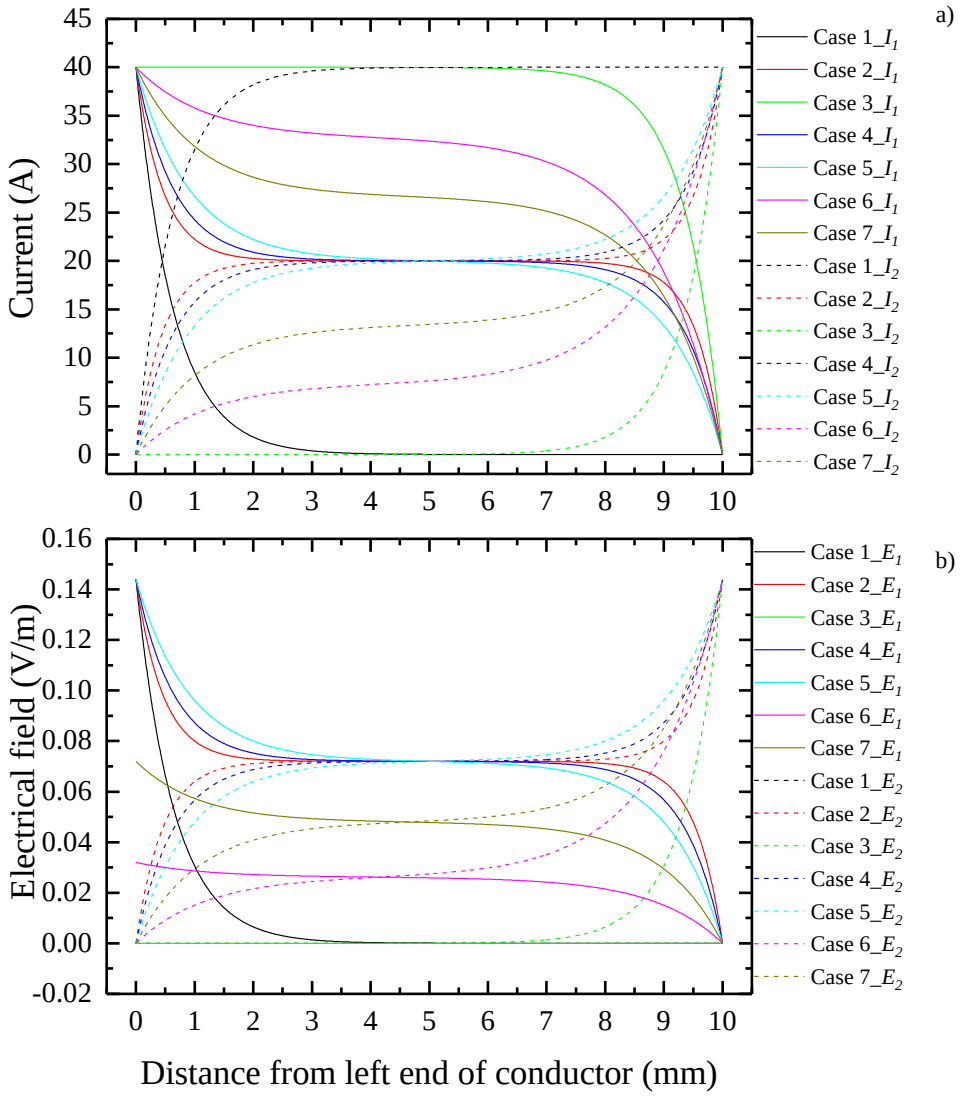

Figure 4.2: The plot of a) current distribution and b) electrical field distribution within both conductor 1 (I_1 and E_1) and conductor 2 (I_2 and E_2) corresponding to the resistivity variation of two conductors and contact as shown in Table 4.2.

The joint length would become the only parameter that has an effect on the overall contact resistance in accordance with Equation 4.18 for the minimum overall contact resistance. This happens when the ratio between the two conductors and contact resistance are certain values for the lap joint. Figure 4.3 shows the resistance ratio (R_J/R_{Jmin}) versus the length ratio (L/L_{opt}) with different conductor resistance ratio (r_1/r_2). When the joint length is smaller than the optimal joint length. The overall joint resistance decreases fast for all conductor resistance ratios, and it

decrease faster with a smaller conductor resistance ratios, when the joint length is closed to L_{opt}. However, it seems that a more slowly increase from the minimum overall joint resistance happens when the joint is longer than L_{opt} for large resistance ratio between two conductors.

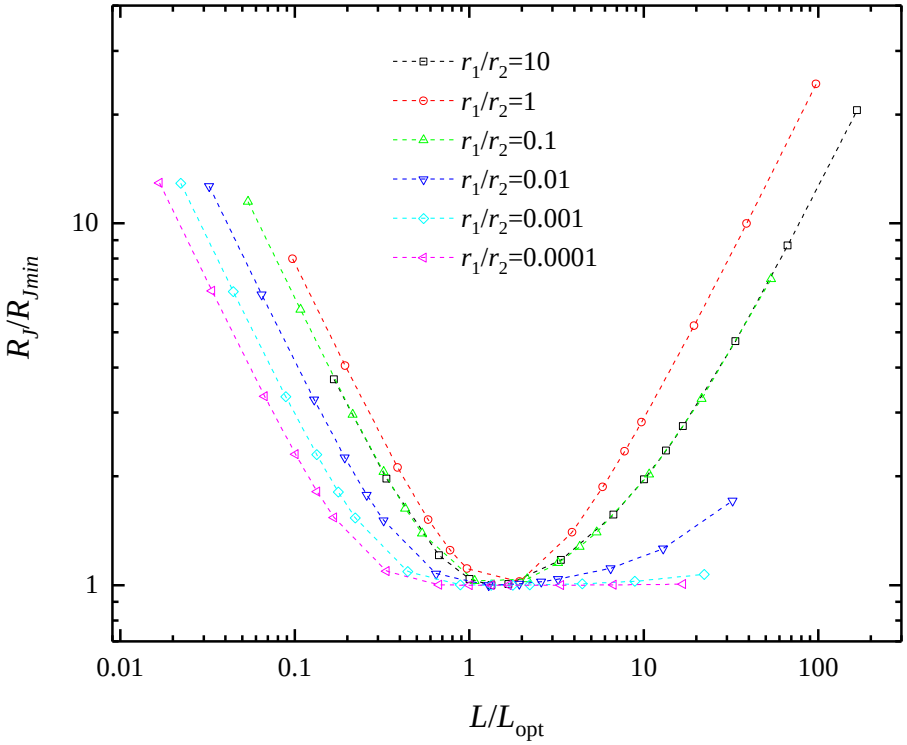

Figure 4.3: The plot for the resistance ratio (R_J/R_{Jmin}) as versus the length ratio (L/L_{opt}) with different conductor resistance ratio (r_1/r_2).

4.3.2 Methodology of Nano-heater made 2G-tapes soldering joints

In order to make use of the advantages of the simple manufacturing process and fast energy dissipation of the nanobond reaction process without nanofoil existing in the 2G-tape joints, a nano-heater method was developed for 2G-tape joints soldering. The schematic drawing of this method installment is shown in Figure 4.4. The bottom G10 block was the base for the bonding process, and four 50 mm long M5 bolts were used for the sliding tracks for the top G10 block that can provide the loading pressure. The loading pressure was adjusted by compressing 4 springs (4.74 N/mm each). Two rubber films were attached to the G10 blocks as the compliant layers to spread loading force during the reaction. The nanofoil was placed at the bottom of the joint components as the heat source. The reaction was ignited by a 9 V voltage pulse. The process of the nano-heater method is presented below:

1. Solder preparation*:
   a. Rolling the non-flux solder into a long film with a thickness around 30-35 μm.
   b. Pressing load (200 bar) is applied to compress the solder film between two smoothed surface strainless steel blocks, which an even thickness of the solder film can be achieved in this process.
   c. Acetone is applied to clean the surface, and solder film is cut into the pieces according to the dimensions of the contact area.

2. Joint component preparation:
   a. Acetone is applied to clean the joint bonding components (2G tapes or copper shims**) to the surface. In order to achieve good adhesion between the solder and copper or 2G tape, emery paper (1200 Grit) was used to make the metal surface rough before the Acetone cleaning process.
   b. Acid flux is applied to move the oxdiation layer of the bonding components surface, then a tissue is used to wipe over the surface.
   c. Stacking of the joint components, solder film and nanofoil, as shown in Figure 4.4. According to OI nanobond manual as shown in Table 3.4, a loading pressure of 3 bar is suggessted for the 2G to 2G joint and 5 bar for the copper to 2G joint.
3. A nine-voltage pulse is applied to ignite the nanofoil to bond the joint. Scapel and Acetone are applied to move the reacted nanofoil pieces.

Note:* A higher temperature solder, such as 240 °C melting solder (Sn99.3Cu0.3, wt. %) or 296 °C melting solder (Sn5Pb93.5Ag1.5, wt. %) is suggested for the copper to 2G tape joint, then a lower temperature melting solder can be applied to solder between the copper shim and the current lead.

**100 µm thick copper shim is suggested.

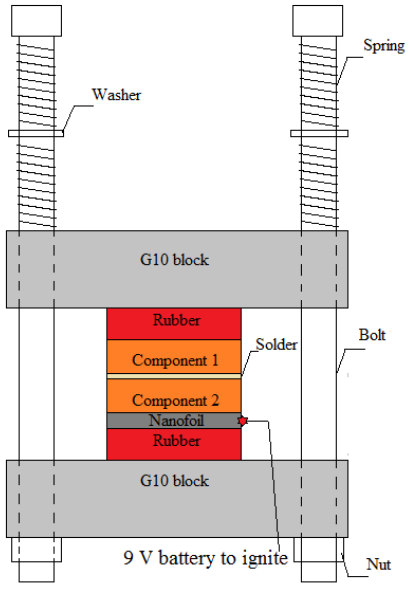

Figure 4.4: The schematic drawing of nano-heater joint manufacturing installment.

4.3.3 Overall electrical contact resistance measurements of on trials of nano-heater made 2G tape joints

The contact resistance of two nano-heater made copper to 2G tape joints and a nano-heater made 2G tape to 2G tape joint have been performed in LN2 at 77 K.

4.3.3.1. The electrical contact resistance of two 2G-tape to copper joints

Two ends of a Superpower 2G-tape were soldered with two 100 µm thick copper shims with

296 °C melting solder (Sn5Pb93.5Ag1.5, wt. %) by nano-heater method. The schematic drawing of this sample is shown in Figure 4.5. The cross-section of both two 2G-tape to copper joints, joint 1 and joint 2, are 1.6 cm^2 (4 cm×0.4 cm). Voltage taps 1 and 2 were soldered on the copper shim and 2G-tape respectively to measure the contact voltage across joint 1. The voltage tap 3 and 4 soldered on the 2G tape and copper shim were placed to measure the contact voltage across joint 2. Two voltage tap pairs were twisted together to compensate the induction voltage. This sample was mounted in a variable temperature rig. The contact resistance was measured at 15 K, 25 K, 35 K, 40 K and 77 K separately by 4-contact method. The voltages were meaured and recorded through a NI SCXI-1000 data logger.

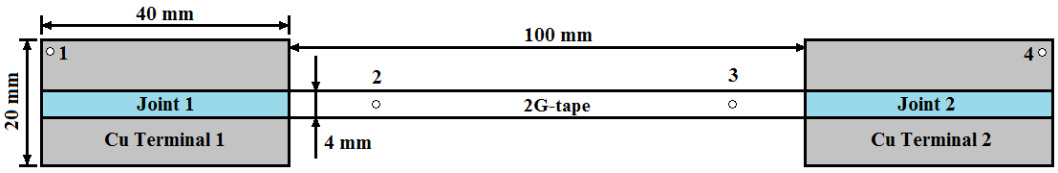

Figure 4.5: Schematic drawing of the the nano-heater made 2G-tape sample with dimension for contact resistance measurment. Number 1 to 4 show the position of the voltage taps.

4.3.3.2. The electrical contact resistance between two 2G-tapes

A 2G-tape to 2G-tape (Superpower) lap joint sample, made by nano-heater method with 296 °C melting solder (Sn5Pb93.5Ag1.5, wt. %), is shown in Figure 4.6a. The schematic drawing of this sample to measure the contact resistance is shown in Figure 4.6b. The surface area of the contact joint (T-T') between the two 2G tapes is 1 cm^2 (2.5 cm×0.4 cm). At each end of 2G tape, a 21 mm long current injection contact (A-T or B-T') between the copper shim and the 2G tape was made with 296 °C solder using the same method. The voltage tap 1 and 2 were soldered on two HTS tapes to measure the contact voltage V1-2. Two voltage-taps were twisted together to compensate the induction voltage. Then the sample was submerged into the LN2, and DC current was injected in steps from 0 to 60 A with an interval of 10 A for each step. The 4-contact method was applied to acquire the contact voltage at each current, using a Keithly 2000 voltmeter.

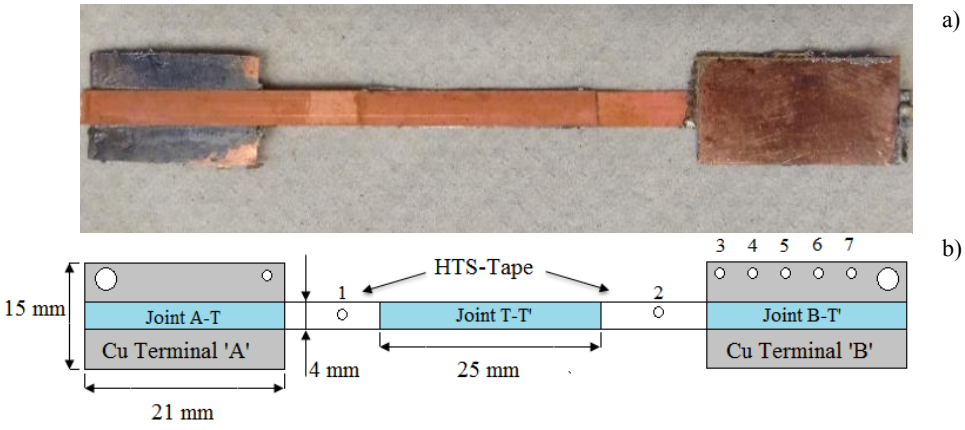

Figure 4.6: a) The picture of the nano-heater made 2G to 2G joint sample, and b) Schematic drawing of the the nano-heater made 2G to 2G joint sample with dimensions, and number 1 to 7 show the position of the voltage taps.

4.3.4 A new method for measuring current transfer characteristics and electrical contact resistance

According to the description in the analytical lap joint model described in subchapter 4.3.1.1, the key to defining the current distribution within the conductors, is to acquire the electrical field profile of the conductor that goes through the joint. In the earlier trials of the contact resistance measurements, the electrical field was calculated from the voltage measured by several voltage taps soldered at different positions along the contact. However, this method was limited by the error in the distance measured between two voltage taps on the 2G tape/copper shim. For instance, 1 mm wide voltage tap in 10 mm long lap joint has a 10 % error, and this error would accumulate when more voltage taps are added into the measurements. A better way is to trace the voltage change continuously along the conductor with the distance from one end of the joint. Then, the length error would only be the tap that was soldered at the end of the joint. Consequently, a new voltage measurement methodology called sliding needle contact method was introduced during the lap joint current transfer characteristics determination. Furthermore, compared with the traditional 4-contact method that can only measure the overall contact resistance of the lap joint, the pure contact resistance without two bonding components can be estimated by fitting the curve between the measured voltage along the distance of the conductor and the voltage profile as a function of the distance, in accordance with the lap joint analytical model.

4.3.4.1. Sample preparation

Three lap joint samples (2G-tape to copper), as shown in Figure 4.7, were prepared for the lap joint contact resistance measurements. The 2G-tapes (Bruker EST) were taken from the strands (I_c = ~63 A) of the Roebel cable described in Chapter 5. The copper strips were cut from a 100 μm thick copper shim. First, two lap joints samples (Sample 1 and Sample 2) were made with manual soldering method. Both 2G-tape and copper tape ends were pre-tinned with 146°C melting solder (In97Ag3, wt. %) on a hot plate at 150 °C, and the flux and excess of solder were removed by wiping the surface. Sample 3 was made in nano-heater method with a 146 °C melting solder. The contact surface of the 2G tapes were polished with emery paper (1200 grit) and cleaned before the bonding process. The dimension parameters of the three lap joint samples are shown in Table 4.3.

Figure 4.7: Three 2G tape to 2G tape joint nano-heater made samples.

Table 4.3: The dimension parameters of three lap joint samples.

Parameters / Sample	2G tape		Copper tape		Lap joint		
	Thickness (μm)	Width (mm)	Thickness (μm)	Width (mm)	Overall thickness (μm)	Area (mm×mm)	Contact thickness (μm)
Sample 1	175	5.50	100	5.50	318	5.50×8.00	~32
Sample 2	239	5.50	100	5.80	341	5.50×7.40	~5
Sample 3	192	5.50	100	5.76	325	5.50×9.00	~30

As shown in Figure 4.8, two copper shims were soldered at the each far end of 2G tape and copper tape via a 240°C melting solder (Sn99.3Cu0.7, wt. %) separately. Then each lap joint sample was glued onto a G10 strip by epoxy impregnation. The fiberglass tapes between the sample and G10 can give a mechanical support to prevent the damage of the sample from the thermal contraction during cooling down. Another small piece of fiberglass was inserted between the copper tape and 2G tape, which is used for electrical insulation layer underneath the copper to prevent current transferring at the position of the voltage tap 2 as shown in Figure 4.8.

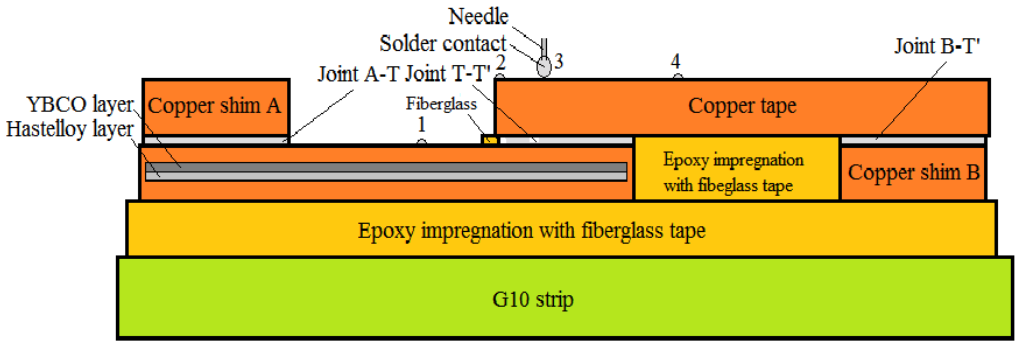

Figure 4.8: Schematic drawing (bottom) of the cross section of a 2G-tape to copper joint, and number 1, 2, 3 and 4 show the position of the voltage tap.

The sample holder is shown in Figure 4.9. The lap joint sample was soldered onto two current leads (terminal A' and B') with 180°C melting solder (Sn60Pb40, wt. %). Two current leads A′ and B′ were bolted on a G10 block. The numbers (n = 1, 2, 3 and 4) show the position of the voltage taps. Voltage tap 1 was soldered on the 2G tape, and voltage tap 2 and 4 were soldered on the copper tape. It needs to be noted that the voltage tap 3 was a sliding needle with a solder ball contact sliding on the copper, and that dash line shows the sliding path (L_d) between the voltage tap 2 and 4. Voltage-tap pair between 1 and 4 was used to measure the overall lap joint (Joint T-T′) contact voltage (V1-4), and voltage-tap pair between 2 and 3 was used to measure the continuous voltage changes $V(x)$ on the copper from the left joint end towards voltage tap 4 on the copper, where V2-4 gives a voltage baseline find the position of the sliding contact when is on the pure copper part, when $V(x)$ is equal to V2-4. The position of voltage tap 2 (left joint end of the copper side) is assumed as the zero position. All the voltage-tap pairs were twisted to compensate the inductive voltage with extended wire connections to the data logger through a wire board on the G10 block.

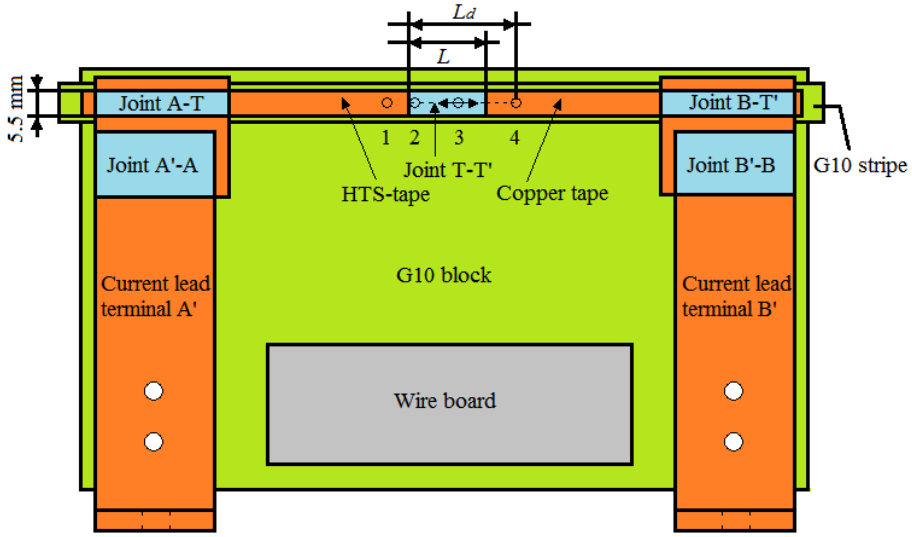

Figure 4.9: Schematic drawing of the lap joint sample holder, and the number 1, 2, 3 and 4 show the position of the voltage tap.

4.3.4.2. Test bed set up

Figure 4.10 shows the test bed for the lap joint contact resistance measurement in LN2 at 77 K. The sample holder was bolted at the end of an insulation board as the base. The other side of the base was fixed with a sliding set unit. A 25 mm wide G10 pillar was bolted on the sliding set, and it extends to the top above the sample holder. As shown in Figure 4.10, the voltage tap 3 is a needle that was soldered with a copper washer with a spring set between the G10 pillar and copper washer to provide compression strength for the needle touching on the lap joint sample. The other side of the G10 pillar was fixed with a G10 block that has a pin holder for the linear position (linear variable differential transformer/LVDT) sensor. Once the sample holder was inserted into liquid nitrogen, the rotary knob could drive the movement of the G10 pillar, and the sliding needle voltage tap moved between voltage taps 2 and 4. The displacement of the needle was recorded by a data logger that was connected to the linear position sensor. Figure 4.11 shows the calibration of the displacement the sensor, which has the voltage and displacement transfer function as shown below:

$$l\ (mm) = 1.536 \times V\,(\mathrm{V}) \qquad 4.30$$

Where l (mm) is the displacement of the sliding voltage tap, V in units of V is the voltage measured from the displacement sensor, and the constant of proportionality is 1.536.

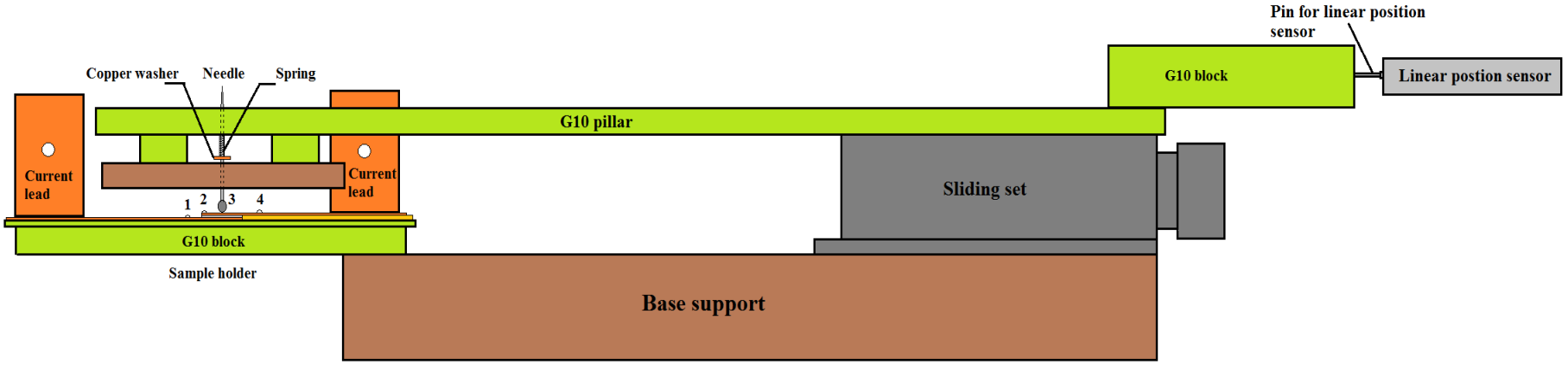

Figure 4.10: Sliding need contact test bed for lap joint contact resistance measurement.

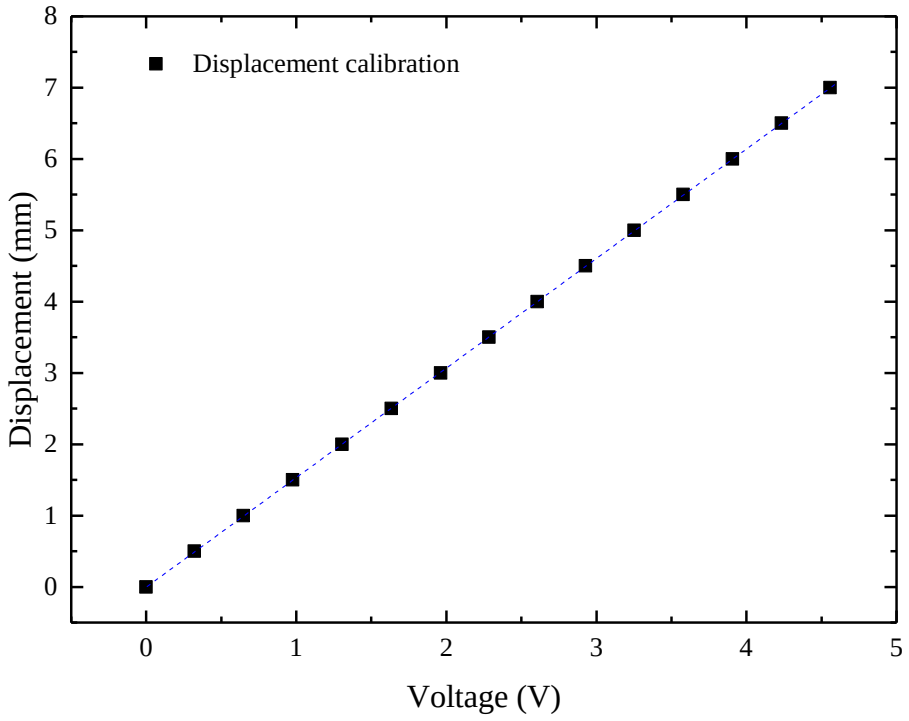

Figure 4.11: Displacement sensor (LVDT) voltage calibration.

4.4 Results and discussion

4.4.1 Electrical contact resistance of nano-heater made 2G-tape joints

4.4.1.1. Electrical contact resistance of 2G-tape to copper joints at different temperatures

The electrical contact resistance of two 2G-tape to copper joints were measured in a variable temperature cryostat rig at different temperatures. Figure 4.12 shows *VI* characersitics of two 2G-tape to copper soldered (Sn5Pb93.5Ag1.5, wt. %) joints at 15 K, 25 K, 35 K, 40 K and 77 K separately. Table 4.4 shows the resistance in units of nΩ and the contact resistance in units of nΩ×cm^2 for each joint at different temperatures. The surface area of each joint is 1.6 cm^2, and the contact resistances of joint 1 and joint 2 are 409.82 nΩ×cm^2 and 329.86 nΩ×cm^2 at 77 K respectively. Unfortunately, the overall contact resistance of these two joints were only smaller than one nanobond 2G-tape to copper joint sample. Bagrets et al has investigated the overall contact resistance of manually made SuperPower 2G-tape to copper soldered (Sn63Pb37, wt. %) joint (660 nΩ×cm^2) and SuNAM 2G-tape to copper soldered joint (694 nΩ×cm^2) with the same solder at 77 K [144]. The overall contact resistance of both nanobond and nano-heater 2G-tape to copper joints reduced by almost one third compared with 2G-tape joints made by Bagrets et al [144].

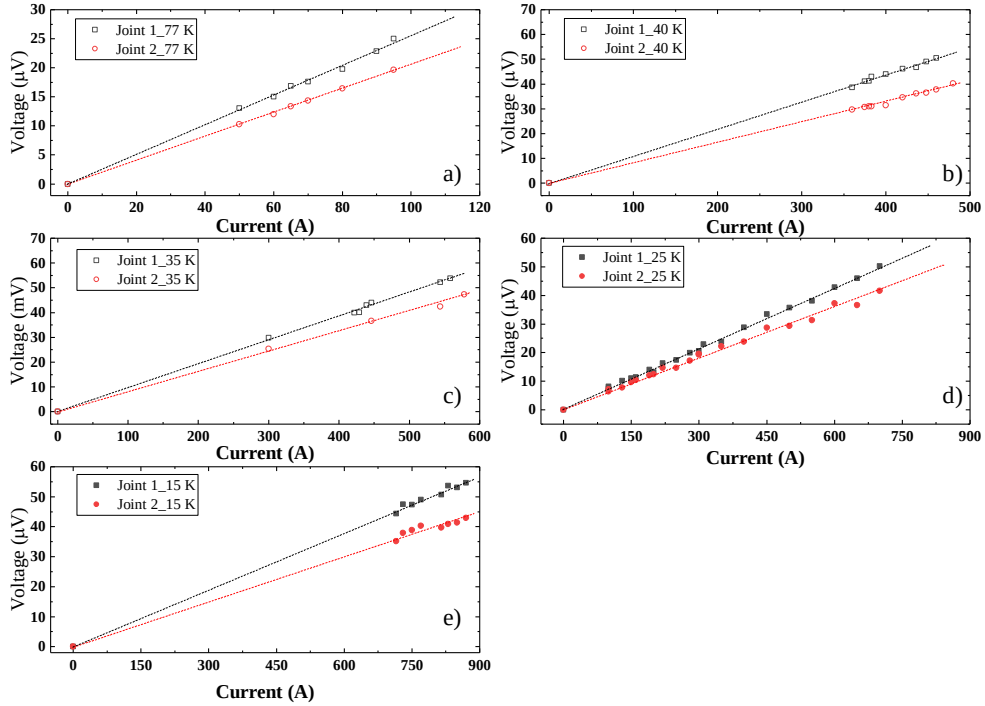

Figure 4.12: *VI* charactersitics of two 2G-tape to copper joints at a) 77 K, and b) 40 K, and c) 35 K, and d) 25 K and e) 15 K.

Table 4.4: Overall contact resistance of 2G to copper joints at different temperatures.

Sample	**Resistance**	**15 K**	**25 K**	**35 K**	**40 K**	**77 K**
Joint 1	Resistance (nΩ)	63.12	70.57	95.98	109.30	256.14
	Area contact resistance (nΩ×cm^2)	100.99	112.91	153.57	174.88	409.82
Joint 2	Resistance (nΩ)	49.57	57.77	80.07	82.41	206.16
	Area contact resistance (nΩ×cm^2)	79.31	92.43	128.11	131.86	329.86

4.4.1.2. Electrical contact resistance of 2G-tape to 2G-tape joint at 77 K

Electrical contact resistance of 2G-tape to 2G-tape joint was measured in LN2 at 77 K. Figure 4.13 shows the voltage-current (*VI*) characteristics of the 2G-tape to 2G-tape soldered (Sn5Pb93.5Ag1.5, wt. %) joint (1.6 cm^2) at 77 K. The slope of the dash line shows the linear fitting for the *V-I* characteristics, which gives an overall contact resistance (~136 nΩcm^2) of the 2G-tape to 2G-tape soldered joint. This value reduced more than 50% from the OI nanobond made 2G-tape to 2G-tape joints. For manually soldered 2G-tape to 2G-tape (Sn63Pb47, wt. %) joints, Bagrets et al has measured the overall contact resistance of SuperPower tape joints and SuNAM tape joints their results are 41 nΩ×cm^2 and 280 nΩ×cm^2 at 77 K respectively [144]; Tsni et al. also measured the contact resistance of SuperPower joints with solder, Pb38Sn62 (wt. %), In52Sn48 (wt. %) and Sn60Pb40 (wt. %), with the overall contact resistances of 47-59 nΩ×cm^2, ~34-66 nΩ×cm^2 and ~75 nΩ×cm^2 respectively [7].

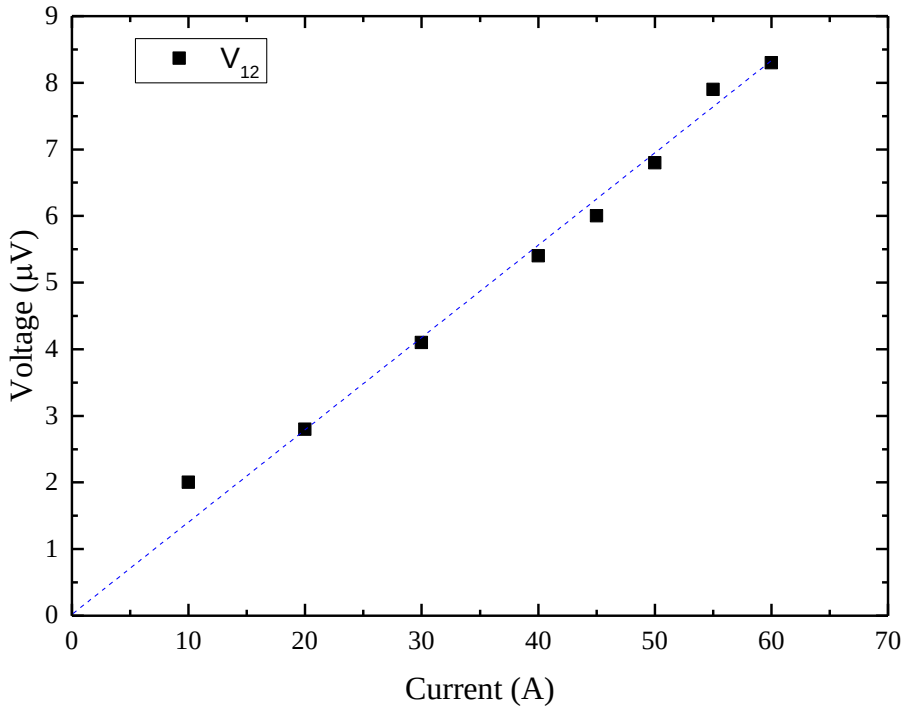

Figure 4.13: The plots for current-voltage characteristics of the joint contact between 2G-tape to 2G-tape (SuperPower™) joint.

4.4.1.3. Overall electrical contact resistance comparison of HTS tape joints

Table 4.5 shows a summary of the comparison for the overall contact resistance of soldered HTS joints at 77 K. These joints were made via the nanobond, nano-heater and manual soldering joint techniques with different HTS tapes and solders. Unfortunately, there is no data for 2G-tape to 2G tape joints made by manual soldering. There is one nano-heater made sample, with contact resistance (132 nΩ×cm^2), around one third of the nanobond made samples. For 2G-tape to copper joints, it is apparent that the joint with the lowest contact resistance (< 50 nΩ×cm^2) is the sample made via manual soldering using SuperPower 2G-tape and solder In97Ag3. However, there is a wide variation on overall contact resistance of 2G-tape to copper joints via manual soldering (In97Ag3) with Bruker 2G-tape, with their resistance varying from several hundred nΩ×cm^2 to several thousand nΩ×cm^2. The contact resistance of nanobond made 2G-tape to copper joints has a similar situation than manually soldered joints, which implies that these joints are irreproducible. The contact resistance of nano-heater made 2G-tape to copper shim joints with SuperPower 2G-tape and solder Sn5Pb93.5Ag1.5 are in an intermediate range, 330 - 410 nΩ×cm^2. These joints are more reproducible compared with HTS joints via other methods. This is due to a quantified process applied in the fabrication of the joints. The nano-heater process involves a controllable released energy, a constant compressive pressure and a uniform thickness solder film. Nevertheless, it needs to be noted that the overall contact resistance for 2G tape involves the interfacial resistance between copper or silver and the superconducting layer, the resistance of metallic stabilizer around the superconductor layer, solder resistance and copper resistance. Particularly, the effect of the copper thickness can have an obvious impact on the overall contact resistance as discussed in subchapter 4.3.1.1. The following subchapter will introduce a new

method that combined experimental work with 1-D lap joint analytical model to estimate the real contact resistance between two conductors.

Table 4.5: The overall contact resistance comparison at 77 K among the nanobond, nano-heater and manually soldering HTS-tape joints with different HTS tapes and solders.

Joints		Overall R_J (nΩcm^2)	Quantity	HTS Tape	Solder components
Nanobond	*2G to 2G*	300 - 470	6	Unknown	Sn/nanofoil/Sn
	2G to copper	200 - 1082	12	Unknown	Sn/nanofoil/Sn
Nano-heater	*2G to 2G*	132	1	SuperPower	Sn5Pb93.5Ag1.5
	2G to copper shim	330 - 410	4	SuperPower	Sn5Pb93.5Ag1.5
	2G to copper shim	3677	1	Bruker	In97Ag3
Manually soldering	*2G to copper*	276 - 3750	6	Bruker	In97Ag3
	2G to copper	81.8 - 677	2	Bruker	Sn60Pb40
	2G to copper	41 - 47	2	SuperPower	In97Ag3
	BSCCO to copper	60 - 78	2	Sumitomo	In97Ag3

4.4.2 Results from sliding needle contact resistance measurements

4.4.2.1. Measured voltage as a function of the continuous position x

Figure 4.14 (a, c and e) displays the measured voltages $V(x)$ as a function of the continuous position x with transport currents of 30 A, 40 A and 50 A for three samples from the new sliding needle contact resistance measurements. Figure 4.14 (b, d and f) show three similar resistance profiles that are obtained from the measured voltages at each current, which are used for evaluating there was no significant temperature increase when increasing the transport current. Three dash lines (black, red and green) as shown in Figure 4.14 (a, c and e) represent analytical voltages for the linear function versus the distance along the pure copper conductor at 30 A, 40 A and 50 A for each sample. To use the linear curve fitting for each measured voltage profile $V(x)$, the right end of the joint for each sample was defined via a vertical black dash line in each plot. Then the copper resistance per unit length and the joint length can be obtained from this curve fitting.

The estimated joint length for sample 1, sample 2 and sample 3 is 8.26 mm, 7.6 mm and 9.0 mm respectively. The left end of the joint is assumed as the starting point of the joint, but it needs to be noted that the soldering spot for the voltage tap at the left end of the joint for each sample is approximately 1 mm wide, with a small piece of fiberglass as the electrical insulation layer underneath of the copper to prevent the current injection at this region. This is treated as an already known error (8.3%-10%) on joint length compared with the distance (10-12 mm) between the voltage tap at the left point of the joint and the far end on the copper. When measuring the sliding voltage $V(x)$ versus the distance along the joint, $x = 0$ was set at the position where the continuous voltage was the minimum value within ~ ±5 μV scale. Compared with the measured joint length of sample 1 (8.0 mm), sample 2 (7.4 mm) and sample 3 (9.0 mm), the estimated joint length for each sample is acceptable within an error within 5 %.

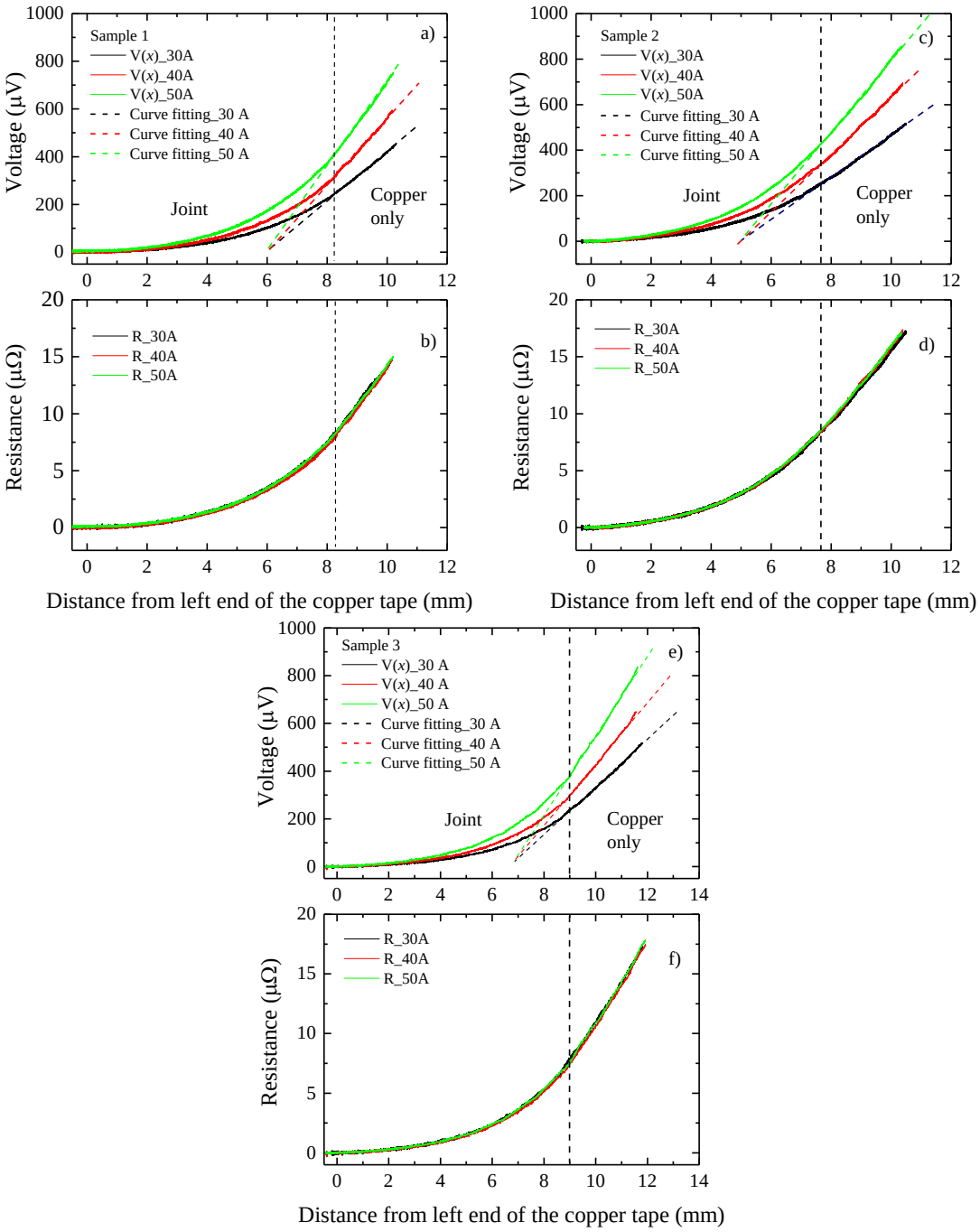

Figure 4.14: Left top plot shows a) measured voltage and b) resistance as a function of continuous position on the copper for sample 1, and right top plot shows c) measured voltage and d) resistance as a function of continuous position on the copper for sample 2, and bottom plot shows e) measured voltage and f) resistance as a function of continuous position on the copper for sample 2 with transport current of 30 A, 40 A and 50 A. Three dash lines (black, red and green) as shown in this figure (a, c and e) representing the slope of the voltage as a function of the position of the copper conductor only at 30 A, 40 A and 50 A for each sample. The vertical black dash line in each plot is used for defining the right end of the lap joint for each sample.

The relationship between the linear voltage profile $V(x)$ and the distance from the right end of the joint is shown below in accordance with Ohm's law:

$$V(x) = IR = I\frac{\rho x}{A} \qquad 4.31$$

With

$$A = wd \tag{4.32}$$

Where I is the transport current, R is the copper resistance, ρ is the copper resistivity at 77 K, A is the cross-section of the copper tape, w is the copper width and d is the copper thickness (100 μm). $I\rho$/A is the slope for each linear curve fitting as shown in Figure 4.14. The slope at different transport current for each sample and the nominal copper resistivity of the copper for each sample at 77 K are presented in Table 4.6. These parameters will be used in the contact resistance estimation in the analytical model and optimal joint distance estimation.

Table 4.6: The slope for the linear fitting of voltage changes on the copper only verses the distance from the right end of the joint and estimated copper tape resistivity for each sample at 77 K.

Slope \ Current	**30 A**	**40 A**	**50 A**	**Resistivity** (nΩ×m)
Sample 1	0.1047	0.1396	0.1745	1.92
Sample 2	0.0977	0.1303	0.1629	1.89
Sample 3	0.0990	0.1319	0.1649	1.90

4.4.2.2. Curve fitting of the measured voltage $V(x)$

Sample 3 is used as an example to show the curve fitting of the measured voltage $V(x)$ with the analytical model. This model was divided into two parts, the joint part $V_{Cu\_joint}(x)$ and copper only part $V_{Cu\_joint}(x)$.

Firstly, the formula for $V_{Cu\_joint}(x)$ versus the distance from left end of joint can be obtained in accordance with Equation 4.5 and Equation 4.13:

$$V_{Cu\_joint}(x) = \int_0^x r_2 I_2(x)dx \tag{4.33}$$

With

$$V_{Cu\_joint}(x) = r_2 \int_0^x (I_0 - \frac{I_0}{r_1 + r_2} \frac{r_2\left(\sinh\left(\frac{L}{L_t}\right) - \sinh\left(\frac{x}{L_t}\right)\right) + r_1 \sinh\left(\frac{L-x}{L_t}\right)}{\sinh\left(\frac{L}{L_t}\right)})dx \tag{4.34}$$

Where $x \leq L$ = 9.0 mm; r_2 is the copper resistance per unit length; r_1 is the superconductor resistance per unit length, with r_1 assumed as 0 initially; I_0 is 40 A and L_t was assumed as the transfer length obtained by Equation 4.3 and Equation 4.8.

The formula for the linear voltage $V_{Cu}(x)$ versus the distance from right end of joint (x = 9 mm) can be obtained as:

$$V_{Cu}(x) = V_{Cu\_joint}(x = 0.009) + r_2(x - 0.009) \tag{4.35}$$

Where r_2 is the copper resistance per unit length.

Figure 4.15 shows the measured voltage $V(x)$ for sample 3 compared with the analytical V_{Cu_joint} and V_{Cu} versus x at 40 A with a range of the contact resistance from 960 to 1440 nΩ×cm^2. The measured $V(x)$ is higher than all the analytical profiles of $V_{Cu\_joint}(x)$ when x is smaller than 6.0

mm. After x is above 6.0 mm, the measured $V(x)$ starts to cross the analytical $V_{Cu\_joint}(x)$ profiles and reaches ~300 μV at x = 9.0 mm, which is just above value of $V_{Cu\_joint}(x$ = 9.0 mm) with a contact resistance R_c = 1020 nΩ×cm^2. When x is above 9.0 mm, the measured voltage $V(x)$ starts to increase linearly, and the voltage profile starts to be parallel to other analytical profiles of $V_{Cu}(x)$, which implies all the current has transferred into the copper side.

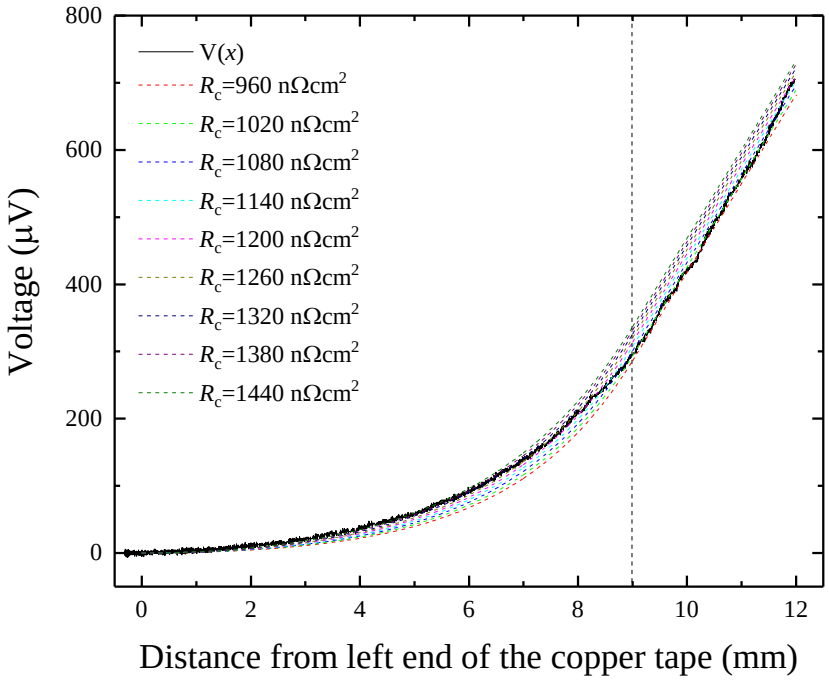

Figure 4.15: The plot for the measured voltage $V(x)$ for sample 3 compared with the analytical model $V_{Cu\_joint}(x)$ and $V_{Cu}(x)$ versus the continuous position at 40 A with the contact resistance assumed from 960 to 1440 nΩ×cm^2.Vertical dash line represents right end of the joint.

The study of the relationship between the voltage at the right end of the joint and these parameters become very important for the performance of the lap joint. The voltage $V_{Cu\_joint}(x)$ at the right end of the joint rises with the increase of the contact resistance. Furthermore, this voltage can be treated as the overall contact voltage when the superconductor resistance is assumed as 0 in accordance with Equation 4.16. Now, the superconductor resistance will be changed to investigate the voltage at the right end of the joint. In order to fit the measured $V(x)$, the contact resistance was assumed to start from 960 nΩ×cm^2 and increase with an interval of 60 nΩ×cm^2 at each step. The superconductivity resistivity (ρ_1) was assumed as another variable to increase from 0 to 18.28e-15 Ωm with an interval of 4.57e-15 Ωm (~1/400000 of the copper resistivity) at each step. A resistivity of 9.14e-15 Ωm corresponds to the critical current (I_c = ~ 63 A) of the superconductor based on 1 μV/cm criteria. The thickness of the superconductor was assumed as 1 μm. Then, the analytical $V_{Cu\_joint}(x)$ and $V_{Cu}(x)$ can be obtained by Equation 4.34 and 4.35.

Figure 4.16 shows the plot for the measured voltage $V(x)$ for sample 3 (black solid line) compared with the analytical $V_{Cu\_joint}(x)$ and $V_{Cu}(x)$ at 40 A. The superconductor resistivity (ρ_1) was assumed to be 0, 4.57e-15, 9.14e-15, 18.28e-15 Ωm and the contact resistance was assumed as 960 nΩ×cm^2. The profiles of analytical $V_{Cu\text{-}joint}(x)$ with different superconductor resistivities were almost similar with each other and the voltage of all the cases is smaller than the measured values when x < 9

mm. The profiles of analytical $V_{Cu}(x)$ start to match with the measured voltage when $x > 9$ mm. The overlapping profiles of analytical $V_{Cu\text{-}joint}(x)$ mean that the resistivity of the superconductor varying in a scale of 10e-15 Ωm has a minimum effect on the voltage of the conductor that was overlapped in the joint. When the superconductor resistivity ρ_1 was increased to 1.52e-12 Ωm, the analytical profile, $V_{Cu\text{-}joint}(x)$, was almost similar to the measured voltage $V(x)$, with $0 < x < 9$ mm. However, the voltage across 1 cm length on the superconductor is already around ~100 μV at 40 A. This value is impossible for a superconductor with a transport current below the critical current. It needs to be noted that the superconductor was assumed as a 1 μm thick lump layer without the stabiliser (~25-30 μm each side) or silver layer into consideration. These resistive layers can contribute to the resistance of the superconducting tape. Compared with the superconductor resistance, the copper resistance and contact resistance account for the main part of the overall contact resistance, corresponding to the voltage $V_{Cu\text{-}joint}(x = 9$ mm) according to Equation 4.16. Consequently, we believe that the estimated contact resistance ($R_c = 960$ nΩ×cm^2) is close to the real value. The shift of $V(x)$ to the left of the analytical $V_{Cu}(x)$ when $x > 11$ mm, may be caused by an experimental error issue. Furthermore, the same procedure was used for lap joint sample 1 and 2. Figure 4.17 and Figure 4.18 show the measured voltage profiles for sample 1 and sample 2 respectively compared with the analytical $V_{Cu\_joint}(x)$ and $V_{Cu}(x)$ at 40 A. In these results the superconductor side resistivity (ρ_1) was assumed to be 0, 4.57e-15, 9.14e-15, 18.28e-15 Ωm and 1.52e-12 Ωm, and the contact resistance was assumed as 1024 nΩ×cm^2 for sample 1 and 1700 nΩ×cm^2 for sample 2.

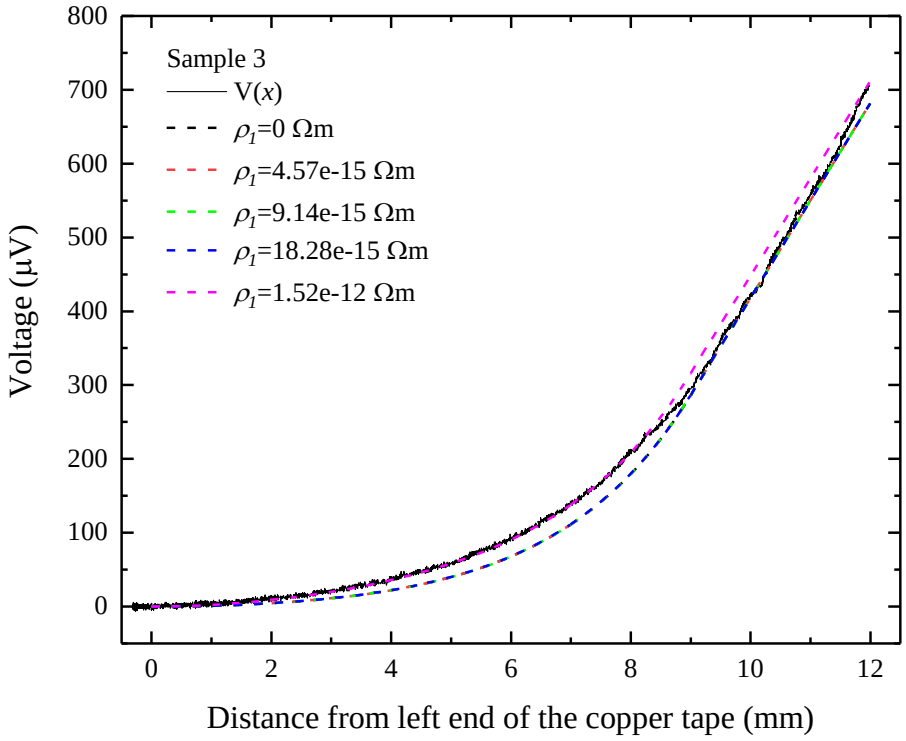

Figure 4.16: The plot for the measured voltage $V(x)$ for sample 3 compared with the analytical model $V_{Cu\_joint}(x)$ and $V_{Cu}(x)$ versus the continuous position at 40 A. The superconductor side resistivity (ρ_1) was assumed to be 0, 4.57e-15, 9.14e-15,18.28e-15 and 1.52e-12 Ωm, and the contact resistance was assumed as 960 nΩ×cm^2.

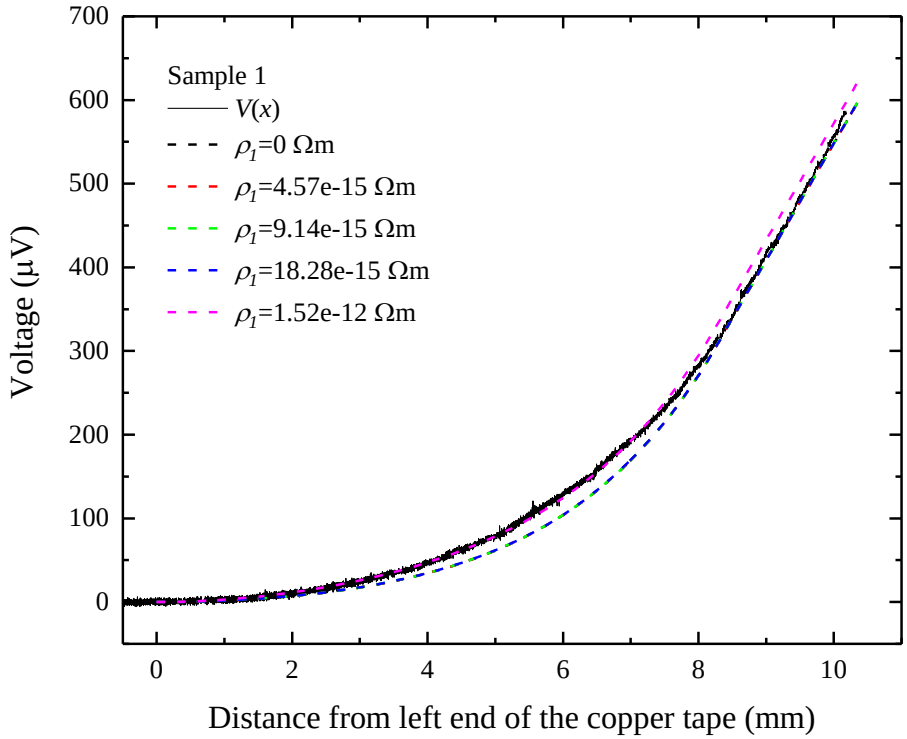

Figure 4.17: The plot for the measured voltage $V(x)$ for sample 1 compared with the analytical model $V_{Cu\_joint}(x)$ and $V_{Cu}(x)$ versus the continuous position at 40 A. The superconductor side resistivity (ρ_1) was assumed to be 0, 4.57e-15, 9.14e-15,18.28e-15 and 1.52e-12 Ωm, and the contact resistance was assumed as 1024 nΩ×cm^2.

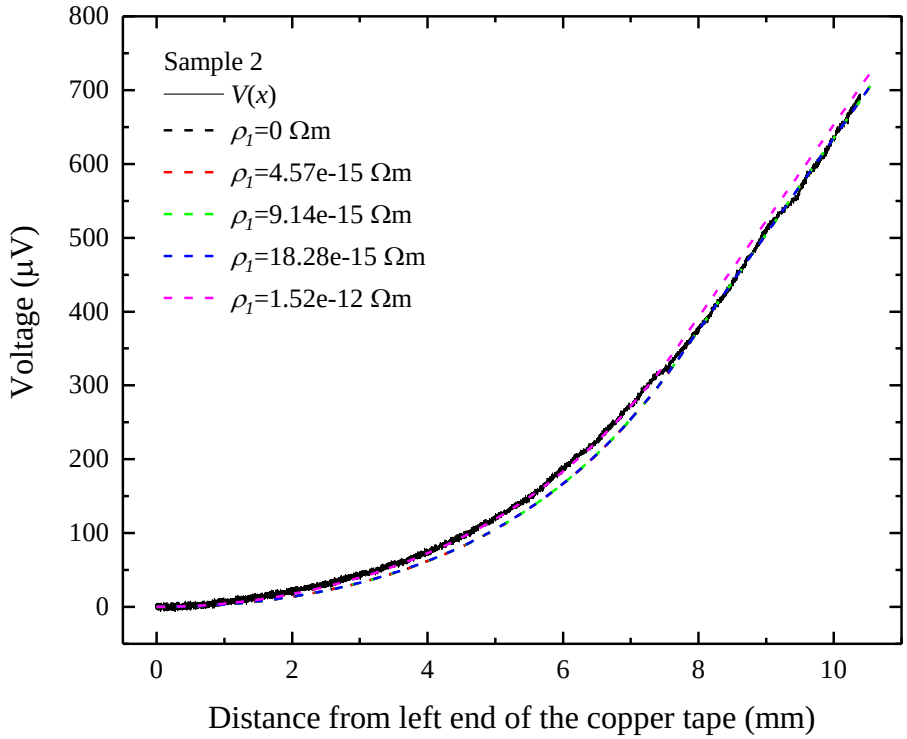

Figure 4.18: The plot for the measured voltage $V(x)$ for sample 2 compared with the analytical model $V_{Cu\_joint}(x)$ and $V_{Cu}(x)$ versus the continuous position at 40 A. The superconductor side resistivity (ρ_1) was assumed to be 0, 4.57e-15, 9.14e-15,18.28e-15 and 1.52e-12 Ωm, and the contact resistance was assumed as 1700 nΩ×cm^2.

4.4.2.3. 'Shape Prescriptive Modelling' curve fitting

The noise is the main problem in the derivation of the measured function $V(x)$. A new method was developed for smoothing the measured $V(x)$. It is a function tool in MATLAB for curve fitting [149], [190], called 'Shape Prescriptive Modelling'(SLM), which is used for smoothing the measured voltage $V(x)$ when calculating the electrical field of the conductor. The MATLAB code of the curve fitting method described in this subchapter is presented in the Appendix I. A continuous smoothed approximation of the measured voltage profiles of $V(x)$ in the copper tape was processed using the MATLAB SLM function. Unlike other spline function and curve fitting methods, the SLM function provides a controllable adjustment for the curve spline approximation based on known mathematic function patterns and physical factors such as the slope, the value at the end of the applied function, monotonicity of the function or curvature of the function. It can be set up for the curve shape adjustment by graph inspection.

Sample 3 at 40 A is an example for the SLM spline approximation. The data of $V(x)$ was imported into MATLAB. The adjustments were added in a function named 'slmengine' in the SLM as seen in the code shown in Appendix I. The adjustment set up is described below:

- Boundary conditions: The left end of $V(x)$ with x at 0 has been set as a default value in the SLM. As the slope of the right end of $V(x)$ with $x > 9.0$ is approaching to the slope of $V_{Cu}(x)$. The 'rightslope' is set as 0.1319 for 40 A, in accordance with the slope reference as shown in Table 4.6.
- Curvature and monotonicity: An increasing monotonicity and a monotone increasing slope are shown in $V(x)$ profile, 'increasing' and 'concaveup' are set as 'on'.
- The position and numbers of knots: The number (n) of knots are controlled for the equally spaced anchor points in the data of the approximated curve. These points separate the applied function into n-1 independent functions. Then the spline approximated data is smoothed with a continuous section from one independent function to the next at each knot [149], [190].

The advantage of this method is to observe the effect of various positions of the knots on the shape of the generated data curves. In the development of SLM function 'slmengine' in MATLAB, evenly spaced knots were applied to generate a smoothed function of $V(x)$. The SLM calculated function was assumed as $V(x)$_SLM. The evenly spaced knots were set as n = 6, 8,…, 12, 25 and 30, and the generated continuous function $V(x)$_SLM with different knots is shown in Figure 4.19 (a-h) compared with the measured $V(x)$. The dash line in each figure represents the generated smoothed data for function $V(x)$_SLM with different knot numbers. By comparing the selected knot numbers with expected features found in the calculated $V(x)$_SLM, it is possible to identify the positions of the knots that may lead to a reasonable spline model to achieve a good curve fitting. According to the comparison in Figure 4.19, when the knot number is above 8, the curve fitting is in good agreement due to the monotonic nature of the measured $V(x)$.

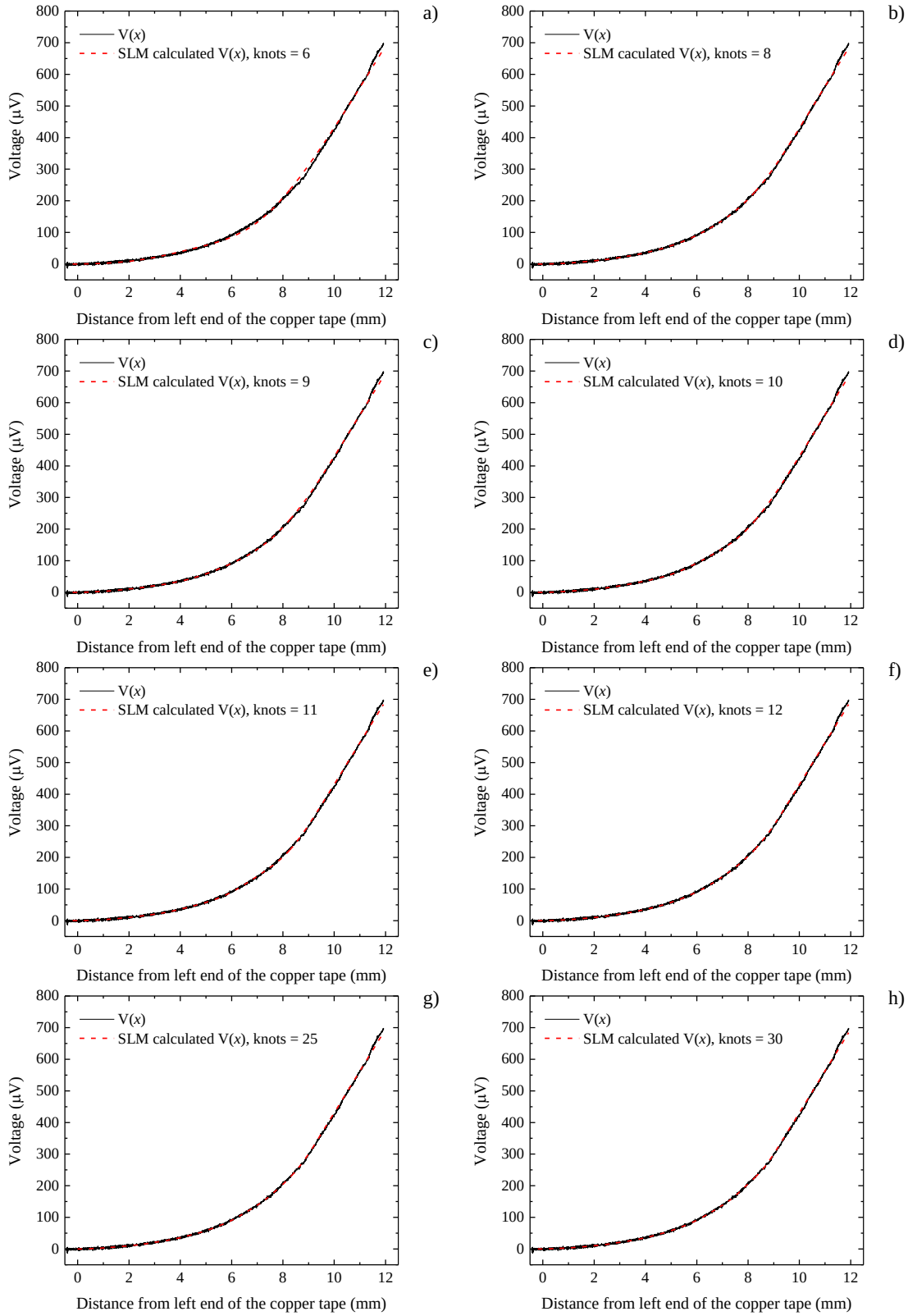

Figure 4.19: The plot of V(x) for sample 3 as a function of the continuous position along the copper tape at 40 A compared with SLM_V(x) with a) knots = 6, b) knots = 8, c) knots = 9, d) knots = 10, e) knots = 11, f) knots = 12, g) knots =25, and h) knots= 30.

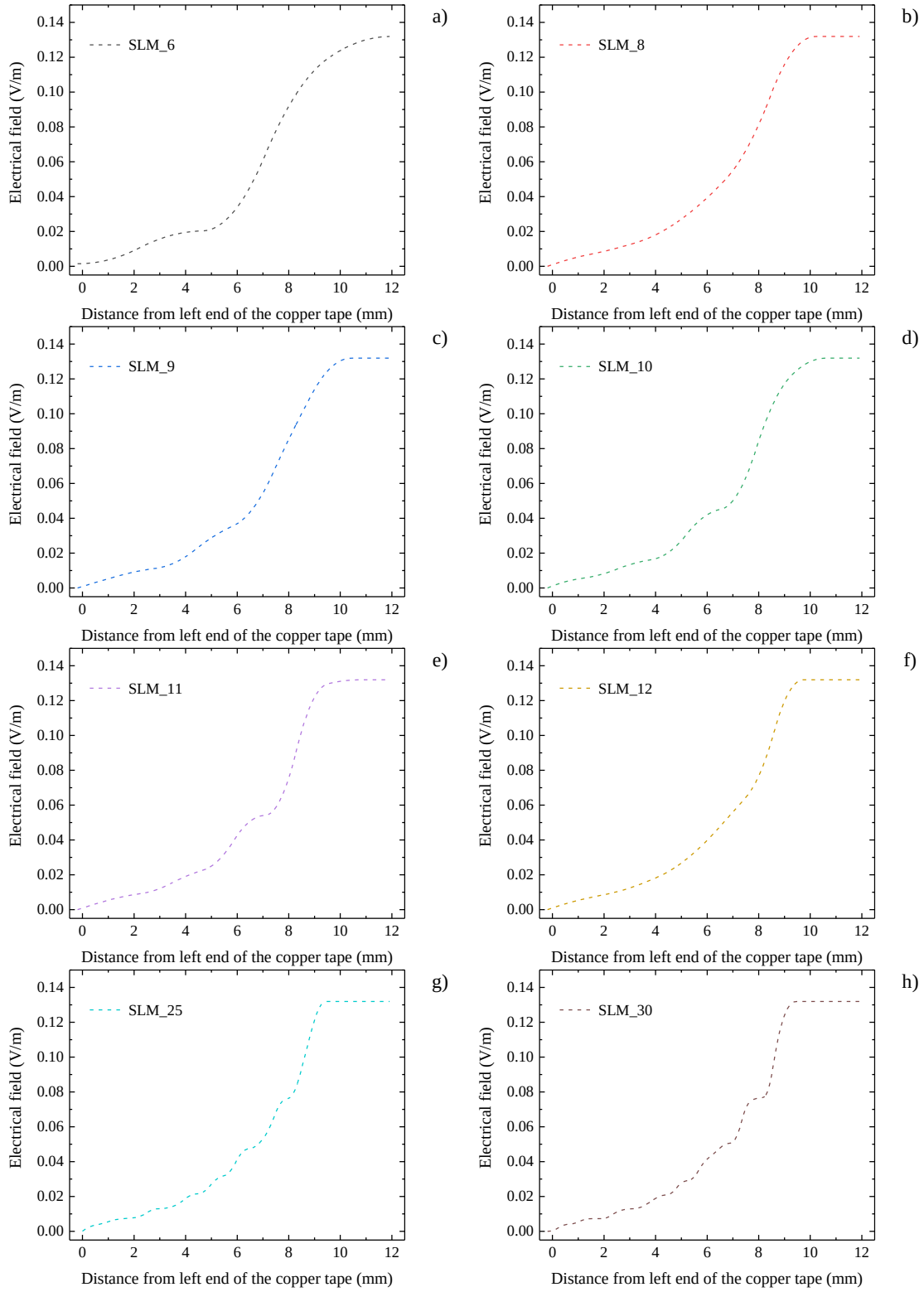

Figure 4.20: The plot for first order differential function SLM_$V'(x)$ for sample 3 with a) knots = 6, b) knots = 8, c) knots = 9, d) knots = 10, e) knots = 11, f) knots = 12, g) knots =25, and h) knots= 30.

The rest of the problem is how many knots are needed for SLM to process the spline model. The aim of the curve fitting is to estimate the current distribution by investigating the changes of electrical field along the joint. A first order derivation can be applied to function $V(x)$_SLM to check the curve fitting results. With more knots applied to the curve spline model, the estimated

length of the joint from the spline model is closer to the estimated value (9 mm). However, there are more knobbles in the first order derivation of function $V(x)$_SLM profiles when knots are set at higher numbers (n = 25 and 30). This may not be a real refection on electrical changes along the copper tape overlapped the joints. The tutorial description in [190] stated that the use of too many knots did not result in a singularity. The key point is that there is enough supported information for achieving a reasonable fit. Consequently, the smooth plot of profile $V(x)$_SLM with knots = 12 was considered as the best for the further analysis of this case.

4.4.2.4. Current transfer characteristics of HTS joints

The electrical field $dV(x)/dx$ is proportional to the local current density at each position along the joint in accordance with Equation 4.4 and 4.5. Consequently, the features of the current distribution along the joint can be investigated from the plot of $dV(x)/dx$ at each position of the joint. Figure 4.21 shows a first order differential plot for the interpolation (black scatters) of the measured $V(x)$ and the best fit SLM_$V(x)$ (cyan solid line) for sample 3 at 40 A. They are compared with the analytical functions $V'_{Cu\_joint}(x)$ and $V'_{Cu}(x)$ for different superconductivity resistivities (ρ_1), 0 (black dash line), 4.57e-15 Ωm (red dash line), 9.14e-15 Ωm (green dash line), 18.28e-15 Ωm (blue dash line) and 1.52e-12 Ωm (magenta dash line). The electrical field SLM_$V'(x)$ at x = 4.5 mm is around 20 % of that at x = 9.0 mm, which implies almost 80 % current still flows within the 2G tape side at this position. A steep electrical field increase appears between x = 6.0 mm and x = 9.0 mm of the lap joint, and more than 70 % current transfer occurs at this range based on the electrical field changes. This is in agreement with the estimation in the analytical model as discussed in chapter 4.3.1. According to the monotonicity of the electrical field of the function, it does not matter if the polarity of the current transfer direction is from superconductor to copper or copper to superconductor. Most current transfer occurs towards the right end of the lap joint. This is good for conduction cooling due to the short path of the cooling power along the copper tape.

The starting point of constant $V'(x)$_SLM (cyan solid line) implies that the real joint length may be longer than the estimated value. However, logging noise leads to scattered points as shown in the interpolation plot that fluctuates up and down when x > 9.0 mm. Fortunately, the $dV(x)/dx$ at the right of the joint is only based on the copper resistivity, which can reduce the effect of this error on the contact resistance estimation from the curve fitting between the measured voltage profile and the analytical model. Furthermore, Figure 4.22 and Figure 4.23 show the first order differential plot interpolation (black scatters) of the measured $V(x)$ and the best fit SLM_$V(x)$ (cyan solid line) for sample 1 and 2 respectively at 40 A, compared with the analytical functions $V'_{Cu\_joint}(x)$ and $V'_{Cu}(x)$ with different superconductivity resistivity (ρ_1), 0 (black dash line), 4.57e-15 Ωm (red dash line), 9.14e-15 Ωm (green dash line),18.28e-15 Ωm (blue dash line) and 1.52e-12 Ωm (magenta dash line).

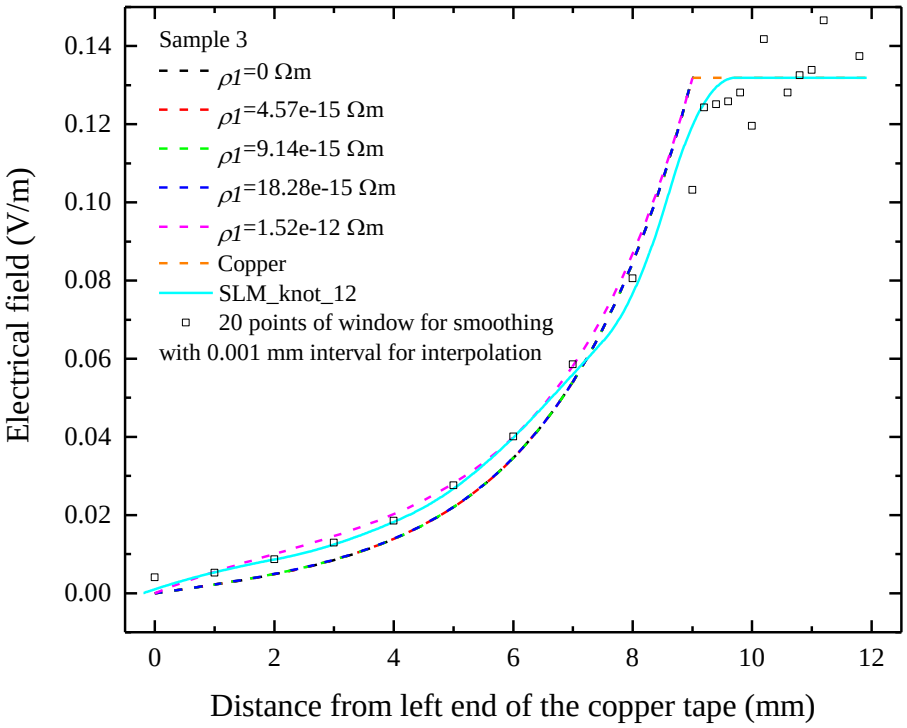

Figure 4.21: The analytical electrical field (SLM_knot_ 12) from the measured $V(x)$_SLM for sample 3 with 12 knots versus the continuous position x compared with the calculated electrical field from the measured $V(x)$ with 20 points of window for averaged smooth at 40 A with the superconductor side resistivity (ρ_1) assumed to be 0, 4.57e-15, 9.14e-15,18.28e-15, 1.52e-12 Ωm and the contact resistance was assumed as 960 nΩ×cm^2.

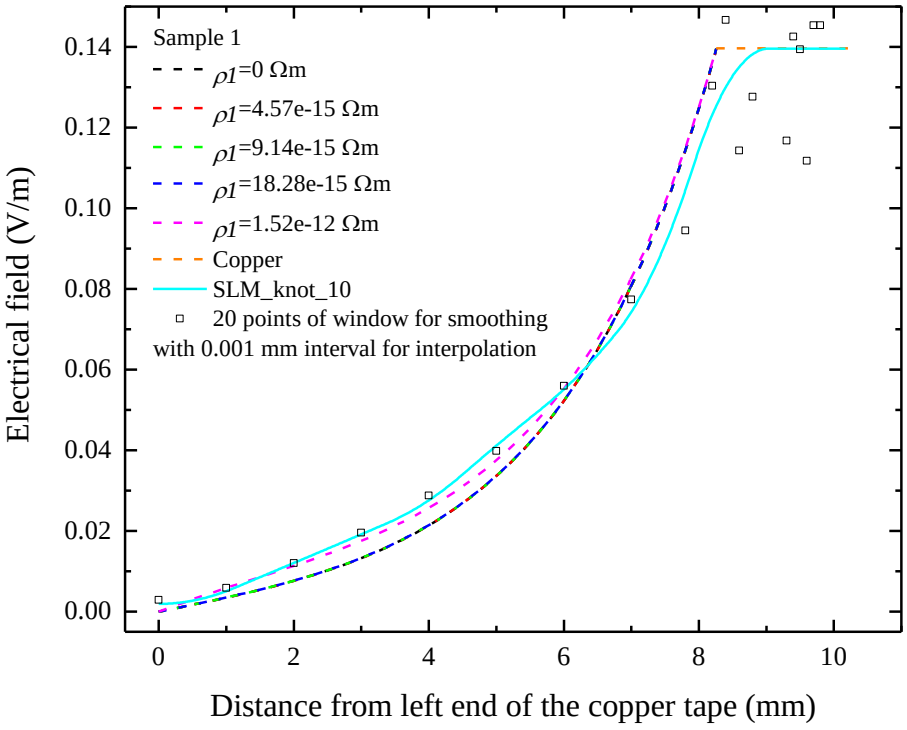

Figure 4.22: The analytical electrical field (SLM_knot_ 10) from the measured $V(x)$_SLM for sample 1 with 10 knots versus the continuous position x compared with the calculated electrical field from the measured $V(x)$ with 20 points of window for averaged smooth at 40 A with the superconductor side resistivity (ρ_1) assumed to be 0, 4.57e-15, 9.14e-15,18.28e-15, 1.52e-12 Ωm and the contact resistance was assumed as 1024 nΩ×cm^2.

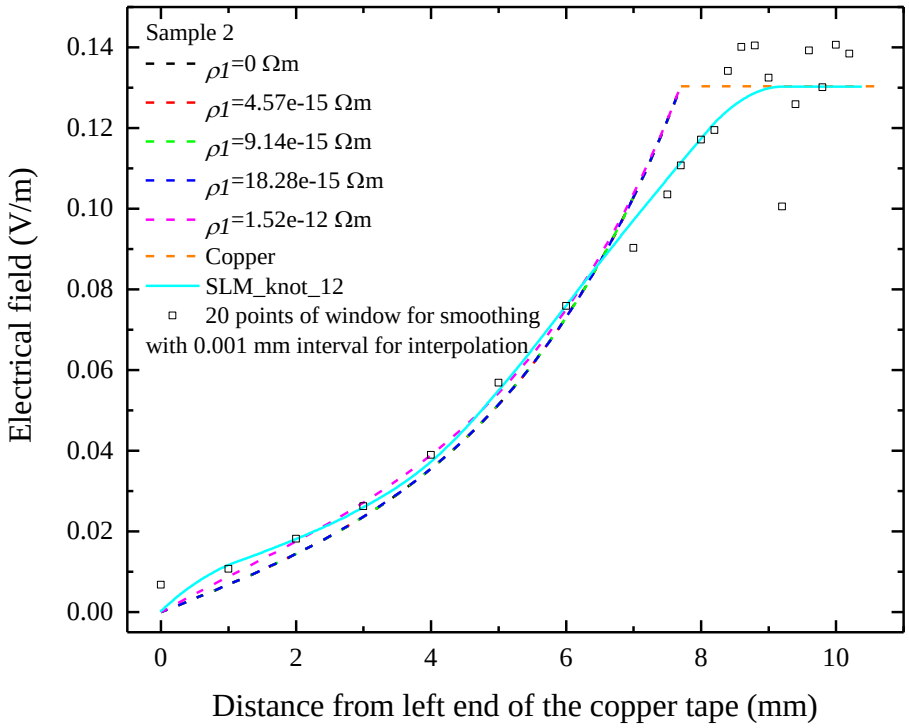

Figure 4.23: The analytical electrical field (SLM_knot_ 10) from the measured $V(x)$_SLM for sample 2 with 10 knots versus the continuous position x compared with the calculated electrical field from the measured $V(x)$ with 20 points of window for averaged smooth at 40 A with the superconductor side resistivity (ρ_1) assumed to be 0, 4.57e-15, 9.14e-15,18.28e-15, 1.52e-12 Ωm and the contact resistance assumed as 1700 nΩ×cm^2.

4.4.2.5. Overall joint contact resistance comparison among three lap joint samples

Table 4.7 shows a summary of contact resistance, solder resistance, joint length (estimated length and optimized length) and overall contact resistance (measured overall contact resistance, analytically estimated overall contact resistance and minimum overall contact resistance) for three lap joints samples. The same curve fitting method can be used for the contact resistance estimation of sample 1 (1024 nΩ×cm^2) and sample 2 (1700 nΩ×cm^2). Compared with the resistance of 146 ^{o}C melting solder (In97Ag3, wt. %) at 77 K as shown in Table 4.7, the contact resistance of each sample is almost more than 100 times larger. It needs to be noted that real contact resistance involves the interfacial resistance between the superconductor and silver stabiliser; and the copper resistance around the superconductor with the solder resistance. According to literature review from [7], [8], [145], [184], the interfacial resistance accounts for the main part of the contact resistance. In the meantime, the void or defects existing within the solder can cause poor adhesion between the solder and the two bonding component surfaces, which can also contribute larger contact resistance.

The overall contact resistance of the three lap joint samples can be obtained in accordance with the measured voltage across the entire joint, and the results of sample 1, sample 2 and sample 3 are 8.26 μΩ, 8.52 μΩ and 7.55 μΩ respectively. Taking the superconductor resistivity (9.14E-15 Ωm) into consideration, the estimated overall contact resistances are 8.08 μΩ, 9.78 μΩ and 7.43 μΩ for sample 1, sample 2 and sample 3 respectively, based on the analytical model. These values are quite big compared with the overall contact resistance measured from the same solder made

joints in an similar cross-section (4 mm× 10 mm) for SuperPower made 2G-tape (~110 nΩ) and Sumitomo BSCCO tape (~180 nΩ) as shown in Table 4.5. Furthermore, this unusual larger contact resistance for this single strand needs to be analysed with Roebel cable contact resistance measurements. This issue will be discussed in the next chapter.

The analytical model implies the overall contact resistance is dominated by the contact resistance for the short length joints and the parallel resistance of the conductors for the long joints respectively. For instance, sample 2 has a larger contact resistance that is almost 2 times that of other two samples, but overall resistance is only ~5 % larger than the other two samples. This is partially due to a shorter joint length on sample 2 so less copper resistance was involved. An optimised joint length of each sample was evaluated for a balance between the contact resistance and copper resistance for the overall contact resistance contribution. The reduction of overall contact resistance is not obvious when a high resistance ratio between r_1/r_2 is present, as shown in Figure 4.3, but a shorter joint length design is helpful for conduction cooling of the lap joint.

Table 4.7: The estimated contact resistance, solder resistance, copper resistance and overall contact resistance of three lap joint samples.

Sample	Analytical contact resistance R_{con} (μΩcm^2)	Solder resistance		Superconductor resistance		Copper resistance		Joint length (mm)		Overall contact resistance		
		Resistivity ρ_{solder} (μΩcm)	R_{solder} (μΩcm^2)	Resistivity ρ$_1$ (μΩcm)	r_1 (μΩ)	Resistivity ρ_2 (μΩcm)	r_2 (μΩ)	L	L_{opt}	R_J (μΩ)	Analytical R_J (μΩ)	Analytical R_{Jmin} (μΩ)
1	0.96	2.12	6.78e-3	9.14E-15	0.0137	0.192	28.8	8.26	3.81	8.26	8.08	8.08
2	1.7	2.12	1.06e-3	9.14E-15	0.0121	0.189	25.1	7.70	4.56	8.52	9.89	9.78
3	1.024	2.12	6.36e-3	9.14E-15	0.0143	0.190	29.7	9.00	3.70	7.55	7.43	7.43

4.5 Conculsion

The annealing process is an effective way to reduce the resistivity of the reacted nanofoil, but this is not suitable for 2G-tape soldered joints. How to make use of the advantages of the simple manufacturing process and fast energy dissipation of nanobond reaction process at room temperature for soldering the 2G-tape joints has been investigated. A new methodology for 2G-tape joints bonding, called nano-heater, was first developed to make use of the thermal energy produced from the nanofoil reaction without the foil staying between the two bonding components. This method is reproducible due to a quantified process nature. The average overall contact resistance of nano-heater made 2G-tape to copper joint and 2G to 2G joint with solder Sn5Pb93.5Ag1.5, wt. % are ~350 nΩ×cm^2 and ~130 nΩ×cm^2 respectively. In order to evaluate the performance of nano-heater made soldered joints for 2G-tapes, the overall contact resistance of lap joints with different solders (such as Sn60Pb40, wt. %) can be measured at different low temperatures in the future works.

A 1D analytical model was develepped to analyse the current transfer characteristics of a lap joint. The effect of contact resistance, conductors' resistance and joint length on current distribution and overall contact resistance have been investigated. The analytical model shows that when a lap joint has a high resistance ratio between the two conductors, most of the current flows within the conductor with the lower resisitivity and the current transfering occurs towards the end of this conductor. Furthermore, the analytical model shows that the overall contact resistance of a joint would decrease fast when the joint length increases to the optimal length L_{opt}, but a slower increase from the minimum overall joint resistance will be produced when the joint is longer than L_{opt} for large a resistance ratio between two conductors.

A needle sliding contact method for contact resistance measurement combined with 1D lap joint analytical model were developed to evaluate contact resistance and current distribution of the lap joints. One nano-heater made and two manully made soldered (In97Ag3, wt. %) copper to 2G-tape lap joints were performed in LN2 at 77 K. The advantage of a needle sliding contact method is to trace the voltage continuously on the conductor that has overlapped the joint. Therefore the current distribution along the joint can be evaluated by derivating from the voltage changes as a function of the distance from one end of the joint along the conductor, due to the proportional relationship between the electrical field and local current density. Large overall contact resistance (~8 μΩ) were observed for these three samples using Bruker 2G-tape compared with lap joints using SuperPower 2G-tape (~ 110 nΩ) and BSSCO tape (~ 180 nΩ). Furthermore, a simple 1D joint analytical model is can only evaluate the resistance for a single layer conductor by fitting the measured voltage. It can provide a good indication of current distribution for a HTS-tape lap joint and joint geometry design for thermal conduction. An analytical model will be developed for a lap joint with multilayer conductors in the future works.

Chapter 5
Performance and Quench Characteristics of a Pancake Coil Wound with 2G YBCO Roebel Cable

5.1 Introduction

The high current carrying capability and strong pinning in high magnetic field make the 2G HTS Roebel cable for future high energy accelerators at CERN and tokamak devices [5], [80], [191], [192]. Some researches have already shown a more complex current sharing and normal zone propagation is expected for Roebel cables than those found in traditional superconducting composites due to the non-continuous touch contacts among the Roebel strands [5], [77], [80], [191], [193]–[195]. The standard method of experimental quench studies on an adiabatic short conductor is carried out in a cryocooled cryostat, where the short sample was thermally anchored at two current contacts, and connected via thermal links to the cryocooler head [161], [196], [197]. However, this method becomes impractical for a 2 m long Roebel cable, with long current sharing length in an isothermal condition [80].

In the present work, quench studies on Roebel cables were carried out on a simple pancake coil in order to incorporate a length of cable sufficient to achieve full development of current sharing profiles among strands. Although the simplicity of 1D quench of adiabatic conductors is lost through lateral thermal contacts; the quench of Roebel pancake coil is actually more relevant to real applications and the added complexity can be readily dealt with by suitably developed computer modelling.

We present the details of the preparation of the pancake coil, localised heater, and instrumentation setup of voltage taps and thermocouples in this chapter. The experimental results on the cable performance and quench measurements at 77 K in liquid nitrogen are decribed.

5.2 Research aim and objectives

The performance and quench measurements at 77 K in liquid nitrogen are described and analysed, and the outline of this chapter is listed below:

- To fabricate a pancake coil wound with 2G YBCO Roebel cable and set up the localised heater, and voltage taps and thermocouples.
- To investigate the critical current of the pancake coil and the current injection contacts resistance and current distribution along the current injection contact.
- To investigate quench characteristics such as the response of the strands voltages, contact voltages, hot spot temperature, and Minimum Quench Energy (MQE), with different heat pulses and different transport currents applied.
- To investigate current redistribution among the strands during the quench.

5.3 Methods and Experimental Details

5.3.1 Roebel pancake coil

Figure 5.1 shows a piece of 2 m long Roebel cable with 15 strands (5.5 mm wide) of punched 2G YBCO tapes (Bruker EST) wound into a simple pancake coil with seven turns. The cable with a transposition pitch of 226 mm was assembled at Karlsruhe Institute of Technology (KIT). A length of 200 μm thick fiberglass ribbon was co-wound as the electrical insulation layer. The inner diameter (former) of the pancake coil was ~70 mm, and every strand on the inner turn of the superconductor side, was directly soldered to the copper former as shown in Figure 5.2a. In order to match the thermal contraction of the Roebel coil with the former, a G10 core was inserted inside the copper former. On the penultimate turn, a copper ring was joined to a copper disk was slid over the assembly. The last turn of the cable was wound and soldered to the outside of the same copper ring. This configuration allows direct current injection to the superconductor side on the inside of the Roebel strands. A stainless steel shim was wound around the last turn of the Roebel cable prior to soldering for reinforcement. Current injection was via two, half meter long copper bars as shown in Figure 5.2b. The coil was vacuum impregnated with epoxy (Stycast^{TM}) [108].

5.3.2 Instrumentation

At the centre of the 4th pitch in the middle of the coil, a miniature heater (33 Ω) was soldered to a piece of copper shim and soldered on strand 7 in the middle inside face of the cable as shown in Figure 5.2a. A T-type thermocouple was soldered to the same copper shim next to the Heater 1. An epoxy impregnated fiberglass thermal insulation layer 20 mm long, 6 mm wide and 2 mm thick was applied over the heater and thermocouple. Two nickel-chrome strips (15 × 1 × 0.7 mm) were counter-wound in a series connection, to compensate the inductive voltage of the second heater (18.2 Ω) that overlapped all the strands on the outside of the coil assembly. A 50 μm thick fiberglass ribbon was applied as the electrical insulation layer between this heater and Roebel coil. A third (9.8 Ω) made from insulated constantan wire heater was attached to the strand nearby the

end of outer contact. Two additional T-type thermocouples were attached to the strands, which were adjacent to the two heaters respectively. To complete the coil assembly, a total of seven turns of 150 μm thick, 15 mm wide fiberglass ribbon was wrapped over Heater 2, Heater 3 and two thermocouples and impregnatated to act as thermal and electrical insulation.

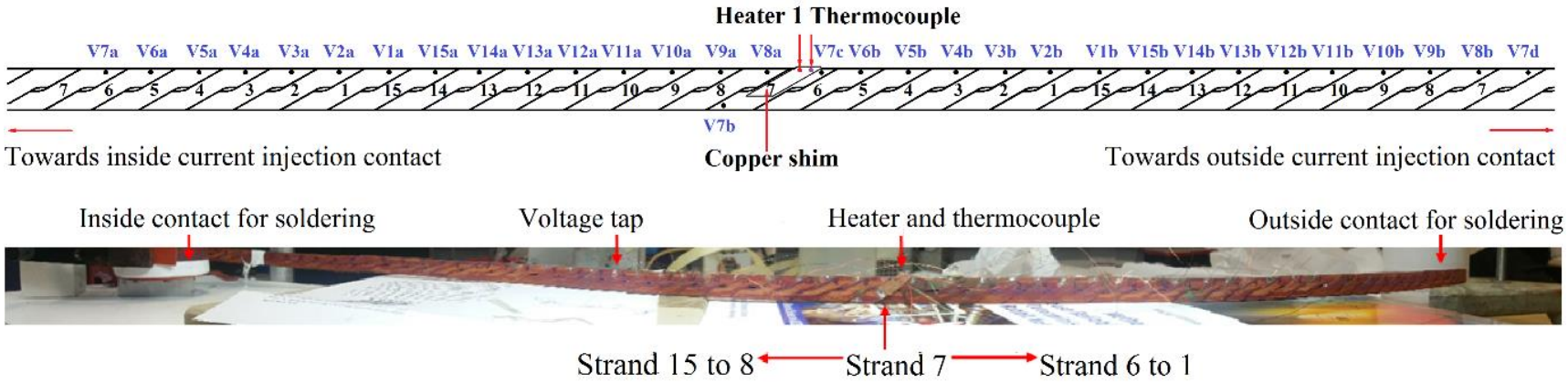

Figure 5.1: The whole scale view of the Roebel cable instalment.

A pair of voltage taps (V7b and V7c in Figure 5.1) were soldered to the strand on either side of transposition section enclosing the heater. A further pair of taps (V7a and V7d) were soldered one pitch length away from V7b and V7c and towards the inner and outer contacts. For each of the remaining 14 strands within V7a and V7d, the voltage-tap pairs (Vna and Vnb, n=1..6,8..15) were separated by one pitch length and soldered on opposite sides of the heater. The signal voltage-tap pairs (Vna and Vnb, n=1..6, 8..15) were separated by a single pitch length and were soldered on opposite side of the heater. The signal wires for each measured voltage pair V*n* (V*n*a-V*n*b) were counter-wound along the respective cable path and the then twisted together to compensate the inductive voltage. The contact voltages for each strand were also measured with the corresponding voltage-tap pair (Vc_{in} -V#n_a and Vc_{out} -V#n_b), using voltage taps Vc_{in} and Vc_{out} (far end) located on the inner and outer current terminals respectively.

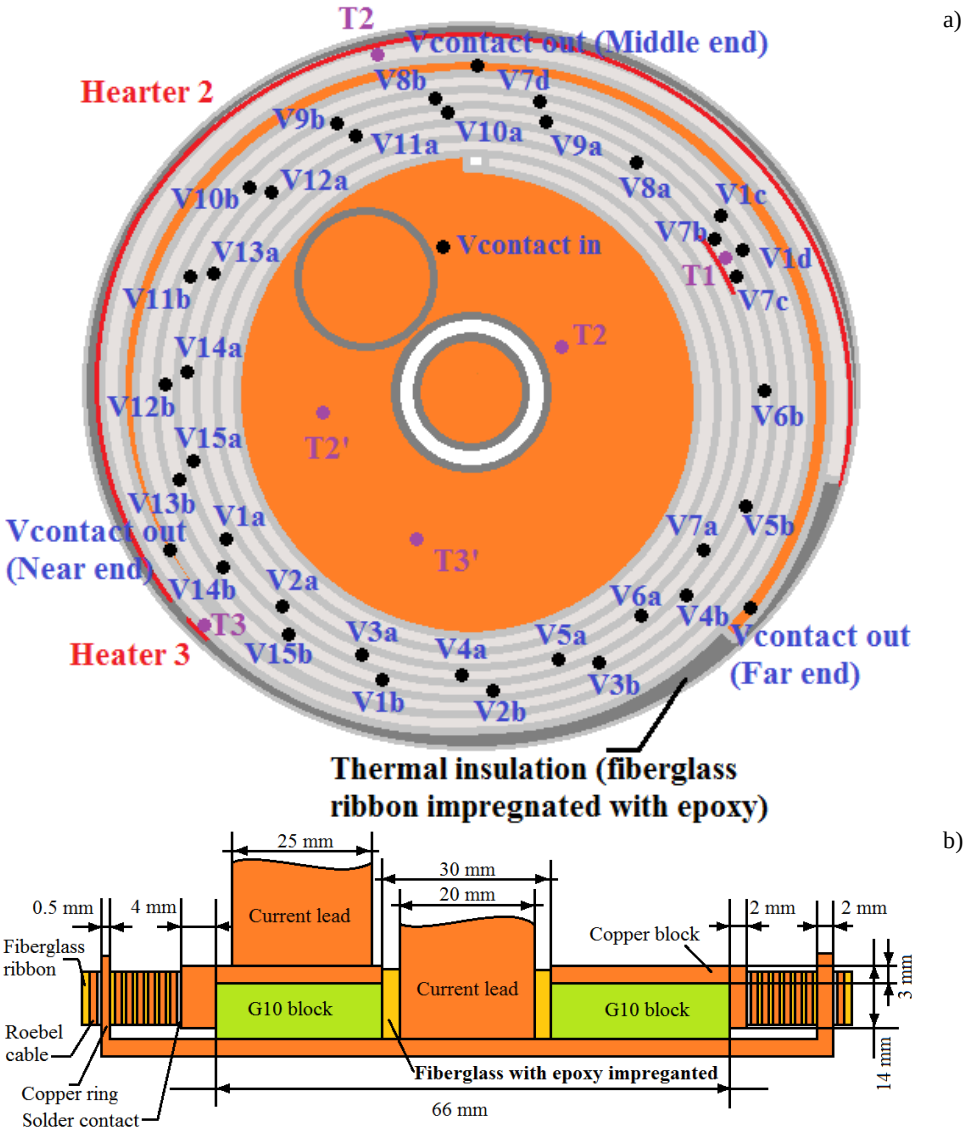

Figure 5.2: Schematic drawing of the a) top view of Roebel pancake coil to show the voltage taps (black points), heaters (red line, heater 1: 33 Ω, heater 2: 18.2 Ω and heater 3: 9.8 Ω) and thermal couple (purple points), and b) the front view of the cross-section of Roebel pancake coil to show the coil lay out and dimensions.

5.3.3 Experimental set up

Figure 5.3 shows a picture of the test bed developed to measure the performance and quench characteristics of the pancake coil wound with 2G YBCO Roebel cable. The rig was designed in such a way to enable it to be supported in an open Dewar and the coil submerged in a bath of LN2. The four corners of the supporting plate were modified to fit the top edge of the Dewar. Two current leads were connected to the current source with a 4.9 mΩ shunt load placed in a parallel connection for circuit protection. A pair of tubes made from cardboard were mounted around the extended current leads and underneath the supporting plate, to collected LN2 vapor and provide gas cooling to the current leads. The intermediate circuit board collecting the wiring looms from voltage taps, thermocouples and heaters wire was fixed at the top of pancake coil, and extended instrumentation leads with Fischer connectors were plugged into the data logger to capture and record the signal data.

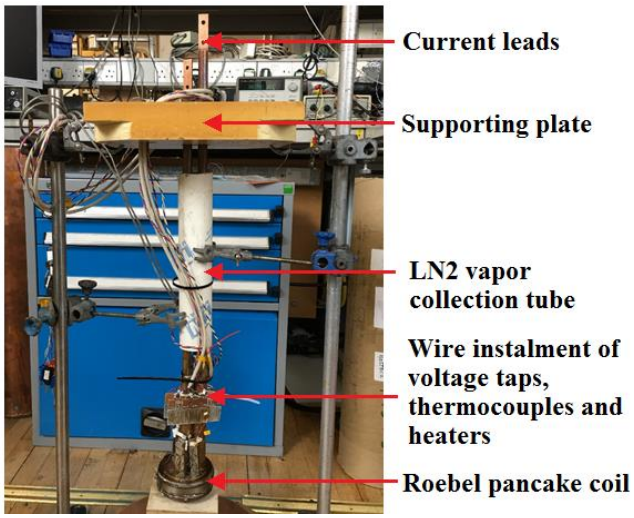

Figure 5.3: The picture for the test bed set up.

5.3.3.1. Current leads injection contact resistance and critical current and measurements

The tests presented in this section were performed with the Roebel pancake coil submerged in liquid nitrogen at 77 K. The pairs of voltage-taps were used to collect the voltage data to analyse the critical current and *VI* characteristics of the Roebel coil. The contact resistance was also measured simultaneously. Steady state local heating could be applied by Heater 1 (strand 7), and used to extend temperature range over which the critical current could be measured.

During the measurements, the inner contact voltages were found to be higher than the measured at the outer contact, when the transport current was increased above 200 A. Furthermore, there were no obvious changes observed in the outer contact voltages, while the inner contacts were always first to approach the quench condition. This was believed to be caused by the field effect on the critical current at different positions in the coil. A schematic drawing of the critical current to temperature curves (I_c vs T) for strand 7 (in the middle of the coil), and the inner and outer

contacts is shown in Figure 5.4 and the critical current is determined in accordance with Equation 5.1 [198], [199]:

$$I_c(T) = I_c(0)\frac{T_c - T}{T_c} \qquad 5.1$$

Where $I_c(T)$ is the critical current as a function of temperature, T is the temperature, and T_c is the critical temperature of the superconductor. The different slopes show the reduction of critical current with increasing temperature at different locations in the Roebel coil. The inner contact is assumed to have the highest self-field effect, and the outer contact the lowest self-field effect when both are at the same temperature and carry the same transport current. It can be seen that the critical current (I_{c1}) of outer contact is higher than that (I_{c3}) of inner contact at temperature of T_1 (unbalanced condition). Consequently, in order to make both inner contact and outer contact reach a same critical current condition at I_{c3}, the temperature at the outer contact needs to be increase to T_2 (balanced condition).

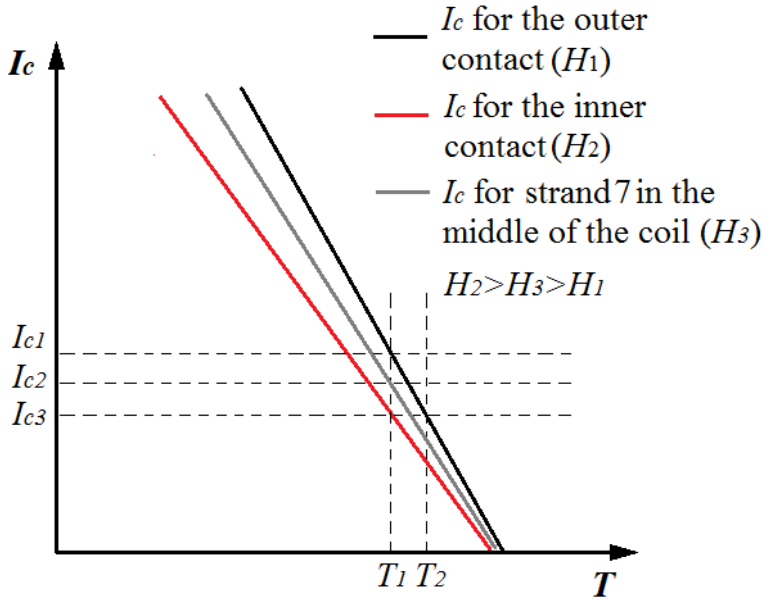

Figure 5.4: The plot of the critical current against temperature for the outer contact, the inner contact and strand 7 in the middle of the coil under different magnetic fields.

An external constant DC voltage (8.0 V) was applied to Heater 2, and this constant heat caused the temperature of the outer contact joint to increase, and in conjunction, the strand outer contact voltages also increased, making the outer contact perform in similar conditions as the inner contact, and without causing a thermal run away, when the transport current approached the critical current. Thereafter, the nominal critical current (I_{c2}) of the strands in the middle of the coil were defined by moderating heat applied to the steady state local via Heater 1 on strand 7, in order to extend the critical current measurements at higher temperatures. A series of quench measurements were conducted in the middle of the coil, using this methodology referred to as the 'balanced' quench measurement in future discussions.

5.3.3.2. Quench measurement

Further quench measurements were conducted at a given transport current range (350-450 A) by applying a heat pulse to the localised heater on strand 7 at 77 K in LN2. The heat pulse was triggerred by applying a constant DC voltage to create a local thermal disturbance in the middle turn of the coil. The time dependence of temperature at the hot spot, strand voltages and strand current injection contact voltages were monitored using the thermocouples and volatge taps connected to the data logger, recording at a sampling rate of 100 Hz. The minimum quench energy was determined by increasing the pulse power intensity and pulse duration until all strands developed a thermal run-away. Once a quench event was triggered, the Roebel cable pancake coil was allowed to cool down for ~10 minutes before conducting any further measurements. This procedure was essential to ensure the thermal condition of the coil was fully restored to enable capture of repeatable data.

To determine the minimum quench energy (MQE), the known magnitude and duration of the heat pulse was applied to Heater 1 (33 Ω) on the strands and used to calculate the applied energy, which is considered to be the MQE required to induce quench of the Roebel cable in an adiabatic condition. This energy applied by the heater is obtained by Equation 5.2:

$$MQE = \frac{V_h^2}{R_h} \times t_p = P_h \times t_p \qquad 5.2$$

Where V_h is the pulse voltage across the heater, R_h is the resistance of the heater, P_h is the heating power and t_p is the length of the pulse. The voltage and current applied on the heater remained constant during the measurement and the resistance of the heater did not change when the temperature was increased. It should be noted that the heat pulse is not a uniform square wave, especially the when the pulse is initially triggerred and switched off. A more accurate calculation can be achieved by the integrating the area from the voltage pulse as shown in Equation 5.3:

$$MQE = \int_0^{t_p} \frac{V_h^2}{R_h} dt \qquad 5.3$$

For these experimental measurements, the MQE was defined by taking the mean value between two pulses and considered the irreversible quench and the recovery.

5.3.4 Data logger and Protection

A parallel shunt resistor (R_{shunt} = 4.7 mΩ) was connected to protect the Roebel coil at room temperature. The shunt voltage (V_{shunt}) and the total current (I_{total}) are used to obtain the coil current that I_{coil} is obtained by Equation 5.4:

$$I_{coil} = I_{total} - \frac{V_{shunt}}{R_{shunt}} \qquad 5.4$$

A communication data-logger (NI SCXI-1300 signal conditioning module) and LabVIEW software were used to the create the measurement interface for collecting and recording data. Two Agilent 6671 DC current power sources were placed in parallel connection and controlled by LabVIEW software to ramp the current in a controlled mannor. A switch was used to cut off the

power from the DC power source when any voltage exceeded 6 mV. The output limits of theDC power source was set to a maximum voltage at 0.6 V for all the measurements.

5.4 Results and Discussion

5.4.1 Current injection contacts resistance

Both the inner and outer contact voltages of each strand were measured as a function of current and shown in Figure 5.5. The overall inner resistance is around 0.25-0.3 μΩ. The nominal contact resistance per strand is around 4.2 μΩ (9.83 μΩ×cm^2), which is almost double of the overall contact resistance (~4 μΩ×cm^2) of lap joint for a single strand. The overall outer contact resistances are around 0.28 μΩ and 0.098 μΩ, measured by the voltage taps located at the near and far ends of the copper ring respectively. This difference seems to imply that the current injection was inhomogeneous among different strands on the outer copper ring, and neither the near nor far ends included all of the current passing through the contacts. According to the inner contact resistance (around 0.25-0.3 μΩ), the value of 0.28 μΩ may be closer to the real overall outer contact resistance.

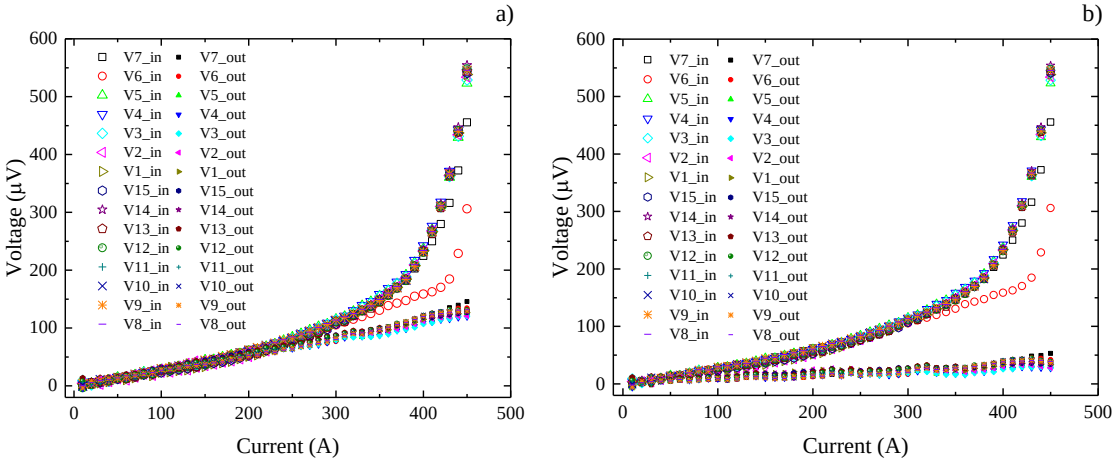

Figure 5.5: The plot for a) inner (open symbols) and outer (filled symbols) contact voltages (tap on the near end) and b) inner (open symbols) and outer (filled symbols) contact voltages (tap on the far end) of all the strands as a function of transport current at 77 K.

The inner contacts (open bars shown in Figure 5.6) correlate well with the behaviour of the outer contacts. The nonlinearity of *VI* characteristics for the inner contacts is likely caused by the field effect on the critical current at the inner turns. The strands with lower voltages may have a larger current share, which leads to the maximum shown on corresponding outer contacts.

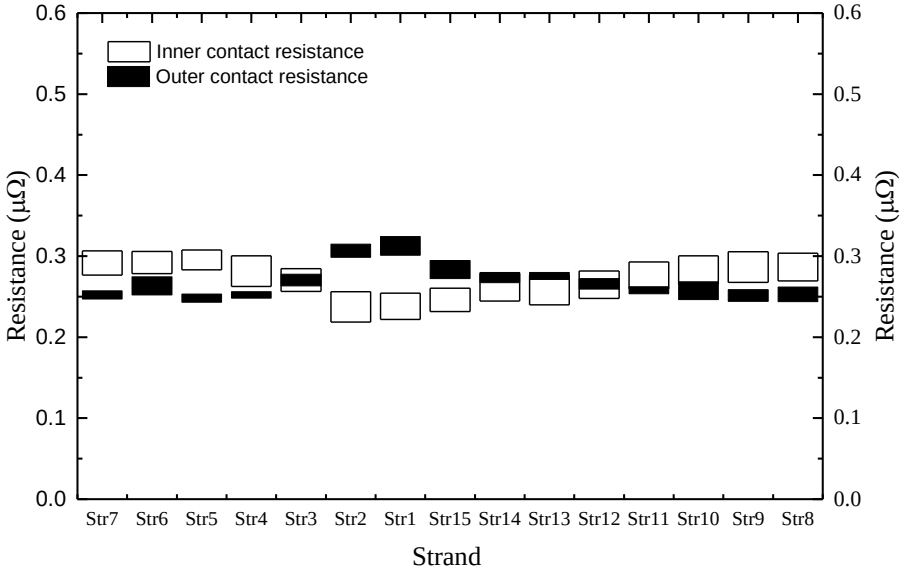

Figure 5.6: Apparent inner (solid bars) and outer (open bars) contact resistances according to voltage taps on different strands (outer contact voltage tap is on the near end) at 77 K.

It needs to be noted that both the inner and outer contact resistances presented also partly include a proportion of resistance attributed to the current leads. In addition, the inner contact voltage taps soldered at the top of the round copper block includes more copper resistance, compared to the outer contact voltage tap fixed at the end (near and far end) of the copper ring. In order to estimate the effect of the copper block upon the contact resistance measurements, a simple copper cylinder contact model was study to represent the inner contact copper block shown in Figure 5.7a. A schematic drawing including dimensions is shown in Figure 5.7b. The maximum copper block resistance can be obtained by Equation 5.5:

$$R_{copper} = \frac{\rho}{2\pi d} ln(\frac{b}{a}) \qquad 5.5$$

Where ρ is the resistvivity (~1.8 nΩm) of the copper at 77 K, a (15 mm) is the radius of the current lead, b (around 33 mm) is the radius of the copper block, and d (around 3 mm) is the width of the copper block. The copper block resistance R_{copper} is ~75.2 nΩ in total, which is approximately 25% of the total experimental contact resistance. Consequently, this may suggest that the contact resistance developed by the soldering is the main contribution to the measured resistance.

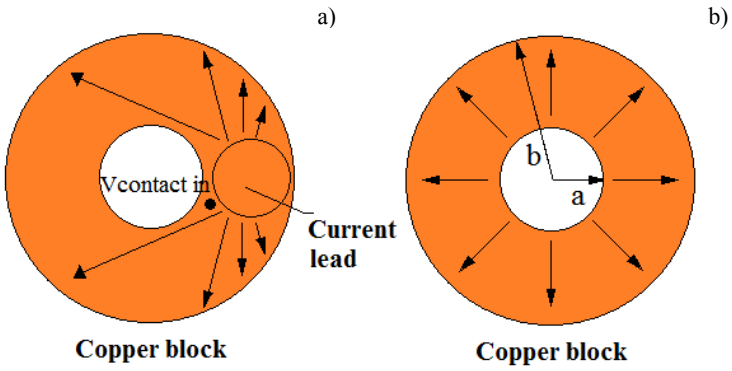

Figure 5.7: a) Schematic drawing of the top side of the copper block and b) the assumed copper block model for the inner contact of the pancake coil.

5.4.2 Nonlinearity of the inner contact voltage

Figure 5.8 shows the *VI* characteristics of each strand (end to end voltage involving two current lead injection contact voltages and strand voltages) with different transport currents from 0 to 450 A. The trend plotted are very similar among all the strands. This is confirmed by the parallel electrical network for each strand shown in Figure 5.9 and worth noting that the nonlinearity in the current above 200 A is shown by the inner contact voltages in Figure 5.5.

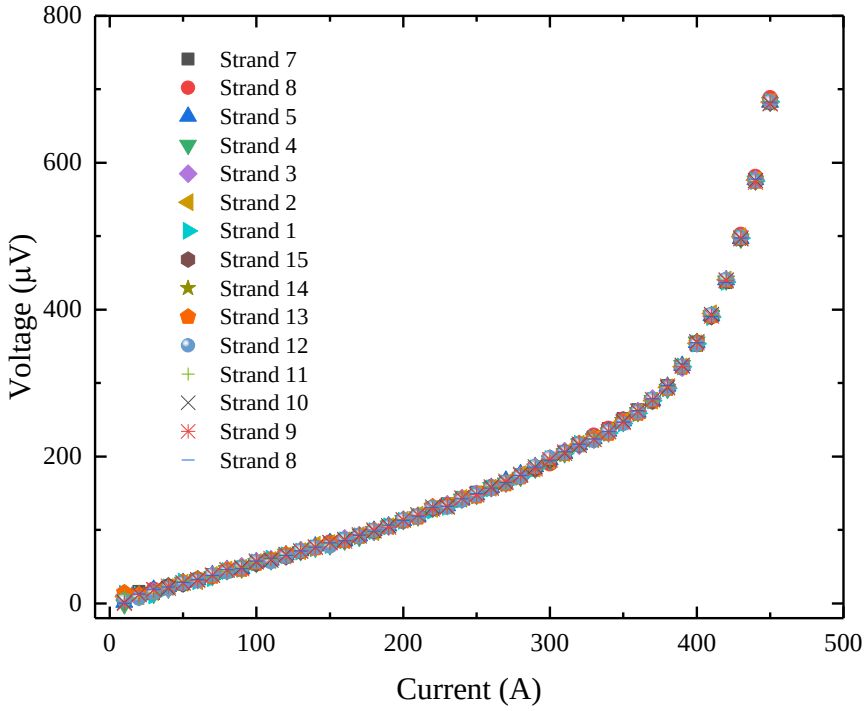

Figure 5.8: *VI* characteristics of each strand (end to end) with the current from 0 to 450 A at 77 K.

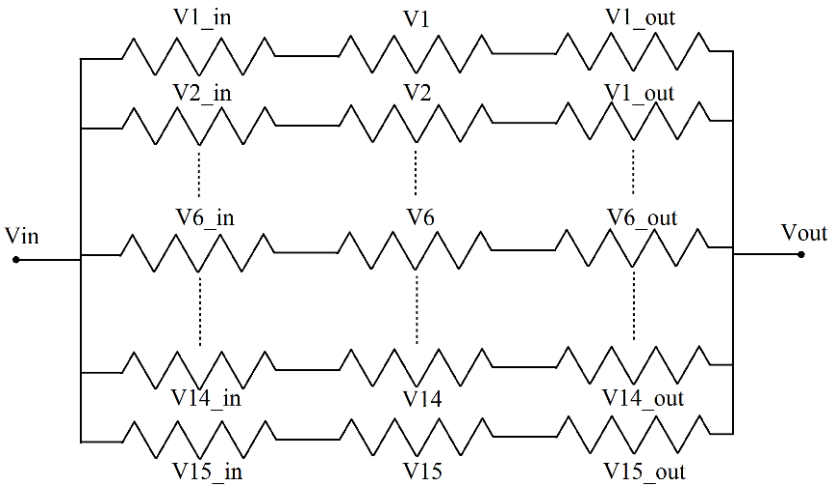

Figure 5.9: Schematic drawing of the end to end elctrical network of the roebel pancake coil.

Figure 5.10 shows the inner contact voltage where the overall contact resistance has been subtracted as a function of current using the standard 1 μVcm^{-1} criteria (blue dash line), and the inner contact voltage of strand six is shown to increase much less compared with other strands, when the total current increases.

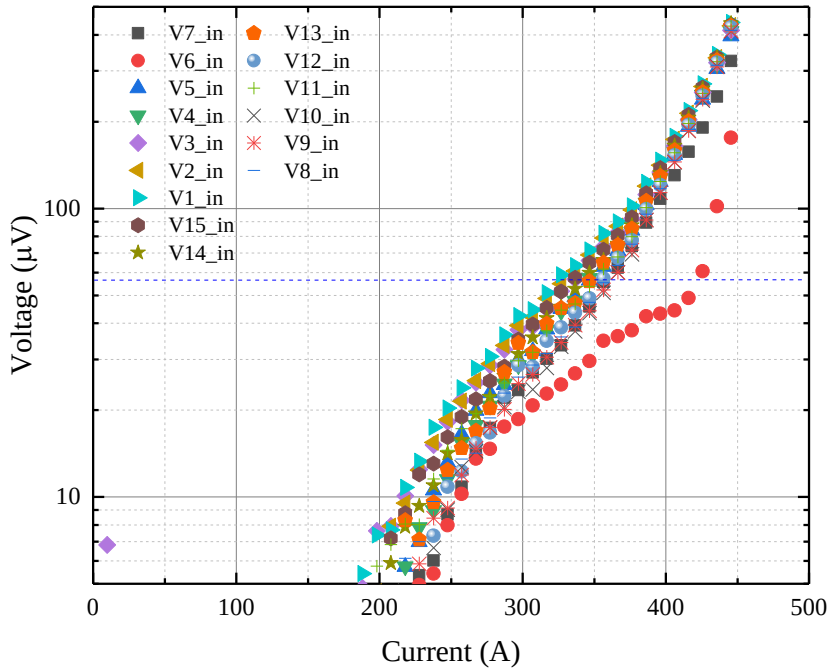

Figure 5.10: *VI* characteristics (contact resistance subtracted) of each strand inner contact with the current from 0 to 450 A at 77 K, and the blue dash line represents 1 μVcm^{-1} criteria.

The power law as shown in Equation 5.6 is applied to further analysis of the strand contact *VI* characteristics:

$$V_{con} = R_{con}I + E_c l(\frac{I}{I_c})^n \qquad 5.6$$

Where V_{con} is the contact voltage, R_{con} is the contact resistance, I is the current in the coil, E_c is 1 μVcm^{-1} criteria, l is the length of the strand, and I_c is the critical current. The contact voltage derives from two parts, i.e. the contact resistance and strand metal matrix resistance. When the total DC current is below 200 A, the current in the contact of each inner strand should only depend on the contact resistance. This part is recognised as the linear component of *RI* shown in Equation 5.6. When the total current is above 200 A, the current in each inner strand contact is mainly driven by the critical current of the inner turn where the parallel field is the highest, which is the non-linear part $E_c l(I/I_c)^n$ as shown in Equation 5.6. Table 5.1 shows the *n*-value of each strand within the inner turns of the coil, which values are between 9.7 and 11.25 except the strange strand 6. The *n*-value of a single strand in self-field is around 20. The field effect on the reduction of critical current of inner turns of the assembled cable, causes the decreasing of the *n*-value for all the strands.

Table 5.1: *n*-value of each strand in inner turns of the coil.

Strand No.	Inner contact end to strand		Strand No.	Inner contact end to strand	
	Critical current I_c (A)	*n*-value		Critical current I_c (A)	n-value
7	347.3	9.72	***14***	347.1	10.48
6*	N/A	N/A	***13***	348.0	10.65
5	327.4	10.11	***12***	357.5	10.90
4	327.2	10.29	***11***	352.5	10.84
3	317.1	9.90	***10***	362.9	11.22
2	311.7	9.72	***9***	362.4	11.18
1	307.8	9.73	***8***	359.9	11.12
15	336.0	10.03			

*Strand 6 was not taken into consideration.

5.4.3 Current distribution along the outer strand contacts

Seven stainless steel needles were punched into the outer contact copper ring and copper disk as shown in Figure 5.11. Twelve pairs of voltage taps were applied to measure the voltages along the cooper ring (27 mm long, 2.5 mm wide) and voltages between the copper ring and copper disk. Three pairs were applied to measure in a vertical direction and the copper ring was divided into two parts by the tap position at near end, middle end and far end repectiviely. Six pairs were applied to measure in horizontal direction, which are top near end to top far end (V31), top middle end to top far end (V21), top near end top middle end (V32), bottom near end to bottom far end (V46), bottom middle end to bottom far end (V56) and bottom near end to bottom middle end (V46). Another three pairs between the positions (4, 5 and 6) at the bottom of the copper ring and the copper disk (V47, V57 and V67).

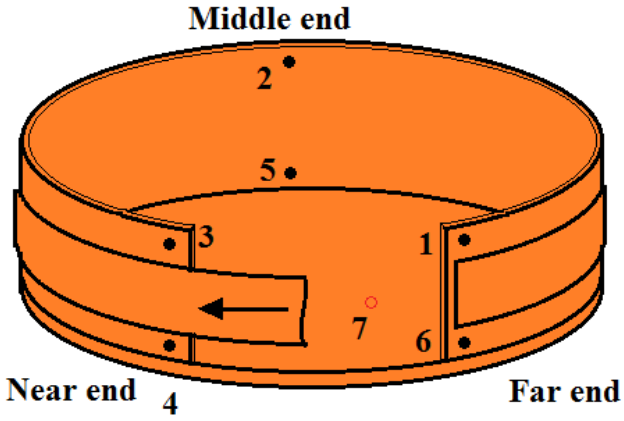

Figure 5.11: 3D schematic drawing of the outer contact shows the outer contact copper ring with 6 voltage taps layout, and number shows the position of the voltage taps (1: Top far end, 2: Top middle end, 3: Top near end, 4: Bottom near end, 5: Bottom middle end, 6: Bottom far end and 7: Underneath of the copper disk).

5.4.3.1. Current distribution along the outer contact copper ring at 77 K

Figure 5.12 shows nine voltages on the copper ring plotted as a function of the current from 0 to 450 A without any heat applied. Seven voltages increase linearly with the increase in transport current, and four voltages, top near end to top far end (V31), top near end to top middle end (V21), bottom near end to bottom far end (V46) and bottom near end to bottom middle end (V45) show negative polarity.

Furthermore, the bottom near end to bottom far end voltage (V46) is almost the same as the bottom near end to bottom middle end (V56). This behaviour is consistent with the voltages measured across the bottom middle end to bottom near ends of the winding. Figure 5.13 shows three voltages, bottom middle end and copper disk (V57), bottom far end and copper disk (V67) and bottom near end and copper disk (V47) plotted with respects to current from 10 A to 50 A. Voltage tap V57 is almost equal to V67, and both of them are larger than V47. This seems to be the main location where current injected from the copper ring to the copper disk disperses between the middle and far ends.

Outputs from the three vertical voltages are plotted as a function of the position (the near end, middle end and far end) at each current step is shown in Figure 5.14. The whole length of the copper ring was around 27 cm, and the position of the far end, middle end and near end taps were assumed to be 0 cm, 13.5 cm and 27 cm respectively. It is obvious that the local vertical voltage increases from the far end to the middle end at each current step. Then the local current density (J_{local}) in unit of A/m can be estimated by:

$$J_{local}(x) = \frac{I_{outer}(x)}{A} d_{copper}(x) = \frac{V_{outer}(x)}{R_{outer}A} d_{copper}(x) = \frac{V_{outer}(x)}{\rho_{copper} l_d} d_{copper}(x) \qquad 5.7$$

Where $V_{outer}(x)$ is the local vertical voltage, $I_{outer}(x)$ is the local current, R_{outer} is the copper resistance and $d_{copper}(x)$ is the thickness of copper at the postion of near end (~ 0.5 mm), middle end (~ 2 mm) and far end (~ 2 mm), and ρ_{copper} is the copper resistivity (~1.8 nΩ×m) at 77 K, and l_d is the distance (1.5 cm) between two voltage taps in vertical direction. The estimated overall transport current in accordance with the current density:

$$I_{outer} = AJ_{average} = W_{copper} d_{average} (J_{near\ end} + J_{middle\ end} + J_{far\ end})/3 \qquad 5.8$$

Where I_{outer} is the overall current, $J_{average}$ is the overall current density in units of A/m^2, $J_{near\ end}$, $J_{middle\ end}$ and $J_{far\ end}$ are the local current densities in units of A/m^2, A is the copper ring cross section, W_{copper} is the length (27 cm) of the copper ring, and $d_{average}$ is the average copper thickness (~ 1.5 mm) of the copper ring. The local vertical current densities and estimated transport current are shown in Table 5.2.

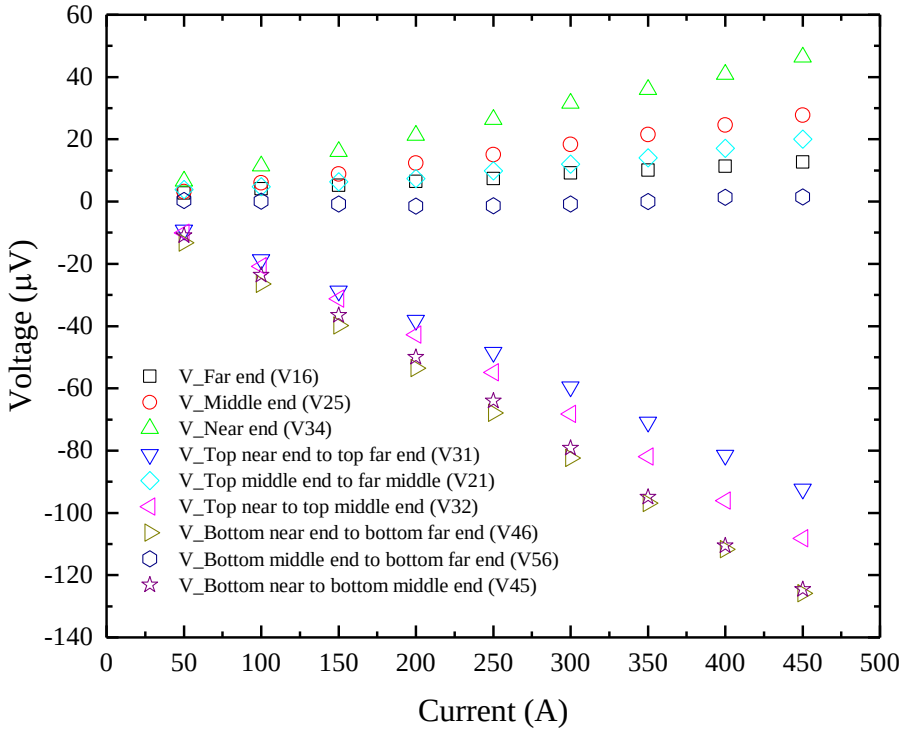

Figure 5.12: The plot for voltages measured on the outer contact copper ring with a current from 50 A to 450 A at 77 K.

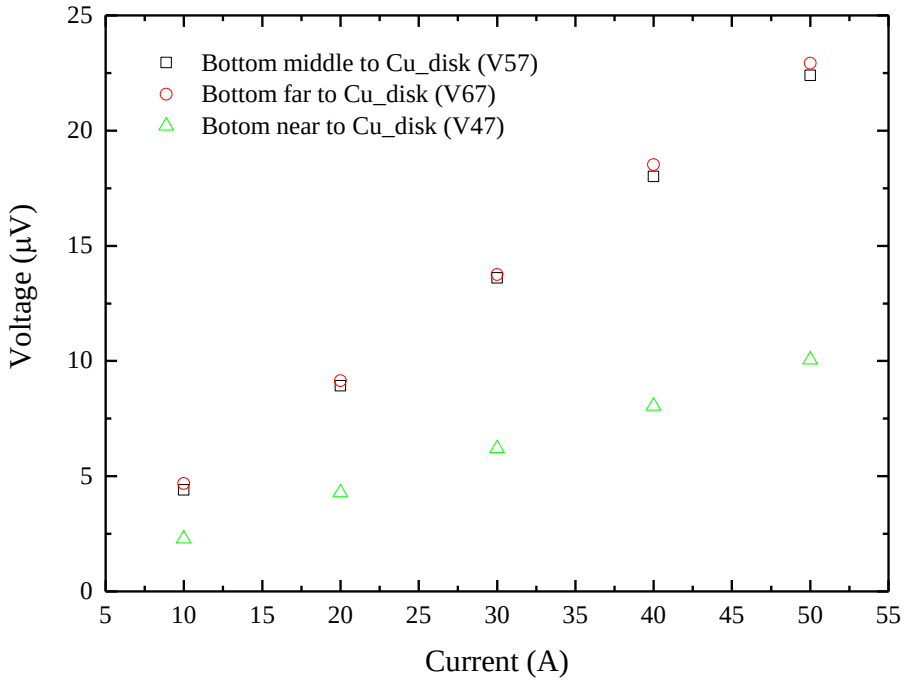

Figure 5.13: The plot for the voltage across bottom middle end and copper disk (V57), bottom far end and copper disk (V67) and bottom near end and copper disk (V47) separately with a transport current from 10 A to 50 A at 77 K.

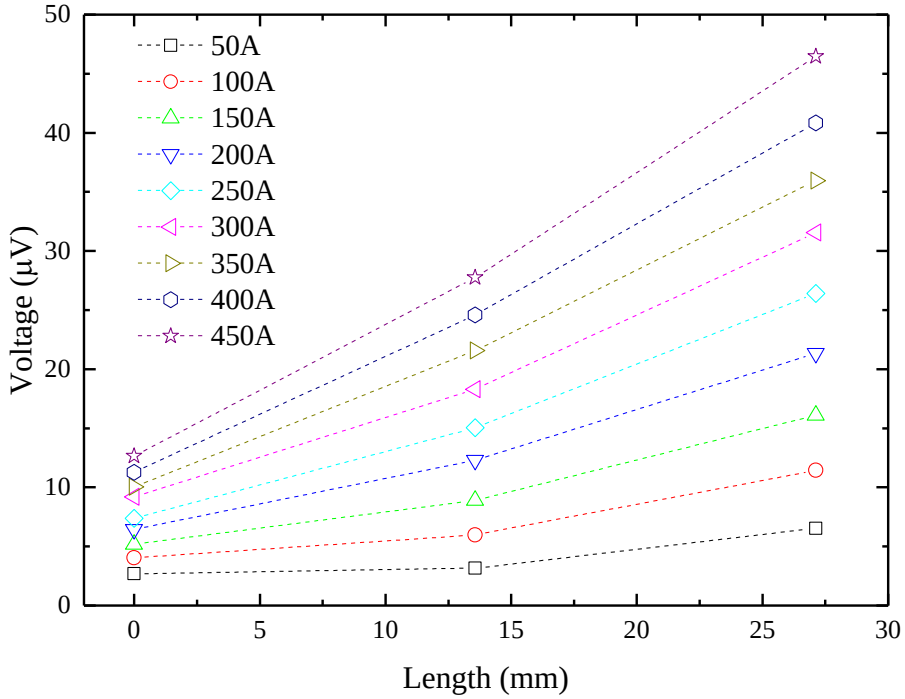

Figure 5.14: Far end, middle end voltage and near end vertical voltages on the copper ring versus the position from far end to near end with different transport currents from 50 to 450 A at 77 K.

The thickness of the copper ring changes from 0.5 mm (near end) to 2 mm (far end). If there is an even contact resistance along the joint with a homogeneous current distribution, then the thin wall of the copper ring should produce a larger resistance, and will exhibit higher local voltages, which is true for the vertical voltage (V34) at near end. However, the estimated local current density result presented in Table 5.2 implies the local vertical current density at middle end is the highest,

which corresponds to the highest current injection occuring towards the middle end of the winding assembly. This is in agreement with the assumption suggesting the main current injection occurs between the middle end and far ends, and the negative voltages observed along the copper ring come from the near end to far end, and therefore is evidence of current flowing back along the copper ring between near end and middle end.

Table 5.2: Vertical current density at near end, middle end and far end positions and estimated transported current at 77 K.

Current	Local current density (A/m)			Calculated current I_{outer} (A)
	Far end	Middle end	Near end	
50 A	200.02	233.72	120.98	62.94
100 A	299.89	443.19	211.99	107.39
150 A	383.71	658.43	298.19	150.85
200 A	476.56	911.79	394.96	200.35
250 A	547.08	1114.79	489.17	244.25
300 A	681.65	1355.32	584.58	295.33
350 A	743.74	1597.80	665.97	337.86
400 A	835.47	1820.42	756.35	383.48
450 A	936.53	2055.64	860.18	434.22

It was known that the polarity of V46 (bottom near end to bottom far end) and V13 (top near end to top far end) were indeed opposite to the direction of the current flowing along the cable. Two hypothesis were considered to explain this phenomena; which includes the possibility of having differences in the quality of the soldered contact between the cable and copper ring, creating larger contact resistance in the copper ring, compared with the smaller internal contact resistances among the strands. This could initiate the current sharing among the strands and the dynamics of thermal transport would evolve behaving more so like a “lumped cable”, forcing more current transfer towards the far end of the cable. The increasing thickness of the copper ring from near end to far end will also contribute to this effect. The analytical model discussed in previous subchapter 4.3.1.1 for the lap joint between two conductors has confirmed this behaviour.

Another possibility was for inhomogeneities in the soldered contacts between the cable and copper ring arising due to differential thermal contraction. For instance, the copper ring at near end side was thinner and more compliant with more freedom to accommodate to any deformations that arise in the structure during cooling. In addition, the space underneath of the bottom copper disk (see in Figure 5.2b) could fill up with liquid and have a different rate of contraction compared to the top. Any small deformations could distrub the soldered contact between the cable and the copper ring at near end side and change its resistance. Furthermore, there is a total of 18 contacts on the copper ring, and this means that there are three strands that make contact with the copper ring twice. Consequently, the current flowing within the first three strands may divert into the copper ring towards the far end side instead of the near end side creating a reverse flow back of current.

In response, to these finding two 3D models were developed to verify these two considerations using COMSOL Multiphysics base on Ohm’s law and using the scalar electric potential as the dependent variable. The geometrical outline of the two models are shown in Figure 5.15. The first

model in Figure 5.15a considered a total of 15 strands compiled as a lumped cable, with an even and consistent soldered contact made along the copper ring. This model was used to verify the application of different contact resistances and the resulting effects upon on the current distribution. The current injection terminal was set at the domain towards the near end side, and the ground was set at the central cylinder of the bottom copper disk. The second model as shown in Figure 5.15b was constructed in such a way that a total of 18 overlapped blocks made up the copper ring. This would enhance the investigation and provide the ability to adjust and simulate the current transfer in each strand through the cross-sectional interface.

In this model design, the contacts are allocated as the current injection terminals in accordance with the earlier assumption. The key geometrical and material properties of the two models are presented in Table 5.3. The geometry of the pancake coil was taken from the coil produced for the experimental work. In order to simplify the geometry in the modelling environment, a nominal thickness of (2 mm) was taken as the thickness of the copper ring used in the model, and each independent section designated for current transfer was simplified and represented by a rectangular block.

Key material properties of the superconductor (YBCO), i.e. resistivity was assumed as 1.8×10^{-12} Ω×m (1/1000 of copper resistivity at 77K). A transport current of 300 A was applied to the terminals in model 2, with a zero current injected in the first three blocks at near end side of the coil assembly and a 20 A current injected in each of remaining 15 blocks. This setup means the first three strands that overlap the copper ring in the experimental coil, had current injected through the contacts towards the far end. Furthermore, the overall contact resistance obtained from the experimental work was around 8.8 $\mu\Omega cm^2$. Consequently, the contact resistance was swept from 7.5 to 11.2 $\mu\Omega cm^2$ in model 1 simulations, and the contact resistance was fixed at 8.8 $\mu\Omega\times cm^2$ in each of the contact block in model 2 simulations.

Table 5.3: The parameters setting up of two models at 77 K.

Parameters	Model 1	Model 2
Copper ring length (mm)	270.0	270.0
Copper ring width (mm)	26.6	26.6
Copper ring thickness (mm)	2	2
Copper resistivity @77 K (Ωm)	1.8e-9	1.8e-9
Cable length (mm)	270.0	13.7*
Cable width (mm)	13.0	13.0
Cable thickness (mm)	1.5	1.5
Cable (YBCO) resistivity (Ωm)	1.8e-12	1.8e-12
Contact resistance @77 K ($\mu\Omega cm^2$)	7.5 - 11.2	8.8
Bottom copper disk radius (mm)	52.5	52.5
Bottom copper disk thickness (mm)	0.604	0.604

*The single contact length is 13.7 mm.

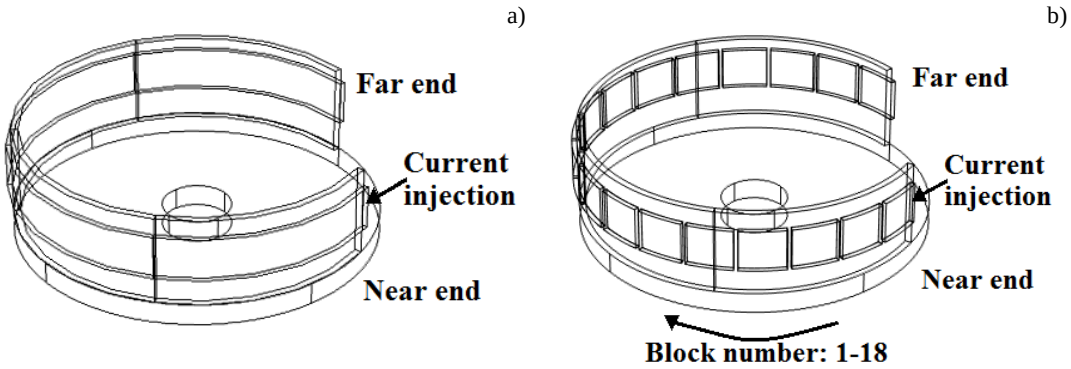

Figure 5.15: The geometry plot for the a) Model 1 with current of 300 A that injected at near end and b) Model 2 with current 300 A for block 1-3: 0 A, and block 4-18: 20 A that injected at each block.

Figure 5.16 summarises the results from the two models, and compares the surface potential. The surface arrows show the direction of flow of current density, and the voltage potential along the top and bottom edges of the copper ring. The surface potential plot of model 1 in Figure 5.16a shows the potential at the middle of the copper ring is the highest, and the voltage starts to decrease from the middle, moving outward towards the ends (far end and near end), where the terminals are located. This finding is in agreement with the two line potential profiles generated to show the behaviour in the middle of the copper ring in Figure 5.16e. The line potential at the top is larger than at the bottom, which also agrees to the positive polarity of three measured vertical voltages. Furthermore, the small difference between each potential profile in models 1 and 2, demonstrates how varying the contact resistance in model 2, does not influence the voltages accumalated in the top and bottom edges of the copper ring.

Figure 5.16c presents the plot showing the direction of flow of current density. In the same figure, the arrow in the copper ring indicate how a small amount of current is able to flow backwards from the middle end to the near end of the winding. In contrast, the profile of voltage potential along the copper ring is almost symmetrical and indicates how the current may transfer from the cable to the copper ring from the near end to far end. This behaviour does not correspond with the trends observed during the experimental measurements, where there was conclusive evidence of negative voltage difference emerging between the near end and far end of the coil.

In model 2, Figure 5.16 (b and f) do not show any sign of a negative voltage difference between near end and far end of the coil, and neither is this highlighted in the two electric potential profiles along the copper ring. However, Figure 5.16d shows the direction of the flow of current density in the surfaces and it can be seen majority of the current in the copper ring flows concurrently with the direction of current flow in each strand; but in the section labelled (middle end to near end), there are indications that a small portion of the current may indeed flow back into the copper ring.

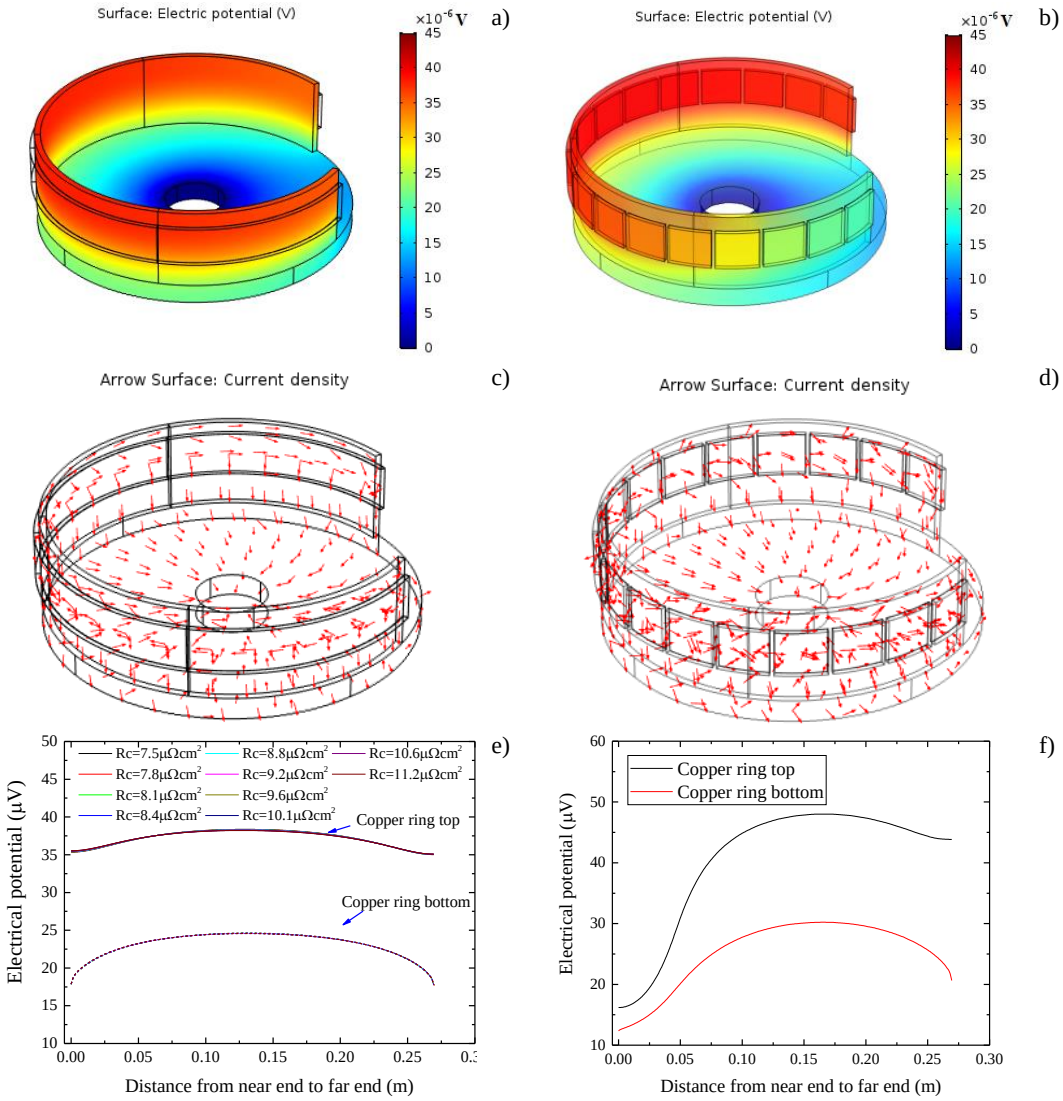

Figure 5.16: The plot of a) surface electrical potential of model 1 and b) surface electrical potential of model 2 and c) surface arrow of current density for model 1 and d) surface arrow of current density for model 2 and e) line electrical potential of both top and bottom edge of the copper ring with contact resistance from 7.5 to 11.2 μΩcm^2 for model 1 and f) line electrical potential of both top and bottom edge of the copper ring for model 2. The transport current is assumed as 300 A, and the temperature is assumed at 77 K.

Table 5.4 shows the summary of the horizontal voltages along the copper ring simulated by the two models and the experimental measured results at 77 K. The direction current flowing from near end to far end is assumed as the positive. In model 1, all the strands were assumed as a lump cable, and the current injection terminal was defined at the cross-section domain at near end. The surface electrical potential and line potential on the copper ring indicate the minimum effect of varying contact resistance on the homogeneous current distribution on the copper ring. The polarity of all the horizontal voltages from model 2 has a good agreement with the measured results, but there are large difference in values between the model and measured results espeially for the bottom side voltages.

In model 2, the first three strands were assumed as zero current transfer to simulate a bad contact at the near end side. The model provides one possibility to explain the current distribution along

the copper ring and the reason for the unusual polarity of the voltage along the copper ring. However, the independent current injection set up cannot verify the details of real current transfer of each strand and the current sharing among each strands before all the current transfers to the copper ring. Furthermore, six voltage taps along the copper ring cannot define the amount of current transfer locally at each strand current transfer section that face the copper ring. More voltage taps needed to be applied to the measurement, to fully trace the voltage on the copper ring and investigate the current transfer in details for all strands.

Table 5.4: The summary of the horizontal voltages along the copper ring in accordance with model 1, model 2 and the experiments results at 77 K (V31: Top near end to top far end, and V32: Top near end to top middle end, V21: Top middle end to top far end, V46: Bottom near end to bottom far end, V45: Bottom near end to bottom middle end and V56: Bottom middle end to bottom far end). The transport current is 300 A.

	Current flowing direction	**V31 (μV)**	**V32 (μV)**	**V21 (μV)**	**V46 (μV)**	**V45 (μV)**	**V56 (μV)**
Model 1	Positive	~0	-3.4	3.4	~0	-6.8	6.8
Model 2	Positive	-28	-33	5	-8.5	-17.5	9
Experiments	Positive	-57	-68	12	-80	-79.7	~0

5.4.3.2. Current distribution along the outer contact copper ring at room temperature

The same measurement was performed with a current from 5 A to 20 A at room temperature in order to check the uniformity of current distribution on the copper ring between the low temperature case at room temperature. The polarity of the transport current was the same as that of the measurement performed at 77 K. Figure 5.17 shows the results for nine voltages (V16, V25, V34, V31, V21, V32, V36, V56 and V32) on the outer contact copper ring and three voltages (V57, V67 and V47) across the bottom copper disk. All the voltages on the copper ring increase linearly with the increasing transport current. They keep the same polarity with the current flowing direction, which is different from the situation at 77 K. Furthermore, the three voltages across the bottom copper disk imply the highest current density was found between the bottom near end and copper disk, and this is also different from the situation at 77 K.

Three measured vertical voltages reflect the local current density in the vertical direction at the near end, middle end and far end on the copper ring respectively. Table 5.5 shows the vertical current density at near end, middle end and far end positions at room temperature. The highest local vertical current density appears at near end on the copper ring, and the magnitude of the current density at near end side is almost two times larger than that of the middle end. This estimation agrees to the highest measured voltage found across the near end and bottom copper disk. This implies the current injection from the Roebel cable to the copper ring occurs towards the near end side at room temperature.

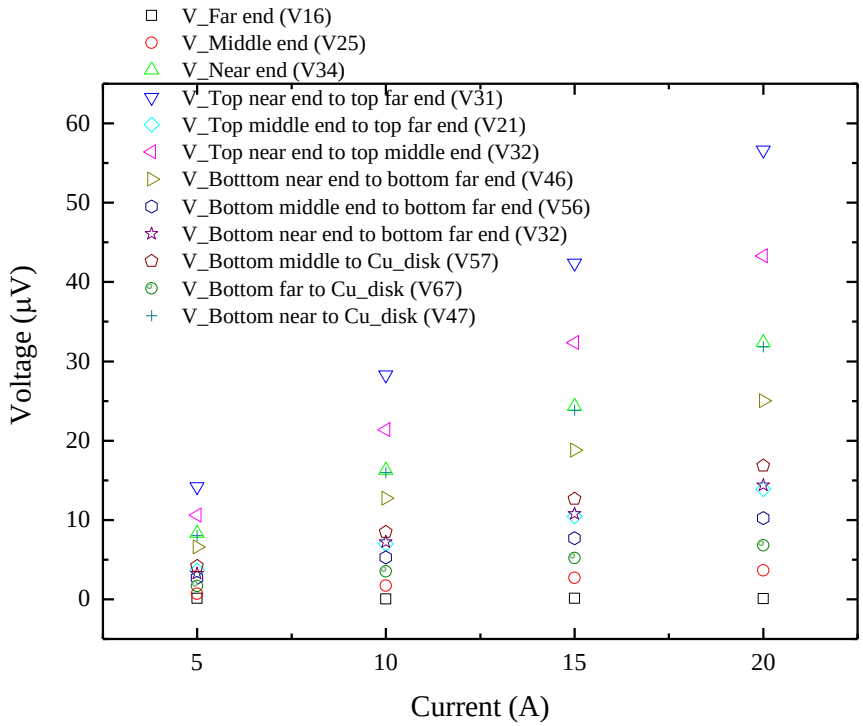

Figure 5.17: The plot for voltages measured on outer contact copper ring with a current from 5 A to 40 A at room temperature.

***Table 5.5*:** Vertical current density at near end, middle end and far end positions and estimated transported current at room temperature.

Current (A)	Local current density (A/m)			Calculated current I_{outer} (A)
	Near end	Middle end	Far end	
5	15.39	5.26	6.66	4.96
10	30.08	12.84	1.74	9.11
15	45.05	20.04	7.15	13.99
20	59.93	26.98	3.78	18.26

The current transfer between the Roebel cable and copper ring corresponded to the local contact resistance between each strand and copper ring and inter uncontinuous contact resistance among each strand at 77 K. But for the room temperature case, the situation would be more complex. Because all the strands that overlapped the copper ring became resistive at room temperature, especially the three strands that had one extra pitch length compared with other strands, and therefore included more copper resistance compared to other strands. The current transfer between each strand and the copper ring would be a combination of the local contact resistance between each strand, copper ring inner uncontinuous contact resistance among each strand, and strand copper resistance. Consequently, the *VI* characteristics of each strand and both inner and outer strand contacts need to be known. Figure 5.18 shows the *VI* characteristics of each strand with a transport current from 5 A to 20 A at room temperature. All the strands show a homogeneous voltage at each current due to a parallel connection among each strand, and the nominal resistance of each strand with one pitch length (22.6 cm) is around 910×15 μΩ.

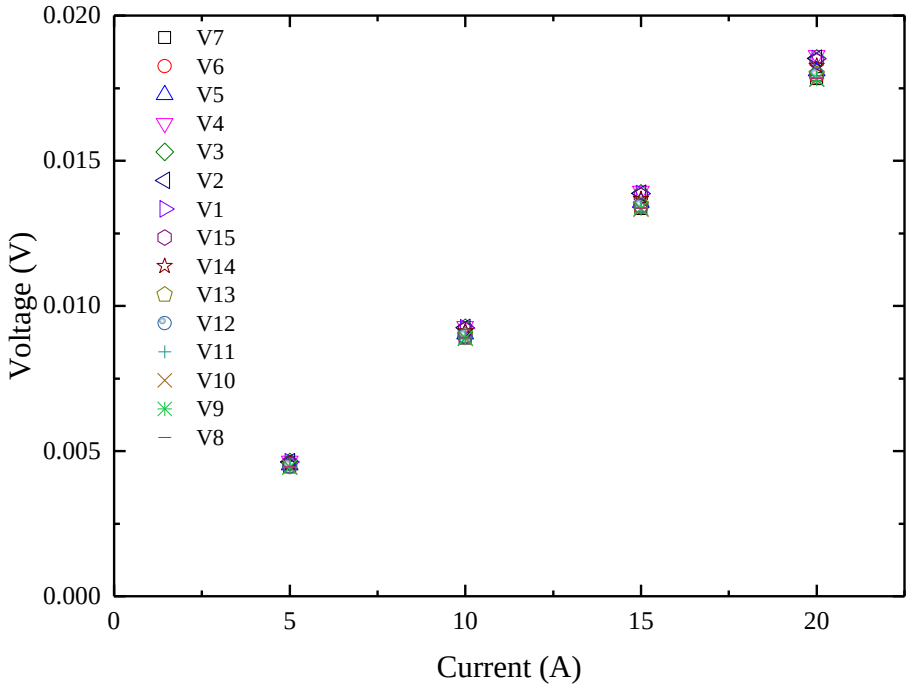

Figure 5.18: The plot for *VI* characteristics of each strand within the pancake coil at a transport current from 5 A to 20 A at room temperature.

Figure 5.19a shows the plot for both inner and outer contact voltages for each strand at a transport current of 0.5 A, and the strand number sequence in *x*-axis implies the order of the first voltage tap and last voltage tap on each strand from inner turn to outer turn. Both inner and outer contact voltage of each strand is different from each other, and they show a linear variation following the location of voltage tap on each strand. The reason for this difference is that each strand contact voltage involves the voltage across the strand due to the copper resistance, and this copper resistance is proportional to the length of each strand. Consequently, if the length between the voltage tap on each strand and each contact is known, the real contact resistance can be estimated by eliminating the copper resistance of each strand from the overall contact resistance.

The distance between first voltage tap V7a on strand 7 is known and the end point of the inner contact is around 1.5 pitch (33.9 cm) of strand length. Figure 5.19b shows the plot for inner contact voltage (black squares) versus the equivalent length between first voltage tap (from inner turn to outer turn) on each strand and the end point of the inner contact, and outer contact voltage (red circles) versus the length between last voltage tap (from inner turn to outer turn) on each strand and the end point of the outer contact.

Compared with the strand voltage versus the length and voltage between voltage tap V7a and Vna (n = 6, 5,…, 1, 15, 14,…, 9, 8) versus the length, both the inner and outer contact voltages as a function of the equivalent length return the same slope that correspond to the linear relationship between strand copper resistance and strand length. The intercept of the linear fitting line for both inner and outer contact voltages as a function of the equivalent length would be the real contact voltage for each contact at 0.5 A. Both inner and outer contact resistance are around 256 μΩ, and the nominal contact resistance of each strand is around 256×18 μΩ. The resistance of each strand with one pitch length is almost three times larger than the nominal contacts resistance.

Consequently, there is a possibility that most of the currents transfer from the first three strands (overlapped with the copper ring at near end side) instead of the far end of the winding at room temperature.

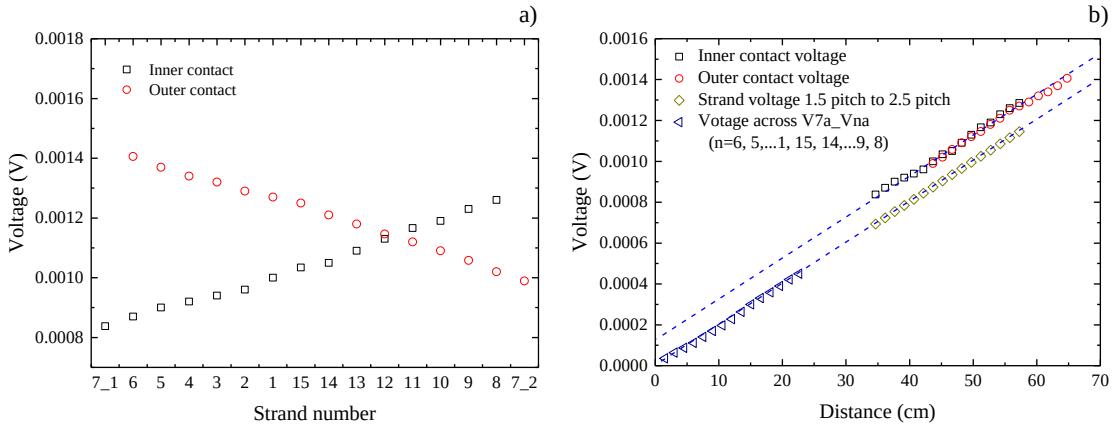

Figure 5.19: The plot for a) both inner and outer contact voltage for each strand at a transport current of 0.5 A and b) inner contact voltage versus the equivalent length between first voltage tap (from inner turn to outer turn) on each strand and the end point of the inner contact, and outer contact voltage versus the equivalent length between last voltage tap (from inner turn to outer turn) on each strand and the start point of the inner contact compared with the voltage across one strand within the pancake coil versus the length, and voltage across voltage tap V7a and Vna (n = 6, 5,…, 1, 15, 14,…, 9, 8) versus the equivalent length between each voltage tap at a transport current of 0.5 A.

Two 3D models were built to investigate the current distribution along the copper ring at room temperature. The geometries used in both models was the same as the geometries used in the previous models produced for the low temperature studies and shown in Figure 5.15. The key geometrical and material properties required for input into the two models are listed in Table 5.6. The resistivity of strand resistivity was assumed as 1.8×10^{-8} Ωm. In model 3, a transport current of 15 A was injected into the current terminal located at near end side of the winding. In model 4, a total of 18 independent blocks were allocated to represent each strand. After performing a series of trials, the following current distribution was applied; a current of 3 A was injected in the first three blocks located at near end side, 1 A current on each block 4-9, and 0 A on each block 10-18. The main results show how the simulations revealed similar voltages on copper ring. Furthermore, the global contact resistance was estimated at around 256 μΩ, and the overall area contact resistance (8986 μΩ×cm^2) taken from experimental measurements was used in model 3. In model 4, an independent area contact resistance (8986 μΩ×cm^2) was applied between each block and copper ring.

Figure 5.20 shows the results of the comparison of the surface potential, surface arrow of current density and line potential along the top and bottom edge of the copper ring between two models. Figure 5.20a displays the surface potential from model 3 and identifies the highest potentials as those appearing towards near end side of the coil. This results agrees with the electrical potential profiles produced for along the copper ring in Figure 5.20e. The upper curve in this figure, is always higher than the bottom curve, and agrees to the positive polarities of the three measured vertical voltages. Figure 5.20c shows the plot where the arrow show the flow of current density acquired in model 3, and the direction of the arrows on the copper ring shows how the current

flowing within the copper ring remains in the same direction and concurrent with the current flow in the Roebel cable.

Table 5.6: The parameters setting up of two models at room temperature.

Parameters	Model 3	Model 4
Copper ring length (mm)	270.0	270.0
Copper ring width (mm)	26.6	26.6
Copper ring thickness (mm)	2	2
Copper resistivity @ room temperature (Ωm)	1.8e-8	1.8e-8
Cable length (mm)	270.0	13.7*
Cable width (mm)	13.0	13.0
Cable thickness (mm)	1.5	1.5
Cable (YBCO) resistivity (Ωm)	1.8e-12	1.8e-12
Contact resistance @ room temperature ($m\Omega cm^2$)	8.986	8.986
Bottom copper disk radius (mm)	52.5	52.5
Bottom copper disk thickness (mm)	0.604	0.604

*The single contact length was assumed as 13.7 mm.

The plot of surface electrical potential as shown in Figure 5.20b reveals how the highest potential appears in the first three strands at the near end side of the coil, and this result is in agreement with the electrical potential profiles produced for along the copper ring in Figure 5.20f. The potential changes in the surface electrical potential maps and the electrical potential profiles match the case, when the current is injected in the 18 independent blocks (model 4) and where it can be seen that most of the current is transferred from the Roebel cable towards the near end side of the coil.

Figure 5.20d shows the surface maps with arrows, indicating the direction of flow of the current density, and it can be seen that some currents tends to flow from the near end to the copper disk, and continues to flow back towards the far end side copper ring. This implies there is a potential effect arising in the copper ring, due to zero current injection from the Roebel cable imposing on the far end side of copper ring. However, this flow back of current did not cause the changes in voltage typified by the electrical potential profiles, which may therefore suggest the amount of current flowing back is minimal.

Table 5.7 shows the summary of the horizontal voltages along the copper ring from two models and the measured results at room temperature. In model 3, all the strands were assumed as a lump cable, and the current injection terminal was defined at the cross-section domain at near end. The model results are very different from the measured results. The horizontal voltages from model 4 has a good agreement with the measured results on both the polarity and the values. However, in model 4, the first three strands were assumed to have 3 A transferring in each block at near end side, and 1 A for each block from four to nine, and 0 A current transferring for the other 9 blocks. The main current injection position is completely different from the low temperature cases. Then the assumption of having poor contact between the Roebel cable and the copper ring becomes unpredictable for low current injections at the near end side of the coil. It is true the resistance of each strand with one pitch length is almost three times larger than the nominal contact resistance of each strand at room temperature. But the lack of information about the inter contact resistance

among each strand in the longitudinal direction make it difficult to compare the contact resistance with current injection and each strand resistance.

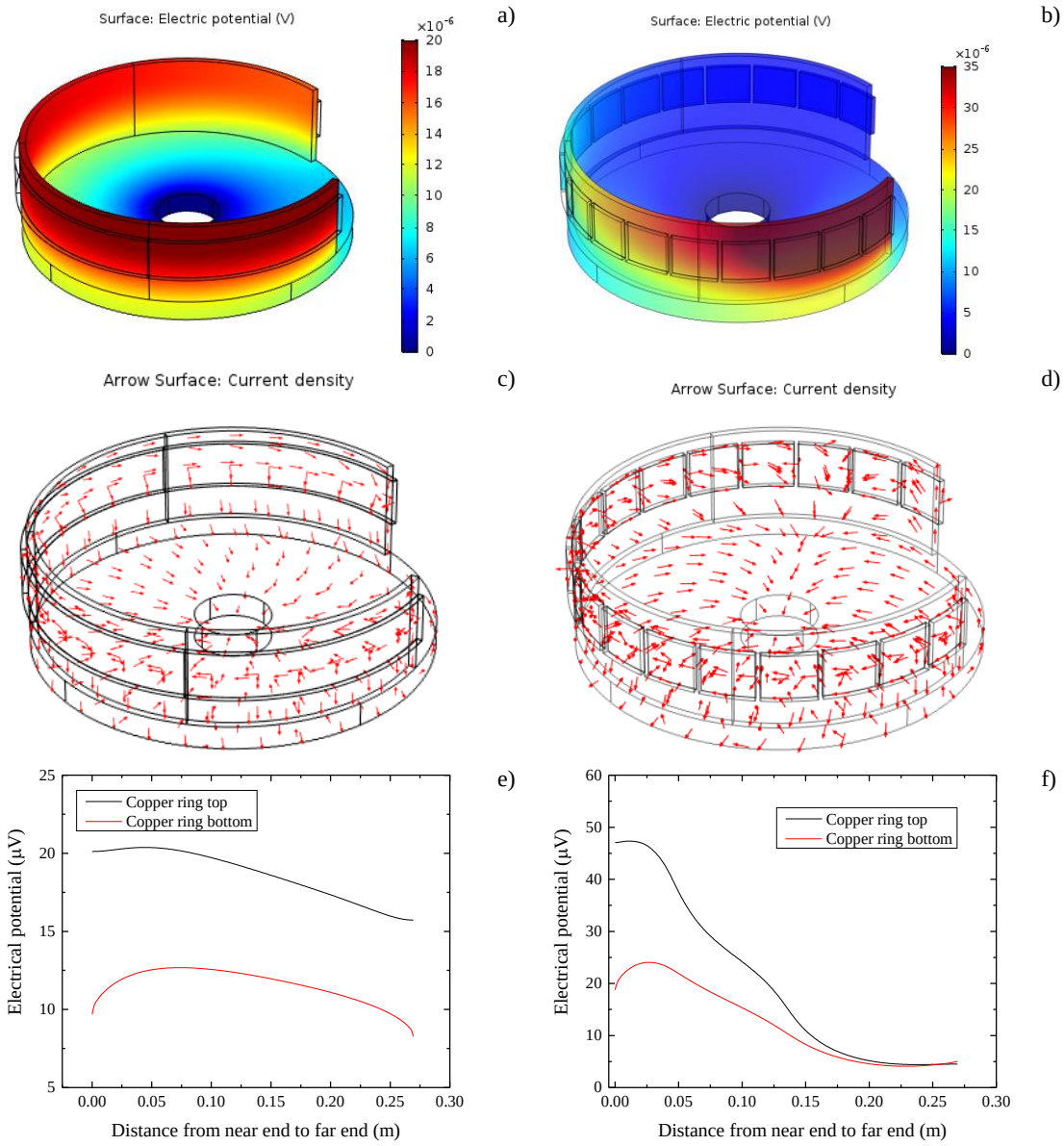

Figure 5.20: The plot of a) surface electrical potential of model 3 and b) surface electrical potential of model 4 and c) surface arrow of current density for model 3 and d) surface arrow of current density for model 4 and e) line electrical potential of both top and bottom edge of the copper ring for model 3 and f) line electrical potential of both top and bottom edge of the copper ring for model 4 at room temperature.

Table 5.7: The summary of the polarity of horizontal voltages along the copper ring in accordance with model 3, model 4 and the experiments (V31: Top near end to top far end, and V32: Top near end to top middle end, V21: Top middle end to top far end, V46: Bottom near end to bottom far end, V45: Bottom near end to bottom middle end and V56: Bottom middle end to bottom far end). The transport current is 15 A at room temperature.

	Current flowing direction	**V31 (μV)**	**V32 (μV)**	**V21 (μV)**	**V46 (μV)**	**V45 (μV)**	**V56 (μV)**
Model 3	Positive	4.4	1.3	3.1	1.3	-2.5	3.8
Model 4	Positive	42.5	31.3	11.2	14.23	8.5	5.73
Experiments	Positive	42.3	32.3	10	18.6	11.0	7.6

5.4.4 'Balanced' inner and outer contact voltages

In order to make the outer contact voltages perform similarily with inner contact as much as possible, an an external constant DC voltage (8.0 V) was applied to Heater 2 along the outer contact as discussed in subchapter 5.3.3.1. Figure 5.21 shows the plot for inner (open symbols) and outer (filled symbols) contact voltages of all the strands as a function of current from 280 A to 460 A in 'balanced' condition. It can be seen that the outer contact voltage of each strand starts to increase non-linearly like inner contact compared with the linear *VI* characteristics of outer contact voltages shown in Figure 5.5. Furthermore, not all the outer contact voltages increase dramatically like the inner contact voltages, and the increasing rate of the outer contact voltage in each strand is different as the transport current is increased.

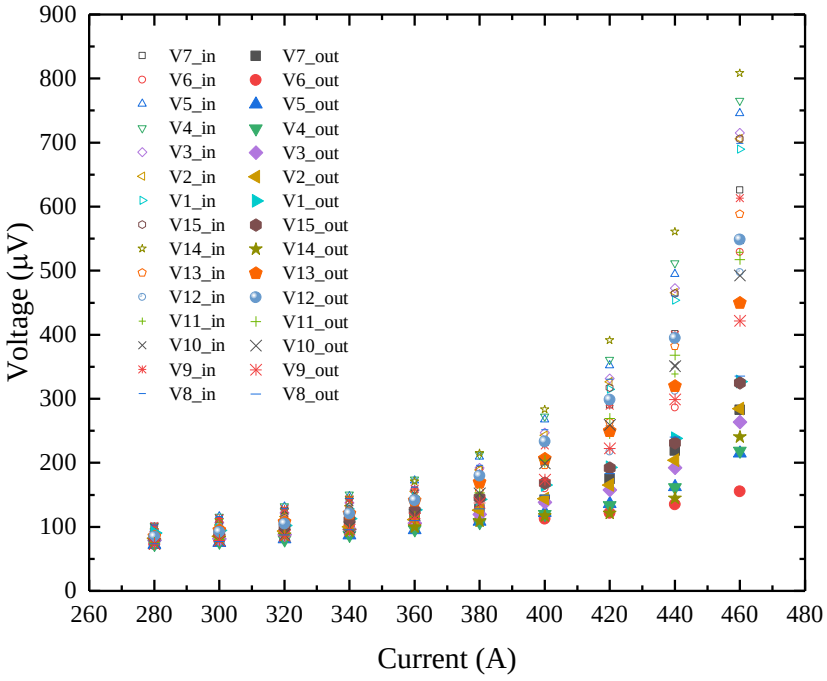

Figure 5.21: The plot for inner (open symbols) and outer (filled symbols) contact voltages of all the strands as a function of current in 'balanced' condition.

Figure 5.22 shows an example to give the comparison between inner and outer contact voltage of each strand between the 'unbalanced' condition and the 'balanced' condition at a transport current of 420 A. Referring to the 'unbalanced' condition, the outer contact voltages are between 100 μV and 120 μV that are one third of the inner contact voltages. Unfortunately, the strand outer contact voltages do not homogeneously increase in a 'balanced' condition, even though Heater 2 overlaps all the strand outer contacts, and they are wound with fiberglass and epoxy impregated for greater thermal isolation. Both inner contact voltages and outer contact voltages of strands 1, 15,..., 8, 7 are between 190 and 320 μV in the 'balanced' configuration. However, both inner contact voltages and outer contact voltages of strands 7, 6,.., 2, 1 show a definite increase in a 'balanced' condition. It was found that there is no obvious current sharing with the shunt when the heat was applied onto the outer contacts, and Table 5.8 shows the difference of transport current flowing within the coil between the 'balanced' and 'unbalanced' condition at each step is not beyond 0.4

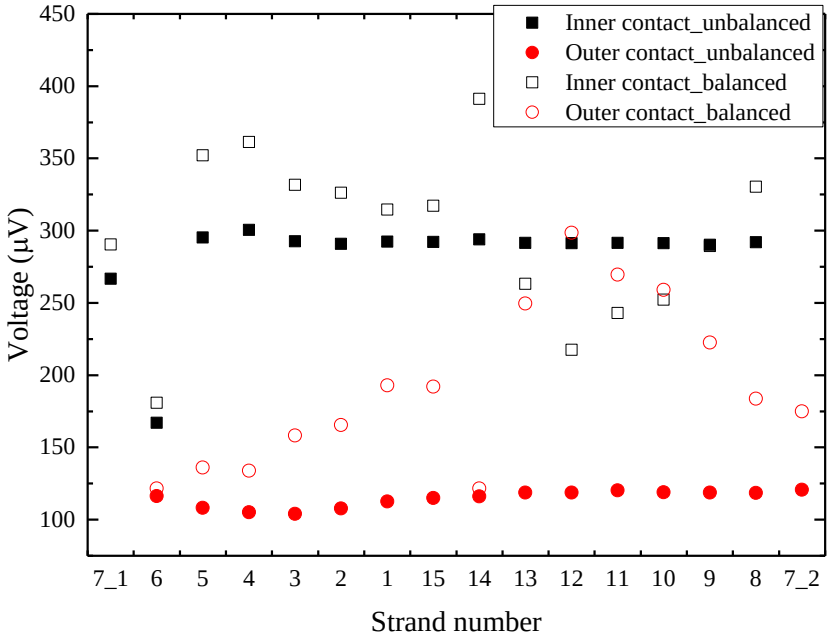

Figure 5.22: Strand inner contact voltage and outer contact voltage comparison between the 'unbalanced' condition and the 'balanced' condition with transported current at 420 A.

Table 5.8: The comparison of transport current flowing within the coil between 'balanced' and 'unbalanced' condition.

Source current (A)	**280**	**300**	**320**	**340**	**360**	**380**	**400**	**420**	**440**	**460**
***I_{coil} in 'Balanced' condition* (A)**	277.33	297.14	316.95	336.75	356.56	376.36	396.15	415.94	435.71	455.44
***I_{coil} in 'Unbalanced' condition* (A)**	277.03	296.81	316.60	336.39	356.17	375.95	395.73	415.51	435.27	455.01

A. Consequently, the increasing of inner contact voltage in strands (7_1 to 1) is caused by a current redistribution where more current flows into strands 7, 6,.., 2 and 1.

5.4.5 Critical current in the middle of the coil

The original 2G YBCO tape has a homogeneous critical current of 130 A (±10%) along the length at 77K in self-field, corresponding to I_c ~ 65 A for the punched strands [200]. The pancake coil field distribution at 450 A in Figure 5.23 shows the maximum parallel and perpendicular fields are located at the inner most, 0.12 T, and the edge of turns 3/4, 0.08 T respectively. The critical current of one short single tape was measured in liquid nitrogen at 77 K. The results shown in Figure 5.24 confirmed the single strand I_c (self-field) = 63 A, I_c ($B_{||}$ = 0.12 T) = 30 A and I_c ($B\perp$ = 0.08 T) = 33 A. The critical current of the pancake coil is likely to be limited by the parallel field on the inner turn, which for 15 strands should be 450 A that has a 52 % reduction from the calculated critical current of 15×I_c (strand).

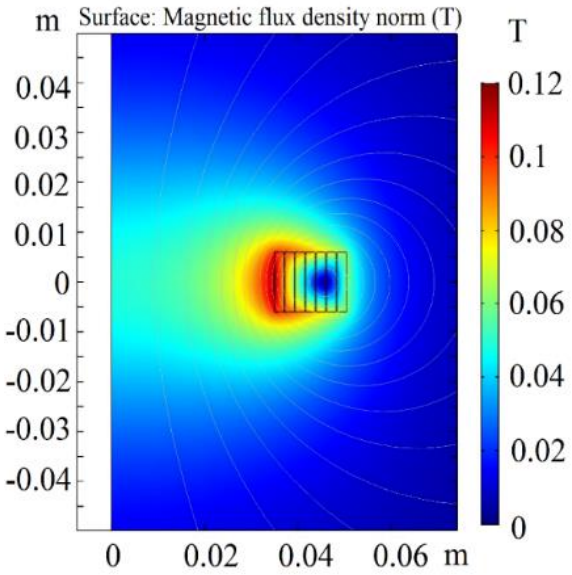

Figure 5.23: Magnetic field density map of the Roebel pancake coil at 450 A (Left side: inner turns, and right side: outer turns).

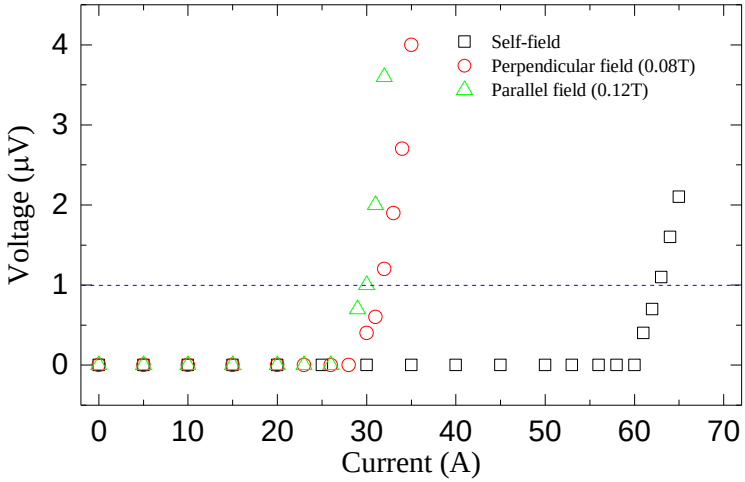

Figure 5.24: Single strand *VI* curve with self field, perpendicular field (0.08T) and parallel field (0.12 T), and blue dash line represents 1 μVcm^{-1} criteria.

The voltage-current (*VI*) characteristics of all the strands on turns 2-4 in 'unbalanced' condition are shown in Figure 5.25, where non-linear increases of voltage with current can be seen on all strands starting at different currents. Then the nominal critical current using a 1 μVcm^{-1} criteria is around 365 A for V6 and above 470 A for strands 8-15. Strand 6 shows the highest voltage with an critical current around only 300 A - a nominal 20 A per strand. For strand 6, despite higher strand voltage as shown in Figure 5.25 (black squares) above 200A and the relatively lower contact voltage as shown in Figure 5.10 (red circles) demonstrates it is carrying less current because it is being stabilised by current sharing in the other strands. The remaining strands exhibited different currents ranging from 310 A to 450 A. The voltage span of each strand between 300 A and 470 A are shown as a bar-chart in Figure 5.26. The *x* axis is plotted in the sequence the strands transpose at the inner face in turn 2. The strand furthest towards the inner turns exhibit the highest voltages.

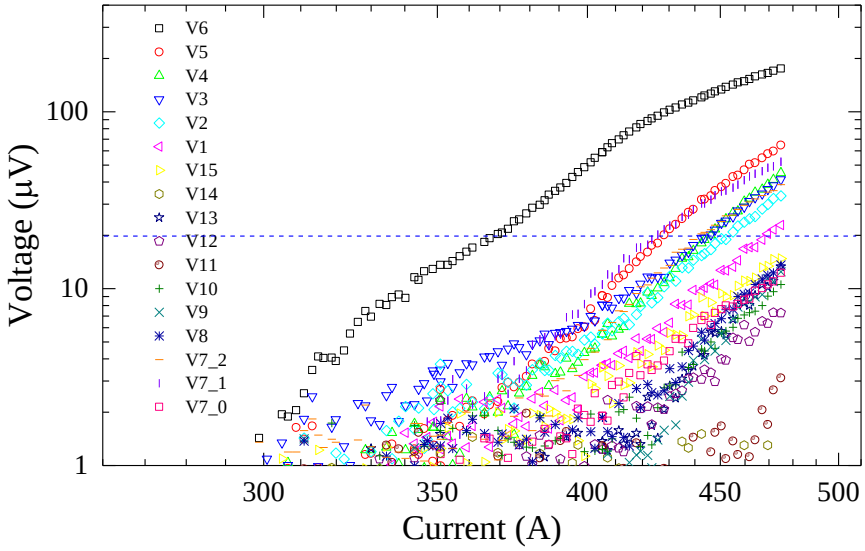

Figure 5.25: Strand voltages as a function of current between 300 A and 470 A in 'unbalanced' condition, and dash line represents 1 μVcm^{-1} criteria.

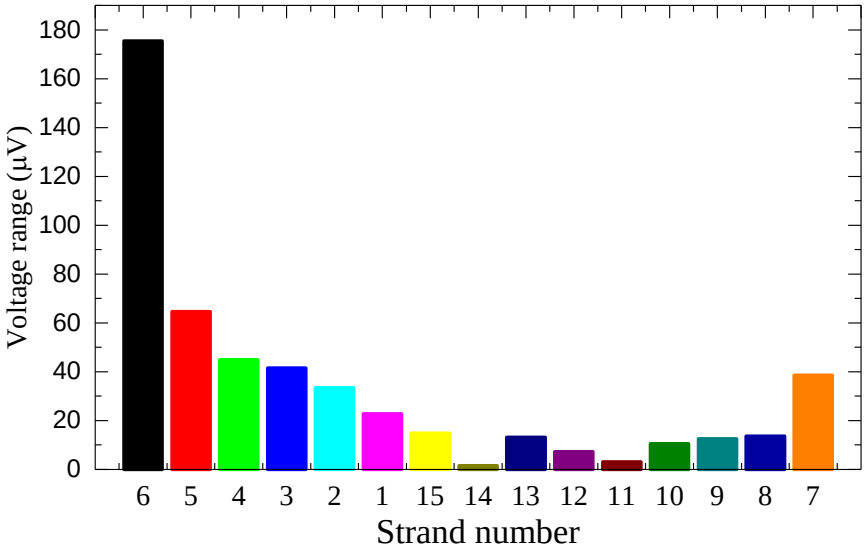

Figure 5.26: Voltage across of each strand (1 pitch) across the same current ramping range from 300 A to 470 A (Str_= Strand).

The uneven contact resistance with a small inductance of the pancake coil would drive a non-uniform current distribution among different strands when the strands current is below I_c, but this is expected to play a minor role when the pitch length is the same as the inner solder joint length (turn 1), and the outer contact is over one pitch length (turn 7) [9], [80]. Another possibility would cause the non-uniform critical current among the strands is due to the non-uniform critical current of the original tape along the length. This is considered as a minor role because a homogeneous critical current of 130 A (±10%) along the length of the original tape is decribed in [200], consequently it is expected that I_c for 15 strands of the Roebel cable over the length has a good uniformity. Such a voltage pattern as shown in Figure 5.26 is consistent with a higher parallel magnetic field on the inner turns as shown in Figure 5.23, consequently the parallel field exhibits an impact on the critical current of the inner turns of the Roebel cable.

Figure 5.27 shows the comparison for *VI* characteristics of all the strands in the middle of the coil between the 'balanced' condition and 'unbalanced' condition with a transport current ramping from 280 A to 460 A. A similar trend of non-linear increase in voltage with stepwise rises in current are observed for the 'balanced' condition compared with 'unbalanced' condition. The strand furthest towards the inner turns exhibits the higher voltage for 'balanced' condition, which implies the possibility of the parallel field effect on the inner turns of the coil. However, it needs to be noted that is faster to reach 1 μVcm^{-1} criteria in those strands (Strand 7(7_1) to 1) located toward inner turns in the 'balanced' condition compared to the 'unbalanced' condition. This is further evidence that more current flows into strand 7, 6,.., 2, 1.

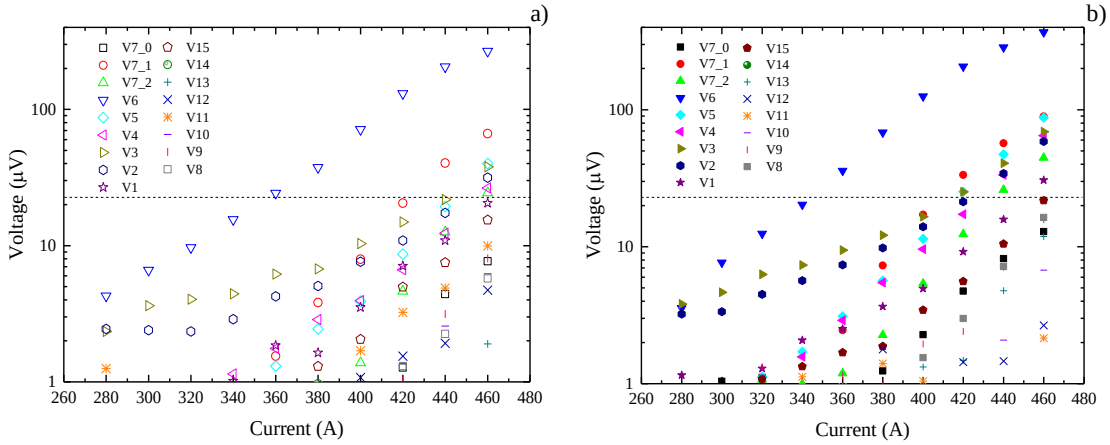

Figure 5.27: The plot for a) strand voltages in 'unbalanced' condition compared with b) strand voltages in 'balanced' condition as a function of current between 280 A and 460 A, and dash lines represent 1 μVcm^{-1} criteria.

To further ascertain the nominal strand critical current, different powers were applied to the heater on strand 7 at different transport current for both'unbalanced' and 'balanced' thermal conditions. The voltage onset at different temperatures and currents in Figure 5.28 leads to a local critical current as determined by V7_0 with 1 μVcm^{-1} criteria as a function of temperature shown in Figure 5.29, where the right axis corresponds to the nominal critical current per strand. It needs to be noted that there is no voltage changes on other strands including V7_1 and V7_2 when V7_0 reaches the critical current. Consequently there is no current sharing in a few seconds after the heat pulse is applied on Heater 1. However, it needs to be noted that the similarity of voltage increasing trend was observed and compared with the *VI* characteristics as shown in Figure 5.27, V7_0 increases faster in 'balanced' condition with the same heating power applied on Heater 1 in 'unbalanced' condition. This maybe due to a current resditribution that results in more current flowing into strands 7, 6,.., 2, 1 in a 'balanced'condition.

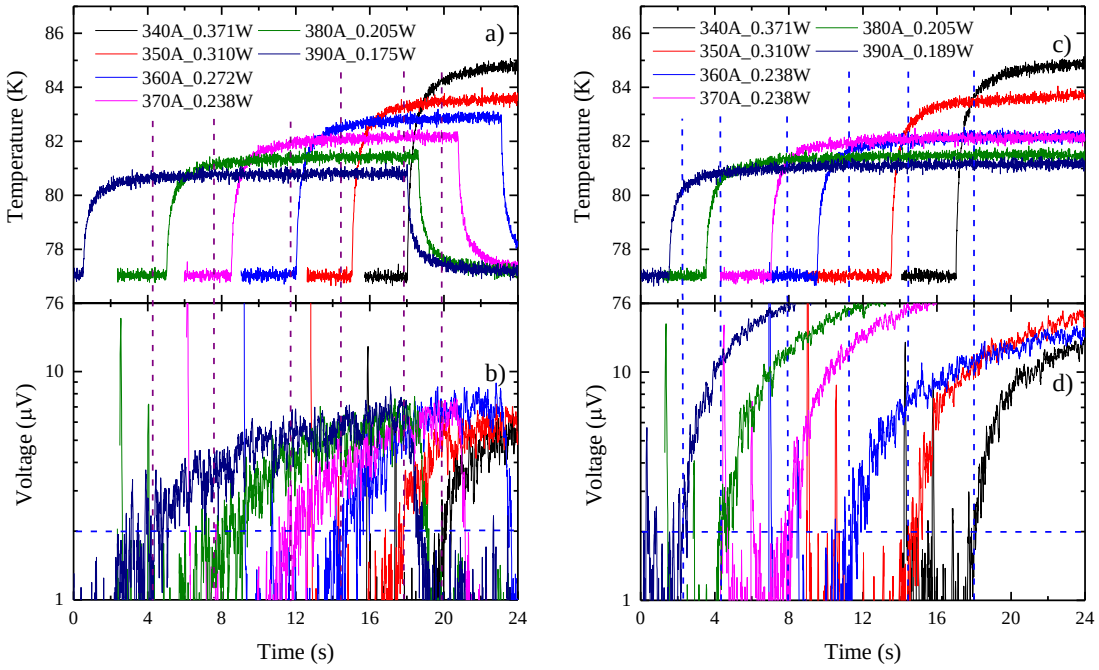

Figure 5.28: a) The tracing of temperature on strand 7 due to different heater power and b) voltage V7_0 around the hot spot at the corresponding heating power and transport current for the 'unbalanced'thermal condition; c) The tracing of temperature on strand 7 due to different heater power and d) voltage V7_0 around the hot spot at the corresponding heating power and transport current for the 'balanced' thermal condition. Two horizontal dash lines in figures represent the standard 1 μVcm^{-1} criteria.

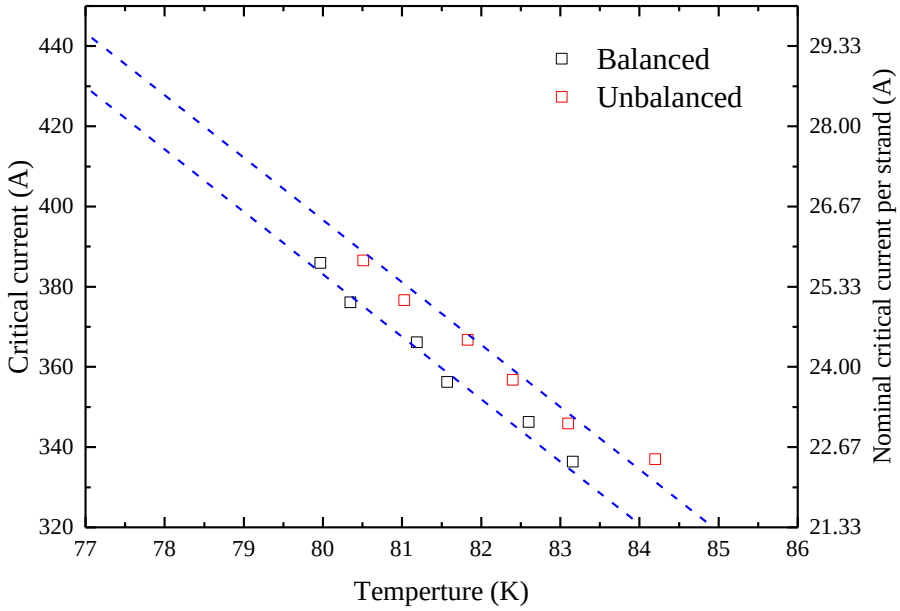

Figure 5.29: Nominal critical current at different temperature.

Both the 'balanced' (black squares) and the 'unbalanced' (blue squares) results show a reducing linear relationship between critical current and temperature. The critical temperature for the 'balanced' condition has a reduction of around 2% compared with the 'unbalanced' case at the same critical current. Furthermore, the estimated critical current (I_c) at 77 K for the 'unbalanced' case is around 440 A, which is not far from the modelling result (~ 450A). The predicted critical current of the Roebel cable at 77 K for the 'balanced' case is around 430 A. The nominal critical

current of strand 7 at the position of Heater 1 for 'balanced' and 'unbalanced' condition is 28.66 A and 29.33 A respectively at 77 K, which is very similar to the I_c (~ 30 A) of single strand measured with 0.12 T parallel field. Furthermore, ideally the critical current of strand 7 at the position of Heater 1 should be same in both 'balanced' and 'unbalanced' condition at each temperature, because the base thermocouple was set in LN2. One possibilty of this difference is that the external constant heat applied on Heater 2 along the outer contact caused the temperature to increase at the position of Heater 1. Another possibility is that the current redistribution in 'balanced' condition limits the current sharing of strand 7 with other strands towards the inner turns when temperature rose up at the position of Heater 1. Consequently, the critical current of strand 7 measured at different temperatures in 'balanced' condition tends to be more real if the second possibility is ture.

Moreover, despite the different voltages among the strands, it is important to note that the pancake coil was found to be stable at 440 A for the 'unbalanced' thermal condition as shown in Figure 5.30, where all the voltages are settled without signs of thermal runaway. A similar way to define the critical current of the pancake coil in the 'balanced' condition, the pancake coil was found to be stable at 430 A with 8.0 V DC voltage applied on Heater 2, where both strand voltages as shown in Figure 5.30 and strand contact voltages as shown in Figure 5.31 are settled without signs of thermal runaway.

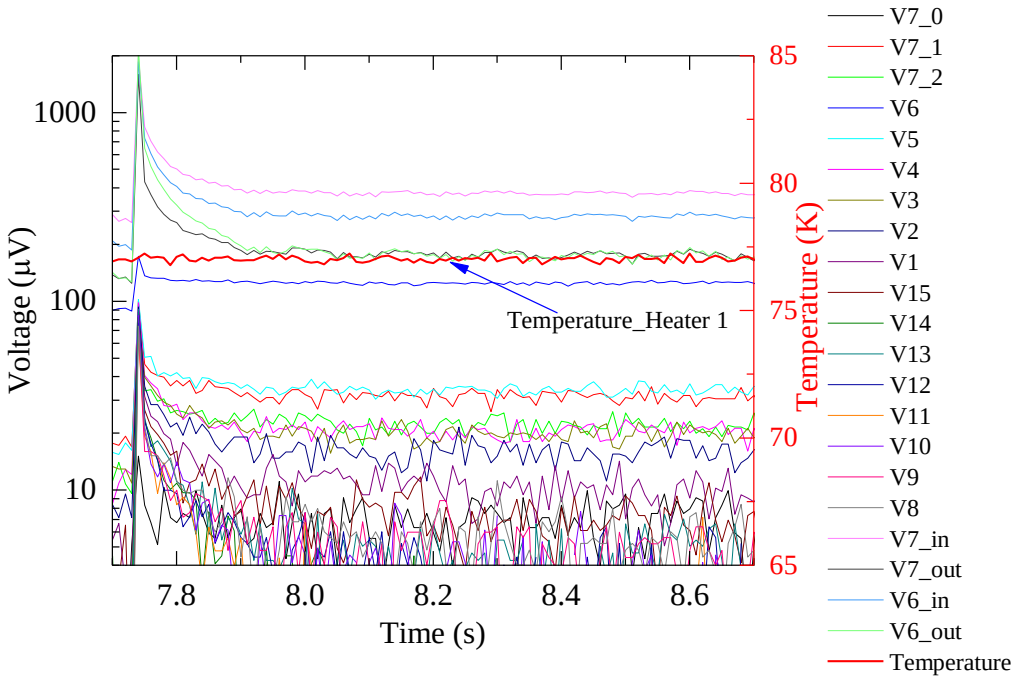

Figure 5.30: Strands voltage and strand 6 and 7 contact voltages at 440 A at 77 K.

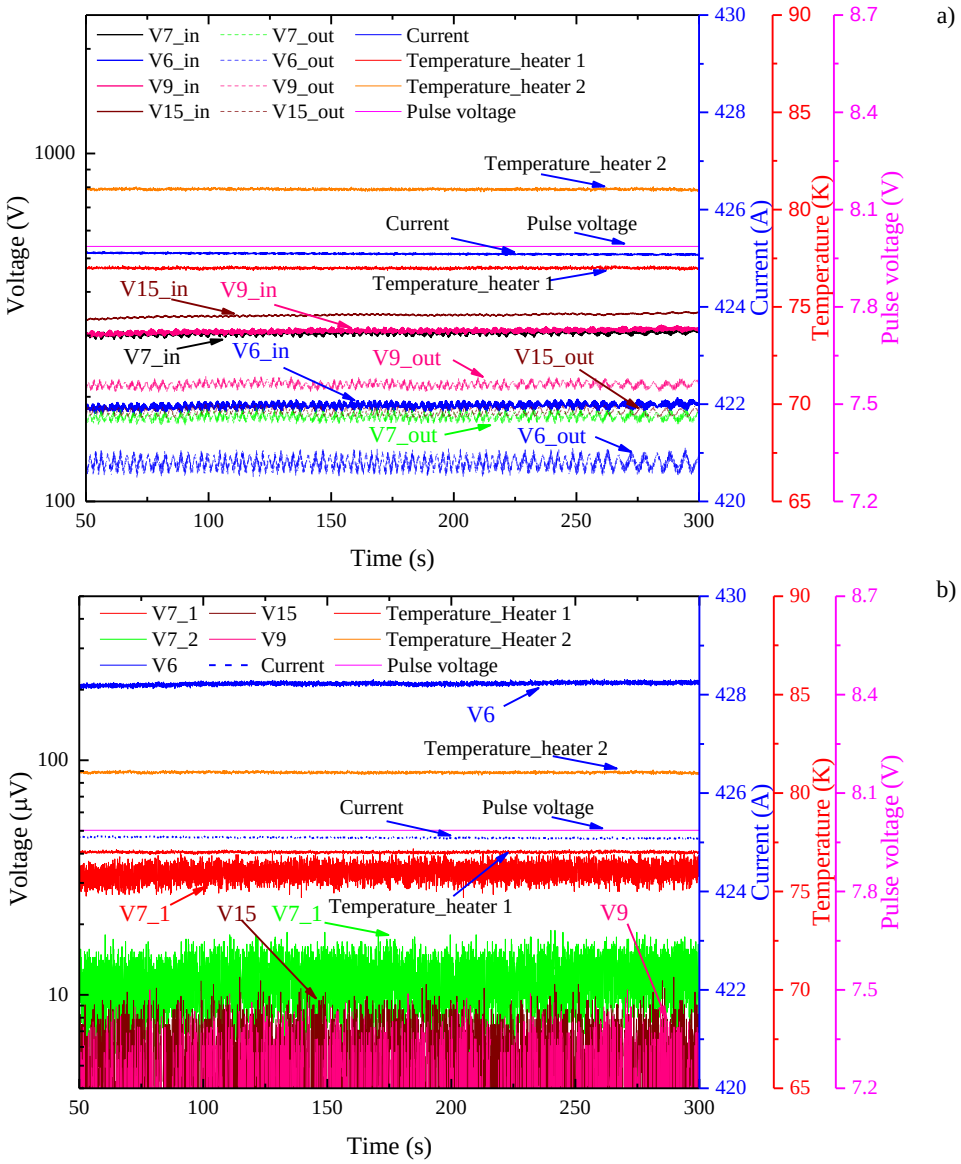

Figure 5.31: a) Strand voltage tracings with a 8.0 V heat pulse on the outer contact joint, and b) Strand inner and outer contact voltage tracings with a 8.0 V heat pulse on the outer contact joint with a transport current of 430 A at 77 K. Strand 6, 7, 9 and 15 are examples of all the strands to show their strand voltages and two contact voltages.

5.4.6 Quench investigation

5.4.6.1. Typical recovery and quench event

Several constant heats were applied to heater 1 on strand 7 in the middle of the coil to generate hot spots in the middle of the coil. Figure 5.32 shows the response of the temperature response to a heat pulse (4.5 V) on Heater 1 without current in the coil. As shown in Figure 5.32, when the heat pulse was applied on the Heater 1, the temperature increased dramatically to above 90 K in a few seconds, which impiles the good performance of the thermal insulation layer above the heater 1. When a transport current ($< I_c$) was injected into the coil, different energies were injected into Heater 1 that was gradually increased until an irreverisble quench was observed.

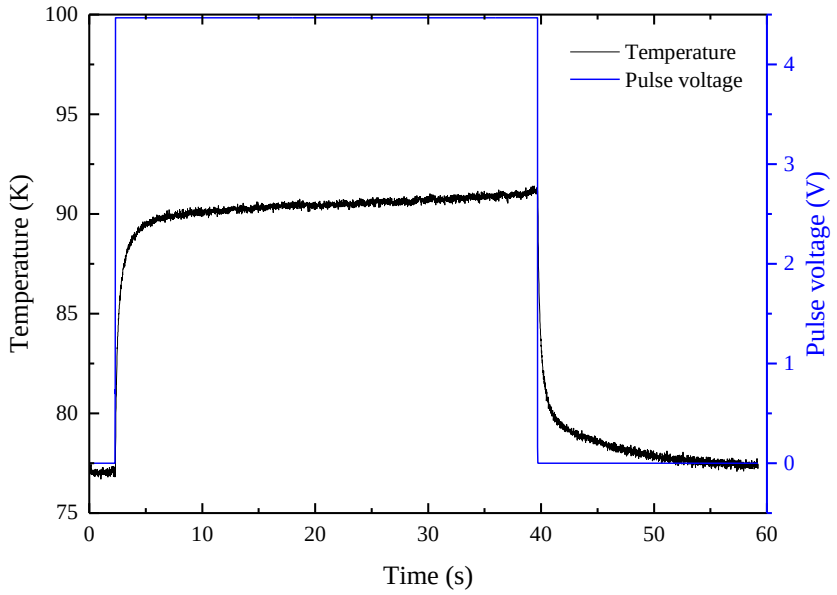

Figure 5.32: The tracing of the response of temperature to a pulse voltage of 4.5 V heat pulse applied Heater 1 with no current in the coil.

The tempertaure was measured by a thermocouple that was adjacent to Heater 1, and strand voltages were traced with voltage taps on each strand along the coil, and the current was transferred from the shunt voltage.

Although high stability is expected for the Roebel pancake coil in liquid nitrogen, it was found that a quench could still be triggered by point-like disturbances with localised heat deposition. Figure 5.33 shows the three voltage (V7_0) tracings from several 'unbalanced' quench measurements with different heat pulse (4.5 V) widths at a transport current around 450 A, which the consequent recovery and quench events can be determined. The pulse starting time was set at 0 s, and the initial current difference was within 0.5 A among these three runs. The first trial (black line) was conducted with a pulse (7.87 s) with an energy of 4.83 J. After the heat pulse was applied, the temperature increased to above 90 K. After the pulse was switched off, both V7_0 and current started to recover. The pulse (9.3 s) with an energy of 5.71 J was applied to the second trial. Both V7_0 (green line) and temperature coincide with previous voltage and temperature profiles and increase further until the pulse is cut off, and both started to drop after the pulse was switched off. For those two cases, the heat energy deposited on the coil is enough to generate the resistive zone around the heater, but the heat applied on this zone was balanced by cooling power from LN2 around the sample, but not enough to cause a quench in all the strands. Consequently, both voltage V7_0 and temperature recovered to the intial values after the pulse was off.

The pulse width reaches 11.3s (6.75 J) in the third trial measurement, which induced an irreversible quench of the coil, and V7_0 (blue line) implies a thermal run away and the current continued to drop below 443 A, even after the pulse is off. The peak temperature reaches 92 K. For this case, the heat generation is enough to cause a normal zone around Heater 1, which the voltage and temperature reached the initial peak due to the external heat pulse. After the heat pulse was switched off, the conduction of the deposited heat cause the voltage and temperature to drop to a plateau state, which V7_0 at the arrow postion as shown in Figure 5.33 is called quench

voltage (V_Q) and correlates to the hot spot temperature in quasi-steady state of the minimum propagation zone (MPZ), and the time for quench voltage is called a quench time constant (t_Q). When the heat generation from the normal zone is balanced out; the system cooling power, both voltage across the hot spot and temperature increased again. In the analysis of the experimental results, the MQE (6.32 J) for this case was defined by taking the mean value between two pulses (9.30 s and 11.3 s) where the cable was able to recover and before it escaltated into an irreversible quench.

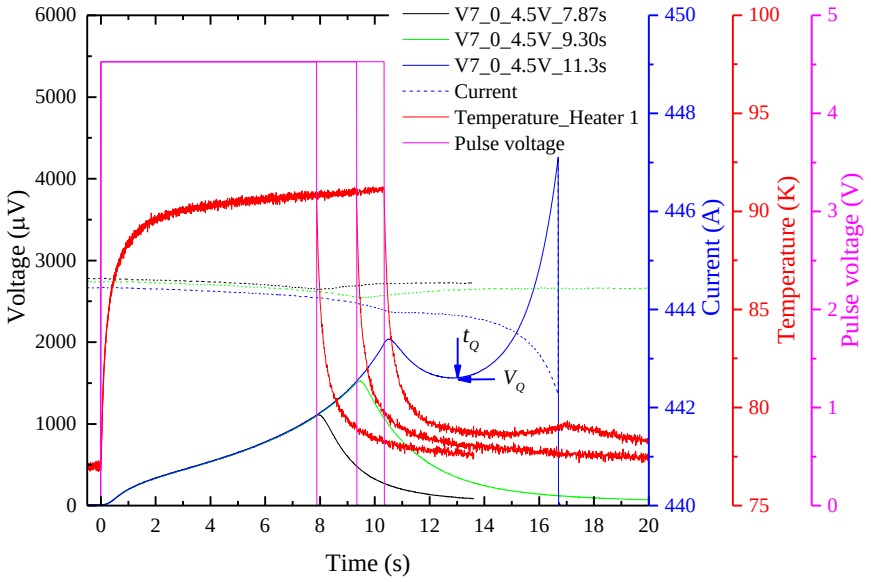

Figure 5.33: The tracing of voltage of each strand, current, temperature and pulse voltage against time with 450 A and different pulse magnitude and length in a 'unbalanced' condition.

5.4.6.2. Evalution of different pulse power

In order to investigate the effect of different pulse powers on the strand voltages and temperature responses; different amplitudes of heat pulses were performed in the 'balanced' quench measurements, and the tracings of the voltage V7_0 across the hot spot, transport current and temperature for seven examples (from 3.5 V to 6.0 V) at same transport current (around 400 A) are shown in Figure 5.34. The first trial was performed with a pulse at 3.5 V for more than 4 minutes. For this case, V7_0 did not evolve into a thermal run away, and temperature increased to above 84 K before it finally reached a steady state. This indicated the presence of a resistive zone on strand 7 that was stabilised by current sharing with other strands. When the pulse voltage increased to 4.5 V with a 20.19 s width and an energy of 12.39 J, V7_0 evolved into a thermal run away, and the temperature incresed to the peak at 91 K, at the time when the pulse was off. As the pulse amplitude increased, V7_0 increased faster and the local temperature increases accordingly. When the pulse voltage reached to 6.0V, V7_0, a thermal run away occurred with a pulse width within 7.1 s and an energy of 7.75 J. It needs to be noted that the quench energy for a 6.0 V pulse case and 4.5 V pulse case are not consistent, and this is due to the heat diffusion in the coil during the pulse period. Further details will be presented in the section of the determination of MQE.

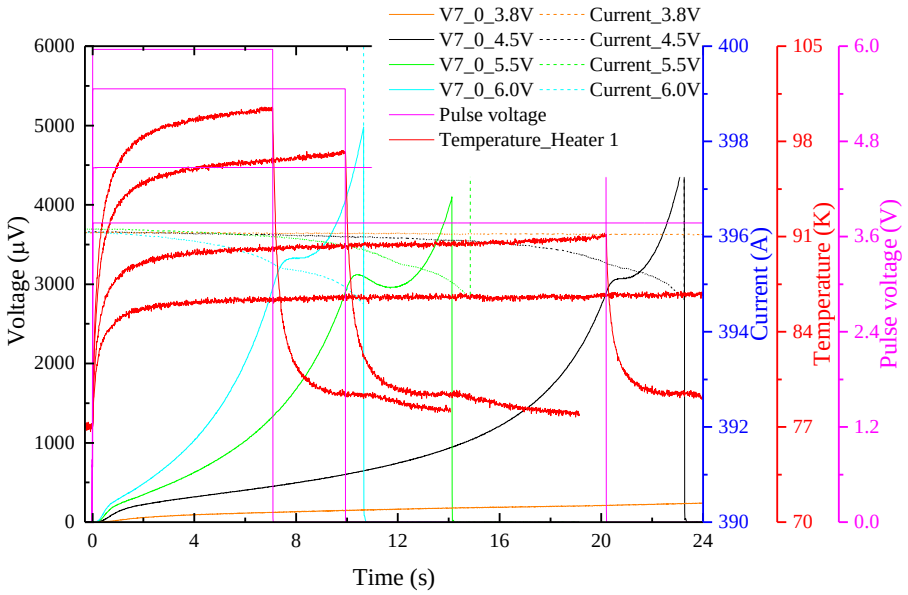

Figure 5.34: The tracing of voltage of each strand, current, temperature and pulse voltage against time with 400 A and different pulse magnitudes at 3.5 V, 4.5 V, 5.5 V and 6.0 V in a 'balanced' condition.

5.4.6.3. Evalution of different transport currents

The quench characteristics of the same heat pulse amplitudes at different percentages of critical current (I/I_c) have been investigated for both 'unbalanced' and 'balanced' conditions. Taking four 'balanced' quench measurements with different currents of 400 A, 410 A, 415 A and 425 A as examples, the tracings of hot spot voltage, current, temperature and pulse voltage against time with heat pulse at 6.0V are shown in Figure 5.35. It can be seen that V7_0 increased faster and achieved thermal run away in a shorter time with high transport currents. Despite the quench voltage (V_Q) not being well defined for each case, the quench voltage tended to reduce at higher transport currents, and it reduced below 2.5 mV when the transport current reached 425 A (0.98 I_c). It needs to be noted that the temperature started to decrease immediately when the pulse was off and before the hot spot voltage reached its peak for all the cases. This was opposite to quench events observed for a single 2G tape in [103]. Furthermore, the temperature increased at almost same rate within the pulse for different transport currents.

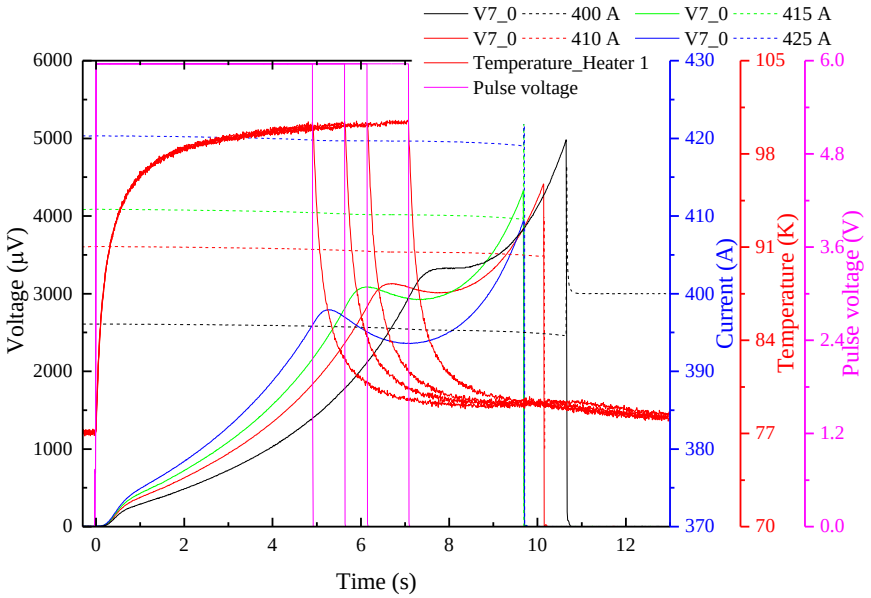

Figure 5.35: The tracing of voltage of each strand, current, temperature and pulse voltage against time with heat pulse at 6.0V at different transport current (400 A, 410 A, 415 A and 425 A).

5.4.6.4. The reponse of strand and contact voltages to the heat pulse

5.4.6.4.1. 'Unbalanced quench measurement'

An example of 'unbalanced' quench measurements for this Roebel pancake coil was undertaken in LN2 with a transport current around 420 A with several heat pulses (4.5 V) in heater 1. The strand voltages, strand contact voltages, transport current, temperature and pulse voltage of two examples are traced and shown in Figure 5.36 and Figure 5.38.

Quench decription:

The first trial as shown in Figure 5.36 was conducted with a 15.15 s heat pulse of 9.3 J in energy. The temperature corresponding to Heater 1 increased to above 90 K before the heat pulse was off, and it has a fast redcution after the pulse was off. The current dropped to below 420 A after the pulse was off, which implies a continued current sharing with the shunt load.

Strand voltages as shown in Figure 5.36a, the voltage V7_0 (black line) across the hot spot increased immediately after the pulse is on, and the voltage V7_1 (red line) across one pitch of strand 7 towards the inner contact and the voltage V7_2 (green line) across one pitch of strand 7 towards the outer contact exhibit a reduction that implies current sharing with other strands, where the reduction of V7_1 and V7_2 is shown in Figure 5.37 with a voltage in a logarithmic scale. V7_2 started to increase before the pulse was off, which implies a heat propagation and normal zone extension. Strand 9 (magenta line) shows a peak voltage around 2.5 mV when the pulse was off, and the order of other strand voltage increasing from the hot spot on strand 7 to the further strands from the heater exhibits a heat propagation effect.

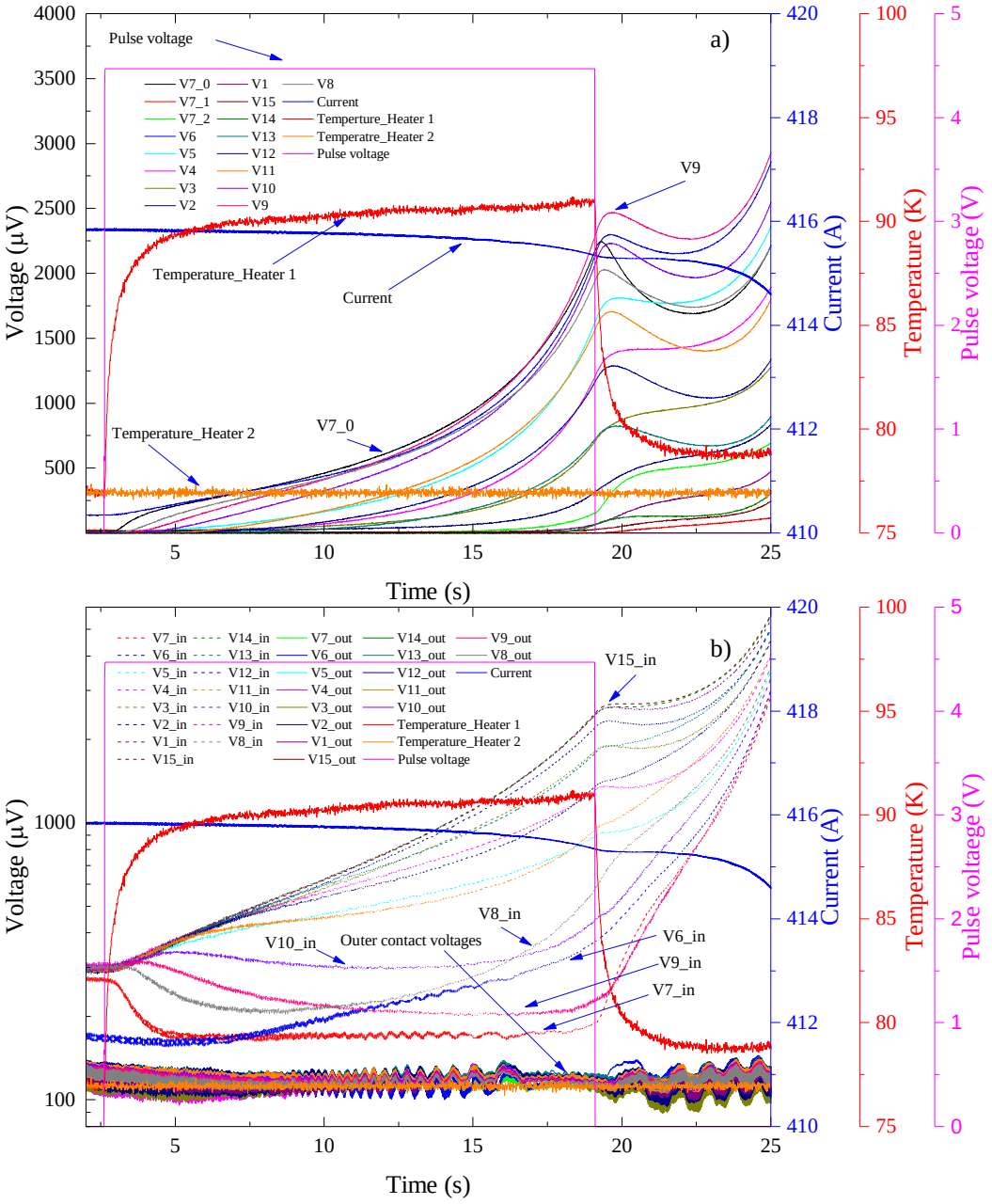

Figure 5.36: The tracing of a) strand voltage, current, temperature and pulse voltage b) strand contact voltage, current and temperature against time for the coil quench case with a transported current at 420 A in 'unbalanced'condition.

For the strand contact voltages shown in Figure 5.36b, most of the inner contact voltage traces (dash lines) show a similar trend variation compared with the strand voltages, and how they start to increase after the pulse was on. In the following inner strands; strand 7 contact in, (red dash line), strand 6 contact in (blue dash line), strand 8 contact in (grey dash line), strand 9 contact in (magenta dash line) and strand 10 contact in (violet dash line) inner contact voltage all start to drop after the heat pulse was applied.

Strand 15 exhibits the highest inner contact voltage of ~2.5 mV that was almost the same as strand 9 peak voltage, before the pulse was swicthed off. However, strand 6 and 8 inner contact voltages start to increase before the pulse was off, which implies the heat propagating on these two strands

nearby Heater 2. All the strand inner contacts are shown to quench as the voltages continue to increase after the heat was off. It needs to be noted that the peak inner contact voltage on strand 15 (~ 5 mV) was already higher than the peak strand voltage on strand 9 (~ 3.0 mV) before the current was cut off. All the outer contact voltages almost had no changes in the whole period.

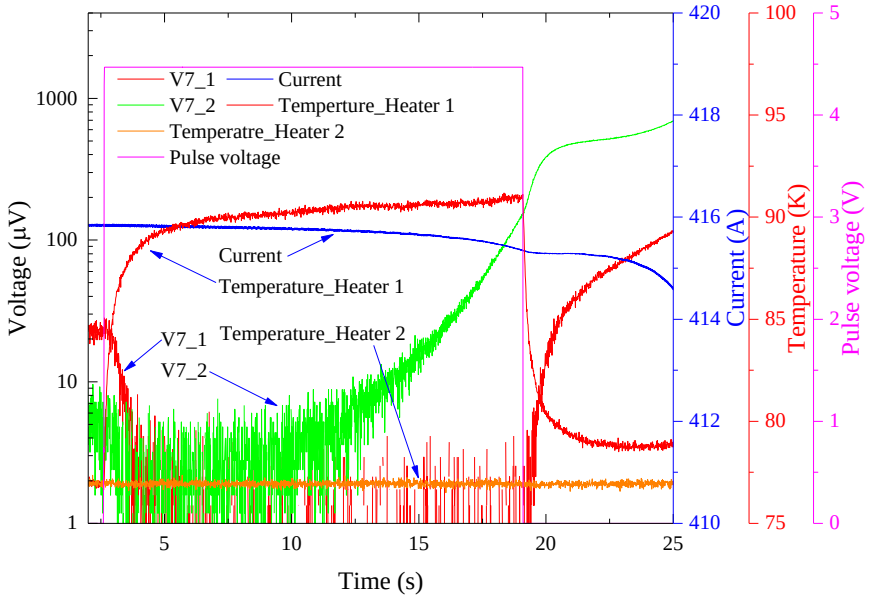

Figure 5.37: The tracing of strand 7 (V7_1 and V7_2), current, temperature and pulse voltage against time for the coil quench case with a transported current at 420 A in 'unbalanced'condition.

Recovery decription:

The second trial of quench measurement shown in Figure 5.38 was conducted with a 15.07 s heat pulse with an energy of 9.25 J. The trend of voltage traces, temperature and current almost coincide with the first example during the period of heat applied. After the heat pulse was off, the current and temperature started to recover.

Most of the strand voltages shown in Figure 5.38a, are able to recover immediately, except V7_1 (red line), V7_2 (green line), V1 (purple line) and V15 (wine line) which recovered after the pulse was off, and where further details about the behaviours are shown in Figure 5.39. Strands 1 and 15 are located furthest from the hot spot generated on strand 7, and the voltages of these two strand continued to increase until 1.5 s after the pulse was finally switched off. This suggests that the heat continued to propagate on these strands with a delay coresponding to the heat pulse. Voltage from V7_2 started to decrease after 1.5 s once the pulse was off, but V7_1 continued to increase in the same moment, which implies the current was flowing back into strand 7.

Strand contact voltages as shown in Figure 5.38b, is used to focus in particular on the inner contacts strands voltages 6, 7, 8, 9 and 10, which reduce after the pulse was on, therefore implying that current started to be shared among these strands. After the pulse was switched off, most of the strand inner contact voltages (dash lines) started to recover immediately except strand 6 contact in (blue dash), strand 7 contact in (red dash line), strand 8 contact in (grey dash line), strand 9 contact in (magenta dash line), strand 10 contact in (violet dash line) and strand 11 contact in (orange dash line) that continued to show increasing voltage in the traces after the pulse was

off. Thereafter, all of voltages started to recover after 6 s once the pulse was off. In the same quench case that the outer contact voltages almost had no changes during the event.

It is interesting how the outer contact voltages show almost no change in both the quench and recover periods. The critical current of the Roebel pancake coil is mainly driven by the inner turn due to the field effect, consequently the inner contact voltages (~ 300 μV) are already almost 2.7 times of the outer contact voltages around 110 μ at 420 A. It is accepted that the inner contact voltages increase a lot in a few Amperes of current rise, because the inner contact voltages are already in the non-linear region of the *VI* response when the transport current is above 200 A.

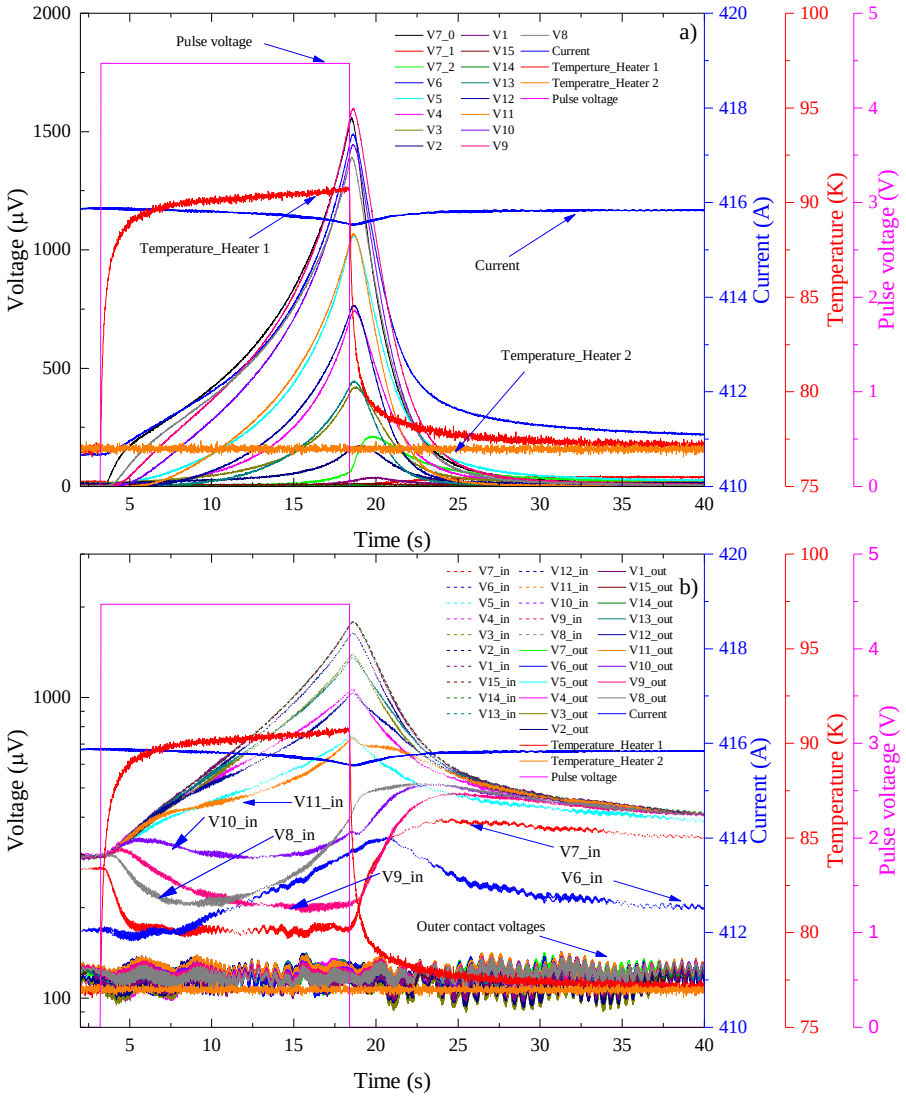

Figure 5.38: The tracing of a) strand voltage, current, temperature and pulse voltage b) strand contact voltage, current and temperature against time for the coil recovery case with a transported current at 420 A in 'unbalanced'condition.

Each strand has a resistance of 112.5 μΩ/cm at a transient temperature, where the distance between two voltage taps across V7_0 is around 2.5 cm, and therefore the resistance for the strand across V7_0 can be calculated: 281.25 μΩ. The voltage V7_0 at 420 A with a 4.5 V pulse is around 2.5 mV when the pulse is off as shown in Figure 5.36 and Figure 5.37. The current within strand 7 can be estimated using Ohm's law: (8.9 A) when the quench happens. Thus, with a

nominal current per strand of 28 A before the heat is applied, the remaining current (19 A) is considered to be current sharing with other 14 strands when the quench happens in strand 7. If the outer contact resistance per strand is ~ 4.2 μΩ, then there would be 5.7 μV nominally increasing per strand, while it should be appreciated that this value is smaller compared with the resolution (> ±20 μV) from the outer contact voltage tracings, and mainly due to the voltage taps jumped from the instrumentation connection box. However, this assumption neglects the effect of heat propagation and the changes in the inner contact voltage, while the current sharing in strand 7 is expected to be more complex.

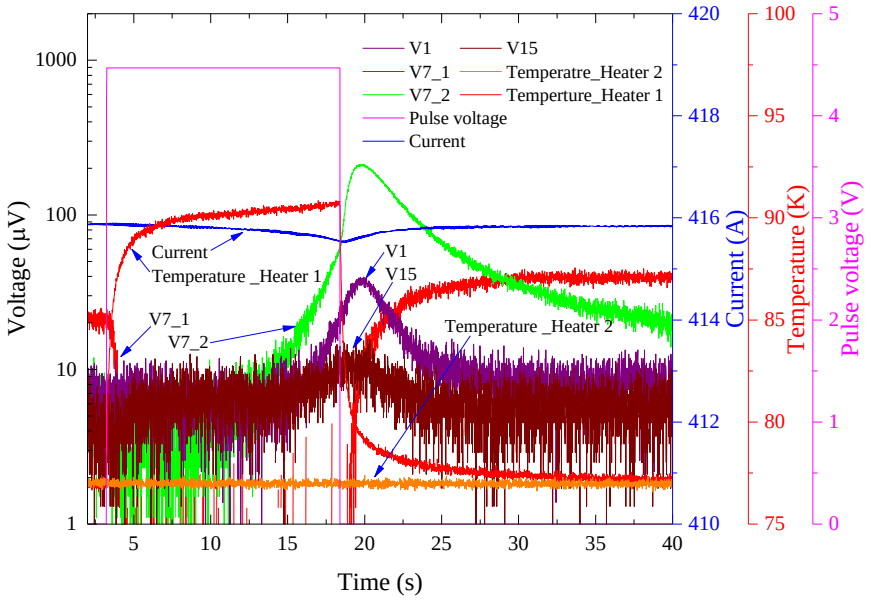

Figure 5.39: The tracing of strand 7 (V7_1 and V7_2), current, temperature and pulse voltage against time for the coil recovery case with a transported current at 420 A in 'unbalanced'condition.

The changes in the inner contact voltages show evidence of the current redistributing when the the quench occurs. However, there is no obvious change in voltage of the outer contacts and they cannot provide any additional information about current sharing. Subsequently, a different type of qunech was initated to make the inner conntact voltages and the outer contact voltages respond in a similar range, which was called 'balanced' quench measurements. These quench measurements were performed on the same Roebel cable pancake coil are described and summarised hereafter.

5.4.6.4.2. Balanced' quench measurements

In order to reduce of the critical current of the strands on the outer contacts, it was necessary to increase the intial voltages before the heat was applied, and therefore a 18.8 Ω heater (Heater 2) was attached on the outer contact joint as shown in Figure 5.2. It has been previously mentioned, that strand outer contact voltages of pancake coil were found to be stable at 430 A with a constant heat (8.0 V DC) on Heater 2 (Figure 5.31). Hence, 430 A was assumed to be the critical current of the Roebel cable in a 'balanced' condition.

Most of the outer contact voltages increase to a similar range (150 - 250 μV) compared with the inner contact voltages in a 'balanced' condition, with all of the voltages settling without any signs

of escalting into a thermal runaway. A trial series of quench measurements for this Robel pancake coil was undertaken in LN2 with a transport current around 420 A. Several heat pulses (4.5 V) on Heater 1 were tried and the strand voltages, strand contact voltages, transport current, temperature on the two heaters and the pulse voltage for two of these trials are traced and shown in Figure 5.40 and Figure 5.42 repectively.

Quench description:

The first trial shown in Figure 5.40 was conducted with a 17.24 s heat pulse with an energy of 10.59 J. In order to maintain similarities to the 'unbalanced' condition, the temperature of Heater 1 was increased to above 90 K before the heat pulse was swicthed off. This resulted in the measured voltages reducing very quickly once the pulse was switched off until the sudden moment when thermal run away evolved. The temperature of Heater 2 was constant (~ 81 K) during the entire measurement. The current continued to drop to below 415 A, even after the heat pulse was finished, which implies a continuation of current sharing with the shunt load.

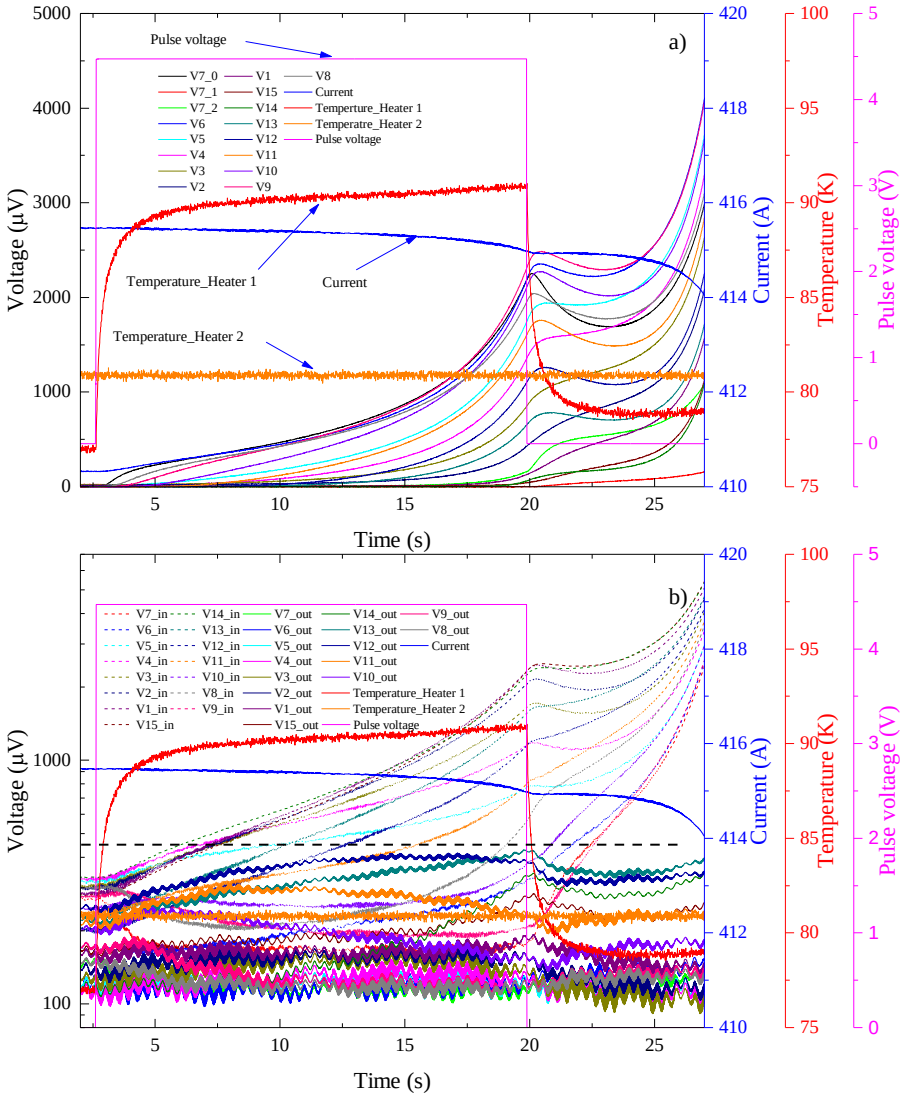

Figure 5.40: The tracing of a) strand voltage, current, temperature and pulse voltage b) strand contact voltage, current and temperature against time for the coil quench case with a transported current at 420 A in 'balanced'condition. All the outer contact voltage proflies are below the black dash line.

Figure 5.40a shows the variation of strand voltages for measurements conducted in a balanced condition. The inner strand contact voltages (dash lines) as shown in Figure 5.40b are consistent with the voltages measured in the 'unbalanced' condition. More attention should be paid to the changes in the outer strand contact voltages (solid lines) in Figure 5.41. Unfortunately, all the signals remain noisy, despite them being smoothed. The voltages of strand 15 contact out (wine solid line), strand 14 contact out (olive solid line), strand 13 contact out (dark cyan line), strand 12 contact out (royal solid line), strand 11 contact out (orange solid line) and strand 10 contact out (violet line) all show an increasing trend immeditately after the heat pulse was applied. The voltages of strand 15 contact out, strand 14 contact out and strand 13 contact out continue to increase before the heat pulse was swicthed off, and strand 12 contact out contiune to increase to its peak value and started to decrease 2 s before the pulse was swicthed off. The voltage of strand 13 contact out shows the highest voltage of ~430 μV, which is one sixth of the highest inner contact voltage (2.5 mV on strand 14 contact in when the pulse was off). It is intresting how strand 11 contact out and strand 10 contact out increase during the initial period of the heat pulse, and both of them start to decrease to below their intial values just before the pulse was switched off. The initial increasing of voltage in strand 11 (contact out) and strand 10 (contact out) may be due to them being located on the side carrying some current from those strands that have quenched. The same strands later reduce in voltage which of implies the continuous heat propagation from the hot spot causes the quenching of strands10 and 11, which leads to further current sharing with other strands, such as strands 12 and 13.

The voltages of strand 8 contact out (grey solid line) and strand 9 contact out (pink solid line) show a voltage reduction when the pulse remain active, which is consistent with their inner contact voltages. Furthermore, all the outer contact voltages start to recover after the pulse was switched off, but strand 15 contact out, strand 14 contact out, strand 13 contact out, and strand 12 contact out all show signs of thermal run away before the current was cut. However, there were no obvious changes observed on other outer strands.

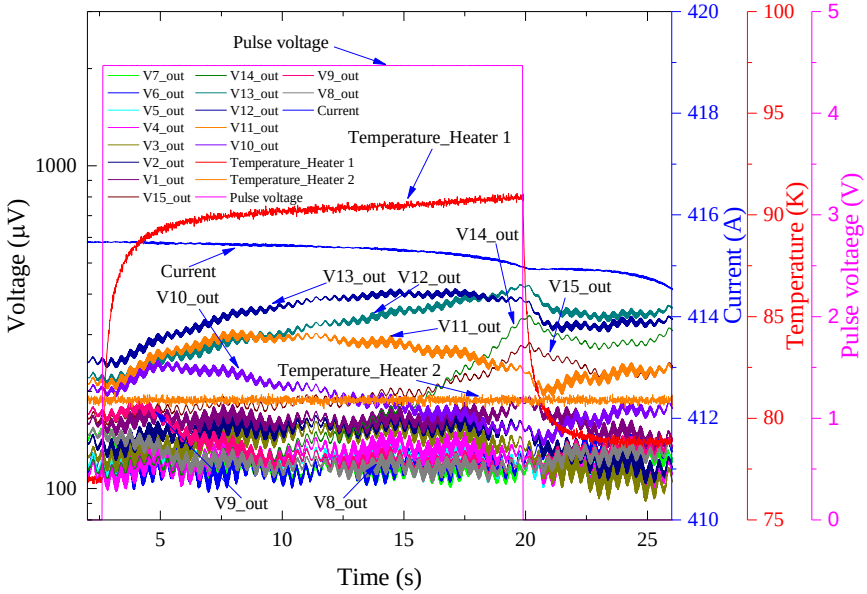

Figure 5.41: The tracing of strand contact out voltage, current and temperature against time for the coil quench case with a transported current at 420 A in 'balanced'condition.

Recover description:

The second trial of quench measurement as shown in Figure 5.42 was conducted with a 15.71 s heat pulse with an energy 9.65 J. The strand voltages, strand contact voltages, temperature and current almost coincide with the quench example during the period of heat applied. After the heat pulse was off, the current and temperature started to recover.

Attention should be paid to the changes in the strand outer contact voltages (solid lines) after the heat was off. As shown in Figure 5.42b, strand 15 contact out (wine solid line), strand 14 contact out (olive solid line), strand 13 contact out (dark cyan line), strand 12 contact out (royal solid line) starts to recover. Strand 8 contact out (grey solid line), strand 9 contact out (pink solid line), strand 10 contact out (violet solid line) and strand 11 contact out (orange solid line) started to increase to the intial values, which implies the current is flowing back to these starnds, which is consistent with the changes observed in the inner strand contact voltages.

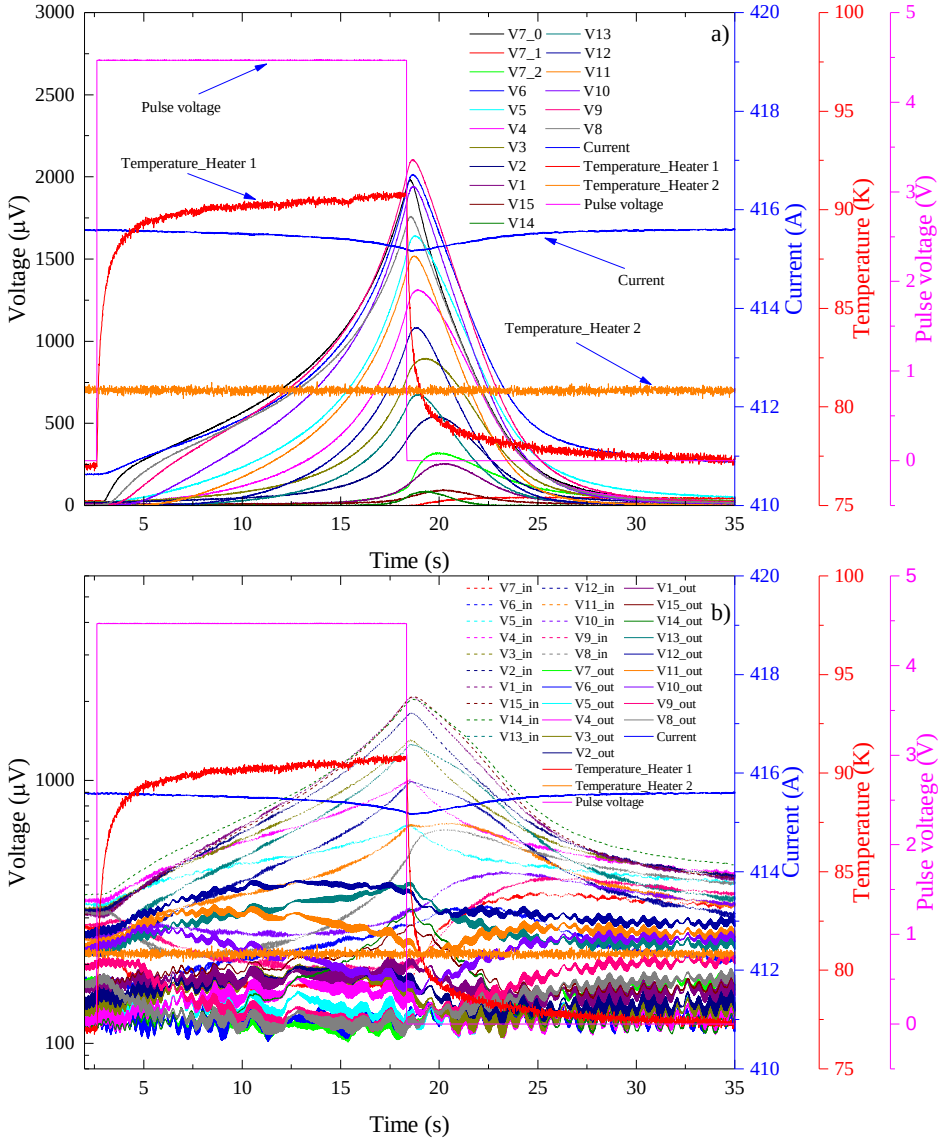

Figure 5.42: The tracing of a) strand voltage, current, temperature and pulse voltage b) strand contact voltage, current and temperature against time for the coil recovery case with a transported current at 420 A in 'balanced'condition.

5.4.6.5. Dertermination of Minimum Quench Eenergy

The important parameter, minimum quench energy (MQE), is introduced to assessed the stablised or non-stablised case of the superconductors.

5.4.6.5.1. MQE versus different heat pulse power

A trial of quench measurements for Roebel pancake coil in 'balanced' condition were conducted in LN2 with several transport currents from 340 A to 425 A, and each current was applied with different heat pulses at 4.5V (0.613 W), 5.0V (0.758 W), 5.5V (0.917 W), 5.8V (1.019 W) and 6.0V (1.091 W). Figure 5.43 shows the experimental MQE and the temperature difference (ΔT) between the start and the end of the pulse, as a function of heating power applied on strand 7 with a transport current at 400 A. For this case, the heat pulse continued to decrease to 2.0 V (0.121 W) in order to identify the thershold power required to induce the quench for tansport current of 400 A.

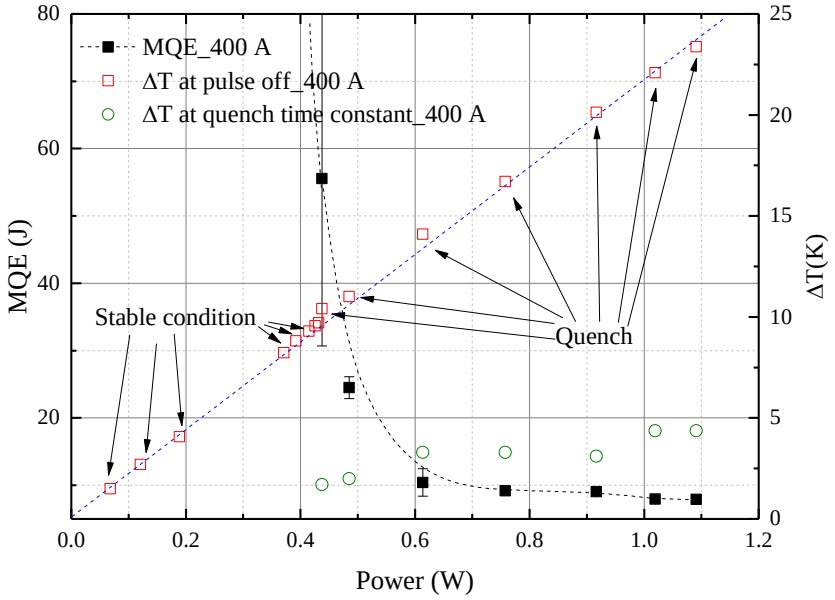

Figure 5.43: Experimental MQE and temperature changing (ΔT) between heat pulse triggering on and cutting off, and temperature changing (ΔT) at quench time constant for different transport currents versus different heating power applied on strand 7.

As shown in Figure 5.43, MQE of the Roebel pancake coil is decreasing with increasing heater power. When the heat pulse reduced from 6.0 V (1.091 W) to 4.5 V (0.613W), the increasing rate of MQE is not fast. Referring to the transport current at 400 A, the MQE increases dramatically and tends to infinite when the heat pulse decreases to 3.8 V (0.438 W), and the variation of the measured MQE becomes larger in this power range. When the heat pulse continued to decrease below 3.8 V, all the strand voltages and contact voltages became rather stable failed to initiate a quench. This impiles that 0.438 W can be assumed to be the thershold power at which this Roebel pancke coil would quench at 400 A.

There is an almost linear increasing relationship between the temperature changes (ΔT) between heat pulse triggering on and cutting off and the applied heat power for the transport current at 400 A, which this relationship is true for other currents, and these (ΔT) values among different currents

at the same applied power is very small. The maximum temperature changes (ΔT) between heat pulse triggering on and cutting off is around 23 K when the heat pulse is at 6.0 V (1.091W). When the applied heat power continued to decrease to approach to the quench threshold power, the temperature changes (ΔT) exhibit a bit higher than the linear trendline. This maybe due to self-heating from hot spots starting to contribute to the temperature increase after a long period of heating with external power source. When the applied heating power continues to drop to 0, these (ΔT) values also linearly decrease to 0. The temperature difference (ΔT) at a quench time constant t_Q implies the temperature difference between the hot spot and LN2 just before strand 7 shows a thermal run away. These (ΔT) values are even smaller than the values (ΔT) between heat pulse triggering on and cutting off when the system was stable with very low applied power. This maybe due to the position of the thermocouple, which was adjacent to Heater 1 and soldered on a copper shim, which located at some distance between the hot spot on strand 7 and Heater 1.

Figure 5.44 shows the quench voltages compared with the stable voltages of strand 7 versus applied heating power with a transport current at 400 A. Compared with MQE against applied power, the trend variation between the average voltage of the Roebel cable and applied heating power is reversed. When the heat pulse is smaller than 3.5 V (0.368 W), the stable voltage slowly increases with the increasing of the applied power, and the average voltage reaches 0.273 mV that pulse volatge is 3.5 V (0.368W). Below powers of 0.368 W, all the strands reach the constant state without thermal run away and the temperature difference between the heater and ambient liquid temperature was below 10 K, while all the strands remained in superconducting state. Once the pulse voltage was above the assumed threshold power (0.428 W), the average strand voltage starts to increase dramatically above 2.0 mV, which implies the high voltage across the hot spot. Then quench voltage increases and approaches a constant, with respects to the increasing heating power. The reason for this behaviour, is because the strands voltages are limited by the changes in the MQE shown in Figure 5.43 when the heat pulse is above 4.5 V (0.614 W).

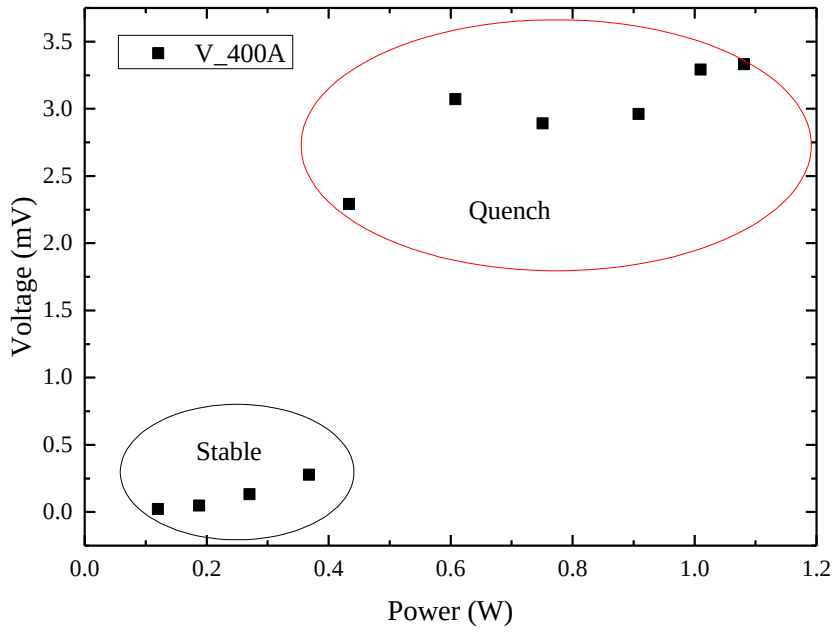

Figure 5.44: Quench voltage and steady voltage of strand 7 versus different applied heating power with a transport current at 400 A.

5.4.6.5.2. MQE versus different transport currents

Figure 5.45 shows the MQE as a function of the scaled current (1-*j*), where *j* is the percentage of the critical current (I/I_c), and has been normalised with the critical current of the Roebel cable in 'balanced' thermal condition at 430 A. It is obvious that the MQE reduces with increasing applied heat power at each current, which implies a shorter pulse width with higher power. This can thereforeinduce a quench of the Roebel coil with less thermal energy. Shorter heat pulse widths correspond to shorter heat diffusion times, and there is less thermal conduction in the coil and heat leak from the top of Heater 1. Consequently, when the pulse voltage increases to 6.0 V, the MQE obtained is believed to approach to the real MQE of this particular pancake coil at each transport current.

Figure 5.45 also shows the MQE data of a single SuperPower 2G HTS tape with different current at 77 K [103]. and the blue dash line shows the trend of a single 2G HTS tape MQE with the scaled current (1-*j*) compared with the MQE (magenta symbols) of this Roebel coil. When comparing the single 2G tape, with the 15 strand Roebel cable, the MQE at same percentage critical current is more stable and 100 times larger. The MQE of the Roebel cable increases with the reducing current, especially when 1-*j* is above 0.1 ($I/I_c < 0.9$). This is due to the lower transport current of the Roebel pancake coil, which needs a much higher thermal energy to induce the quench, and requires a longer time to quench for the same power input. However, the thermal diffusion has a important impact on the coil that thermally run aways when when quenched by long heat pulses (wide pulses) at lower transport current..

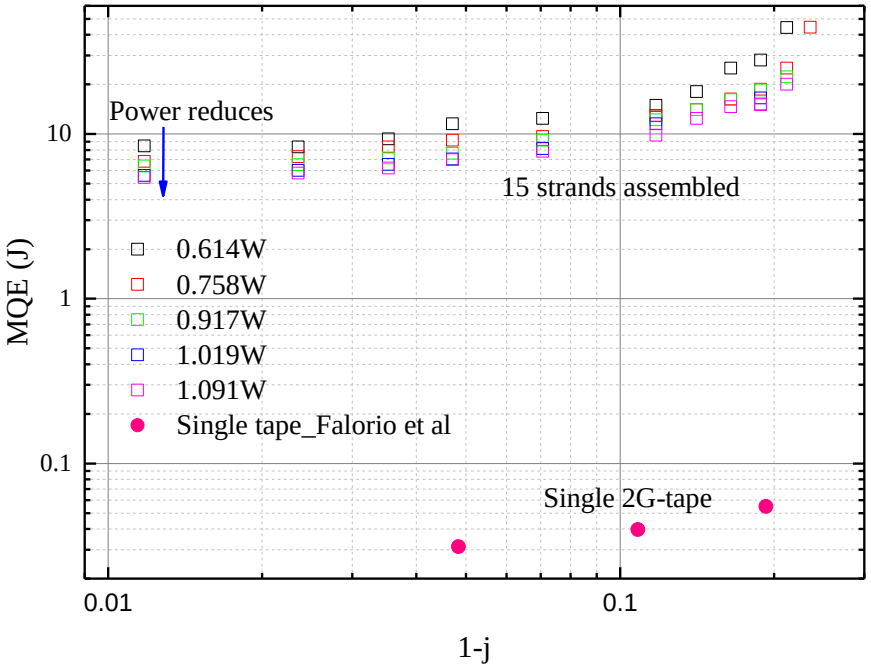

Figure 5.45: 'Balanced' experimental MQE of the Roebel cable as a function of scaled current (1-*j*) with different transport current at 77K. Pink round scatter shows the experimental MQE data (corresponding to right y-axis) of a single SuperPower 2G HTS tape with different current at 77 K [103].

A slow reduction of the MQE is exhibited in both this Roebel pancake coil and single 2G-tape, when 1-*j* is below 0.1 A. A similar dependence current on the MQE is also observed in a Bi-2212

solenoid [201], a single 2G-tape [103] and MgB_2 solenoid coil [202]. However, this behaviour has not been observed in several LTS quench measurements, such as MgB_2 filement [203] and MgB_2 pancake coil [204] and NbTi Rutherford cable and NbTi solenoid [205].

5.4.6.5.3. The thermal transport effect on MQE estimation

In an adiabatic system, the minimum quench energy is fully depending on the input energy applied to a small volume of a short superconductor in a short duration. It will take a longer time to trigger the quench in a single superconductor with a lower power input because of the heat diffusion, but the MQE should be same as the high power input cases, to quench the superconductor in an ideal adiabatic system. However, the Roebel pancake coil is submerged in LN2. Furthermore, when comparing the Roebel coil quenched by heat pulses with widths (> 5 s) with the single wire quench measurements in [196], [197], [206], the Roebel pancake coil takes much longer because the rate of heat diffusion becomes more significant on the MQE. This is also the case at for intermediate power between 0.42 W and 0.618 W and there are large varitations in the measured MQE at 400 A as shown in Figure 5.43.

Referring to the self-heating energy $J \times E$ (T, J) from the metal matrix, this joule heat can be estimated from the integartion of the strand voltage traces with pulse width times nominal current per strand by Equation 5.9, and the sum of all the strands self-heating can be defined:

$$V_{average} = \frac{\sum_{i=1}^{15} \int_0^{t_p} V_i(t) \times I_n dt}{15 I_n} \qquad 5.9$$

Where t_p is the pulse width, and $V_i(t)$ is the voltage function of time within the applied pulse period for each strand with one pitch length in the middle of the coil, and i is the strand number, and I_n is the normnal current per strand.

Figure 5.46 shows the self-heating energy recorded at different current and comparing this with the experimental MQE with a 6.0 V heat pulse (1.091 W). The trend of self-heating energy and the experimental MQE increases with the reducing current, and the self-heating energy accounts for 12%-17% of the experimental MQE. Consequently the initial heat pulse energy should occupy the main part of the quench energy. Furthermore, the heat diffusion along the longtitude direction is based on the thermal properties of the strands themselves. This can then explain why the temperature changes at the end of the pulse is proportional to the initial heating power applied.

Normally the heat flux Q_{leak} will be transferred to the LN2 bath and it should be same as the heat flux transfering from the hot spot to the epoxy, given series thermal link between the LN2 and the epoxy (in series). However, this heat flux is expected to be small and the expression in Equation 5.10 can be applied to determine this heat flux:

$$Q_{leak} = \frac{\kappa_2 (T_2 - T_1)}{d} = H(T_\infty)(T_\infty - T_2) \qquad 5.10$$

Where κ_2 is the thermal conductivity of the epoxy, d is the thickness of the epoxy, T_1, T_2 and T_∞ are the tremperatures of Heater 1, the top surface of the epoxy v and the LN2 bath, and $H(T_\infty)$ is the heat transfer coefficient.

For the input values to determine $Q_{leak,}$ the thermal conductivity of the epoxy (Stycast™ 1266) is 0.255 W/(m×K) at 77 K [207]. An infinite $H(T_\infty)$ is assumed, and T_2 is equal to T_∞ (77 K). It has mentioned that the largest temperature difference between Heater 1 and LN2 is around 23 K with a heat pulse at 6.0 V (1.019 W), and the area of epoxy insulation area A is 20×6 mm^2, then the minimum thermal transport length can be estimated, which is around 0.715 mm compared with the real thickness of the insulation which is ~2 mm. Low thermal conductivity and long thermal transport length leads to a large thermal resistance of ~65.4 K/(W×m^2), in accordance with thermal resistance $R_{thermal} = d/(A \times \kappa_2)$. Furthermore, the whole pancake coil has been impregnated, the extended epoxy layer would lead to a larger thermal resistance even in a very thin thickness. Consequently the pancake coil can be treated as in an adiabatic system.

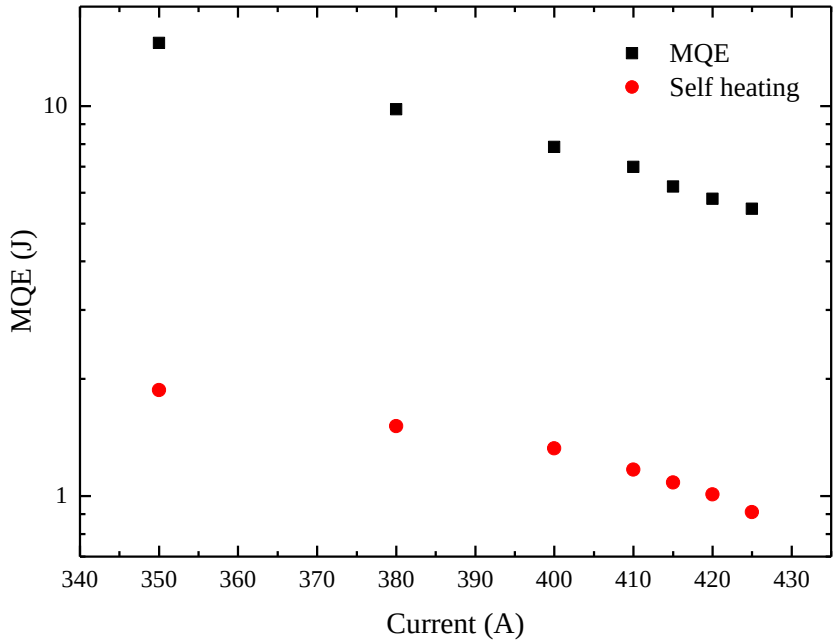

Figure 5.46: The self-heating energy at different current compared with the experimental MQE with 6.0 V heat pulse.

However, the boiling condition at the top of the epoxy is unknown, because the heat transfer coefficient $H(T_\infty)$ based on different boiling conditions can cause large changes in heat flux, which can be induced by the heat leak above the heater on strand 7. Figure 5.47 shows an example of a quench measurement with a transport current around 400 A and a 3.8 V heat pulse (~ 100 s width). When the heat pulse was applied, all the strand voltages continued to increase. The temperature increases to above 86 K, and current continues to decrease with current sharing of the shunt load. The temperature profile shows an obvous fluctuation after 25 s (arrow 1). Then in all of the strand voltages appears a ‘kink’ at 30 s (arrow 6), and the slope of the decreasing current also changes at the same time. After this event, the temperature almost becomes constant around 86.8 K and a second fluctuation appears at 40 s (arrow 2), and in the strand voltages the second ‘kink’ appeared (arrow 7) at same time. Then all the strand voltages start to decrease, and the current starts to flow back to the coil, which implies a recovery of the Roebel pancake coil.

The temperature almost remains constant around 86.8 K and several fluctuations appear for a short while, but all the strands start to thermally run away after 60 s. The current contiuned to drop below 395 A and before the pulse was cut off. The pulse is contant in the whole period,

which implies a constant heat input. The two 'kinks' recorded are believed to be due to the changes of the heat flux transfering to the LN2. Therefore, the cooling condition of LN2 above the top of the tinsulation layer above Heater 1 is a region where the thermal conditions could certainly change (~10 K). For example shifting between different boiling regimes can result in a heat transfer coefficient of LN2 which is almost 100 time [208], [209]. In order to reduce the effect of heat diffusion on the estimated MQE in quench measurements, a higher heat pulse with a shorter pulse width is suggested for the heat pulse applied by Heater 1 in these studies.

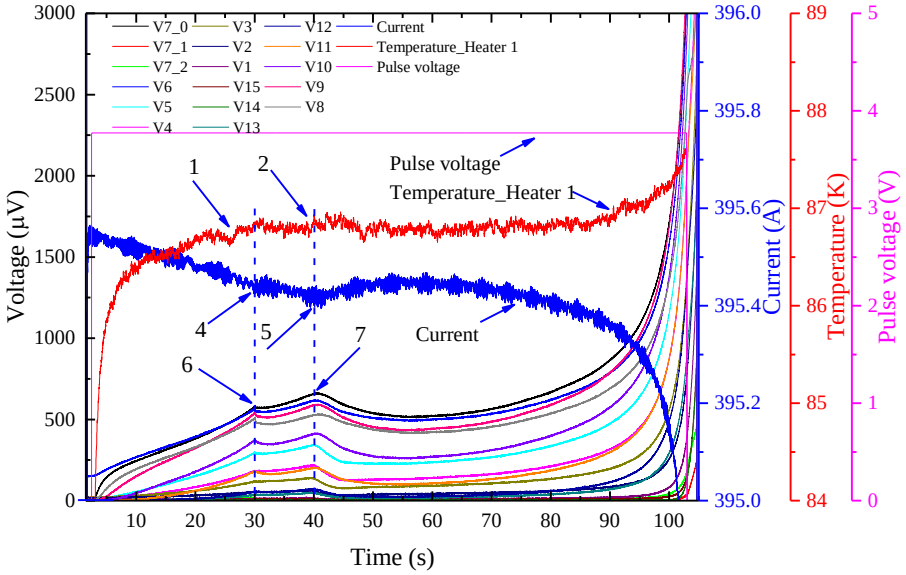

Figure 5.47: The tracing of voltage of each strand, current, temperature and pulse voltage against time for the coil quench.

5.4.6.5.4. MQE comparison between 'unbalanced' and 'balanced' thermal conditions

It has been previously discussed in earlier section how the MQE obtained at a high voltage pulse at 6.0 V approach those measured experimentally. Unfortunately, the unbalanced quench measurements were only conducted with 4.5 V heat pulses, thus the MQE for both 'balanced' and 'unbalanced' at different currents with a 4.5 V heat pulse is shown in Figure 5.48. The same figure includes the MQE for 'balanced' condition with a 6.0 V heat pulse for comparison. Due to the different critical current between the 'balanced' and 'unbalanced' condition, the scattered points for the MQE at each current is highlighted with the current applied. The MQE for 'unbalanced' conditions was obtanied at a high percentage of the critical current from 93% I_c (410A) to 97% I_c (435 A), and 'balanced' conditions at at a percentage of the critical current from 79 % I_c (340 A) to 101.2% I_c (435 A).

Both cases show the reduction of MQE with increasing current. The MQE for the 'balanced' condition with a 4.5 V heat pulse reduced by around 10% compared with the 'unbalanced' case with the transport current from 415 A to 425A. This may be due to the reduction of the critical current of the Roebel cable for the 'balanced' condition when applying the constant heat to the strands (outer contacts). In reference to the 'balanced' condition with a 6.0 V pulse, there is more than 40% reduction in MQE at each current compared with pulse of 4.5 V, which demostrates a

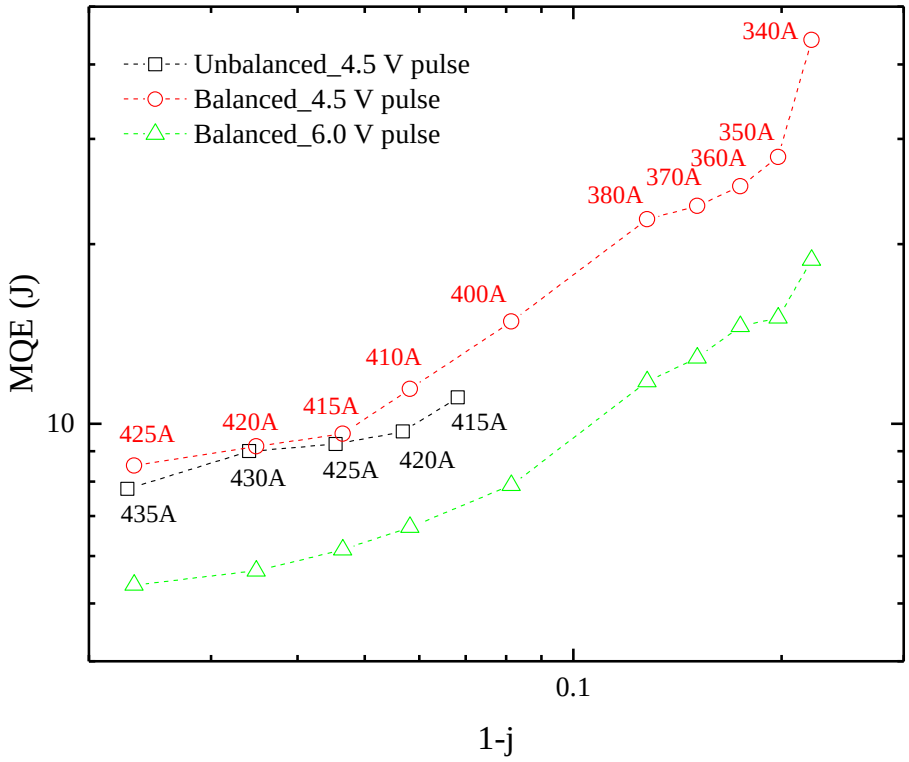

Figure 5.48: 'Balanced' experimental MQE of the Roebel cable as a function of scaled current (1-*j*) with different transport current at 77K.

reduced effect of heat diffusion on the quench of the Roebel pancake coil with high heat input pulses.

5.4.6.6. Curent distribution in the Roebel cable during the quench in a 'balanced' condition

Some papers have discussed how the current distribution may play an important role in the stability of a multi-strand superconducting cable like a Roebel cable [80], [84], [210], [211]. The Roebel cable consists of many strands with uncontinuous electrical inter-strand contact, which increases the complexity of current sharing and normal zone propagation during quench. A detailed understanding of the key parameters affecting the current distribution and stability of the Roebel cable is helpful in manufacturing and optimisation of its thermal design for magnets. In the quench measurements invistigated in this study, the response of strand voltages and contact voltages created aftera variety of heat pulses. In this section we investigated several 'balanced' quench measurements as examples to identify the behaviour of the strand voltages and the current injection terminal contact voltages to verify the redistribution of current at different stages of the quench.

5.4.6.6.1. Current distribution on strands

The first quench example was performed at 410 A with a heat pulse at 6.0 V. The increasing rate and magnitude of all the strand voltages responding to the pulse voltage have been investigated, 3 μV, 10 μV, 30 μV and 100 μV and assumed as 4 voltage baseline for further measurements. The period it takes for each strand voltage to react from its initial state (no heat on Heater 1) to

reach the corresponding baseline voltage (outlined above) after the heat pulse was applied on Heater 1 is presented in Figure 5.49. The change in voltage of V7_0 across Heater 1 is assumed to be the centre of the strands layout. In Figure 5.49, the strand number on the left of V7_0 shows the strand location based on the distance between the first voltage tap V*n*a (*n* = strand number) and Heater 1 from the inner turn to the outer turn. The number on the right side shows the strand location based on the distance between the last voltage tap V*n*b (*n* = strand number) and Heater 1 from the inner turn to the outer turn. The pulse starts at 0 s, and the dashed line shows when the pulse was swicthed off time.

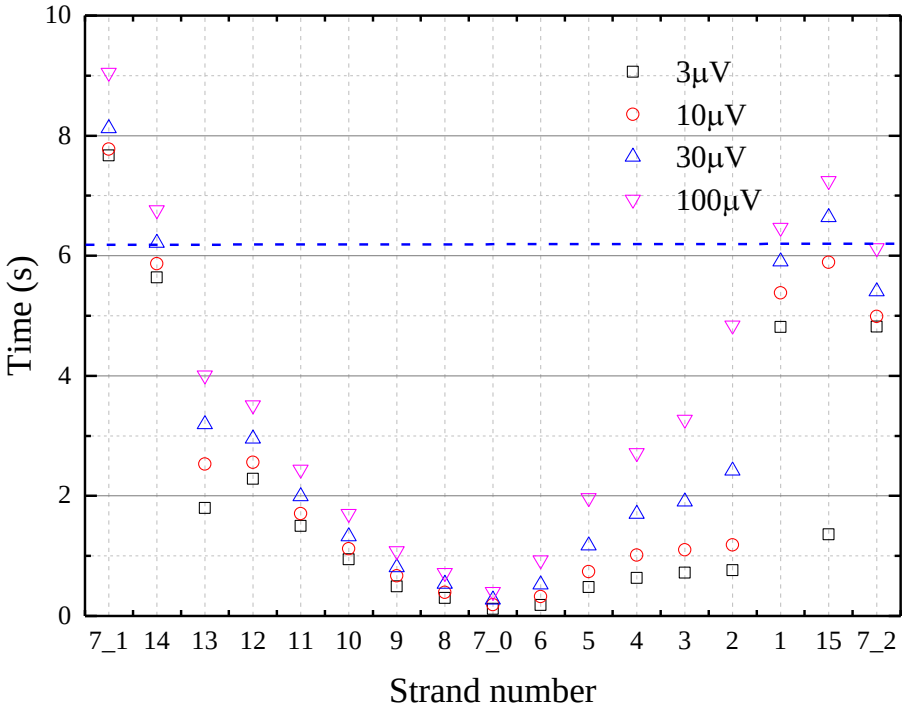

Figure 5.49: The time for each strand voltage to reach 3 μV, 10 μV, 30 μV and 100 μV at 410 A with a heat pulse at 6.0 V, and the dash line shows the pulse off time.

In Figure 5.49, each strand (*x* axis) takes a shorter time for the strands closer to the hot spot to reach the corresponding voltage, and as a results the shape of the profiles plotted for the 3 μV, 10 μV, 30 μV and 100 μV baseline voltages are 'V' shaped. For instance, the change of V7_0 reaches 100 μV in 0.5 s after the pulse is activated, and the changes of V6 and V8, (two strands adjacent to strand 7), both reach 100 μV in 1 s. In contrast, changes of V14 and V15, (two furthest strands from heater 1 on strand 7), take more than 6.5 s to reach 100 μV, and therefore the time difference is related to the rate of heat propagation, and the distance of the strand from the hot spot on strand 7. Furthermore, the voltage changes that arrise in the strand located on the left of V7_0 are faster than in strands located on the right of V7_0. This effect is likely a result of the heater position on strand 7 shown in Figure 5.50, which Heater 1 is soldered at the top edge of the copper shim that is closer to these underneath strands (strand 8, 9,…, 13, 14), and it takes longer time for the heat to propagate to other strands (strand 6, 5,…,1, 15) at a further side.

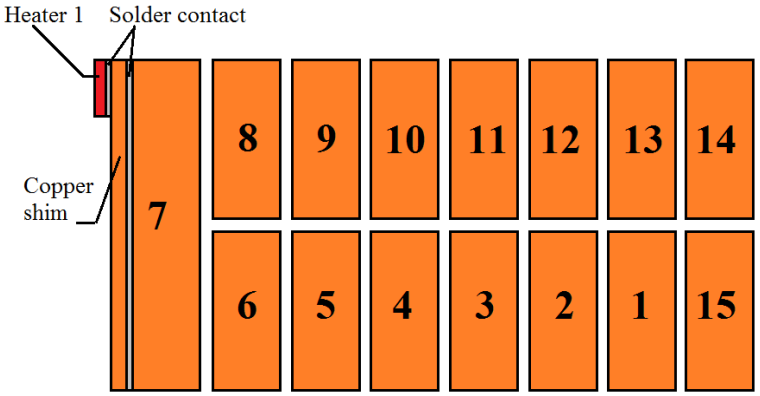

Figure 5.50: The schematic drawing of the Robel cable coil crosssection at the location of Heater 1.

In Figure 5.49, there are two gaps (strand 1 and strand 2, strand 14 and strand 13) in the profile showing the time taken for voltage to changes from 0 µV to 3 µV (black squares). Two gaps represent a limitation in the initial current carrying ability of strands 14, 15 and 1 after the pulse is applied. In other words, it takes longer time for the normal zone extension to reach these strands. Consequently, there should be a corresponding and large contact voltage change in these strands, which would imply that current sharing is active after the heat pulse is applied due to the parallel connection of the strands. The delay of voltage change observed in V7_1 and V7_2, across one pitch of the same strand either side of V7_0, implies a reducing current in strand 7 and a long time for heat to propagte in a longtitude direction toward both inner and outer contacts. A fast voltage increasing in V7_2 is also shown in Figure 5.37, and provides supporting evidence for the effect caused by the location of Heater 1. In addtion, strand 15 exhibited a small voltage (>3 µV) immediately after the heat pulse was applied and remained constant until thermal run away, which occurred just before the pulse was cut. However, the emergence of these small voltage arising just before the onset of quench have not been observed in lower currents. This may be due to other "hotter" strands current sharing with strand 15 at high transport currents..

5.4.6.6.2. Current distribution on current injection contacts

Figure 5.51 shows the changes of the inner contact and outer contact voltages for each strand after the heat pulse was applied at 410 A with a 6.0 V heat pulse. Six time steps, 0 s, 2 s, 4 s, 6.19 s, 8 s and 10 s were chosen as baseline values to generate the profile, with 6.19 s defined as the pulse width. When comapring the strand voltages from this study, the variation in strand contact voltages is not monotonic.

Figure 5.51a shows specifcally the changes of the strand inner contact voltages. The inner contact voltage plotted with respects to the strand number is a 'V' shape profile. The shape implies there is current redistribution evolving after the pulse is activated, with those strands located furthest from the hot spot on strand 7, exhibiting higher voltages and carrying morecurrent. The negative voltages that arises in strands 7, 8 and 9 during the initial phase of the heat pulse implies that current sharing in onging with other strands, and the change in sign, after the pulse is cut, implies that current is flowing backwards. The inner contact voltage of strand 8 starts to increase before the pulse is cut, and it continues to increase much faster than adjacent strands. One possibility for the behaviour observed in V7_2 is attributed to its proximity to Heater 1, and therefore a section

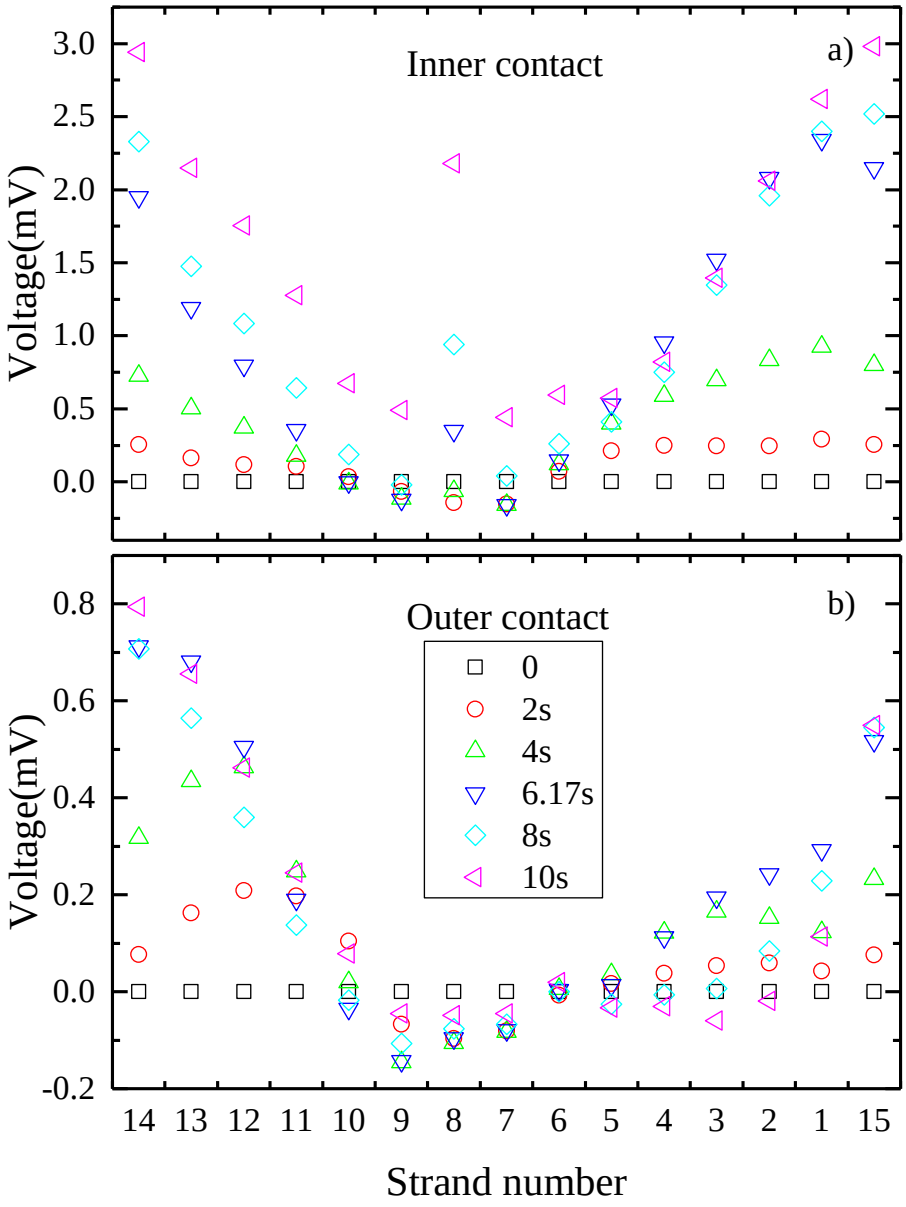

Figure 5.51: Strand contact voltage changes for a) inner contact and b) outer contact at different time after the pulse is applied with a transport current around 410 A and a 6.0V heat pulse, the pulse width is 6.17s.

of strand 8 receives more heat from the hot spot on strand 7 and the inner turn of strand 8 experiences an extension in its active normal zone.

Figure 5.51b shows the changes in the strand outer contact voltages. The profile of voltage plotted against strand number is also 'V' shaped, but shows greater scattering, especially in the strands located on the left side of strand 7. Strand 12 exhibits the greatest change in outer contact voltage (~ 0.5 mV) when the pulse is active, which is different to the voltage profile in Figure 5.51a, where the greatest change in voltage arise in the furthest strand 15 (~ 0.75 mV). However, there are some similar behaviours (between Figure 5.51a and Figure 5.51b) that are identified. For instance, the outer contact voltage originating from strands on the left side, change must faster than in strands located on the right side, which again reinforces the influence of the heater on the voltage response. A negative change voltage is also observed in strands 7, 8 and 9 during the

initial phase when the pulse is activated. The outer contact voltage of strand 9 reduces the most before the pulse is cut. Strand 9 also has the highest peak voltage immediately before the pulse is cut, and identifying it as the most susceptible strand to quench.

According to the changes in contact voltage at 410 A (95 % I_c) with a 6.0 V heat pulse, the inner contact shows more voltage changes compared with the outer contact especially after the pulse is cut. The field effect on the wound cable maybe one reason causing this difference. Another possiblity is the current sharing ability at the outer contact side is already limited by the critical current at high transport currents. The behaviour of current sharing is small for all the strand voltages and contact voltages to reduce when the transport current is also small, and in those strands that are located furthest from the hot spot, which maintain a higher capacity to carry current.

Figure 5.52 shows changes in both inner contact voltage and outer contact voltage at 8 time steps after activating a 6.0 V heat pulse with a winding current of 340 A (~64 % I_c), and the pulse switched off at 18.44 s. Figure 5.52a shows the changes in the inner contact voltage over the same period and is very similar to inner contact voltage response with 410 A (Figure 5.51a).

Figure 5.52b shows the behaviour of the outer contacts, the changes in voltage are much more scattered compared to Figure 5.51b (410 A), and strands 14, 13, 12 and 11 exhibit positive changes in voltage over the duration of the measurement. The greatest change in outer contact arises in strand 13 (0.1 mV), this is slightly lower than the corresponding voltage (~ 0.25 mV) of the inner contact on the same strand. The change in the inner contact voltage increase to around 1.7 mV when the pulse is cut. Negative voltage is evdient in strands on the right side of strand 7, where and the changes in voltage are between -15 μV and -25 μV. This seems to suggest current sharing occuring between the strands on the left side of Heater 1. The changes in the outer contact voltage are still small compared with 9 of 15 of the inner strands, which are above 1 mV. It is believed that the main current sharing occurs towards the inner contact side and via inter uncontinues contacts among the strands, instead of the outer contact for current injection.

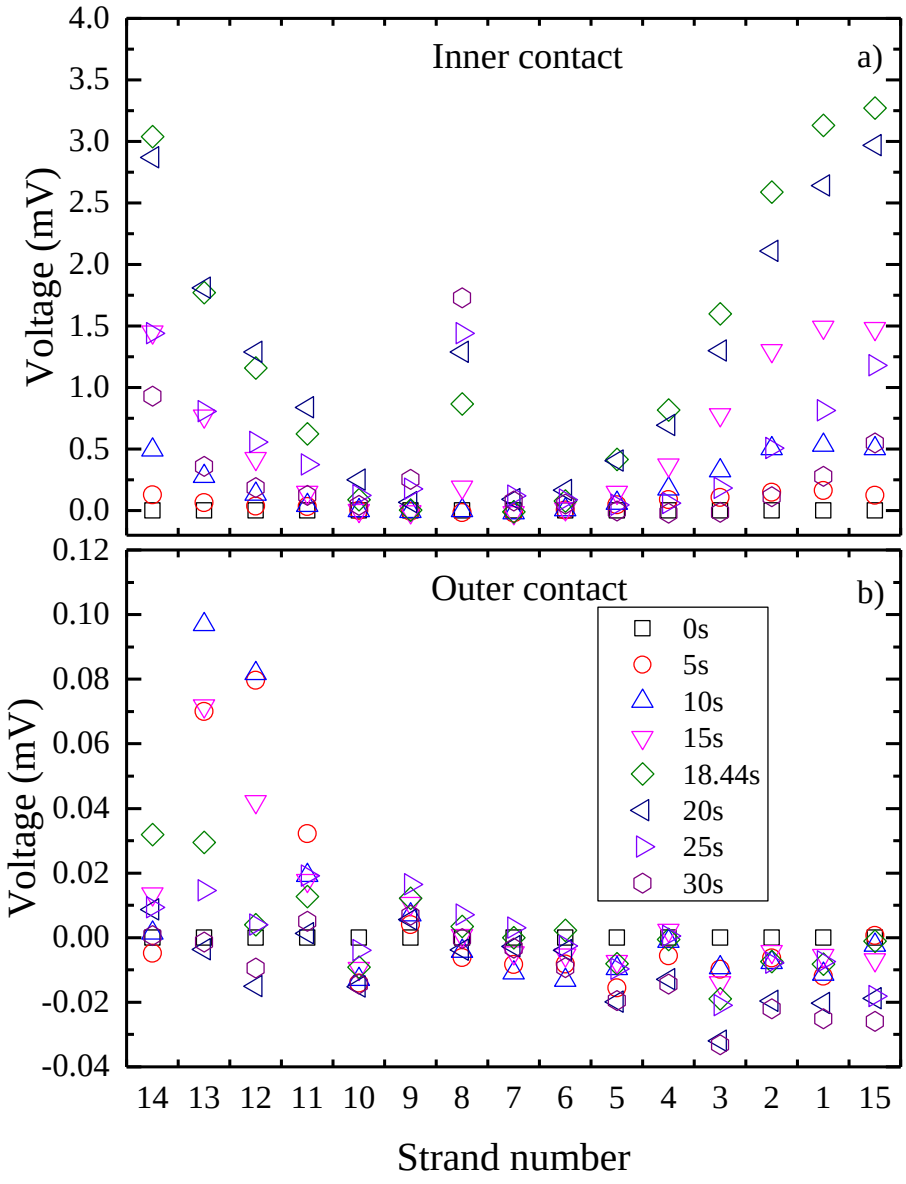

Figure 5.52: Strand contact voltage changes for a) inner contact and b) outer contact at different time after the pulse is applied with a transport current around 340 A and a 6.0V heat pulse, the pulse width is 18.44s.

5.4.6.6.3. Current distribution on outer contact copper ring

The possibility of current redistribution in the outer contact used for current injection was investigated by interogating the change in voltage of the outer contact at the copper ring at three different vertical positions, (near end voltage, middle end voltage and far end voltage) and the distribution of current density at three horizontal positions along the copper ring; at top near end to top far end voltage, top middle end to top far end voltage, bottom near end to bottom far end volatge and bottom middle end to bottom far end voltage. Figure 5.53 and Figure 5.54 show the voltage tracings on the copper ring for quench measurements at current of 410 A and 340 A and with a heat pulse at 6.0 V. It can be seen that all the voltages on the copper ring for both cases, almost remain constant for the duration of the the quench measurement.

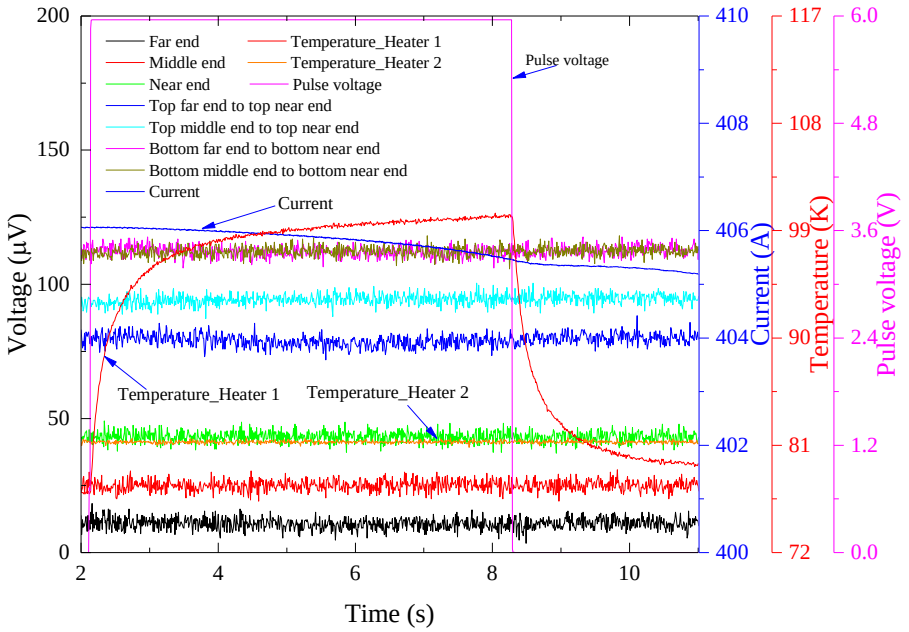

Figure 5.53: The tracings of near end voltage, middle end voltage, far end voltage, top near end to top far end voltage, top middle end to top far end voltage, bottom near end to bottom far end voltage and bottom middle end to bottom far end voltage on the copper ring, current, temperatures of Heater 1 and Heater 2 for the quench measurement at around 410 A with a 6.0 V pulse voltage.

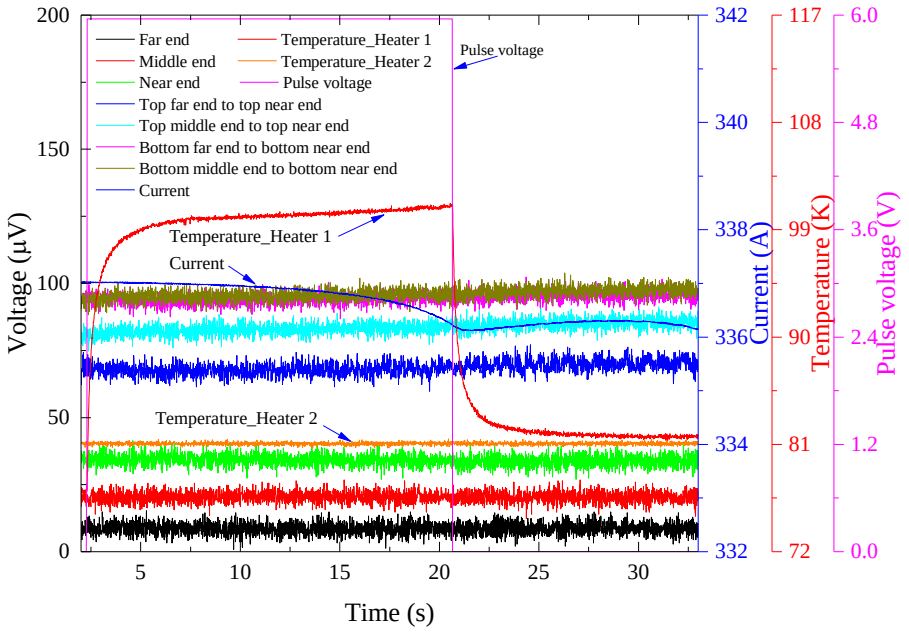

Figure 5.54: The tracings of near end voltage, middle end voltage, far end voltage, top near end to top far end voltage, top middle end to top far end voltage, bottom near end to bottom far end voltage and bottom middle end to bottom far end voltage on the copper ring, current, temperatures on strand 7 adjacent to Heater 1 and Heater 2 for the quench measurement at around 340 A with a 6.0 V pulse voltage.

5.4.6.7. The new current leads injection design

The main problem in contact voltage measurements is that current density in each strand is not measured identically. For example, the current transfer each strand of the 15 strands arranged in a parallel connection differ due to inhomogeneities in the soldered contacts and inter uncontinous

contact among the strands. The local current density in each independent strand contact cannot be defined from the contact voltage directly. In order to eliminate this effect, the copper block and copper ring could be with grooves to divide the contact into 15 independent contacts as shown in the 2D schematic drawing in Figure 5.55. This would create a series of independent current transferring interfaces between the current lead and each strand that would eliminate the current sharing to between strands in the jointed region.

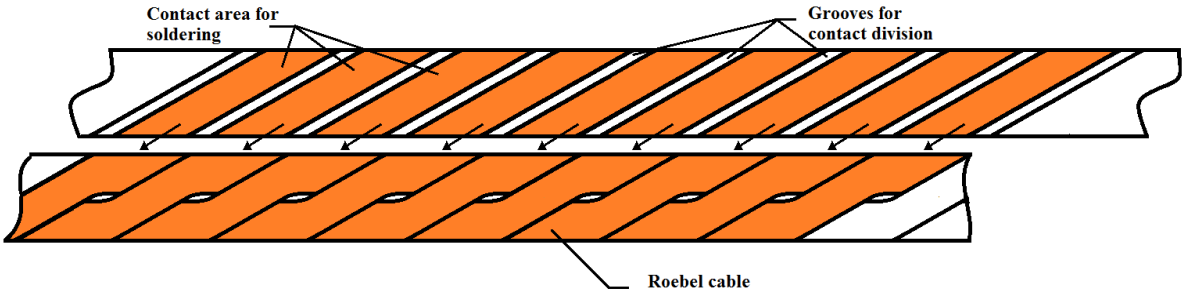

Figure 5.55: 2D schematic drawing for the current leads with grooves for Roebel cable soldering.

5.5 Conclusion

This chapter has described the preparation of a pancake coil made from a Roebel cable and instrumentated with a local heater, voltage taps and thermometers. The coil was immersed in a bath of LN2 at 77 K to analyse its performance and quench characteristics.

The critical current of this Roebel pancake coil is likely to be influenced by the parallel field on the inner turns of the coil, and where the thermodynamic condition of the coil under was called ‘unbalanced’ condition. Additional constant heat (8.0 V) was applied with a heater on the outer contact to make the outer strands (used for current injection) behave in a similar voltage range as the inner contacts (also used for current injection). This condition for quench measurement was called a ‘balanced’ condition.

The critical current at the middle of the coil was measured in both ‘unbalaced’ and ‘balanced’ conditions, and I_c was established as 440 A and 430 A repectiviely with no thermal run away observed in the strands and or the contact used for current injection. Both the inner contact and outer contact resistance was around 250-300 nΩ, and inner strand contact voltage traces showed nonlinearities when the transport current was above 200 A. The *n*-value of each strand in the inner turns of the coil was around 10.5. From studies of the current density distribution along the outer contact, most of the current seemed to transfer through the contacts towards the section of copper ring between the middle end and far end of the outer contact.

A quench in the winding could still be induced by activating point-like disturbances such as localised heating (via a smaller heater) even though the Roebel pancake coil has high stability in LN2. A series of trial quench measurements were perfomed in both ‘unbalanced’ and ‘balanced’ conditions. The responses of strand voltages, strand contact voltages, heater temperatures to the heat pulse were invistigated. The strand voltage profiles showed the normal zone propagation and how the transport of heat by conduction within the coil structure developed from the hot spot. The

MQE of both ‘unbalanced’ and ‘balanced’ conditions were estimated, and the MQE evaulated as function of different transport currents and heat pulse amplitude. The studies concentrated on determining the MQE for the coil maintained in the ‘balanced’ condition. For the same transport current, the MQE increased with the reduction of the applied heating power, and the MQE converged to infinite when the heating power approaches to a threshold power. Thereafter, all the strands remained in a steady state without drifting into a thermal run away, at a lower heating power. The temperature difference measured for the heat pulse on and for the heat pulse off was linearly increasing with the increasing applied heating power. Unfortunately, the threshold power required to trigger the quench at a single transport current (400 A) could be performed in this work, and therefore leaves scope to investigate how this threshold power may vary with different transport current in future work. The effects of different transport current on the MQE with the same heat pulse amplitude applied, the MQE increased proportionally with 1-j (scaled current), and increased dramatically when 1-j was above 0.1, and indicated that heat diffision is significant at low transport currents.

The response of the strand and the current injection contact voltages with respects to the heat pulse was investigated. The measurements revealed how voltages reduce on either sides of strand 7 and around the location of the hot spot. The behaviour of these strand contact voltages implied that current was being redistributed during the quench event. Consistent voltage responses in the three contacts distributed vertically on the outer copper ring, established that current redistribution occured towards the inner turns of the coil. However, the parallel connections and uncontinuous inter connections among the strands along the coil make the anayltics of the current sharing during the quench rather complex. Large voltages measured in the inner strand contacts located far from the hot spot imply that current sharing tends to occur over a longer period of time in the inner turns of the coil, and in a longitudinal direction. It is suggested that in future investigations, the voltage across different strands in the radial direction could be measured and anaylsed to acquire more details of current sharing during quench and to further reinforce the findings in this work.

Chapter 6
Conclusion and future works

This project has studied the electrical characteristics and thermal stability of HTS winding applications combined with experimental works on HTS nanobond/nano-heater joints and a Robel cable pancake coil. For the first time, nanobond technology has been used on HTS winding applications at Oxford Instruments (OI). The physical properties of nanofoil corresponding to their nanobond applications at low temperatures have been studied, and a new soldering methodology, nano-heater, was developed for HTS tape soldering joints. A 2 m long 2G YBCO Robel cable was wounded in a pancake coil to test the quench characteristics. Its length was enough to produce a a full development of current sharing among strands in LN2 at 77 K. These works are applicable to the optimisation design of HTS windings for large scale electrical applications, NMR device, high energy accelerator and tokamak devices [186]–[188].

6.1 Nanobond

Nanofoil provides an option for manufacturing HTS tapes soldering joints in-situ at room temperature. NiAl, is the main reaction product of the nanofoil. Its resistivity and thermal conductivity have been measured by several groups, but for the first time it has been applied in cryogenics. There are few papers that analyse the physical properties of nanofoil at low temperatures. The resistivity, thermal conductivity and heat capacity for both reacted and unreacted nanofoil have been measured from 4 K to 300 K by PPMS. These results have been evaluated and compared with the results from other research groups. The data of these physical properties are an important reference for geometry design parameters and performance evaluation of nanobond joints in HTS winding applications.

SEM with EDX investigation and XRD patterns indicate that the different grain size and the existence of other phases of nickel aluminide (such as Ni_2Al_3) in reacted nanofoil can be the reason for its higher resistivity compared with bulk NiAl. The cracks or voids existing within the reacted nanofoil cause a variable resistivity among the reacted nanofoil samples at each temperature. Optical and SEM microscopy of the cross-section for the nanobond joints show evidence of the cracks in the reacted nanofoil were filled with sufficient solder, which contributes to a good thermal and electrical stability. However, an analysis of the parallel

electrical circuit between nanofoil and solder implies the overall contact resistance of 2G-tape joints was in fact dominated by the resistivity of the reacted nanofoil (NiAl).

Both unreacted and reacted nanofoil have an obvious resistivity reduction with the decreasing of the temperature, and the measured thermal conductivity of reacted nanofoil is very similar to the thermal conductivity of 99 % pure aluminum at low temperatures (< 20 K). The Lorenz number and specific heat measured at room temperature, both indicate the properties of the unreacted nanofoil behave like the mixed phases of two metals, behaving in agreement with the Wiedemann-Franz law, Dulong and Petit law. However, the values of reacted nanofoil are larger than the metal specific constant and Sommerfeld constant at room temperature. The thermal resistance of one copper to copper nanobond joint, Al_2O_3 to Al_2O_3 nanobond joint and Al_2O_3 to copper solder joint have been measured from 4 K to 300 K. For the two nanobond joints samples, the measured results did not show any temperature dependence like the reacted nanofoil. The Al_2O_3 to copper soldering joint shows a similar trend variation between thermal conductivity and temperature compared with pure dense Al_2O_3. However, the thermal conduction performance of the two nanobond joint samples and copper to Al_2O_3 soldering joint presents degradation compared with reacted nanofoil. Especially for the Al_2O_3 to copper sample, there were only some point inter connections within the joint. The dissolubility of gold in solder alloy is considered as the reason for the soldering surface de-wetting and joint fracture.

Lap shear tests show the mechanical properties of the nanobond joints. Shear strength of 4 stainless steel to stainless steel dog bone lap joints were measured around 11-16 MPa. The homogeneous fracture of the soldered surfaces indicated good adhesion of the nanobond joints. Later six copper to copper (6 mm thick) nanobond joints with 240 ºC solder and 180 ºC solder were manufactured. The shear strength of these copper to copper nanobond joints for both two solders made on a hot plate at 60 ºC are around 11-15 MPa, and two samples made at room temperature exhibit very poor shear strength. This may imply that increasing the ambient temperature is helpful when attempting to fabricate a nanobond joint with good adhesion.

Therefore, the thermal conductivity of Al_2O_3 and reacted nanofoil and the strong mechanical performance of metallic nanobond joints indicate the nanobond process is an new option for bonding components for cryogenic engineering. DBC Al_2O_3 has been used for the electrical insulation in first stage current lead in our 10 T variable temperature insert rig. Furthermore, Nanofoil is a good candidate to perform the joint without the need of warming up several times since the reaction takes place in a localised spot. Additional work can be done to the determine the lap shear strength of metallic nanobond joint samples at cryogenics temperatures or at room temperature after several cooling cycles. The lap shear strength of conventional manually soldered metallic joints and nano-heater made metallic joints can be tested to give a comparison of the mechanical stability of these lap joints via different methods. After the lap shear strength tests, the morphology of the fractured surfaces of all the specimens can be checked via SEM and the fracture compositions can be analysed by EDX.

6.2 Nanoheater

The advantages of using nanobond for soldering HTS joints are simple manufacturing process at room temperature and fast energy dissipation. However, the high resistivity of reacted nanofoil makes it difficult to apply to HTS soldering joints directly. In order to achieve the requirements of good electrical and thermal transport for HTS winding applications, a new methodology for 2G-tape joints soldering, called nano-heater, was firstly developed. It makes use of the thermal energy produced during the nanofoil reaction without the foil staying between the two bonding components. The overall contact resistance of these new nano-heater made HTS joint samples, involving one 2G-tape to 2G-tape joint and two 2G-tape to copper joints was measured and presented in this work. The average overall contact resistance of nanoheater made soldered (Sn5Pb93.5Ag1.5, wt. %) joints between 2G-tape to copper was ~350 $n\Omega \times cm^2$, which is very similar with 2G-tape to copper nanobond joints' results. The average overall contact resistance of nanoheater made soldered (Sn5Pb93.5Ag1.5, wt. %) joint between two 2G-tapes was ~130 $n\Omega \times cm^2$. This value reduced more than half compared with 2G-tape to 2G-tape nanobond joints' results.

A 1D analytical model for lap joints between two simple conductors was performed with a formula to investigate the current transfer characteristics of a lap joint. The effect of contact resistance, conductor resistance and joint length on current distribution and overall contact resistance have been studied. Later, a new joint contact voltage method was developed. A sliding needle was applied to trace the voltage changes continuously along the distance from the end of the joint to the conductor. Three 2G-tape to copper lap joints were made. Two samples were soldered manually, and one made with the nano-heater method. These 2G-tapes were cut from the strands (Bruker EST) of a Roebel cable (assembled at KIT). The contact resistance and current transfer characteristics between two conductors for these samples was estimated by curve fitting using measured voltage profiles and analytical model results. The current distribution within the copper conductor that was overlapped on the joint, both measured and analytical model show that when a higher contact resistance ratio exists between two conductors for a lap joint, most of the current flows in the conductor (2G-tape) with lower resisitivity, and the current transfer occurs from 2G-tape to copper within the joint towards the end of 2G-tape. The 1D lap joint analytical model provides a formula to estimate optimal joint length, L_{opt}, for a minimum overall contact resistance. Moreover, large overall contact resistance (~8 μΩ) was observed for these three samples compared with lap joints using SuperPower 2G-tape (~ 110 nΩ) and BSSCO tape (~ 180 nΩ) with same solder (In97Ag3, wt. %) and a similar contact area.

The remaining problem is that this analytical model is for a joint between two simple conductors, and 2G-tape was assumed as a lump conductor instead of multilayers (superconductor, silver and copper laminate layer) in this model. Copper resistance and contact resistance (solder resistance and interfacial resistance between each layer) dominate the overall contact resistance compared with that of of silver and copper laminate layers. Consequently, a reasonable contact resistance can be estimated by using the measured voltage and measured copper resistance to the analytical model formula. However, in order to achieve

a good curve fitting beween the measured voltage and the analytical model, the superconductor resistivity needs to be assumed as a value that makes the electrical field much higher than 1 μV/cm at 40 A (2/3 of I_c). This may be true when the superconductor has current sharing with the metal matrix that is overlapped in the joint. Then if Ag/YBCO interfacial resistance and copper stabiliser resistance were known, the analytical model can be developed for a joint between two multilayer conductors. In future works, the overall contact resistance of lap joints with different solder (such as Sn60Pb40, wt. %) can be measured at different temperatures, in order to evaluate the performance of nano-heater made soldering joints for 2G-tapes..

6.3 Roebel cable

A Roebel cable can transport a higher current compared with isolated HTS tapes allowing a reduction in the number of turns of coils and providing the same fields with smaller inductance [9]. For single isolated HTS wires, the 1D quench characteristics of adiabatic systems have been widely studied via both experimental and analytical model by several research groups. But for Roebel cables, it is found that the traditional method of experimental quench studies on adiabatic short conductors becomes impractical due to the non-continuous touch contacts among the strands and the more complex current sharing and normal zone propagation present in the cable. We developed a new method to study the performance and quench characteristics of a 2 m long 2G YBCO (Bruker EST) Roebel cable (assembled at KIT) in LN2 at 77 K. This cable was co-wound with fiberglass ribbon into an adiabatic pancake coil via epoxy impregnation. The quench characteristics of Roebel pancake coils are important to real applications, and the *VI* characteristics and critical current measurement results can provide information that can be readily dealt with by a suitably developed computer modelling.

The *VI* characteristics and critical current of this pancake coil have been studied in LN2. Both the overall inner and outer contact resistances were between 250-300 nΩ. The strand inner contact voltages start to present a nonlinearity when the transport current was above 200 A. In order to make the outer current injection contact voltages to reach a similar scale a constant heat (8.0 V) was applied on the outer contact, establishing a ‘balanced’ condition. However, not all the strand contact voltages increase to a similar range, and the increasing of both inner and outer contact voltages of some strands seems to be related to the current redistribution in the Roebel cable. Fortunately, these changes have a minimum effect on the thermal stability in the middle of the coil. Another problem is the current distribution on the outer contact copper ring. The polarity of the local longitudinal voltages along the copper ring implies that there was current flowing opposite to the current direction within the Roebel cable. The COMSOL models indicate there would be a high possibility of an inhomogeneous current injection between strand and copper ring due to an uneven soldering contact.

A set of quench measurements were perfomed in both ‘unbalanced’ and ‘balanced’ conditions for this Roebel pancake coil in LN2 at 77 K. The responses of strand voltages, strand contact voltages and temperatures to the heat pulse have been studied. The strand voltage profiles show the normal zone propagation and heat distribution within the coil from the hot spot. The

MQE as a function of different transported currents from 350 A to 425 A in the 'balanced' condition has been studied. MQE increases with the increasing of 1-*j* (scaled current), and it increases dramatically when 1-*j* is above 0.1. At a transport current of 400 A, the MQE increases when reducing the heating power until MQE is going to infinte when the heating power approaches to a minimum power that can induce a quench. Afterwards, all the strands keep steady state without thermal runaway with the continuous reduction of the heating power. The Roebel cable has a much higher thermal stability due to a 100 times larger MQE at the same percentage critical current, compared with a single HTS conductor. The parallel connection and uncontinuous point inter connections among the strands along the coil make a complex current sharing profile during the quench process. Strands that are far from the hot spot have large inner contact voltages. These large voltages seems to be accumulated from the current sharing among the strands during a long period in the inner turns of the coil in the longtitudal direction.

The reduction of both strand voltage and strand contact voltage on some strands that were close to the hot spot suggest a current sharing with other strands during the quench. The increasing in the voltage of a strand may be due to the increasing current or the thermal runaway, especially for inner turns of the coil suffering higher field compared with the outer turns. This makes difficult the study of the current redistribution among the strands. Applying constant heat on outer the contact for a 'balanced' condition makes it possible to investigate contact voltage changes when a point hot spot was induced in the middle of the coil. The study of combined results of strand voltage changes and two injection contact voltage changes indicate that the current sharing tends to be along the inner turns of the coil in a longitudinal direction. For future work, the local changes of voltage polarity among different strands can be investigated to trace the current sharing among nearby strands when a heat disturbance is applied in the middle of the coil. Later this pancake coil will be tested to measure the critical current and quench characteristics in a 10 T variable temperature insert rig. Furthermore, if a new Roebel cable sample was used to make a new coil, the copper block and copper ring for current injection could be cut with grooves to match the face of each strand current transfer section. This design can limit the current sharing among the contacts. Placing local pairs of voltage taps on the copper ring can trace the voltage changes to estimate local current density changes.

Reference

[1] S. K. Baik *et al.*, "Electrical parameter evaluation of a 1 MW HTS motor via analysis and experiments," *Cryogenics (Guildf).*, vol. 49, no. 6, pp. 271–276, 2009.

[2] I. Petrov and J. Pyrhonen, "Performance of low-cost permanent magnet material in PM synchronous machines," *IEEE Trans. Ind. Electron.*, vol. 60, no. 6, pp. 2131–2138, 2013.

[3] H. Wen, W. Bailey, K. Goddard, M. Al-Mosawi, C. Beduz, and Y. Yang, "Performance test of a 100 kW HTS generator operating at 67 K-77 K," *IEEE Trans. Appl. Supercond.*, vol. 19, no. 3, pp. 1652–1655, 2009.

[4] J. B. Song, Y. H. Choi, D. G. Yang, Y. G. Kim, K. L. Kim, and H. G. Lee, "Review of core technologies for development of 2G HTS NMR/MRI magnet: A status report of progress in Korea University," *Results Phys.*, vol. 7, pp. 3264–3276, 2017.

[5] G. A. Kirby *et al.*, "Accelerator-quality HTS dipole magnet demonstrator designs for the EuCARD-2 5-T 40-mm clear aperture magnet," *IEEE Trans. Appl. Supercond.*, vol. 25, no. 3, 2015.

[6] N. Bagrets, G. Celentano, A. Augieri, R. Nast, and K. P. Weiss, "Investigation of Soldered REBCO Tape-Copper Joints for Superconducting Applications," *IEEE Trans. Appl. Supercond.*, vol. 26, no. 4, pp. 26–29, 2016.

[7] Y. Tsui, E. Surrey, and D. Hampshire, "Soldered joints—an essential component of demountable high temperature superconducting fusion magnets," *Supercond. Sci. Technol.*, vol. 29, no. 7, p. 075005, 2016.

[8] N. N. Balashov *et al.*, "Low-Resistance Soldered Joints of Commercial 2G HTS Wire Prepared at Various Values of Applied Pressure," *IEEE Trans. Appl. Supercond.*, vol. 28, no. 4, Jun. 2018.

[9] W. Goldacker, F. Grilli, E. Pardo, A. Kario, S. I. Schlachter, and M. Vojenčiak, "Roebel cables from REBCO coated conductors: a one-century-old concept for the superconductivity of the future," *Supercond. Sci. Technol.*, vol. 27, no. 9, p. 093001, 2014.

[10] Z. Melhem, *High temperature superconductors (HTS) for energy applications*. Woodhead Pub, 2012.

[11] National Electric Coil, "Resin Rich Coils & Bars Balance Costs & Reliability." [Online]. Available: http://www.national-electric-coil.com/resinrichwindings.php. [Accessed: 31-Aug-2018].

[12] B. D. S, K. W, S. S, and V. G, "3. Characteristics of the coils," *Fusion Eng. Des.*, vol. 7, pp. 23–51, Jan. 1988.

[13] A. P. Verweij and L. Buchsbaum, "Experimental results of current distribution in Rutherford-type LHC cables," *Cryogenics (Guildf).*, vol. 40, no. 8–10, pp. 663–670, 2000.

[14] Indium Corporatrion, "Properties of NanoFoil." [Online]. Available: http://www.indium.com/nanofoil/properties/.

[15] Indium Corporation, "Solder Preforms manufactured by Indium Corporation." [Online]. Available: https://www.indium.com/nanofoil/preforms/. [Accessed: 10-Mar-2019].

[16] Oxford Instruments, "Application of Nanofoil at Oxford Instruments," 2013. .

[17] Indium Corporation, "NanoFoil® User Guide." [Online]. Available: http://www.indium.com/nanofoil/#whitepapers.

[18] Indium Corporation, "NanoBond® and component bonding by Indium Corporation." [Online]. Available: https://www.indium.com/nanofoil/nanobond/. [Accessed: 10-Mar-2019].

[19] J. A. Howell, "Deposition, Characterization, and Thermomechanical Fatigue of Nickel Aluminide and Ruthenium Aluminide Thin Films," Pennsylvania State University, 2010.

[20] X. Qiu, "Reactive Multilayer Foils and Their Applications," Louisiana State University, 2007.

[21] C. Michaelsen, G. Lucadamo, and K. Barmak, "The early stages of solid-state reactions in Ni/Al multilayer films," *J. Appl. Phys.*, vol. 80, no. 12, pp. 6689–6698, 1996.

[22] A. S. Edelstein *et al.*, "Intermetallic phase formation during annealing of Al/Ni multilayers," *J. Appl. Phys.*, vol. 76, no. 12, pp. 7850–7859, 1994.

[23] J. Noro, A. S. Ramos, and M. T. Vieira, "Intermetallic phase formation in nanometric Ni/Al multilayer thin films," *Intermetallics*, vol. 16, no. 9, pp. 1061–1065, 2008.

[24] E. G. Colgan, "A review of thin-film aluminide formation," *Mater. Sci. Reports*, vol. 5, no. 1, pp. 1–44, 1990.

[25] P. Nash, M. F. Singleton, and J. L. Murray, "Phase diagrams of binary nickel alloys," *ASM Int.*, 1991.

[26] E. G. Colgan *et al.*, "Sequence Of Phase Formation In Ni/Ai Contrasted With Ni/Si," *MRS Proc.*, vol. 54, p. 121, Jan. 1985.

[27] K. J. Blobaum, D. Van Heerden, A. J. Gavens, and T. P. Weihs, "Al/Ni formation reactions: characterization of the metastable Al9Ni2 phase and analysis of its formation," *Acta Mater.*, vol. 51, no. 13, pp. 3871–3884, 2003.

[28] A. S. Edelstein *et al.*, "Intermetallic phase formation during annealing of Al/Ni multilayers," *J. Appl. Phys.*, vol. 76, no. 12, pp. 7850–7859, 1994.

[29] A. Tonejc, D. Ročák, and A. Bonefačić, "Mechanical and structural properties of Al-Ni alloys rapidly quenched from the melt," *Acta Metall.*, vol. 19, no. 4, pp. 311–316, 1971.

[30] F. Takahashi and A. L. Greer, "Interfacial reactions in Al/Ni multilayers," *Mech. Alloy. Metastable Nanocrystalline Mater. Part 2*, vol. 269, no. 2, pp. 601–606, 1998.

[31] U. Rothhaar, H. Oechsner, M. Scheib, and R. Müller, "Compositional and structural characterization of temperature-induced solid-state reactions in Al/Ni multilayers," *Phys. Rev. B*, vol. 61, no. 2, pp. 974–979, Jan. 2000.

[32] A. Ustinov, L. Olikhovska, T. Melnichenko, and A. Shyshkin, "Effect of overall composition on thermally induced solid-state transformations in thick EB PVD Al/Ni multilayers," *Surf. Coatings Technol.*, vol. 202, no. 16, pp. 3832–3838, 2008.

[33] D. B. Miracle, "The physical and mechanical properties of NiAl," *Acta Met. mater.*, vol. 41, no. 3, pp. 649–684, 1993.

[34] Y. Yamaguchi, D. A. Kiewit, T. Aoki, and J. O. Brittain, "Electrical resistivity of NiAl, CoAl, NiGa, and CoGa," *J. Appl. Phys.*, vol. 39, no. 1, pp. 231–232, 1968.

[35] S. R. Butler, J. E. Hanlon, and R. J. Wasilewski, "Electric and Magnetic Properties of B2 Structure Compounds: NiAl, CoAl," *J. Phys. Chem. Solids*, vol. 30, p. 6, 1969.

[36] G. R. Caskey, J. M. Franz, and D. J. Sellmyer, "Electronic ands Magnetic states in

meyallic compounds - II. Electron transport and magnetic susceptibility in NiAl and FeAl.pdf," *J. Phys. Chem. Solids*, vol. 34, pp. 1179–1198, 1973.

[37] H. Jacobi, B. Vassos, and H.-J. Engell, "Electrical properties of β-phase NiAl," *J. Phys. Chem. Solids*, vol. 30. pp. 1261–1271, 1969.

[38] Y. Yamaguchi, T. Aoki, and J. O. Brittain, "Electronic structure of β'-NiAl," *J. Phys. Chem. Solids*, vol. 31, no. 6, pp. 1325–1343, 1970.

[39] H. Jacobi and H.-J. Engell, "Defect structure in non-stoichiometric β-(Ni, Cu)Al.pdf," *Acta Metall.*, vol. 19, no. 7, pp. 701–711, 1971.

[40] T. Yoshitomi, Y. Ochiai, and J. O. Brittain, "Electrical Resistivity of NiAl," *Solid State Commun.*, vol. 20, no. 8, pp. 741–742, 1976.

[41] Y. P. Lee, Y. V. Kudryavtsev, V. V. Nemoshkalenko, J. Y. Rhee, and K. W. Kim, "Effect of the structural disorder on the magnetic, transport, and optical properties of B2-phase Ni 0.50 Al 0.50 alloy films," *J. Appl. Phys.*, vol. 91, no. 7, p. 4364, 2002.

[42] T. J. S. Anand, H. P. Ng, A. H. W. Ngan, and X. K. Meng, "Temperature-coefficient-of-resistance characteristics of sputter-deposited NixAl1-x thin films for $0.5 < x < 1$," *Thin Solid Films*, vol. 441, no. 1–2, pp. 298–306, 2003.

[43] N. Tabatabaie, T. Sands, J. P. Harbison, H. L. Gilchrist, L. T. Florez, and V. G. Keramidas, "Electrical resistivity of thin epitaxial NiAl buried in (Al,Ga) As," *Appl. Phys. Lett.*, vol. 54, no. 21, pp. 2112–2114, 1989.

[44] X. Y. Qin *et al.*, "Resistivity and its temperature dependence of nanostructured NiAl at temperatures from 77 to 300 K," *J. Appl. Phys.*, vol. 80, no. 8, pp. 4776–4778, 1996.

[45] W. S. Walston and R. Darolia, "Effect of Alloying on Physical Properties of NiAl," in *MRS Proceedings*, 1992, vol. 288, p. 237.

[46] Y. Terada, K. Ohkubo, T. Mohri, and T. Suzuki, "Thermal conductivity of intermetallic compounds with metallic bonding," *Mater. Trans.*, vol. 43, no. 12, pp. 3167–3176, 2002.

[47] R. Darolia, "NiAI Alloys for High-temperature Structural Applications," *Jom*, vol. 43, no. 3, pp. 44–48, 1991.

[48] J. C. Zhao, X. Zheng, and D. G. Cahill, "Thermal conductivity mapping of the Ni-Al system and the beta-NiAl phase in the Ni-Al-Cr system," *Scr. Mater.*, vol. 66, no. 11, pp. 935–938, 2012.

[49] M. Kogachi, T. Tanahashi, Y. Shirai, and M. Yamaguchi, "Determination of Va concentration and defect structure in the B2 type NiAl β-phase alloys," *Scr. Mater.*, vol. 34, no. 2, pp. 243–248, 1996.

[50] Z. Tong and H. Bao, "Decompose the electron and phonon thermal transport of intermetallic compounds NiAl and Ni3Al by first-principles calculations," *Int. J. Heat Mass Transf.*, vol. 117, no. December 2017, pp. 972–977, 2018.

[51] S. V Raj, "Thermophysical Properties of Cold- and Vacuum Plasma-Sprayed Cu-Cr-X Alloys, NiAl and NiCrAlY Coatings I: Electrical and Thermal Conductivity, Thermal Diffusivity, and Total Hemispherical Emissivity," *J. Mater. Eng. Perform.*, vol. 26, no. 11, pp. 5456–5471, Nov. 2017.

[52] C. A. Alexander, J. S. Ogden, S. M. Risser, and V. E. Wood, "Thermodynamic characterization of NiAl," *J. Chem. Thermodyn.*, vol. 41, no. 5, pp. 610–616, 2009.

[53] J. C. Ho and D. P. Dandekar, "LOW TEMPERATURE HEAT CAPACITIES OF SEVERAL HIGH STRENGTH MATERIALS," 1988.

[54] P. D. Desai, "Thermodynamic Properties of Selected Binary Aluminum Alloy Systems," *J. Phys. Chem. Ref. Data*, vol. 16, no. 1, pp. 109–124, Jan. 1987.

[55] W. de Dood and P. F. de Chatel, "Low temperature specific heat of Ni3Al and Ni3Ga," *J. Phys. F Met. Phys. J. Phys. F Met. Phys*, vol. 3, no. 5, pp. 1039–1053, 1973.

[56] J. A. Seitchikf And and R. H. Walmsley, "Nuclear Magnetic Resonance Study of Al27 in NiAl," *Phys. Rev.*, vol. 131, no. 4, pp. 1473–1477, 1963.

[57] J. Begot, R. Caudron, P. Faivre, A. Lasalmonie, and P. Costa, "Chaleur spécifique a basse température de la famille Ni1-xCo xAl : observations en relation avec la structure de bandes de ces composés et la transformation martensitique de Ni1+yAl 1-y," *J. Phys. Lettres*, vol. 35, no. 11, pp. 225–228, 1974.

[58] J. Wang *et al.*, "Joining of stainless-steel specimens with nanostructured Al/Ni foils," *J. Appl. Phys.*, vol. 95, no. 1, pp. 248–256, 2004.

[59] J. Wang, E. Besnoin, O. M. Knio, and T. P. Weihs, "Effects of physical properties of components on reactive nanolayer joining," *J. Appl. Phys.*, vol. 97, no. 11, 2005.

[60] W. Zhu, "Soldering interconnects through self-propagating reaction process," Loughborough University, 2016.

[61] T. A. Siewert, D. R. Smith, S. Liu, and J. C. Madeni, "Database for Solder Properties with Emphasis on New Lead-free Solders," *NIST*, 2002. [Online]. Available: https://www.msed.nist.gov/solder/NIST_LeadfreeSolder_v4.pdf. [Accessed: 11-Mar-2019].

[62] J. Pan, B. J. Toleno, T. C. Chou, and W. J. Dee, "The effect of reflow profile on SnPb and SnAgCu solder joint shear strength," *Solder. Surf. Mt. Technol.*, vol. 18, no. 4, pp. 48–56, 2006.

[63] Z. Xie, W. Xue, H. Chen, and Y. Huang, "Mechanical and thermal properties of 99% and 92% alumina at cryogenic temperatures," *Ceram. Int.*, vol. 37, no. 7, pp. 2165–2168, 2011.

[64] "Oxide Ceramics – Aluminum Oxide (Al2O3)," *CeramTec* . [Online]. Available: https://www.ceramtec.com/ceramic-materials/aluminum-oxide/. [Accessed: 10-Jul-2018].

[65] "Aluminum Oxide, Al2O3 Ceramic Properties," *Accuratus*. [Online]. Available: https://accuratus.com/alumox.html. [Accessed: 10-Jul-2018].

[66] L. K. Taiwo, "Developing a ceramic composite for applications in power electronic substrates," King Fahd University of Petroleum & Minerals, 2016.

[67] J. F. Burgess, A. Neugebauer, G. Flanagan, and R. E. Moore, "The Direct Bonding of Metals to Cermamics and Application in Electronics," *Electrocompon. Sci. Technol.*, vol. 2, no. C, pp. 233–240, 1976.

[68] Y. S. Sun and J. C. Driscoll, "A new hybrid power technique utilizing a direct Copper to ceramic bond," *IEEE Trans. Electron Devices*, vol. 23, no. 8, pp. 961–967, Aug. 1976.

[69] T. E. O'BRIEN and A. C. D. CHAKLADER, "Effect of Oxygen on the Reaction Between Copper and Sapphire," *J. Am. Ceram. Soc.*, vol. 57, no. 8, pp. 329–332, Aug. 1974.

[70] V. Hussennether, M. Oomen, M. Leghissa, and H. W. Neumüller, "DC and AC properties of Bi-2223 cabled conductors designed for high-current applications," in *Physica C: Superconductivity and its Applications*, 2004, vol. 401, no. 1–4, pp. 135–139.

[71] M. Leghissa *et al.*, "Development and application of superconducting transformers," *Phys. C Supercond. its Appl.*, vol. 372–376, no. PART 3, pp. 1688–1693, 2002.

[72] M. N. Wilson, "Superconductivity and accelerators: The good companions," *IEEE Trans. Appl. Supercond.*, vol. 9, no. 2 PART 1, pp. 111–121, 1999.

[73] W. Goldacker *et al.*, "High current DyBCO-ROEBEL Assembled Coated Conductor (RACC)," *J. Phys. Conf. Ser.*, vol. 43, no. 1, pp. 901–904, 2006.

[74] W. Goldacker *et al.*, "ROEBEL Assembled Coated Conductors (RACC): Preparation, properties and progress," *IEEE Trans. Appl. Supercond.*, vol. 17, no. 2, pp. 3398–3401, 2007.

[75] N. J. Long *et al.*, "Narrow strand YBCO Roebel cable for lowered AC loss," *J. Phys. Conf. Ser.*, vol. 97, no. 1, p. 012280, Feb. 2008.

[76] W. Goldacker *et al.*, "CRITICAL CURRENTS IN ROEBEL ASSEMBLED COATED CONDUCTORS (RACC)," *AIP Conf. Proc.*, vol. 986, no. 461, 2008.

[77] M. Nii, N. Amemiya, T. Nakamura, T. Tsukamoto, T. Komeda, and Z. Jiang, "Alternating current loss characteristics of a Roebel cable consisting of coated conductors and a three- dimensional structure Three-dimensional model for numerical electromagnetic field analyses of coated superconductors and its application to Roebel cabl," *Supercond. Sci. Technol. Supercond. Sci. Technol*, vol. 27, pp. 35007–16, 2014.

[78] R. A. Badcock, N. J. Long, M. Mulholland, S. Hellmann, A. Wright, and K. A. Hamilton, "Progress in the manufacture of long length YBCO roebel cables," *IEEE Trans. Appl. Supercond.*, vol. 19, no. 3, pp. 3244–3247, 2009.

[79] A. Kario *et al.*, "Investigation of a Rutherford cable using coated conductor Roebel cables as strands," *Supercond. Sci. Technol.*, vol. 26, no. 8, pp. 85019–85025, 2013.

[80] W. Goldacker *et al.*, "Status of high transport current ROEBEL assembled coated conductor cables," *Supercond. Sci. Technol.*, vol. 22, no. 3, p. 034003, 2009.

[81] F. Grilli, E. Pardo, A. Stenvall, D. N. Nguyen, W. Yuan, and F. Gomory, "Computation of losses in HTS under the action of varying magnetic fields and currents," *IEEE Trans. Appl. Supercond.*, vol. 24, no. 1, 2014.

[82] N. J. Long, R. A. Badcock, K. Hamilton, A. Wright, Z. Jiang, and L. S. Lakshmi, "Development of YBCO Roebel cables for high current transport and low AC loss applications," in *Journal of Physics: Conference Series*, 2010, vol. 234, no. PART 2, p. 22021.

[83] E. Pardo, M. Staines, Z. Jiang, and A. -, "The development of a Roebel cable based 1 MVA HTS transformer Related content Ac loss modelling and measurement of superconducting transformers with coated-conductor Roebel-cable in low-voltage winding," *Supercond. Sci. Technol.*, vol. 25, no. 1, p. 014002, Jan. 2012.

[84] W. Goldacker *et al.*, "Improvement of superconducting properties in ROEBEL assembled coated conductors (RACC)," *IEEE Trans. Appl. Supercond.*, vol. 19, no. 3, pp. 3098–3101, 2009.

[85] L. Cavallucci, M. Breschi, P. L. Ribani, and Y. Yang, "Electrothermal modeling of quench in REBCO roebel cables," *IEEE Trans. Appl. Supercond.*, vol. 28, no. 4, pp. 18–22, 2018.

[86] J. R. Bumby, *Superconducting rotating electrical machines*. Oxford: Clarendon Press, 1983.

[87] M. Wilson, *Superconducting Magnets*. Oxford Science, 1983.

[88] J. Bardeen, L. N. Cooper, and J. R. Schrieffer, "Theory of Superconductivity," *Phys.*

Rev., vol. 108, no. 5, pp. 1175–1204, Dec. 1957.

[89] A. Mann, "High-temperature superconductivity at 25: Still in suspense," *Nature*, vol. 475, no. 7356, pp. 280–282, Jul. 2011.

[90] J.G. Bednorz and K.A. Müller, "Possible High Tc Superconductivity in the Ba-La-Cu-O," *Condens. Matter*, vol. 64, pp. 189–193, 1986.

[91] M. K. Wu *et al.*, "Superconductivity at 93 K in a new mixed-phase Y-Ba-Cu-O compound system at ambient pressure," *Phys. Rev. Lett.*, vol. 58, no. 9, pp. 908–910, Mar. 1987.

[92] M. Ono, S. Koga, and H. Ohtsuki, "Japan's superconducting Maglev train," *IEEE Instrum. Meas. Mag.*, vol. 5, no. 1, pp. 9–15, Mar. 2002.

[93] Y. Iwasa, "HTS and NMR/MRI magnets: Unique features, opportunities, and challenges," *Phys. C Supercond. its Appl.*, vol. 445, pp. 1088–1094, 2006.

[94] L. Rossi, "The LHC superconducting magnets," in *Proceedings of the 2003 Bipolar/BiCMOS Circuits and Technology Meeting (IEEE Cat. No.03CH37440)*, pp. 141–145.

[95] J. A. Demko *et al.*, "Triaxial HTS Cable for the AEP Bixby Project," *IEEE Trans. Appl. Supercond.*, vol. 17, no. 2, pp. 2047–2050, Jun. 2007.

[96] SuperPower, "HTS Materials Technology." [Online]. Available: http://www.superpower-inc.com/content/hts-materials-technology/. [Accessed: 25-Sep-2016].

[97] Metox, "MetOx manufacturing technology produces high quality HTS material using nano-engineering at the atomic level." [Online]. Available: http://www.metoxtech.com/revolutionary-technology/.

[98] Bruker, "YBCO coated conductor." [Online]. Available: https://www.bruker.com/fileadmin/user_upload/8-PDF-Docs/BEST/DataSheets/HTS.pdf. [Accessed: 25-Sep-2016].

[99] S. A. March, "The Application of High Temperature Superconducting Materials tp Power Switches.pdf," University of Southampton, 2009.

[100] Amalia Ballarino, "HTS at CERN & LHC current leads." [Online]. Available: http://at-mel-cf.web.cern.ch/at-mel-cf/html/physicsHTS.htm.

[101] F. Kametani, J. Jiang, M. Matras, D. Abraimov, E. E. Hellstrom, and D. C. Larbalestier, "Comparison of growth texture in round Bi2212 and flat Bi2223 wires and its relation to high critical current density development.," *Sci. Rep.*, vol. 5, p. 8285, 2015.

[102] T. Nakashima *et al.*, "Overview of the recent performance of DI-BSCCO wire," *Cryogenics (Guildf).*, vol. 52, no. 12, pp. 713–718, 2012.

[103] I. Falorio, "E - J Characteristics , Current Sharing and Quench Behaviour of YBCO Coated Conductor Tapes at Different Temperatures," University of Southampton, 2014.

[104] T. P. Sheahen, *Introduction to high-temperature superconductivity*. Plenum Press, 1994.

[105] N. Bay and M. S. Nielsen, "Mechanical processing of Ag/BSCCO high temperature superconductor tape," *Journal of Materials Processing Technology*, vol. 151, no. 1–3 SPEC. ISS. pp. 18–26, 2004.

[106] Sumitomo Electric, "Bismuth-based high temperature superconducting wire," 2011. [Online]. Available: http://global-sei.com/super/hts_e/index.html.

[107] W. O. S. Bailey, Y. Yang, C. Beduz, and K. F. Goddard, "Short circuit tests on a

coreless HTS synchronous generator," *IEEE Trans. Appl. Supercond.*, vol. 23, no. 3, pp. 2–6, 2013.

[108] W. Bailey, H. Wen, M. Al-Mosawi, K. Goddard, and Y. Yang, "Testing of a lightweight coreless HTS synchronous generator cooled by subcooled liquid nitrogen," *IEEE Trans. Appl. Supercond.*, vol. 21, no. 3, pp. 1159–1162, 2011.

[109] W. Bailey, M. Al-Mosawi, K. Goddard, Y. Yang, and C. Beduz, "The Design of a Lightweight HTS Synchronous Generator Cooled by Subcooled Liquid Nitrogen," *IEEE Trans. Appl. Supercond.*, vol. 19, no. 3, pp. 1674–1677, 2009.

[110] EHTS, "HTS Coated Conductors: Up-Scaling to Long Length, Properties, Applications and Expectations." [Online]. Available: http://www.prizz.fi/sites/default/files/tiedostot/linkki1ID358.pdf. [Accessed: 25-Sep-2016].

[111] B. Lukasik, "Design and optimisation of a coreless superconducting symchronous generator," University of Southampton, 2010.

[112] M. W. Rupich *et al.*, "YBCO coated conductors by an MOD/RABiTS^{TM} process," *IEEE Trans. Appl. Supercond.*, vol. 13, no. 2 III, pp. 2458–2461, Jun. 2003.

[113] SuperPower, "2G HTS Wire." [Online]. Available: http://www.superpower-inc.com/content/2g-hts-wire. [Accessed: 25-Sep-2016].

[114] Princeton Plasma Physics Laboratory, "Prospects and Challenges of the Use of HTS Materials for Fusion | Princeton Plasma Physics Lab." [Online]. Available: http://www.pppl.gov/events/prospects-and-challenges-use-hts-materials-fusion.

[115] Superpower, "2015 Technology and Manufacturing Innovations at SuperPower." [Online]. Available: http://www.superpower-inc.com/system/files/2015_SPI_New_Innovations.pdf. [Accessed: 25-Sep-2016].

[116] D. Hazelton, Y. Y. Xie, V. Selvamanickam, R. Anthony, J. C. Llambes, and T. Lehner, "High-performance 2G HTS wire for efficient and reliable electricity supply," in *2010 IEEE Conference on Innovative Technologies for an Efficient and Reliable Electricity Supply, CITRES 2010*, 2010, pp. 42–46.

[117] L. Miu *et al.*, "High Vortex Depinning Temperatures in YBCO Films with BZO Nanorods.: Discovery For University of Southampton," *J Supercond Nov Magn*, vol. 26, no. 4, pp. 1167–1173, 2013.

[118] Yi-Yuan Xie *et al.*, "Second-Generation HTS Conductor Design and Engineering for Electrical Power Applications," *IEEE Trans. Appl. Supercond.*, vol. 19, no. 3, pp. 3009–3013, Jun. 2009.

[119] C. Kittel, *Introduction to solid state physics*. Wiley, 1986.

[120] J. G. Hust and L. L. Sparks, "Lorenz Ratios of Technically Important Metals and Alloys," *U.S. DEPARTMENT OF COMMERCE*, 1973. [Online]. Available: https://www.gpo.gov/fdsys/pkg/GOVPUB-C13-893f0102eec4d085d3730c71fa07d231/pdf/GOVPUB-C13-893f0102eec4d085d3730c71fa07d231.pdf.

[121] C. James, "The residual resistance of metals," *Phys. Educ.*, vol. 2, no. 6, pp. 315–316, 1967.

[122] D. Gall, "Electron mean free path in elemental metals," *Cit. J. Appl. Phys.*, vol. 119, p. 85101, 2016.

[123] W. Zhang *et al.*, "Influence of the electron mean free path on the resistivity of thin metal films," in *Microelectronic Engineering*, 2004, vol. 76, no. 1–4, pp. 146–152.

[124] Z. Cheng, L. Liu, S. Xu, M. Lu, and X. Wang, "Temperature dependence of electrical and thermal conduction in single silver nanowire," *Sci. Rep.*, vol. 5, no. 10718, 2015.

[125] Z. Cheng, "Temperature-dependent thermal and electrical conduction in metallic nanostructures," 2015.

[126] M. V. Kamalakar and A. K. Raychaudhuri, "Low temperature electrical transport in ferromagnetic Ni nanowires," *Phys. Rev. B - Condens. Matter Mater. Phys.*, vol. 79, no. 20, 2009.

[127] L. Sun *et al.*, "The electrical resistivities of nanostructured aluminium films at low temperatures," *J. Phys. D. Appl. Phys.*, vol. 50, no. 41, p. 415302, Oct. 2017.

[128] R. E. B. Makinson and A. H. Wilson, "The thermal conductivity of metals," *Math. Proc. Cambridge Philos. Soc.*, vol. 34, no. 03, p. 474, Jul. 1938.

[129] B. Feng, Z. Li, and X. Zhang, "Prediction of size effect on thermal conductivity of nanoscale metallic films," *Thin Solid Films*, vol. 517, pp. 2803–2807, 2008.

[130] R. C. Munoz and C. Arenas, "Size effects and charge transport in metals: Quantum theory of the resistivity of nanometric metallic structures arising from electron scattering by grain boundaries and by rough surfaces," *Appl. Phys. Rev.*, vol. 4, no. 1, 2017.

[131] A. J. Learn and D. W. Foster, "Resistivity, grain size, and impurity effects in chemically vapor-deposited tungsten films," *J. Appl. Phys.*, vol. 58, no. 5, pp. 2001–2007, 1985.

[132] S. A. Anderson, "THE THERMAL CONDUCTIVITY OF INTERMETA," University of Cape Town, 1994.

[133] H. M. Rosenberg, *Solid State: Introduction to the Physics of Crystals for Students of Physics, Materials Science and Engineering*. Oxford University Press, 1978.

[134] S. Yoneoka *et al.*, "Electrical and thermal conduction in atomic layer deposition nanobridges down to 7 nm thickness," *Nano Lett.*, vol. 12, no. 2, pp. 683–686, 2012.

[135] H. Lin, S. Xu, X. Wang, and N. Mei, "Thermal and electrical conduction in ultrathin metallic films: 7 nm down to sub-nanometer thickness," *Small*, vol. 9, no. 15, pp. 2585–2594, 2013.

[136] G. S. Kumar, G. Prasad, and R. O. Pohl, "Experimental determinations of the Lorenz number," *J. Mater. Sci.*, vol. 28, no. 16, pp. 4261–4272, 1993.

[137] HyperPhysics, "Law of Dulong and Petit." [Online]. Available: http://hyperphysics.phy-astr.gsu.edu/hbase/thermo/Dulong.html#c1. [Accessed: 19-Jul-2018].

[138] HyperPhysics, "Debye Theory of Specific Heat." [Online]. Available: http://hyperphysics.phy-astr.gsu.edu/hbase/thermo/Debye.html#c2. [Accessed: 19-Jul-2018].

[139] Y. Y. Xie *et al.*, "Second-Generation HTS conductor design and engineering for electrical power applications," in *IEEE Transactions on Applied Superconductivity*, 2009, vol. 19, no. 3, pp. 3009–3013.

[140] S. B. Kim *et al.*, "Study on the Electrical Contact Resistance Properties With Various Winding Torques for Noninsulated HTS Coils," *IEEE Trans. Appl. Supercond.*, vol. 24, no. 3, pp. 1–5, Jun. 2014.

[141] M. Polak *et al.*, "Current transfer lengths and the origin of linear components in the voltage – current curves of Ag-sheathed BSCCO components," *Supercond. Sci. Technol.*, vol. 10, no. 10, pp. 769–777, 1997.

[142] M. Polak, P. N. Barnes, and G. a Levin, "YBCO/Ag boundary resistivity in YBCO tapes with metallic substrates," *Supercond. Sci. Technol.*, vol. 19, no. 8, pp. 817–820, 2006.

[143] A. Kuršumović, R. P. Baranowski, B. A. Glowacki, and J. E. Evetts, "Current transfer at superconducting Bi2Sr2CaCu2O8+δ–Ag joints," *J. Appl. Phys.*, vol. 86, no. 3, pp. 1569–1573, Aug. 1999.

[144] N. Bagrets, A. Augieri, G. Celentano, G. Tomassetti, K. P. Weiss, and A. Della Corte, "Investigation of ReBCO conductor tape joints for superconducting applications," *IEEE Trans. Appl. Supercond.*, vol. 25, no. 3, 2015.

[145] N. Bagrets, K.-P. Weiss, R. Nast, and R. Heller, "Correlation Between Resistances of Face-to-Face Soldered Joints and Interface Resistance Between Layers in Superconducting Tapes," *IEEE Trans. Appl. Supercond.*, vol. 28, no. 4, Jun. 2018.

[146] A. Stenvall, A. Korpela, J. Lehtonen, and R. Mikkonen, "Current transfer length revisited," *Supercond. Sci. Technol.*, vol. 20, no. 1, pp. 1253–1253, Jan. 2007.

[147] H. Dreuth and H. Dederichs, "Evaluation of low resistance contacts on YBa2Cu3O7 thin films using the transmission line model," *Supercond. Sci. Technol.*, vol. 6, no. 21, pp. 464–468, 1993.

[148] D. Shi, Ed., *High-temperature superconducting materials science and engineering : new concepts and technology*. Pergamon, 1995.

[149] J. Spurrell, "Thermal Stability and Current Transfer in Twisted-pair Helium Gas-cooled MgB 2 DC Cables by," University of Soutahmpton, 2017.

[150] Y. Iwasa, *Case Studies in Superconducting Magnets*. Boston, MA: Springer US, 2009.

[151] M. N. Wilson and R. Wolf, "Calculation of minimum quench energies in Rutherford cables," *IEEE Trans. Appiled Supercond.*, vol. 7, no. 2, pp. 950–953, 1997.

[152] A. Stenvall, A. Korpela, J. Lehtonen, and R. Mikkonen, "Formulation for solving 1D minimum propagation zones in superconductors," *Phys. C Supercond. its Appl.*, vol. 468, no. 13, pp. 968–973, 2008.

[153] A. Ishiyama *et al.*, "Normal transition and propagation characteristics of YBCO tape," *IEEE Trans. Appl. Supercond.*, vol. 15, no. 2 PART II, pp. 1659–1662, 2005.

[154] E. Martínez *et al.*, "Quench development and propagation in metal/MgB2conductors," *Supercond. Sci. Technol.*, vol. 19, no. 1, pp. 143–150, 2006.

[155] A. Stenvall, A. Korpela, R. Mikkonen, and G. Grasso, "Stability considerations of multifilamentary MgB2 tape," *Supercond. Sci. Technol.*, vol. 19, no. 2, pp. 184–189, Feb. 2006.

[156] X. Wang, U. P. Trociewitz, and J. Schwartz, "Near-adiabatic quench experiments on short y Ba2 Cu3 O7-δ coated conductors," *J. Appl. Phys.*, vol. 101, no. 5, p. 053904, Mar. 2007.

[157] S. B. Kim, A. Ishiyama, H. Okada, and S. Nomura, "Normal-zone propagation properties in Bi-2223/Ag superconducting multifilament tapes," *Cryogenics (Guildf).*, vol. 38, no. 8, pp. 823–831, 1998.

[158] M. N. Wilson, *Superconducting Magnets*. Clarendon, 1982.

[159] R. H. Bellis and Y. Iwasa, "Quench propagation in high Tc superconductors," *Cryogenics (Guildf).*, vol. 34, no. 2, pp. 129–144, Feb. 1994.

[160] T. Huang, E. Martínez, C. Friend, and Y. Yang, "Quench characteristics of HTS conductors at low temperatures," *IEEE Trans. Appl. Supercond.*, vol. 18, no. 2, pp.

1317–1320, 2008.

[161] E. A. Young, S. Chappell, I. Falorio, and Y. Yang, “Quench characteristics of a Stabilizer-Free 2G HTS conductor,” *IEEE Trans. Appl. Supercond.*, vol. 19, no. 3, pp. 2500–2503, 2009.

[162] SuperPower, “Soldering Instruction.” [Online]. Available: http://www.superpower-inc.com/system/files/SP_Soldering+Instructions_2012FEC_v1.pdf. [Accessed: 25-Sep-2016].

[163] SuperPower, “High Quality Joints for Superpower 2G HTS Wire.” [Online]. Available: http://www.superpower-inc.com/system/files/SP_2G+Wire+Joints_2012FEC_v1_0.pdf. [Accessed: 25-Sep-2016].

[164] ASTM International, “Standard Test Method for Apparent Shear Strength of Single-Lap-Joint Adhesively Bonded Metal Specimens by Tension Loading (Metal-to-Metal),” 2005. [Online]. Available: https://www.astm.org/Standards/D1002.htm.

[165] Copper Development Association Inc, “Application Data Sheet : Mechanical Properties of Copper and Copper Alloys at Low.” [Online]. Available: http://www.copper.org/resources/properties/144_8/.

[166] J. E. Jensen, W. A. Tuttle, R. B. Stewart, H. Brechna, and A. G. Prodell, *Electrical Resistivity of Some Metallic Elements and Commercial Alloys*. 1980.

[167] O. Prakash, A. Kumar, A. Thamizhavel, and S. Ramakrishnan, “Evidence for bulk superconductivity in pure bismuth single crystals at ambient pressure,” *Science (80-.).*, vol. 355, no. 6320, 2017.

[168] Hyperphysics, “Superconductivity.” [Online]. Available: http://hyperphysics.phy-astr.gsu.edu/hbase/Solids/scond.html. [Accessed: 24-Jul-2018].

[169] H. Search, C. Journals, A. Contact, M. Iopscience, and I. P. Address, “The low temperature electrical resistivity of aluminium,” *5. Phys. F Met. Phys*, vol. 19, pp. 3–6, 1973.

[170] D. P. Joshi and K. Sen, “Effect of grain size on the resistivity of polycrystalline material,” *Sol. Cells*, vol. 9, no. 4, pp. 261–267, 1983.

[171] A. S. Rogachev *et al.*, “Structure evolution and reaction mechanism in the Ni/Al reactive multilayer nanofoils,” *Acta Mater.*, vol. 66, pp. 86–96, 2014.

[172] M. A. Easton and D. H. StJohn, “Improved prediction of the grain size of aluminum alloys that includes the effect of cooling rate,” *Mater. Sci. Eng. A*, vol. 486, no. 1–2, pp. 8–13, 2008.

[173] J. E. Jensen, W. A. Tuttle, R. B. Stewart, H. Brechna, and A. G. Prodell, “Thermal conductivity of some solids,” *Brookhaven Natl. Lab. Sel. Cryog. Data Noteb.*, 1980.

[174] J. J. Corruccini, R.J. , Gniewek, “Specific Heats and Enthalpies of Technical Solids at Low Temperatures,” 1960.

[175] J. E. Jensen, W. a Tuttle, R. B. Stewart, H. Brechna, and a G. Prodell, *VIII. Specific heat of some solids*. 1980.

[176] J. J. Begot, R. Caudron, P. Faivre, A. Lasalmonie, and P. Costa, “Chaleur spécifique a basse température de la famille Ni1-xCo xAl : observations en relation avec la structure de bandes de ces composés et la transformation martensitique de Ni1+yAl 1-y,” *J. Phys. Lettres*, vol. 35, no. 11, pp. 225–228, 1974.

[177] Y. S. Touloukian and E. Al, “Thermophysical Properties of Matter - Specific Heat: Nonmetallic Solids,” 1970.

[178] J. E. Keem and J. M. Honig, “Selected electrical and thermal properties of undoped nickel oxide,” 1978.

[179] J. A. T. B. Costa, “In situ electrical resistivity of thin-film β-NiAl under Ar irradiation at 77 K,” *Phys. Rev. B*, vol. 45, no. 17, pp. 9626–9628, 1992.

[180] J. Matteau, “NanoBond ® Assembly – A Rapid , Room Temperature Soldering Process,” 2012. [Online]. Available: https://nccavs-usergroups.avs.org/wp-content/uploads/TFUG2014/2014_7matteau_INDIUM.pdf.

[181] NIST, “Crystallographic Databases,” 2016. [Online]. Available: https://www.nist.gov/programs-projects/crystallographic-databases.

[182] NIST, “Instrument Response Std for X-Ray Powder Diffraction,” 2008. [Online]. Available: https://www-s.nist.gov/srmors/view_detail.cfm?srm=1976a.

[183] R. W. Powell, C. Y. Ho, and P. E. Liley, “Thermal conductivity of selected materials,” 1966.

[184] N. Bagrets, C. Barth, and K. P. Weiss, “Low temperature thermal and thermo-mechanical properties of soft solders for superconducting applications,” *IEEE Trans. Appl. Supercond.*, vol. 24, no. 3, pp. 2013–2015, 2014.

[185] D. M. Jacobson and G. Humpston, “Gold coatings for fluxless soldering,” *Gold Bull.*, vol. 22, no. 1, pp. 9–18, 1989.

[186] “Soldering to Gold,” *Indium Corporation*. [Online]. Available: http://www.indium.com/soldering-to-gold/. [Accessed: 13-Jul-2018].

[187] Copper Development Association Inc, “Cryogenic Properties of Copper.” [Online]. Available: https://www.copper.org/resources/properties/cryogenic/. [Accessed: 17-Mar-2019].

[188] H. Murrmann and D. Widmann, “Current Crowding on Metal Contacts to Planar Devices,” *IEEE Trans. Electron Devices*, vol. 16, no. 12, pp. 1022–1024, 1969.

[189] S. Grover, “Effect of Transmission Line Measurement (TLM) Geometry on Specific Contact Resistivity Determination Effect of Transmission Line Measurement,” Rochester Institute of Technology, 2016.

[190] J. D’Errico, “Shape Language Modeling,” *MATLAB*, 2017. [Online]. Available: https://uk.mathworks.com/matlabcentral/fileexchange/24443-slm-shape-language-modeling. [Accessed: 14-Jun-2018].

[191] G. A. Kirby *et al.*, “First Cold Powering Test of REBCO Roebel Wound Coil for the EuCARD2 Future Magnet Development Project,” *IEEE Trans. Appl. Supercond.*, vol. 27, no. 4, 2017.

[192] J. Fleiter, A. Ballarino, L. Bottura, W. Goldacker, and A. Kario, “Characterization of roebel cables for potential use in high-field magnets,” *IEEE Trans. Appl. Supercond.*, vol. 25, no. 3, pp. 3–6, 2015.

[193] W. Goldacker *et al.*, “High current DyBCO-ROEBEL Assembled Coated Conductor (RACC),” *J. Phys. Conf. Ser.*, vol. 43, no. 1, pp. 901–904, 2006.

[194] S. Terzieva *et al.*, “Transport and magnetization ac losses of ROEBEL assembled coated conductor cables: measurements and calculations,” *Supercond. Sci. Technol.*, vol. 23, no. 1, p. 14023, 2010.

[195] N. Glasson, M. Staines, R. Buckley, M. Pannu, and S. Kalsi, “Development of a 1 MVA 3-phase superconducting transformer using YBCO Roebel cable,” *IEEE Trans. Appl. Supercond.*, vol. 21, no. 3 PART 2, pp. 1393–1396, 2011.

[196] E. A. Young, S. Chappell, I. Falorio, and Y. Yang, "Quench characteristics of a Cu-stabilized 2G HTS conductor," *IEEE Trans. Appl. Supercond.*, vol. 21, no. 3 PART 3, pp. 3062–3065, 2011.

[197] I. Falorio, E. A. Young, and Y. Yang, "Quench characteristic and minimum quench energy of 2G YBCO tapes," *IEEE Trans. Appl. Supercond.*, vol. 25, no. 3, pp. 2–6, 2015.

[198] H. Onnes, "Further experiments with liquid helium. H. On the electrical resistance of pure metals etc. VII. The potential difference necessary for the electric current through mercury," *KNAW, Proc.*, no. September, pp. 1406–1430, 1913.

[199] D. Dew-Hughes, "The critical current of superconductors: An historical review," *Fizika Nizkikh Temperatur (Kharkov)*, vol. 27, no. 9–10. pp. 967–979, 2001.

[200] A. Kario, "HTS Roebel cables for the EuCARD-2 'Future Magnets,'" *3rd EuCARD-2 Annual Meeting*, 2016. [Online]. Available: https://indico.cern.ch/event/489475/contributions/1166833/attachments/1263291/1868932/23.04.2016_Malta_Kario.pdf. [Accessed: 13-Dec-2017].

[201] Y. Yang *et al.*, "Quench characteristics of bi2212 solenoid insert coils in background field up to 20 T," *IEEE Trans. Appl. Supercond.*, vol. 21, no. 3 PART 2, pp. 2432–2435, 2011.

[202] L. Ye, D. Cruciani, M. Xu, S. Mine, K. Amm, and J. Schwartz, "Magnetic field dependent stability and quench behavior and degradation limits in conduction-cooled MgB 2 wires and coils," *Supercond. Sci. Technol.*, vol. 28, no. 3, p. 035015, Mar. 2015.

[203] X. Wang, S. V. P. S. S. Pamidi, U. P. Trociewitz, and J. Schwartz, "Self-field quench behavior of multifilamentary MgB2 wires in liquid helium," *Cryogenics (Guildf).*, vol. 48, no. 11–12, pp. 469–477, 2008.

[204] L. Shirshov *et al.*, "STABILITY STUDY OF HIGH-CURRENT SUPERCONDUCTING CABLES FOR ACCELERATOR MAGNETS," in *21st Russian Particle Accelerator Conference*, 2008.

[205] A. V. Gurevich, R. G. Mints, and A. A. Pukhov, "Quench energies of composite superconductors," *Cryogenics (Guildf).*, vol. 29, no. 3, pp. 188–190, Mar. 1989.

[206] F. Grilli, M. Vojenčiak, A. Kario, and V. Zermeño, "HTS Roebel Cables: Self-Field Critical Current and AC Losses Under Simultaneous Application of Transport Current and Magnetic Field," *IEEE Trans. Appl. Supercond.*, vol. 26, no. 4, 2016.

[207] A. Iwamoto, R. Maekawa, and T. Mito, "Thermal Conductivity of Stycast 1266 and 2850FT at Cryogenic Environment."

[208] K. Muneo, K. Yoshihiro, T. Osamu, and M. Itaru, "Pool-Boiling Heat Transfer in Liquid Nitrogen," *J. Nucl. Sci. Technol.*, vol. 18, no. 7, pp. 501–513, 1981.

[209] T. M. Flynn, J. W. Draper, and J. J. Roos, "The Nucleate and Film Boiling Curve of Liquid Nitrogen at One Atmosphere," in *Advances in Cryogenic Engineering*, Boston, MA: Springer US, 1962, pp. 539–545.

[210] M. Majoros, M. D. Sumption, E. W. Collings, and N. J. Long, "Stability, inter-strand contact resistance, and AC losses in YBCO Roebel cables," *IEEE Trans. Appl. Supercond.*, vol. 24, no. 3, pp. 6–10, 2014.

[211] M. Majoros, M. D Sumption, E. W. Collings, and N. J. Long, "Inter-strand current sharing and ac loss measurements in superconducting YBCO Roebel cables," *Supercond. Sci. Technol.*, vol. 28, no. 5, 2015.

Appendix I: MATLAB code

MATLAB code is used to investigate current transfer characteristics of lap joint by using SLM function in section 4.4.2.3.

```
% The data of L(:,1) and V(:,1) for the measured voltage V(x) versus the distance from left end joint.

[slm_1(:,1),Xp(:,1),Yp(:,1)]=slmengine(L(:,1),V(:,1),'plot','on','degree',3,'knots',n,'increasing'
,'on','leftvalue',0,'concaveup','on','rightslope',slope);

Yp(:,1) = slmeval(Xp(:,1),slm_1(:,1));

plotslm(slm_1(:,1));

% Create and plot SLM spline approximation of V(x).

% ‘knots' - controls the number of knots used, or the number of equally spaced knots.

% ‘degree’ - controls the degree of the piecewise Hermite function.

%       = 'constant' --> Use a piecewise constant "Hermite"

%       = 'linear' --> Use a piecewise linear Hermite

%       = 'cubic' --> Use a piecewise cubic Hermite

% As a concession to memory, valid synonyms for 'constant', 'linear', and 'cubic' are respectively

% integers 0, 1, & 3.

% 'increasing' - controls monotonicity of the function.

% leftvalue' - controls the function value at its left hand endpoint.

% 'concaveup' - controls curvature of the function.

% 'rightvalue' - controls the function value at its right hand endpoint basing on the slope for the linear

% curve fitting with measured V(x).

dYp(:,1) = diff(Yp(:,1));

dXp(:,1) = diff(Xp(:,1));

xlabel Displacement;

for i=1:1:1000

X(i,1)= (Xp(i,1)+Xp(i+1,1))/2;

Y(i,1)= dYp(i,1)/dXp(i,1);

end

plot(X(:,1),Y(:,1),'b')

% Create and plot differential function SLM_V’(x).
```

Appendix II: Publications

1. W. Bailey, Q. Zhang, I. Falorio, J. Pelegrin and Y. Yang, “Locked Rotor and Transient Tests of a 100 kW HTS Machine,” *IEEE Trans. Appl. Supercond.,* vol. 27, no.4, June 2017.
2. E. A. Young, Q. Zhang and Y. Yang, “Transport Properties of Single MgB2 Filaments Extracted from Multifilamentary Conductors,” *IEEE Trans. Appl. Supercond.,* vol. 27, no.4, June 2017.
3. Q. Zhang, E. Young, L. Cavalucci, A. Kario, W. Goldacker, A. Usoskin, L. Bottura, and Y. Yang, “Performance and quench characteristics of a Pancake Coil Wound with 2G YBCO Roebel Cable” *IEEE Trans. Appl. Supercond.,* vol. 28, no.4, June 2017.